Summer 1998

Nonlinear Stability and Control of Three-Dimensional Boundary Layers

Erik Janke
Old Dominion University

NONLINEAR STABILITY AND CONTROL OF THREE-DIMENSIONAL BOUNDARY LAYERS

by

Erik Janke
Diplom-Ingenieur für Luft- und Raumfahrttechnik, November 1993
Technische Universität Berlin, Germany

A Dissertation Submitted to the Faculty of
Old Dominion University in Partial Fulfillment of the
Requirement for the Degree of

DOCTOR OF PHILOSOPHY

AEROSPACE ENGINEERING

OLD DOMINION UNIVERSITY
August 1998

Approved by :

(Director) Ponnampalam Balakumar

Robert L. Ash

Colin P. Britcher

Chester E. Grosch

ABSTRACT

NONLINEAR STABILITY AND CONTROL OF THREE-DIMENSIONAL BOUNDARY LAYERS

Erik Janke
Old Dominion University
Director: Prof. P. Balakumar

The linear and nonlinear evolution of steady and traveling disturbances in three-dimensional incompressible boundary layer flows is studied using Parabolized Stability Equations (PSE). Extensive primary stability analyses for the model problems of Swept Hiemenz flow and the DLR Transition experiment on a swept flat plate are performed first. Second, and building upon these results, detailed secondary instability studies based on both the classical Floquet Theory and a novel approach that uses the nonlinear PSE are conducted. The investigations reveal a connection of unstable secondary eigenvalues to both the linear eigenvalue spectrum of the undisturbed mean flow and the continuous spectrum, as well as the existence of an absolute instability in the region of nonlinear amplitude saturation. Third, a passive technique for boundary layer transition control using leading edge roughness is examined utilizing a newly developed implicit solution method for the nonlinear PSE. The results confirm experimental observations and indicate possible means of delaying transition on swept wings.

In the present work, both the solution of the boundary layer equations for the mean flow and the explicit PSE solver are based on a fourth-order-accurate compact scheme formulation in body-oriented coordinates. In the secondary instability analysis, the Implicitly Restarted Arnoldi Method is applied.

ACKNOWLEDGEMENTS

First and foremost, I would like to express my sincerest appreciation to my dissertation advisor, Professor Ponnampalam Balakumar. His high academic standards and goals, as well as his genuine interest in science were both very challenging and motivating, and also of a significant impact on the present work. I am truly thankful for his profound guidance and look forward to continuing our collaboration on new research projects. Further, I feel obligated to express my special recognition for the details of his recent development of a implicit solution method for the PSE, that he provided me with.

Special thanks also to the members of my dissertation committee, Prof. Robert L. Ash, Prof. Colin P. Britcher and Prof. Chester E. Grosch of Old Dominion University for reviewing this dissertation and for valuable comments. Generous access to computational resources was provided by the Institute for Computer Applications in Science and Engineering (ICASE) in Hampton, Virginia, U.S.A., without which this research would not have been possible. I would further like to extend my appreciation to my former advisor Prof. Dr.-Ing. Nitsche of the Technical University of Berlin, Germany and his former student Dr. Svoboda, as well as to Debbie Carraway of NASA Langley Research Center for pointing me to Old Dominion University in 1994.

I am also indebted to my parents and my brother in every possible way for their support during the years abroad. It is my distinct goal to return that care within the years to come.

Finally, I want to thank my classmates for many discussions and useful comments, in particular Dr. Menzies, Dr. Massey and Dr. Pandya, as well as K. Ghayour, D. Kaushik, P. Martin and J. Samarasingham.

NOMENCLATURE

English Symbols

A	Disturbance amplitude
AL	Attachment-line
c	Chord length
CF	Crossflow
C_p	Pressure coefficient
C_{gr}	Group velocity
C_{ph}	Phase velocity
f, F	Frequency
l	Length
m	Similarity factor
N	N-factor
p, P	Pressure; disturbance and mean flow quantity
Q	Freestream velocity
Re	Reynolds number
t, T	Time
TS	Tollmien-Schlichting
Tu	Turbulence level
x_1, x_2, x_3	Body-oriented coordinate system
$\bar{x}_1, \bar{x}_2, \bar{x}_3$	Galilean coordinate system

Greek Symbols

α	Angle of attack

α_1, α_3	Primary and secondary wave number in the x_1-direction
β_1, β_3	Primary and secondary wave number in the x_2-direction
β_h	Hartree-parameter
δ	Boundary layer thickness
λ	Wave length
η	Wall-normal coordinate
ν	Kinematic viscosity
ϕ	Sweep angle
Φ	Stream function
Ψ	Wave angle
σ	Growth rate
θ	Phase of the disturbance quantities
Θ	Angle of the inviscid streamline
ω	Frequency

Vector Quantities

$\mathbf{k}$	Wave vector
$\mathbf{Q}$	Mean flow
$\mathbf{q}$	Disturbances
$\mathbf{v}$	Disturbance velocities

Subscripts

avg	Average
cf	Crossflow
c, cross	Direction of the crossflow component
tang	Direction tangential to the inviscid streamline

e	edge
imag	Imaginary part of complex quantity
max	maximal
real	Real part of complex quantity
rms	Root-mean square
rough	Roughness
s, stat	Stationary
t, trav	Traveling
tot	Total
0	basic flow, or local quantity
∞	freestream

Superscripts

*	dimensional quantity, complex conjugate

CONTENTS

LIST OF FIGURES

LIST OF TABLES

CHAPTER 1

INTRODUCTION

The physics of the flow transition from laminar to turbulent in a wall-bounded flow is of great importance for a variety of industrial applications. Whether it is the flow over a heat-exchanger on a high-altitude aircraft, the flow approaching a supersonic engine-inlet, or the envisioned implementation of hybrid laminar flow control into future swept wing designs for commercial aircraft, the thorough understanding of physical mechanisms during the entire transition process is crucial for changing the flow characteristics of any flow of interest favorably.

Laminar Flow Technology (LFT) is one of the key technologies to achieve an improved aerodynamic performance on the next generation commercial aircraft like the Ultra-High Capacity Aircraft A3XX being developed within the European Airbus Industrie consortium, or the High-Speed Civil Transport developed in cooperation between the Boeing Company and the National Aeronautics and Space Administration (NASA). Even though the estimates of potential benefits in the aerodynamic performance of sub-, super- and transonic aircraft through LFT vary widely, it is reasonable to state that a significant decrease in the aerodynamic drag can be achieved by delaying the laminar-turbulent transition of the flow on the main lifting and control surfaces of an aircraft. Since highly swept geometries are an essential part of state-of-the-art aircraft designs, the path of the flow evolution into turbulence on these geometries is of particular interest.

Figures 1.1 and 1.2 show two recent attempts to control the laminar-turbulent transition using the Hybrid Laminar Flow Control (HLFC) technology, i.e. the combined application of a laminar wing geometry and boundary layer suction. Figure 1.1 shows a

---

The format of this dissertation is based on the *American Institute of Aeronautics and Astronautics Journal* and was typeset in LaTeX 2_ε by the author.

scaled model of the vertical stabilizer of the Airbus A320 that will be flown in a free-flight experiment in the Summer of 1998. The suction panel which porous surface contains millions of small laser-drilled holes is seen in the leading edge region of the fin.

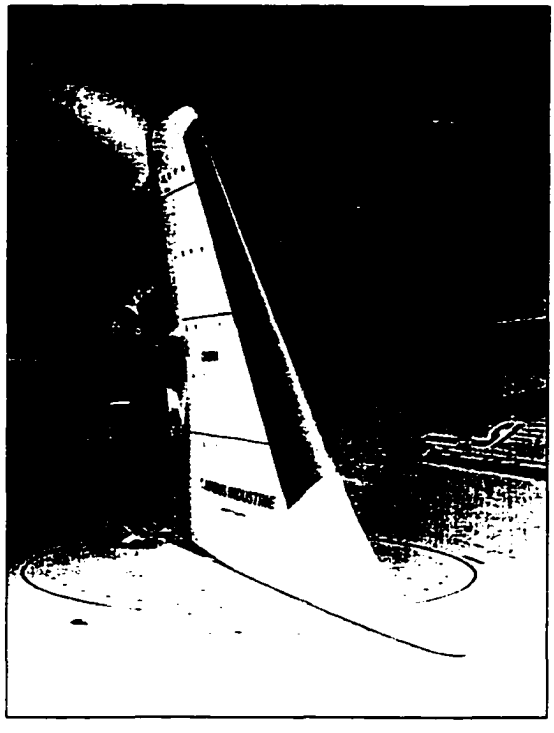

Figure 1.1: Model of the A320 fin in the S1 wind tunnel (courtesy of ONERA)

A supersonic HLFC-experiment was conducted in 1996 on a modified F-16 at NASA Dryden Research Center, U.S.A. Figure 1.2 shows the top-view of the modified F-16 where the suction glove is seen as the dark area on the left-hand side of the wing. Despite a successful control of the laminar-turbulent transition, this technology will not be utilized for the first generation High-Speed Civil Transport because of a need for further subsystem demonstrations.

In order to show the complexity of the flow field that needs to be modeled computationally while studying the effects of boundary layer suction, figure 1.3 shows the

close-up view of the suction glove of the modified F-16 in comparison to a dime. Typical hole spacings are of the order of 0.2-0.5mm, and the applied suction distribution com-

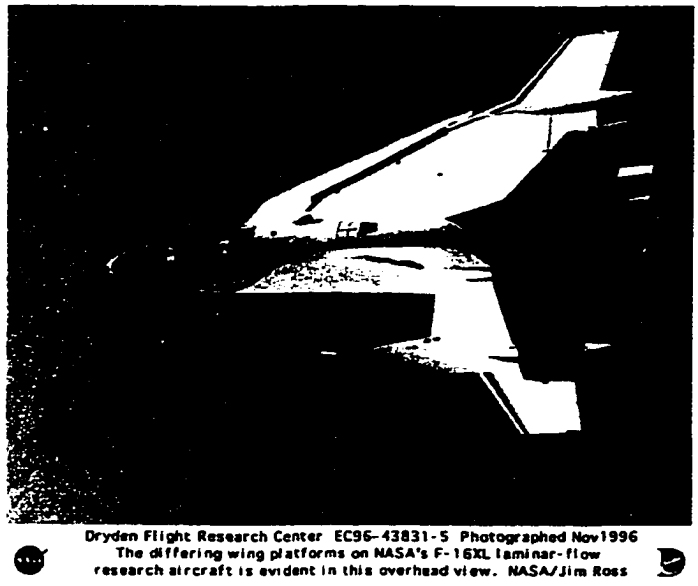

Figure 1.2: Top-view of the F-16XL with HLFC-glove (courtesy of NASA Dryden)

monly varies in space. Thus, the challenges for the development of adequate numerical tools are remarkable.

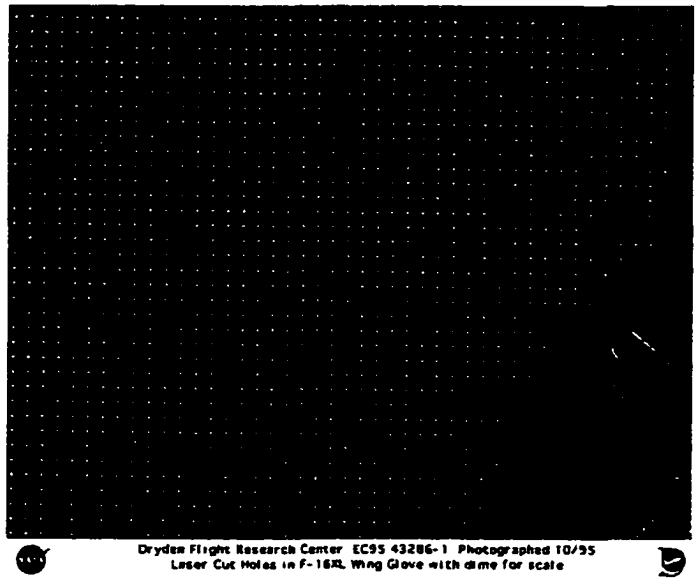

Figure 1.3: Hole configuration for F-16XL suction panel (courtesy of NASA Dryden)

1.1 Basics of Crossflow Instability

The flow across infinite swept geometries is usually characterized as quasi-three-dimensional, since the inviscid mean flow quantities do not vary in the spanwise direction. The terminology of three-dimensional boundary layer profiles chosen herein considers the fact that the local boundary layer profiles are indeed functions of all three coordinates, as shown below. Assuming that care has been taken to avoid an early transition due to leading edge contamination[1], the stability of such a mean flow to finite disturbances present in the boundary layer is governed by three instability mechanisms. First, the stagnation flow along the line where the flow attaches to a swept geometry, called attachment-line flow and depicted in figure 1.4, is subject to a viscous[2] attachment-line instability mechanism. An unstable attachment-line flow can make any attempt of maintaining laminar

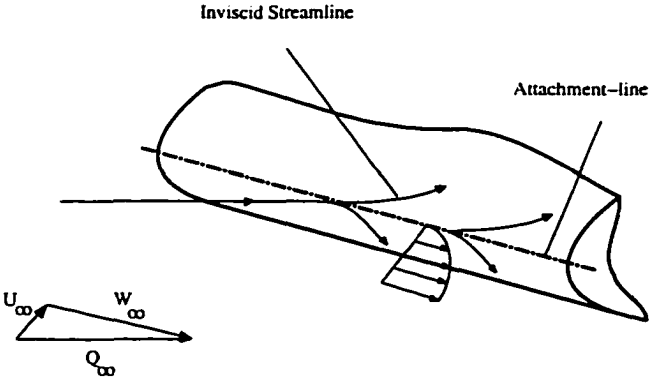

Figure 1.4: Attachment-line region on an infinite swept geometry

flow along the chordwise direction obsolete by causing the transition to turbulence at the attachment-line. Second, the inviscid mechanism of the crossflow (CF) instabil-

[1] Leading edge contamination refers to the presence of isolated turbulent spots near the leading edge that can be caused by turbulent structures originating from the junction of wing and fuselage that travel along the leading edge and across the wing, or by surface imperfections and insect debris.

[2] An instability mechanism is denoted as viscous when inviscidly stable mean flow profiles (no inflection points are present in the mean flow profiles) become unstable due to the presence of viscous forces. This was first shown by Tollmien and Schlichting for the Blasius boundary layer in 1929.

ity develops in the region directly behind the attachment-line where strong favorable pressure-gradients exist. Third, another viscous mechanism, referred to as Tollmien-Schlichting (TS) instability, is dominant in regions of small, or zero pressure gradients along the chord. There, the boundary layer flow is approximately two-dimensional.

Since the present work is entirely related to the investigation of the crossflow instability, its origin will be explained in the following. Figure 1.5 shows the top-view of an infinite swept wing. Due to the constant spanwise outer flow component W_∞ and the variation of the chordwise outer flow component $U_e(x)$ along the chord, the inviscid streamline experiences a varying curvature in that direction. Being parallel to the leading edge at the attachment-line where $U_e(x=0)=0$, its direction gradually changes with an

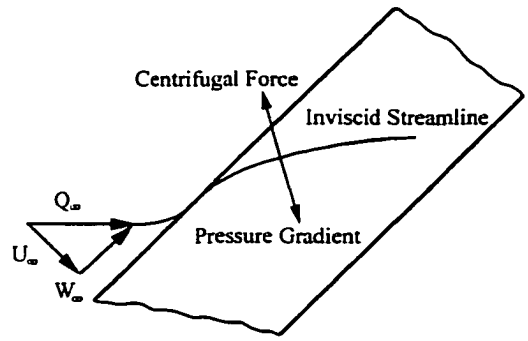

Figure 1.5: Inviscid streamline curvature across a swept wing

increasing distance from the leading edge. Thereby, this streamline curvature causes a centrifugal force at each chordwise position that is balanced by the local pressure gradient at the boundary layer edge (see figure 1.5).

Within the boundary layer, however, the velocity decreases to zero at the wall, whereas the normal pressure gradient remains constant. Consequently, a force imbalance exists perpendicular to the inviscid streamline that causes a velocity component pointing in the direction of the pressure gradient. Because of the balanced forces at the boundary

layer edge and the no-slip condition at the wall, this mean flow component is zero at both locations, but non-zero within the boundary layer. Hence, an inflection point must exist. Figure 1.6 depicts the resulting tilted three-dimensional boundary layer profile. The presence of an inflection point in the mean flow profile of the crossflow component is the origin of the inviscid Rayleigh-instability mechanism called crossflow instability.

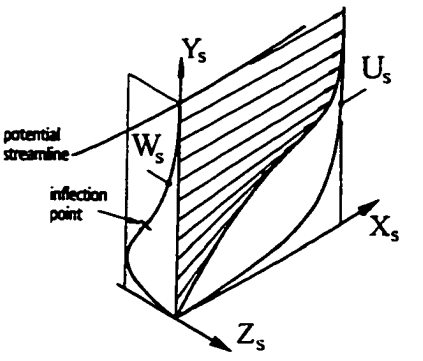

Figure 1.6: 3D boundary layer profile in a streamline-oriented coordinate system

In order to explain the action and interaction of the TS and the CF-instability mechanisms, the three qualitatively different outer velocity distributions as shown in fig-

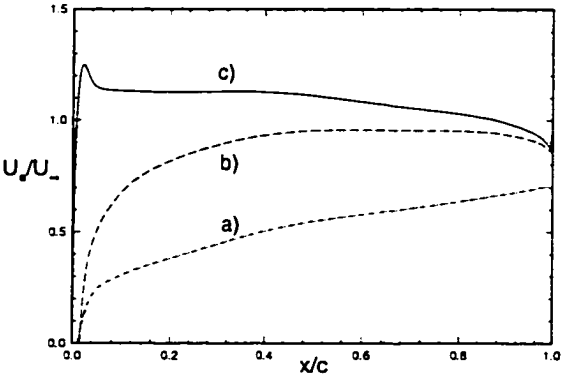

Figure 1.7: Generic outer flow distributions across infinite swept geometries

ure 1.7 will be discussed next. The example shown in Curve a) represents the existence of a favorable pressure gradient over the entire chord length that supports the development

of a flow that is only subject to a crossflow instability. Next, Curve b) shows an example where the velocity increases until x/c=0.50 and then remains almost constant over the rest of the chord. In that case, a region of a favorable pressure gradient gradually merges with a region where the pressure gradient is small, or zero, and both the CF and the TS-instability mechanism are present in the flow. An important observation in this case is that the crossflow component of the mean flow never changes sign along the chord. Finally, Curve c) shows the most typical outer velocity distribution for airfoil designs at an angle of attack. Seen is a region of a very strong flow acceleration near the leading edge with a local velocity maximum that is immediately followed by a region where the velocity remains constant. Hence, the region where the CF-instability mechanism dominates is rapidly followed by a region of a prevailing TS-instability. Also, due to the strong acceleration and deceleration of the flow in the region close to the leading edge, two inflection points are present in the outer flow distribution (see Curve c)). In contrast

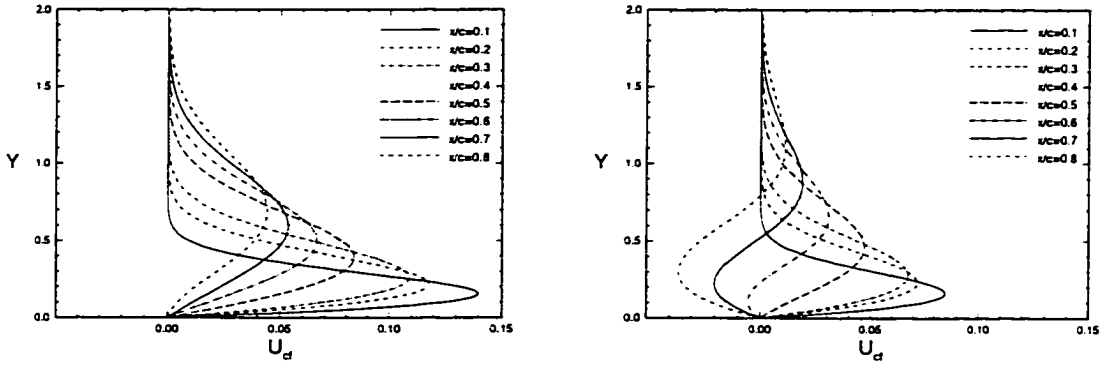

a) Non-inflectional outer flow

b) Inflectional outer flow

Figure 1.8: CF-mean flow profiles for different outer flow distributions

to the case of Curve b), the sign of the crossflow mean flow component now changes sign along the chord. Figures 1.8(a) and 1.8(b) show the mean flow profiles corresponding to

the outer flow distributions for the Curves a), b) and c), respectively. The change of sign in the crossflow components seen for the velocity distribution of Curve c) is assumed to introduce qualitatively new features into the flow. In addition to the presence of both the TS and the CF-instability, the two mechanisms might interact in that case. Evidence for the presence of qualitatively new flow physics is seen in the existence of an additional inflection point in the CF-mean flow profiles (see figure 1.8(b)). Also, convergence problems observed from linear computations using the Parabolized Stability Equations for these outer flow distributions, and strong oscillations in the computed growth rates at some distance downstream of the first sign change occurrence in the CF-mean flow component are further indications for the action of a different mechanism. However, the investigation of this topic is not part of the presented work and will be considered in future projects.

1.2 Motivation

In the region close to the leading edge of swept wings or vertical stabilizers, strong favorable pressure gradients are present in the flow that cause an inviscid crossflow instability as explained in Section 1.1. Due to the strong growth of the disturbances in that region, the transition to turbulence frequently occurs within the first few percent of the chord length. Despite the large volume of previous work, there is still a need to better understand the fundamental physics of this transition process and to obtain quantitative data about the parameters and mechanisms involved in it. For the eventual goal of reliably predicting and delaying the transition location on commercial transport aircraft, it is also necessary to develop mathematical models and numerical tools that appropriately capture the flow physics and that can be applied efficiently and robustly.

Industrial applications require computations for many different configurations within a short turn-around time. The state-of-the-art of transition prediction methods for these applications is still dominated by correlations between experimental data and linear PSE methods (e^N-methods[3]), as well as by data-base methods[4]. Despite the quick access to results obtained from these methods, it is known that the incorporated assumptions miss essential details of the modeled flows. Particularly for the regions governed by the crossflow instability mechanism, where a relatively short region of strong linear disturbance growth is followed by a significantly long region of nonlinear saturation, neglecting the nonlinear interaction of the disturbances has a major impact on the results.

From the above, academic and practical motivations for research on the stability of three-dimensional boundary layer flow can be formulated. The academic motivations include gaining a deeper understanding of the physical mechanisms involved in the transition process and their interaction, as well as expanding the knowledge about their origin. Crucial for successful research in this field is the close cooperation between experimental and numerical work, where the focus of the numerical work gradually shifts into a more guidance-oriented position for the experimental investigations. The practical challenge then is to make the developed numerical tools like the nonlinear PSE methods more efficient, robust and suitable for large-scale industrial applications.

[3]These correlate measured transition locations to predictions of the linear PSE with the aim of finding a universal N-factor for the transition prediction.

[4]These rely on data-bases of boundary layer profiles and growth rates based on similarity solutions for different mean flows and computed using local theory, respectively.

1.3 Present Research

The current research focuses on the linear and nonlinear stability of incompressible three-dimensional boundary layers and their control. The consideration of incompressible flows is particularly motivated by two factors. First of all, the physics of incompressible flows are less complex than those of compressible flows. Hence, for an identification of important instability and transition mechanisms, it is appropriate to study incompressible flows first. Secondly, there is a wide variety of experimental data available for the validation of numerical models for incompressible flows.

The work presented herein is directed towards a further development of efficient and robust computational methods that accurately model the physics of transitional three-dimensional boundary layer flows, and towards explaining experimental observations in the transition region.

This problem is approached by first solving the quasi-three-dimensional boundary layer equations for general infinite swept geometries in order to obtain an accurate mean flow. Second, linear and nonlinear PSE methods are developed and adapted to the present application of three-dimensional boundary layer flow. For the numerical solution of both the boundary layer equations and the nonlinear PSE, a fourth-order-accurate compact scheme formulation has been implemented.

Third, the experimentally observed phenomenon of a secondary instability is investigated taking two approaches. Here, the classical Floquet theory is accompanied by an attempt to model the secondary instability more straightforwardly using the PSE. Finally, a newly developed and very robust implicit solution method for the nonlinear PSE will be presented together with an investigation of passive laminar flow control using leading edge roughness elements.

In particular, Chapter 2 contains a survey of the literature related to the investigation of crossflow instability dominated incompressible boundary layer flows. The most important experimental work will be reviewed first, followed by compilation of recent theoretical and numerical investigations, by selected work on boundary layer control, as well as a summary of the state-of-the-art in transition physics.

In Chapter 3, the approach to the mean flow computation is described. A brief explanation of the panel method used for the outer flow computation is presented in connection with the derivation of a fourth-order-accurate compact scheme formulation for the solution of the boundary layer equations.

In Chapter 4, the stability theory for three-dimensional wall-bounded flows will be discussed. Considering the spatial eigenvalue problem for locally parallel flows in Section 4.2, the linear and nonlinear PSE methods will be derived in Section 4.3. The last section of this chapter contains a description of the Floquet theory applied to the investigation of the secondary instability. The detailed documentation of the Implicitly Restarted Arnoldi algorithm, a solution method for the resulting large eigenvalue problems that was recently developed at Rice University [1], concludes this chapter.

Chapter 5 presents a comprehensive stability analysis of the stagnation flow along a swept infinite geometry, referred to as Swept Hiemenz flow. Presenting the existing similarity solution to the boundary layer equations for this problem in the first section, the second section shows results from an extensive linear stability analysis using local methods and the linear PSE. The findings of this analysis are then used as input for the nonlinear stability analysis using the PSE in Section 5.3. The last section of this chapter studies the secondary instability using temporal Floquet theory and the nonlinear PSE, where both approaches extend previous work.

The investigation of a crossflow instability dominated boundary layer flow in a model experiment performed in Göttingen, Germany is considered in Chapter 6. Following the structure of the previous section, linear and nonlinear PSE results, as well as results from the secondary instability analysis are compared to the experimental measurements. Of particular interest in this chapter is the examination of the region of nonlinear saturation. Experimental observations of an explosive growth of traveling disturbances in that region motivate this investigation of the existence of an absolute[5] instability.

In Chapter 7, a newly developed implicit method for the solution of the nonlinear PSE is presented. Its computational efficiency and robustness are documented and compared to the explicit solution method.

In Chapter 8, this implicit solution method is applied to a passive laminar flow control problem. Results are presented that confirm experimentally observed nonlinear wave-interaction phenomena that lead to a delay of the laminar-turbulent transition in boundary layers with favorable pressure gradients. Finally, Chapter 9 concludes the present study with general remarks and recommendations for future investigations.

[5]Instabilities with a zero phase velocity and an algebraic growth are referred to as absolute instabilities. Instead of developing in the downstream direction, they grow at a fixed location.

CHAPTER 2

LITERATURE REVIEW

2.1 Introduction

The progress in the development of numerical tools for modeling three-dimensional boundary layer flows offers a new approach for the investigation of their fundamental flow physics, and for examining possible and effective ways to control them favorably. Rather than relying primarily on experimental findings in identifying important mechanisms in the flow and performing numerical investigations mainly for the purpose of code validations, the maturing of numerical techniques like PSE methods and Direct Numerical Simulation (DNS) within the last 10 years enables a closer cooperation between the two approaches. In fact, due to the extensive amount of data obtained from highly resolved computations, the focus of the numerical methods is being shifted towards serving as guidance tools for detailed experimental investigations.

Starting with a historical perspective of the research on the stability of flows along swept geometries, this review focuses on three topics. First, the literature on experiments related to the stability and transition of three-dimensional boundary layers will be considered. Second, the substantial amount of theoretical and numerical work on the linear, nonlinear, and secondary stability of three-dimensional boundary layers will be reviewed. Third, selected publications regarding the control of boundary layers will be cited. This chapter will be concluded with a summary of the current state-of-the-art in detected physical mechanisms involved in the laminar-turbulent transition for the considered flows, and in numerical methods for transition prediction.

2.2 Historical Perspective

In 1952, an early boundary layer transition close to the leading edge of swept wings was detected by Gray [6] during flight tests conducted at the Royal Aircraft Establishment in Great Britain. Using evaporation techniques in the experiments, he observed streaky streamwise patterns on the surface and a dependence of the transition location on a critical freestream velocity. The documentation of this experiment might mark the first observation of both the existence of an attachment-line instability, as well as a crossflow instability in the literature.

A decade later, swept wing designs at Handley Page Ltd. in Great Britain and at Northrop in the United States attempted to maintain laminar flow along the entire chord length. Being aware of the above instabilities, the designers used suction systems to control the laminar boundary layer flow for the first time in the history of modern wing design. However, the presence of a strong leading edge contamination, originating from the junction of wing and fuselage and propagating along the leading edge, caused a transition to turbulent flow that was too strong to be controlled by boundary layer suction.

Pioneering experiments were then performed by Gregory et al. [7], Gaster [8], and Pfenninger [9], in order to obtain more qualitative and quantitative insight into the acting instability mechanisms. In addition to the establishment of empirical relations for the prediction of transition and to first achievements in developing the theory of flow stability, these activities eventually lead to the first practicable passive flow control device on swept wings, the Gaster bump. The Gaster bump essentially separates the boundary layer on the outer part of a swept wing from the contamination originating from the junction of wing and fuselage by creating a vortex across the wing, as depicted

in figure 2.1. Thereby, a new stagnation point is introduced in the spanwise direction and an uncontaminated attachment-line boundary layer starts to develop from there.

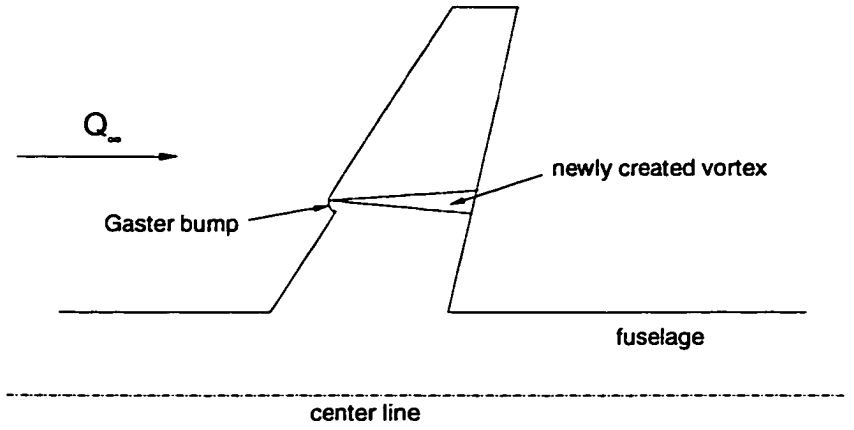

Figure 2.1: Gaster bump configuration on a swept wing

After these initial periods of research activities, it was not until the early 1980's that a new series of experiments emerged due to the need for new aerodynamic technologies for civil transport aircraft.

2.3 Experimental Studies

A variety of experimental investigations on the stability of three-dimensional boundary layers began in the early 1980's at different aerodynamic research centers around the world. Of particular interest for the present study are the experiments performed in France at the Office National d'Études et de Recherches Aérospatiales (ONERA), in Germany at the Deutsches Zentrum für Luft- und Raumfahrt (DLR), in Japan at the National Aerospace Laboratories (NAL), at various institutions in the United Kingdom, and in the U.S.A. at Arizona State University (ASU).

2.3.1 The ONERA D-Wing Experiments

The series of experiments performed between the early 1980's and today began at the French governmental research institution ONERA. Starting with the work of Coustols [5] under the supervision of Guiraud, Arnal, Cousteix and others in 1983, their systematic investigations were aimed at a detailed characterization of the transition due to crossflow instability, at a derivation of empirical relations for a reliable prediction of the transition location, and at a comparison of the experimental findings with results from the linear stability theory. For a symmetric airfoil with a chord length of 0.35 m, measurements were performed for various angles of attack at sweep angles between 40° and 60° and at speeds of around 80 m/s. The applied measurement techniques included the use of pitot probes, hot-wires and hot-films. A generic experimental configuration is depicted in Chapter 8.

In a subsequent publication by Arnal et al. [10] in 1984, a detailed description of the outer flow conditions can be found. The freestream turbulence level was specified as $Tu=1/3\cdot\sqrt{(\bar{u}')^2+(\bar{v}')^2+(\bar{w}')^2}/U_\infty=0.15\%$, and the Reynolds numbers ranged from $Re_\infty=1.8\cdot10^6$ to $Re_\infty=4\cdot10^6$. The major findings of the work in References [5] and [10] are summarized as follows.

For outer flows without a strong suction peak that causes an inflection point in the outer flow distribution, the prediction of the transition location by two empirical criteria was satisfactory. However, large discrepancies between the experiments and the empirical predictions were found for outer flow distributions with a strong suction peak (inflectional). Also, findings from a linear stability analysis were presented. The results for the most amplified wavelength agreed well with the experimental data. Further, the spanwise variation of the streamwise velocity component was documented, and an inter-

esting observation of a downstream variation of the most amplified spanwise wavelength was reported (wavelength coalescence). Finally, a strong dependence of the transition location on the freestream turbulence level was noted.

In a later work by Arnal and Juillen [11] in 1987, the main focuses were on investigating the interaction of the streamwise and the crossflow instability mechanisms, on studying the problems related to leading edge contamination, and on the measurement of the transition location. Two different wing sections were investigated.

First, from the experiments on the symmetric ONERA D-wing, they reported fluctuation amplitudes of 20% of the freestream velocity at x/c=0.60, and unstable frequencies of less than 500 Hz for a freestream velocity of 48 m/s and a non-inflectional outer velocity distribution. As in the previously cited work [10], they found that the ratio of the most amplified stationary wavelength and the local boundary layer thickness remains constant at a value of about four in the chordwise direction. For the same symmetric wing and considering an inflectional outer flow distribution, they investigated the interaction of crossflow and streamwise (TS) instabilities next. Here, they found a significant change in the most amplified frequencies in the regions of negative and positive pressure gradients. The initially present strong low frequency crossflow instabilities ($f < 500$ Hz) were replaced by unstable frequencies of the order of 1 kHz in the region of a positive pressure gradient. This observation was related to the presence of TS-instabilities in the later chordwise regions.

Second, they investigated the problem of a leading edge contamination caused by either an existing attachment-line instability, or by wing/body interference for a cambered wing. They found the critical Reynolds number for the onset of turbulent spots at, or near the leading edge between Re=240 and Re=276.

In 1998, Arnal et al. [12] presented an overview of the capabilities and limitations of current transition prediction methods for wings with applied boundary layer suction. Using the symmetric wing as described above in a low freestream turbulence level environment (Tu=0.07%) and at tunnel speeds of 75 and 95 m/s, they established a data base for various wing configurations. The issue of the leading edge contamination was solved using a Gaster bump close to the wing root. From their results, Arnal et al. [12] concluded that the linear transition prediction method using the assumption of a constant spanwise wave number is superior to the envelope method[1]. Also, they documented the positive impact of suction on the crossflow instability dominated boundary layer and presented results from nonlinear PSE computations including boundary layer suction for different transition scenarios.

2.3.2 The DLR Transition Experiments

Shortly after the start of the experiments on infinite swept wings in France, experimental investigations on the flow across a swept flat plate were started in Göttingen, Germany by Nitschke-Kowsky and Bippes [13] in 1986. A description of the experimental setup and the purely crossflow instability dominated mean flow is given in Chapter 6. The literature on the various experiments performed is substantial. Therefore, the work reviewed herein is limited to the most relevant publications for the presented results.

Besides other findings on primary stationary and traveling disturbances, Bippes and Nitschke-Kowsky [14] discussed experimental observations of inflectional mean flow profiles at later chordwise positions which originate from the presence of spanwise periodic stationary disturbances in 1987. In 1988, these experiments were continued by Müller and Bippes [15]. Their tests were particularly aimed at more detailed measure-

[1]The envelope method considers the disturbances with the maximal growth rate at each chordwise position and is based on local theory.

ments for a comparison of the results with those from a linear stability theory, as well as at obtaining input data for DNS computations and a secondary instability analysis of the flow using a mathematical model developed by Fischer and Dallmann [16]. Using hot-wire and oil-flow visualization techniques, and documenting an additional experiment in a water-towing tank, they found a constant ratio of the most amplified wavelength and the local boundary layer thickness of 3.3, and a significantly long region of nonlinear disturbance growth stretching over 30% of the chord length. The unstable traveling disturbances were found between frequencies of 50 and 200 Hz. Also, they documented an interaction of stationary and traveling disturbances starting at x/c=0.50, and attributed the location of the transition onset to positions where the averaged mean flow component tangential to the inviscid streamline takes minimal values. Performing tests at different freestream turbulence levels (FTL), they found that the stationary disturbances grow faster and larger for lower FTL than for higher FTL, but nevertheless transition occurs at slightly higher Reynolds numbers in the lower FTL environment. By performing the same measurements on a plate that was shifted in the spanwise position, they also showed that the stationary disturbances originate from surface roughness.

Results from finer resolved measurements performed by Bippes et al. in 1989 were presented and compared to linear stability results in [17]. For a freestream Reynolds number of $Re_\infty = 6.3 \cdot 10^5$, they tested the same model as above under different freestream turbulence levels. The following observations were reported. The saturation onset of the stationary disturbance and their final saturation level depended on the freestream turbulence level. The saturation level varied between 10% of the freestream velocity and 20% for freestream turbulence levels of 0.15% and 0.05%, respectively. Also, the most amplified frequency changed depending on the environmental conditions, where

higher frequencies are observed in lower FTL environments. The latter observation was attributed to the presence of secondary instabilities in the flow that were caused by larger amplitude stationary disturbances.

For the purpose of a very detailed comparison of local linear stability results with experimental data, Deyhle et al. [18] performed measurements of the most amplified wavelength and the wave angle, the group and phase velocities, as well as the angle of the group velocity vector at a chordwise position of x/c=0.70 in 1993. Even though this position is situated far in the nonlinear region of the disturbance evolution, the agreement of the linear stability results with the experimental data was good, except for the results for the group velocity and the angle of the group velocity vector. This discrepancy was attributed to measurement uncertainties.

The most comprehensive summary of the performed series of experiments for the swept flat plate model problem at the DLR was given by Deyhle and Bippes [2] in 1996. Besides a detailed review of previous experimental work, they presented results from measurements in systematically varied environmental conditions in order to study the receptivity of this three-dimensional boundary layer to surface roughness, freestream turbulence and sound. Deyhle and Bippes reported that the receptivity to three-dimensional surface roughness was the most important mechanism of introducing and selecting the initial disturbances in the boundary layer, whereas the receptivity to two-dimensional roughness and sound was found to be of negligible influence. Another important result in Reference [2] was the establishment of a relation between the transition Reynolds number, the saturation amplitudes of the stationary disturbances and environmental conditions as surface roughness and freestream turbulence level. Using an intermittency approach to determine the transition location, they concluded that the

longest region of laminar flow is not obtained for the smallest freestream turbulence levels, but for the conditions that provoke the most limited growth of the stationary disturbances.

2.3.3 The Experiments in Japan

A number of experiments on the investigation of crossflow instability dominated flows has been conducted at the National Aerospace Laboratory (NAL) and at Tokyo University in Japan. Three characteristic experiments will be reviewed in this subsection.

In 1994, Takagi and Itoh [19] performed experiments on a yawed circular cylinder in different freestream turbulence level environments at wind tunnel speeds of 25 m/s. Besides the comparison of their data to the predictions by linear stability theory, the main objective of their work was to see whether traveling disturbances can play a role in the transition process in a low freestream turbulence environment when the effect of leading edge roughness is weakened by the presence of a thicker boundary layer. During their very detailed measurements, they found that no stationary crossflow vortices develop, if the boundary layer thickness is large enough to damp micron-sized distributed roughness. In that case, only traveling disturbances were detected in the experiments. Further, they determined the wave angles of the traveling disturbances to be about 11-14° with respect to the constant phase lines, and noted that the most amplified frequencies gradually decreased in the downstream direction. In 1996, Kohama et al. [20] used hot-wire velocimetry and visualization techniques on a swept flat plate model similar to the one used in the DLR experiments to document the final stages of the transition process. They showed some spatial structure of the secondary instability using smoke visualization techniques and determined the propagation angles and spatial locations of the primary and secondary instability structures. Distinguishing a

lower frequency primary instability (f $\simeq$ 100 Hz) at the foot of each crossflow vortex close to the wall and a higher-frequency secondary instability (f $\simeq$ 1 kHz) at the back of the primary vortices, they argued that the transition to turbulence is triggered by the high-frequency secondary instability located at a normal location of about half the boundary layer thickness. The propagation angles were specified as 60° and -55° for the most amplified primary and secondary traveling disturbances, respectively, where the angles were measured with respect to the freestream flow direction.

Recent work by Takagi et al. [21] on the rotating-disc flow problem focused on disturbances caused by streamline curvature (SC). In their experiment, they showed the existence of the theoretically predicted two unstable families of crossflow instabilities (Mack [22], Malik et al. [23]). By means of an acoustic point-source forcing, they were able to excite the otherwise less amplified disturbance family with a critical Reynolds number less than the more amplified crossflow instabilities. Further, they observed that a weak impulse forcing of the SC disturbances drastically suppressed the more unstable crossflow instabilities, and that continuous forcing lead to a bypass-type[2] transition.

2.3.4 The Swept Wing Experiments at ASU

Preceding the series of experiments on the crossflow instability on swept wings at Arizona State University (ASU), U.S.A., a swept flat plate experiment was performed by Saric and Yeates [24] at the Virginia Polytechnic Institute and State University, U.S.A. in 1985. Using an experimental setup similar to the DLR experiment, Saric and Yeates [24] documented the existence of a wave-interaction mechanism in the flow that caused a strong amplification of a wavelength that was half the most amplified

[2]The transition with bypass is described as a transition type where the phases of disturbance growth as described in Chapter 4 are bypassed and the turbulence is reached more directly by a mechanism that is not well understood.

wavelength (half-wavelength periodicity). The existence of this mechanism was also confirmed in theoretical work by Reed [25] where she showed the presence of a parametric resonance between the most amplified wavelength λ_{max} and the wavelength $\lambda_{max}/2$ in the region of finite amplitude saturation. In 1989, the actual work at ASU started with the experiment by Dagenhart et al. [26] on a 45°-swept wing. For a model chord length of 1.83 m and wind tunnel speeds up to 35 m/s, the experiments were performed at an angle of attack of -4°, and for Reynolds numbers of an order-of-magnitude higher than in the DLR experiment. Typically, they obtained Reynolds numbers between $Re_\infty = 2.0 \cdot 10^6$ and $Re_\infty = 4.0 \cdot 10^6$. Also, a favorable pressure gradient was established over 71% of the chord length i.e., the growth of two-dimensional TS-waves was not expected in that region.

In 1991, a detailed investigation of the secondary instability mechanism was performed by Kohama et al. [27]. For the swept wing as described above, they used hot-wire and naphthalene visualization techniques to document the evolution of the disturbances in the region until x/c=0.50. In detail, they showed the development of the multiple inflection points in the averaged mean flow profiles due to the presence of a stationary crossflow vortex that caused the onset of high-frequency inviscid secondary instabilities. They noted that the transition due to the secondary instability was confined to a narrow region in the spanwise direction, and that the energy driving this process was produced by the ejection-like motion of co-rotating vortices near the edge of the boundary layer. Further, the spatial scales in the spanwise and chordwise direction were of the same order and corresponded to the boundary layer thickness in the region of the secondary instability. In detail, they reported high-frequency instabilities of f = 3.5 kHz at x/c=0.46, and a strong increase of the secondary growth rates (a factor of 10)

within half a wavelength. Once the secondary instability developed at one location, a cascade-like development of other instabilities triggered the breakdown to turbulence.

The aerodynamic quality of the ASU wind tunnel was specified by Radeztsky et al. [28] in 1994. They quoted a FTL level of 0.04% over the frequency range of 1-1000 Hz at tunnel speeds of about 20 m/s. Performing their experiments [28] at an angle of attack of 0° and for various configurations of leading edge roughness elements, as well as comparing their data to linear stability results, they concluded that linear stability theory correctly predicts the mode shapes of the stationary crossflow vortex, the wavelengths involved in the transition process (including a correct prediction of the most amplified wavelength), but fails to predict the growth of the stationary disturbances in the downstream direction correctly. The prediction of the disturbance growth was largely improved in the work of Reibert et al. [29] using the nonlinear PSE in 1996. Experimenting with different spanwise spacings of leading edge roughness elements, they showed that a careful spacing of the roughness elements produced well defined stationary disturbances in the flow whose downstream growth was well predicted by nonlinear PSE computations.

Introducing the Proper Orthogonal Decomposition (POD)[3] method for the identification of flow structures close to the transition location from non-intrusive surface shear stress measurements using hot-films, Chapman et al. [30] showed the presence of coherent structures in the flow as a result of the acting instability mechanisms in 1996. They characterized the POD as a useful tool for the detection of large scale structures and the onset of transition in the flow. In a subsequent work [31] in 1998, Chapman et al. used spatial auto-correlations in addition to the POD for the evaluation

[3]The POD was introduced by Lumley in 1967 and represents an objective technique that is used to decompose a flow field into various modes based on the mean-square energy. It is usually used to identify dominant structures in various flow regimes.

of hot-film surface shear stress measurements. There, they proposed a mechanism in the transitional flow that merges two neighboring primary crossflow vortices. Further, they argued that the large and small scale turbulent structures observed immediately after transition originate from the primary and secondary instability mechanisms prior to transition, respectively.

2.3.5 Other Experiments

In his classical experiment in 1985, Poll [32] investigated the flow along a long yawed cylinder at tunnel speeds of about 30 m/s, at freestream Reynolds numbers of $Re_\infty = 1.0 \cdot 10^6$ - $2.0 \cdot 10^6$ and at turbulence levels of 0.16%. Using china-clay and oil-visualization techniques, he documented the presence of stationary crossflow vortices in the flow. At occasional instances, he also measured a high-frequency secondary disturbance riding on top of the primary disturbances, where the frequency of the secondary disturbance was one order-of-magnitude higher than the most amplified primary frequency.

In 1996, Kachanov [33] performed experiments on a swept flat plate at the aerodynamic research facility ITAM in Novosibirsk, Russia. The freestream turbulence level in these experiments was given as 0.06% for tunnel speeds around 10 m/s. Of particular interest for the validation of numerical methods are his results with respect to the receptivity to surface roughness, surface waviness and surface vibrations.

2.4 Theoretical and Numerical Models

2.4.1 Fundamental Theoretical Work

One of the early theoretical developments on the stability of three-dimensional boundary layers was given by Gregory, Stuart and Walker [34] in 1955. Along with the

presentation of experimental results for rotating-disc flow, they developed the linearized equations of motion in curvilinear coordinates for parallel and non-parallel flows. Also, they derived theorems regarding the inviscid stability depending on the location of the inflectional points in the mean velocity profiles. The results were presented for Görtler instabilities and for crossflow instabilities.

In his pioneering work of 1969 [35], Mack presented a complete development of the linear stability theory for incompressible and compressible flows. In this subsection, the review will be restricted to his work on the stability of incompressible flows. There, he derived the stability equations and their linearized version, distinguished between the temporal and spatial stability concepts, reviewed different approaches to relate temporal and spatial stability results (Gaster [36]), and presented different forms of the stability equation. Further, he reviewed previous work on the asymptotic inviscid theory and presented numerical results from the solution of the Orr-Sommerfeld equation. Finally, he discussed earlier work by Gaster and by Stuart [34] on the stability of three-dimensional boundary layers, and even mentioned results on the theoretical investigation of the linear secondary instability (Greenspan-Benney theory[4]).

In 1978, Mack [22] developed the spatial stability theory for three-dimensional boundary layers further. He derived a method for treating spatially amplified disturbances with a complex group velocity and presented extensive results for the stability of Falkner-Skan-Cooke boundary layers for various pressure gradients and at different angles of the inviscid streamline. In his work, he predicted the existence of two unstable families of disturbances in three-dimensional boundary layers that propagate in opposite directions.

[4]In 1963, Greenspan and Benney developed an inviscid stability theory of time-dependent shear layers that approximates the distorted and inflectional mean flow profiles by simple expressions based on experimental data.

The linear stability of nonparallel boundary layers with pressure gradients and suction was studied by Saric and Nayfeh [37] in 1988. The effect of boundary layer growth was accounted for by using the method of multiple scales. They showed that including non-parallel effects bridges the gap between the experimental results for the neutral Reynolds number for Blasius flow and previous results using the parallel flow assumption, and further suggest a N-factor correlation for transition prediction. Meanwhile, however, their results have been re-evaluated and the discussion in Drazin and Reid [38] shows that the presented argumentation in [37] was not entirely consistent.

In 1991, Choudhari et al. [39] presented an alternative to the asymptotic approach to predict the receptivity to freestream disturbances in the infinite Reynolds number limit. Using the method of matched asymptotic expansions and a streamfunction formulation, they reduced the receptivity problem to an Orr-Sommerfeld-type problem in the Fourier space and showed more accurate results than obtained from the asymptotic theory for the Blasius boundary layer, for adverse pressure gradient boundary layers, and for a two-dimensional supersonic boundary layer.

Since the theoretical development of the PSE by Herbert and Bertolotti [40] in 1987, Herbert and co-workers have accomplished a substantial amount of work in documenting the applicability of the method to several two- and quasi-three-dimensional flow problems, and in advancing its effectiveness towards an application to engineering-type problems [41–44]. In 1997, Herbert presented an approach to solve the linear PSE for a fully three-dimensional mean flow [45] and showed the qualitative difference between the results from this novel and the conventional quasi-three-dimensional approach.

2.4.2 Numerical Schemes

The focus of this subsection is on the review of work regarding the development of accurate finite difference schemes for the solution of the PSE and the Navier-Stokes equations, as well as on the stability of these schemes.

In 1982, Malik et al. [46] developed a finite difference method for an application to the flow stability analysis of three-dimensional compressible boundary layer flows. Their two-point, fourth-order-accurate method belongs to the class of compact schemes, where the fourth-order-accuracy is achieved by utilizing the Euler-McLaurin formula (see Chapter 4).

Compact finite differences with spectral-like resolutions for first, second and higher-order derivatives were derived by Lele [47] in 1992. These finite difference schemes can be used on non-uniform grids and are also applicable for accurate interpolation and spectral-like filtering.

In 1995, Li and Malik [48] showed for a two-dimensional base flow that the PSE are not a well-posed initial value problem, and that some approximations are required to obtain a stable marching solution. They argued; however, that for practical applications convergence problems in the marching procedure arise from the elliptic remainder in the PSE consisting of the streamwise pressure gradient. Neglecting this term and thereby removing the limitation on the step size was shown to be of minor influence on the results for boundary layer flow applications.

2.4.3 Linear Stability Theory

Supplementary to the work reviewed in Subsection 2.4.1, selected papers on solely linear stability topics will be reviewed in this subsection. Additionally, most of the publications on nonlinear stability topics cited in Subsection 2.4.3 contain linear

stability results as well. The discussion of these, however, will not be subject of this subsection.

One of the earlier numerical approaches to the investigation of three-dimensional boundary layers was given by Bieler [49] in 1986. Solving the Orr-Sommerfeld problem, he found that stationary disturbances become unstable close to the neutral point, and that the traveling disturbances are more unstable than the stationary disturbances.

In 1992, Balakumar and Malik [50] investigated the linear stability of incompressible and supersonic boundary layer flows over a flat plate that are subject to disturbances originating from a harmonic point source. Computing the receptivity coefficients using Fourier-transformation techniques [51] and including non-parallel effects using the method of multiple scales, they computed the evolution of the most amplified disturbance downstream. Also, they documented the decay of three-dimensional effects close to the location of the point source in the downstream direction. Finally, their results showed the influence of the second unstable mode on the stability for higher Mach numbers, and their results matched experimental measurements of the spreading angle of the disturbances very well.

Stuckert et al. [52] investigated the stability of a supersonic boundary layer flow over swept wings using the linear PSE in body-oriented coordinates in 1993. By comparing their PSE results to different local stability codes, they concluded that the influence of non-parallel effects is Reynolds number dependent and cannot be generalized from the presented results.

Perhaps the most recent comprehensive review of the linear stability theory applied to boundary layer flows was given by Reed, Saric and Arnal [53] in 1996. They summarized previous work on temporal and spatial stability formulations, carefully dis-

cussed the value of the e^N-method by Smith and Gamberoni and by van Ingen for current transition prediction methods in three-dimensional flows, and listed current state-of-the-art numerical codes. Further, they reviewed the stability of two- and three-dimensional sub- and supersonic flows, as well as of the attachment-line flow. For the stability of incompressible three-dimensional boundary layers studied here, they pointed out the existence of both stationary and traveling unstable disturbances in the flow, which is in contrast to the existence of purely traveling unstable disturbances in two-dimensional flow. Also, they attributed the similarity between the angles of the most unstable disturbances and the growth rates for the stability of incompressible and transonic boundary layers to the inviscid character of the crossflow instability. Next, they presented a detailed discussion of different N-factor integration strategies and concluded that the constant spanwise wave number/constant frequency strategy is superior to the envelope method, mainly because of its distinction between crossflow and TS-instability (see also Arnal et al. [12]). Regarding the effects of curvature in the computation, Reed et al. discussed the stabilizing and destabilizing effects of including surface and in-plane curvature, respectively. However, they also pointed out the difficulties in determining a suitable coordinate system to incorporate in-plane curvature effects. Finally, they briefly discussed control concepts for the flow along swept wings.

Different strategies for the N-factor integration were also discussed in detail by Schrauf [54] in 1994 and by Schrauf et al. [55] in 1997. In Reference [55], they evaluated data obtained from flight tests with a Fokker F-100 aircraft for a comparison of the different strategies. Their results show that no universal N-factor for the transition on swept wings could be established. The most consistent correlations for the transition location were obtained by using the envelope method for compressible flows with curva-

ture effects, where the prediction was improved when they distinguished between CF- and TS-dominated transition scenarios. The constant wave number/constant frequency method[5] was considered less effective, since the actual transition occurred after the computed N-factor maximum in about 50% of the considered cases. These findings are in contrast to the results by Arnal et al. [12].

Very recently, the topic of linear stability of three-dimensional boundary layers was revisited by a number of investigators. In 1997, Lingwood [56] theoretically investigated the linear stability of attachment-line and Falkner-Skan-Cooke boundary layers. Using a Green's function formulation to investigate the response to an impulsive disturbance forcing, she determined the onset of an absolute instability along the attachment-line at Re=681, and for the Swept Hiemenz flow problem at Re=545.

Cooper and Carpenter [57, 58] studied the stability of the rotating-disc flow over a compliant wall. Coupling a single-layer viscoelastic model to the system of ordinary differential equations describing the linear stability, their results showed that wall compliance can be used to completely suppress absolute instabilities in this flow.

2.4.4 Nonlinear Stability Theory

Following the review on the development of the nonlinear theory of flow stability by Drazin and Reid in [38], its theoretical foundations were laid by Landau in 1944 and later refined by Landau and Lifshitz in 1959. They introduced the concept of sub- and supercritical stability and also defined the branching curves of neutral solutions as bifurcations. Subsequently, several other theories were developed to approximate the nonlinear evolution of the disturbance quantities in parallel flows. Among these are the concept of weakly nonlinear theory introduced by Malkus and Veronis in 1958, and by

[5]This method traces modes of constant wave number and constant frequency in the chordwise direction. It can be based on local theory, but also represents the typical approach taken in PSE computations.

Stuart in 1958, as well as asymptotic theories developed by Graebel in 1966, by Fraenkel in 1969, and by van Dyke in 1975. Due to the strong increase of available computational resources since the 1980's, and also due to the pioneering work of Herbert and Bertolotti [40] in 1987, the developed PSE methods allow for the physically appropriate modeling of the disturbance evolution including non-parallel mean flow effects with an affordable amount of computational work. The remainder of this subsection will review the work on the nonlinear stability of two- and three-dimensional boundary layers using the PSE.

In 1992, Bertolotti, Herbert and Spalart [59] investigated the linear and nonlinear stability of the Blasius boundary layer using their newly developed PSE formulation and temporal DNS computations. Noting a very good agreement of the PSE with the DNS results, they emphasized that the main benefits of the PSE formulation are the simultaneous incorporation of mean flow non-parallelism and nonlinearity, as well as the correct description of longer wavelength disturbances with drastically reduced computational effort compared to the DNS. They concluded that the impact of including the non-parallel effects on the results is weak, and that the maximal amplified frequency is higher than predicted by linear theory when finite amplitude effects are considered in nonlinear computations. Further, they attributed observed differences between the neutral curve for Blasius flow obtained from experiment and computation to an initial region of transient disturbance growth close to the location where the disturbances were introduced, to the definition of the growth rates, and to experimental uncertainties.

Using an extended PSE formulation that accounts for compressibility, surface curvature and nonlinearity, as well as assuming a linear receptivity to freestream turbulence, Herbert et al. [60] studied the effect of different turbulence levels and surface

curvature on the stability of flows over heated plates and a two-dimensional stator blade in 1993. They showed that the PSE correctly predict the effects of turbulence level, curvature, wall heating and pressure gradient on the transition process, and were able to closely predict the measured location of the transition onset for a stator airfoil.

Malik et al. [23] presented an extensive investigation of the Swept Hiemenz flow problem in 1994. Using their PSE formulation, they studied the linear and nonlinear stability of this flow, and also showed results from a secondary instability analysis using Floquet theory. In particular, they investigated the nonlinear interaction of stationary and traveling modes, showed that including a small amplitude traveling disturbance in the computations leads to an earlier saturation of the stationary disturbances at lower amplitude levels, and that the transition to turbulence is preceded by the onset of a high-frequency secondary instability that rides on top of the stationary vortex. Their work is referred to in more detail in Chapter 5.

Bertolotti [61] developed a method to compute the receptivity to surface roughness for non-parallel mean flows using the linearized Navier-Stokes equations. Expanding the surface geometry and the velocity field in Chebyshev polynomials and substituting this formulation into the linearized Navier-Stokes equations, he derived a set of ordinary differential equations that can be solved within a few minutes on a Sparc-10 workstation. Using the information about the initial disturbance amplitudes thus obtained in a subsequent PSE analysis, he computed the downstream disturbance evolution for the DLR experiment. Including a small traveling disturbance in the computations and allowing for the nonlinear interaction of stationary and traveling disturbances, he was able to very closely predict the experimentally observed amplitude evolution and the shape of the disturbance profiles.

A comprehensive review of the capabilities, advantages and limitations of the PSE was recently given by Herbert [44] in 1997. Starting with a review of the derivation of the PSE and different normalization concepts for incorporating the assumption of the small streamwise variation of the shape function in the growth rate computation, he pointed out that the convective nature of linear instabilities in boundary layer flows allows for an application of the linear PSE. This can be rigorously justified according to [44]. However, for an application of the nonlinear PSE, one needs to closely compare the obtained results to either DNS computations, or experimental results. Using the example of the Blasius boundary layer, he showed that the influence of non-parallel effects on the disturbance growth is larger for three-dimensional disturbances than for two-dimensional disturbances. Also, he presented results from a PSE computation for the modeling of the subharmonic secondary instability on a flat plate. Even though the number of the included Fourier-modes might have been too small in these computations [44], he concluded from the reasonable agreement of the PSE and DNS computations that it should be possible to perform PSE simulations of the transition onset by increasing the number of modes in the wave number and frequency domain. From nonlinear PSE computations for three-dimensional boundary layers and considering the nonlinear evolution of a single primary disturbance mode, he stated a weak influence of the initial amplitude on the saturation amplitude. From an investigation of the nonlinear compressible stability of the flow across a swept wing, he finally attributed the experimentally observed zig-zag transition pattern to the simultaneous growth and the nonlinear interaction of a broad band of disturbances. This observation also explains the often noted failure of the e^N-method to predict transition for three-dimensional boundary layer flows correctly .

2.4.5 Secondary Instability

The investigation of the secondary instability phenomenon in the regions of nonlinear disturbance saturation originated from the experimental studies by Klebanoff, Tidstrom and Sargent [62] in 1962 and the theoretical work by Görtler and Witting [63] in 1958. For other experimental investigations see Section 2.3. Further, a more detailed definition of the secondary instability will be given in Chapter 4.

Starting point for the review presented here is the work by Orszag and Patera [64] from 1983. Due to its origin from inflectional points in the velocity profiles and its persistence at high Reynolds numbers, they described the secondary instability as an inviscid instability and the prototype of a transitional instability that is inherently three-dimensional and has explosive growth rates. In [64], they investigated two-dimensional boundary layer flows for the onset of a secondary instability. After describing the primary stability and its nonlinear saturation for plane and circular Poiseuille flow, they studied the linear stability of these flows to infinitesimal three-dimensional disturbances using the linearized Navier-Stokes equations in a Galilean coordinate system and DNS. They detected secondary instability structures at locations of maximum vorticity in the flow field, and made another observation regarding the energy transfer between the primary disturbances, the secondary disturbances and the mean flow. They found that the energy transfer between the mean flow and the secondary disturbances is much larger than between the primary and the secondary disturbances. Finally, they showed the universality of the secondary instability mechanism by investigating the parallel Blasius boundary layer and plane Couette flow where they found similar instability characteristics.

Also in 1983, Herbert [65] presented results from an investigation of the secondary instability mechanism in plane channel flow. For existing periodic and two-

dimensional solutions to the Navier-Stokes equations on a neutral surface of the nonlinear dispersion relation in a moving frame of reference (equilibrium solutions), he superimposed infinitesimal three-dimensional secondary disturbances on the equilibrium solutions and solved the resulting linearized disturbance equations as an eigenvalue problem. He found that the three-dimensional secondary disturbances travel at slightly different phase speeds than the primary two-dimensional disturbances, and that the secondary disturbances grow by a factor of 100 within five cycles of a TS-wave. He further determined threshold amplitudes for the onset of various secondary instability modes and argued that the threshold amplitude physically represents a minimal vorticity concentration that must overcome the viscous damping of the secondary instabilities. Finally, he concluded that for a large enough amplitude of the secondary disturbances, the transition can be initiated by a single secondary disturbance mode.

As mentioned in Section 2.3, Reed [25] showed the existence of a parametric resonance in the region of the nonlinearly saturated stationary crossflow vortex of swept wing flows in 1987. Using the parallel flow assumption for the mean flow, neglecting the mean flow distortion as well as the amplitude variation in the streamwise direction due to the primary disturbances, and finally superimposing two three-dimensional secondary waves in a moving frame of reference on this flow, she established a Floquet system that was solved using a spectral collocation method. An unstable secondary structure was found away from the wall, and the results closely reproduced the experimentally observed modification of the dominant wavelength.

An investigation of the secondary instability in the flow across a swept wing was presented by Fischer and Dallmann [16] in 1987. They studied the flow over a 21°-swept model wing considering a parallel mean flow that is modified by the presence

of a stationary crossflow vortex. This choice was motivated by the strong receptivity of the stationary disturbances to surface roughness. Neglecting the mean flow distortion and the streamwise amplitude variation of the primary disturbances, and further superimposing three-dimensional secondary disturbances in a moving frame of reference on this flow, they studied the harmonic and subharmonic resonance case, as well as a combination of these two cases. They found a great influence of the higher harmonics of the fundamental secondary waves on the results, and thus, suggested to include at least four or five secondary modes in the computation. From their results, they concluded that the time dependent secondary disturbances modify the primary crossflow vortices in a way that they oscillate around their stationary equilibrium and are weakened and strengthened alternately. Also, they confirmed the half-wavelength periodicity seen by Saric and Yeates [24].

A comprehensive review of the findings and methods related to the investigation of the secondary instability topic was given by Herbert [66] in 1988. Presenting a very detailed overview of previous work on stability and transition analysis first, he summarized the findings on the parametric secondary instability for two-dimensional boundary layers as follows. Three-dimensional secondary instability can lead to different disturbance types. The primary resonance with a TS-wave produces peak-valley splitting once a threshold amplitude of the primary disturbances is exceeded, and initiates the fundamental breakdown to turbulence. A subharmonic resonance can occur at even smaller disturbance amplitudes and leads to the subharmonic turbulent breakdown. Secondary instability originates from the redistribution of vorticity into streamwise-periodic lumps near the critical layer, and the growth of the three-dimensional disturbances arises from a combined vortex tilting and stretching mechanism. Lastly, he pointed out that there is

an intricate connection between linear and secondary instability modes that is revealed by considering the limit of a zero amplitude of the primary disturbance. Next, he presented the mathematical background of the Floquet theory applied to the investigation of the linear secondary instability. Incorporating three assumptions in his analysis, namely the assumptions of a parallel mean flow, of a locally constant amplitude of the primary disturbance, and the neglect of the mean flow distortion (shape assumption), he derived the system of equations that travels with the phase speed of the primary disturbances (Floquet system). In his formulation, he incorporated both the concepts of spatial and temporal secondary growth of the disturbances, where the temporal problem is solved more often because of the linear appearance of the temporal wave number in the equations. Concluding his review on the secondary instability of mostly two-dimensional boundary layers, he stated that two essential elements need to be incorporated in the numerical analysis in order to improve the transition prediction based on a secondary instability analysis. First, the frequency and amplitude composition of the primary disturbances need to be considered, and second, a qualitative criterion for a self-sustained growth of the secondary disturbances needs to be established. Both elements cannot be provided by linear theory and require nonlinear computations.

A primary and secondary stability analysis of the DLR experiment was presented by Fischer and Dallmann [67] in 1991. Considering a purely steady primary disturbance, taking the same theoretical approach as in Reference [16] and using the amplitude information for the primary disturbances directly from the experimental values, they investigated the secondary instability for the harmonic and subharmonic resonance case, as well as for a combination case. Considering four secondary modes in their Fourier approximation, they found the earlier observed half-wavelength periodicity to be

also present in this experiment, but could not detect the very strong secondary growth of frequencies an order-of-magnitude higher than the primarily unstable frequencies.

A qualitatively new result indicating the existence of an absolute instability in the convectively unstable Blasius boundary layer was presented by Koch [68] in 1992. Computing nonlinear equilibrium solutions at finite Reynolds numbers using numerical bifurcation theory first, he examined the secondary instability of the such obtained modified mean flow using Floquet theory secondly. In contrast to previous work, he obtained the modified mean flow from a nonlinear computation, and hence, there was no need for incorporating the shape assumption. The remaining simplification of the problem, though, is the assumption of a parallel mean flow. Investigating the secondary disturbances that travel with the same phase speed as the primary disturbances (phase-locked), Koch found the existence of links between several unstable modes (coalescence) and of a modal degeneracy. The latter is defined as the coincidence of two or more amplified eigenvalues and their eigenvectors that leads to a locally algebraic growth of these disturbances. It is this mechanism that might explain the experimentally observed explosive growth of high-frequency disturbances in the late stages of the transition process.

In 1992, Balachandar et al. [69] studied the secondary instability of the rotating-disc flow problem. The main focuses of their temporal stability investigations were on the parametric dependence of the secondary disturbances on the stationary primary disturbance amplitude, on the vortical structure of the secondary disturbances, and on the nonlinear effects of the primary disturbances on the secondary disturbances. The primary disturbances were computed by solving a generalized linear eigenvalue problem for the complex frequency. For the formulation of the linear Floquet system, they incorporated the shape assumption and the assumption of a locally constant primary amplitude.

Considering six, or seven secondary modes in their computations, they presented very detailed results for the secondary growth rates and their dependence on the primary disturbance amplitudes and the Reynolds number. Further, they documented the shape of the secondary eigenfunctions. Examining both the fundamental and subharmonic resonance case, they found that the secondary frequencies and growth rates are insensitive to the exact nature of the resonance conditions. From these results, they also found the existence of several unstable eigenvalues in the secondary eigenvalue spectrum. For the purpose of a discussion of the effect of including the mean flow distortion in the computations, they performed a temporal DNS computation. From the observed qualitative agreement of the DNS results with the results obtained by solving the generalized eigenvalue problem for the primary disturbances, they concluded that despite quantitative changes due to nonlinearity, the overall picture of the secondary instability can be captured by incorporating the shape assumption. In detail, they reported an inclination of the secondary structure of about 44° with respect to the primary disturbances, and a decrease of the threshold amplitudes of the primary disturbances required for the onset of the secondary instability with increasing Reynolds number. These thresholds amplitudes varied between 7% and 10%.

Fischer, Hein and Dallmann [70] presented results from a secondary instability study for the DLR experiment where they again considered a mean flow that is modified by a saturated purely stationary crossflow vortex. Starting from previous results [67] that showed a low-frequency secondary instability, they artificially increased the amplitude of the primary and determined a higher-frequency secondary disturbance in that case. In a new approach that considered non-local secondary instability effects, Fischer et al. computed the different growth rates for the peaks and valleys in the pe-

riodically varying modified mean flow components along the spanwise direction. They defined a so-called characteristic function that describes the spanwise variation of the primary disturbances independently of the chordwise position. Considering the such described spanwise variations in a non-local secondary instability analysis, they accurately predicted the experimentally measured maximal and minimal streamwise fluctuations. This approach was presented in more detail by Fischer [71] in 1995.

In their previously cited work on the secondary instability in Swept Hiemenz flow, Malik et al. [23] obtained the modified mean flow from a nonlinear PSE computation. In agreement with the results for rotating-disc flow in [69], they found several unstable secondary eigenvalues in the region of the nonlinear saturation of the stationary primary crossflow vortex, an almost linear dependence of the secondary frequency on the secondary wave number, and an inclination of the secondary structure of about 50° with respect to the primary disturbances. In their computations, they included 17 and 33 secondary modes and found good agreement of the results for the two different spectral resolutions. Interestingly and in correspondence with experimental work by Kohama et al. [20], they found that the secondary instability structure rides on the back of the primary stationary vortex where the distortion of the boundary layer is maximal.

2.4.6 Direct Numerical Simulation

With the rapidly increasing power of shared and distributed memory computers, as well as of parallel computational methods, the tremendous computational effort necessary to conduct a well resolved Direct Numerical Simulation (DNS) of a fluid dynamics problem becomes more feasible. For example, the consensus at the First AFOSR International Conference on DNS/LES[6] at Louisiana Tech University in Ruston, Louisiana,

[6]Large Eddy Simulation

U.S.A. in 1997 was that hybrid methods consisting of DNS computations in regions of particular interest, and Euler-, or Reynolds-Averaged Navier-Stokes computations for the remaining flow regions might be a future strategy of investigating complex flow problems.

Starting with the early work on spatial DNS methods by Fasel in 1976 [72], a wide variety of temporal and spatial DNS solvers has been developed within the last 10 years. In the following, a selection of these approaches to solving the incompressible Navier-Stokes equations for three-dimensional boundary layers will be reviewed.

In 1988, Meyer and Kleiser [73] presented results from a temporal simulation of the DLR Transition experiment. In their formulation, they employed Fourier series expansions of the flow quantities in the horizontal directions, and a Chebyshev-matrix collocation method in the wall-normal direction. The pressure was calculated from a Poisson equation using the influence-matrix technique. For preserving the conservation of mass, they used a procedure similar to the "Tau-Method"[7]. Despite some differences between experiment and DNS, their computations predicted the development of the velocity fields at various stages of transition, the mean flow distortions and the development of the wall-shear stress well.

Building upon well tested DNS codes for the transition on a flat plate (References [74, 75]), Joslin et al. [76] showed results from spatial DNS computations for swept wedge flow in 1994. Their formulation in Cartesian coordinates used a Chebyshev collocation method in the wall-normal direction, fourth-order finite differences for the pressure equation, sixth-order compact finite differences for the momentum equations in the streamwise direction, and a Fourier series approximation on a staggered grid in the

[7]The "Tau-Method" uses pre-computed auxiliary solutions to eliminate the errors arising from the decoupling of continuity and momentum equations.

spanwise direction. For the time-advancement, they applied an implicit Crank-Nicholson differencing for the diffusion terms in the normal direction and a fourth-order, three-stage explicit Runge-Kutta method for the time derivatives. The disturbances were introduced using periodic blowing and suction through the surface. They found that adjacent individual stationary disturbances spread in the region of linear growth, eventually leading to the wavelength coalescence experimentally observed by Arnal and Juillen [11].

In 1996, Müller et al. [77] presented temporal DNS results for a mean flow adapted to the DLR experiment. They found that the breakdown to turbulence originated from spanwise positions of minimal vorticity and maximal rms-values. In a similar simulation by Wintergerste and Kleiser [78] in 1996, a secondary crossflow vortex was detected close to the wall and a vortex-splitting mechanism was observed just prior to the turbulent breakdown (see Chapter 5).

Starting in 1991 with the work on grooved channel flow by Liu et al. [79], a number of explicit and implicit, incompressible and compressible spatial DNS codes were developed under the supervision of Liu [80–82]. Liu and co-workers derived multilevel adaptive methods that allow for the simulation of the entire transition process on airfoils and wings. The main features of their codes are summarized as follows. First, they utilized curvilinear coordinates and applied a fourth-, or sixth-order accurate discretization in space. Further, they implemented a multigrid Full Approximation Scheme and the newly developed method of line-distributive relaxation. The time integration was performed using various methods ranging from backward Euler-steps to five-stage Runge-Kutta methods. In the recent work by Liu et al. [82] that perhaps represents the first DNS computation for the compressible flow along a swept wing geometry, they quoted a CPU-requirement of 100 hours on the Cray C-90 for 30,000 time steps.

2.5 Control of Three-dimensional Boundary Layer Flow

The work reviewed in this section represents only a small selection of the available literature on active and passive boundary layer control. It is restricted to cases where the control of a crossflow instability dominated three-dimensional boundary layer was the objective.

Accompanying the experiments at ASU reviewed in Subsection 2.3.4, a systematic investigation of the effect of two- and three-dimensional leading edge roughness, as well as of freestream sound on the flow stability downstream was conducted starting with the work by Radeztsky et al. [83] in 1993. One of the objectives of this work was to establish a data base for the validation of methods to compute the receptivity to surface roughness. Using the ASU swept wing model, they investigated three different surface qualities with distributed roughness heights of 9 μm, 0.5 μm, and 0.25 μm. They suggested that the distributed roughness height near the leading edge might be a quantitative measure for the transition N-factor. Placing different isolated three-dimensional roughness elements near the leading edge, they further investigated the dependence of the transition location on the roughness geometry. They found that a minimum roughness diameter of eight percent of one stationary crossflow wavelength is necessary to influence the transition, and that the transition is a function of the roughness Reynolds number[8] Re_k. Also, the streamwise location of the roughness elements was found to be important. Radeztsky et al. recommended that the roughness elements should be placed closely behind the neutral point to have a significant impact on the downstream transition. Neither a measurable receptivity to two-dimensional roughness, nor to freestream sound was observed in the experiments.

[8]The Reynolds number based on the roughness height is defined as $Re=U_k \cdot k/\nu$ where U_k is the mean flow velocity at the maximal height of the roughness element.

In 1996, Balakumar and Hall [84] determined the optimum suction distribution which gives the longest laminar region for a given total suction using the Lagrange-multiplier method with constraints. Their analysis and computations were performed for two- and three-dimensional boundary layers. They showed that the amount of suction necessary to control the crossflow instability is much larger than for the control of the TS-instability. Controlling the crossflow instability along a swept wedge, they were able to show a potential transition delay of 6-10% of the chord length, depending on the dominance of traveling, or stationary disturbances.

In a recent investigation by Saric et al. [4] from 1998, different spanwise spacings of roughness elements near the leading edge were successfully used to passively control the transition location. Their findings will be explained in Chapter 7.

2.6 Summary

To conclude the literature review, the state-of-the-art in transition prediction methods and models for the mechanisms involved in the laminar-turbulent transition in three-dimensional incompressible boundary layers will be summarized.

Receptivity

Choudhari et al. [39] distinguished different streamwise regions where the non-parallel boundary layer is receptive to freestream disturbances. In particular, they mentioned the region of a rapidly changing boundary layer thickness close to the leading edge, and a region further downstream where the surface boundary conditions are altered either by suction, or surface roughness. Further, the strong receptivity of the stationary crossflow disturbances to surface roughness was shown by Müller et al. [15] in 1988, by Radeztsky et al. [83] in 1993, and by Takagi and Itoh [19] in 1994.

Linear Stability

It has been confirmed experimentally and numerically that three-dimensional boundary layers are unstable to stationary and traveling disturbances. This is in contrast to two-dimensional boundary layers that are unstable only with respect to traveling disturbances. Linear stability theory has been shown to be capable of predicting parameters like the wavelength spectrum (including the most amplified wavelength) and the shape of the unstable disturbances [10, 18] correctly.

Transition Prediction and Detection

For transition prediction using the e^N-method, different strategies are recommended in the literature. Whereas Reed et al. [53] and Arnal et al. [12] preferred the constant wave number/constant frequency method in comparison with the envelope method (mainly because of its ability to distinguish between Tollmien-Schlichting and crossflow waves), Schrauf et al. [55] obtain better correlations with performed flight experiments by applying the envelope method. However, for the prediction of transition in three-dimensional boundary layers, extreme care must be taken in interpreting the results from the linear N-factor computations. This is due to the existence of a relatively short region of linear growth that is followed by a significant region of nonlinear saturation, where the linear theory cannot predict the disturbance evolution correctly. Another complicating factor in the application of the e^N-method in three-dimensional boundary layers is the simultaneous growth of a broad band of stationary disturbances [44] in the linear region that start to coalesce [76] and interact nonlinearly soon thereafter.

In a low-freestream turbulence environment, stationary crossflow disturbances dominate the transition process by causing a strong high-frequency secondary instability. The initial conditions for the disturbance evolution are determined by surface roughness

in that case [83] and a saw-tooth transition pattern prevails. In a high-freestream turbulence environment, the traveling crossflow disturbances dominate the transition process and the saw-tooth pattern is weaker than in the previous case [83].

For the detection of the transition location, two promising techniques were cited. First, a more traditional intermittency technique was described by Deyhle and Bippes [2], and second, a recently developed technique by Chapman et al. [30,31] using surface shear-stress measurements, as well as the method of Proper Orthogonal Decomposition and auto-correlations.

The location of the transition onset was determined in a narrow spanwise region [27] where the averaged velocity component tangential to the inviscid streamline is minimal [15]. In contrast to the findings by Orszag and Patera [64], Müller et al. [77] traced the transition onset back to locations of minimal vorticity and maximal rms-values.

In accordance with findings by Malik et al. [23], Wintergerste and Kleiser [78] detected a secondary crossflow vortex close to the wall in the region of the nonlinear saturation in their temporal DNS results. They further described a vortex-splitting mechanism that leads to transition immediately after the appearance of the secondary crossflow vortex.

Further, the transition Reynolds number was shown to be a function of the surface conditions, the freestream turbulence level and the saturation amplitudes of the disturbances by Deyhle and Bippes [2]. They showed that the highest transition Reynolds number was obtained for conditions that permitted the most limited growth of the stationary disturbances.

Applied PSE Methods

Since the development of the PSE in 1987 [40], explicit solution methods have been implemented and adapted to a variety of two- and quasi-three-dimensional problems in fluid dynamics. The existing PSE formulations in body-oriented coordinates have been shown to accurately predict the flow physics of transitional flows into the later stages of transition. For example, a computation of the secondary instability in the Blasius boundary layer was presented by Herbert [44], and the influence of freestream turbulence and surface curvature, as well as the prediction of the transition onset on a two-dimensional stator airfoil were successfully modeled in 1993 [60]. In 1997, Herbert [45] presented an explicit approach to solve the PSE for fully three-dimensional boundary layer flows. A major short-coming of the explicit PSE methods, however, is the large amount of necessary iterations on the nonlinear terms in the later stages of the transition, where strong gradients are present in the flow.

Secondary Instability

Orszag and Patera [64] determined the onset of the secondary instability in two-dimensional flows at locations of maximal vorticity. The onset of the secondary instability in three-dimensional boundary layer flow requires a much larger amplitude level of the primary disturbances than in two-dimensional flows. In [69], Balachandar et al. compared threshold amplitudes of about 9% for rotating-disc flow with a few tens of a percent required for two-dimensional flows. Also, they found that the secondary instability mechanism in the investigated three-dimensional boundary layer was similar for the fundamental and the subharmonic resonance case.

It has been confirmed experimentally [20,32] and computationally [23] that the high-frequency secondary instability rides on top of the stationary crossflow vortex and

is located away from the wall. The experimentally observed half-wavelength periodicity caused by this secondary instability mechanism was confirmed by Reed [25] and by Fischer and Dallmann [16] using Floquet theory. Herbert [65] showed an intricate connection between linear and secondary instability modes for plane channel flow that is revealed by considering the limit of a zero amplitude of the primary disturbance. In [66], he further argued that for an improved transition prediction using secondary instability theory, the frequency and amplitude composition of the primary disturbances must be specified properly, and a criterion for a self-sustained growth needs to be established.

Finally, an explanation for the experimentally observed explosive growth of traveling disturbances in the late stages of transition was given by Koch [68]. He showed the existence of an absolute instability in the Blasius boundary layer in the region just prior to transition.

CHAPTER 3

MEAN FLOW COMPUTATION

In this chapter, the approach to the computation of the mean flow profiles around arbitrary quasi-three-dimensional geometries is developed. The first section will explain the panel method for the computation of the inviscid outer flow, and a solution method for the quasi-three-dimensional boundary layer equations will be derived in the second section.

3.1 Outer Flow

The assumption of an infinite geometry in the spanwise direction implies that it is sufficient to compute the inviscid outer flow distribution in only one spanwise plane. This outer flow distribution then provides the freestream boundary conditions for the boundary layer equations, the solution of which is explained in the next section. For the outer flow computation in Chapter 7, the panel code by Kuethe and Chow [85] was used. The source code is given and documented in Reference [85]. The remainder of this section will explain the basics of the applied method.

In order to compute the inviscid flow around two-dimensional contours of arbitrary shape at an angle of attack, the surface of the particular contour is approximated by a finite number of flat panels covered with singularities of undetermined strength. These singularities are used to deflect the incoming stream in a way that it will flow around the contour. In the presented method, vortex panels with linearly varying strength along the panel and continuous strength across the panel edges are used. Figure 3.1 shows the panel configuration around a general two-dimensional contour. The boundary points are

defined to be on the surface of the geometry (solid points), whereas the control points (hollow points) are located in the middle of each panel. Starting at the trailing edge and numbering the m panels in the clockwise direction, m+1 boundary points and m control points are created.

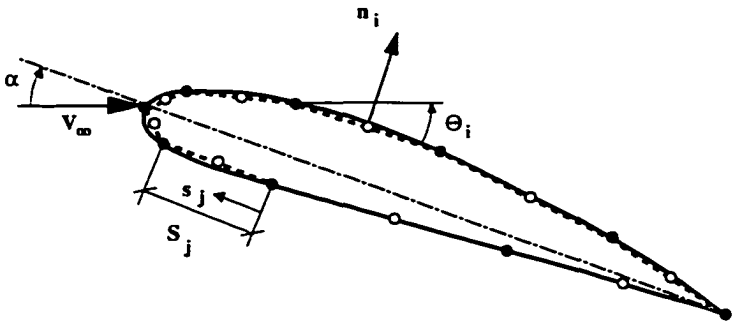

Figure 3.1: Definition of the panel arrangement around the geometry

Defining a uniform incoming flow V_∞ at an angle of attack α, the velocity potential ϕ at the i^{th} control point is given by equation 3.2 [85]. Here, $\gamma(s_j)$ is the unknown nondimensional vortex strength of the i^{th} panel, and s_j and S_j are the distances from the edge of the panel and the total panel length, respectively. Thus, one has to solve for the m+1 unknowns γ_j at the boundary points in order to determine the velocity potential around the contour.

$$\gamma(s_j) = \gamma_j + (\gamma_{j+1} - \gamma_j) \cdot \frac{s_j}{S_j} \ , \tag{3.1}$$

$$\phi(x_i, y_i) = V_\infty \cdot \left[x_i \cos\alpha + y_i \sin\alpha - \sum_{j=1}^{m} \int_j \gamma(s_j) \tan^{-1}\left(\frac{y_i - y_j}{x_i - x_j}\right) ds_j \right] \ . \tag{3.2}$$

Next, the boundary conditions normal to the surface, as well as the Kutta-condition at the trailing edge are formulated. Incorporating these conditions and utilizing geometrical relations around the contour, a well-posed problem is established that can be solved numerically. The homogeneous boundary conditions normal to the surface

require the flow to be tangential to the surface. They are evaluated at the control points and can be written as in equation 3.3, where n_i is the vector normal to the surface. The

$$\frac{\partial}{\partial n_i}\phi(x_i, y_i) = 0 \quad ; \quad i = 1, 2, \cdots, m \tag{3.3}$$

Kutta-condition at the trailing edge requires the flow to leave the airfoil smoothly and without any pressure gradient across the trailing edge. It forces the total vortex strength at the trailing edge to be zero and is written in equation 3.4. Evaluating the normal

$$\gamma_1 + \gamma_{m+1} = 0 \tag{3.4}$$

boundary conditions and expressing them in terms of the control point coordinates, one obtains equation 3.5 [85]. In equation 3.5, the coefficients $C_{n1,ij}$ and $C_{n2,ij}$ are functions

$$\sum_{j=1}^{m} (C_{n1,ij} \cdot \gamma_j + C_{n2,ij} \cdot \gamma_{j+1}) = \sin(\Theta_i - \alpha) \quad ; \quad i = 1, 2, \cdots, m \tag{3.5}$$

of the control points. Their expressions are given in detail in Reference [85]. Equation 3.5 represents the normal velocity at the i^{th} control point induced by the linear vortex distribution on the j^{th} panel.

Combining equations 3.4 and 3.5, a set of m+1 equations for the m+1 unknowns is obtained which can be written in matrix form in equation 3.6. From the previous de-

$$\mathbf{A_n} \cdot \gamma = \mathbf{RHS} \tag{3.6}$$

rivation, the elements of the influence matrix $\mathbf{A_n}$ and the corresponding vector of the right-hand side **RHS** are expressed as follows :

$$\text{for } (i < m+1) \; : \; A_{n,i1} = C_{n1,i1} \;, \tag{3.7}$$

$$A_{n,im+1} = C_{n2,im} \;, \tag{3.8}$$

$$A_{n,ij} = C_{n1,ij} + C_{n2,ij-1} \quad ; \quad j = 2, 3, \cdots, m \;, \tag{3.9}$$

$$RHS_i = \sin(\Theta_i - \alpha) \quad , \tag{3.10}$$

$$\text{for } (i = m+1) \; : \; A_{n,i1} = 1 \quad , \tag{3.11}$$

$$A_{n,im+1} = 1 \quad , \tag{3.12}$$

$$A_{n,ij} = 0 \quad ; \quad j = 2, 3, \cdots, m \quad , \tag{3.13}$$

$$RHS_i = 0 \quad . \tag{3.14}$$

After solving the linear system given by equation 3.6 for the vortex strength distribution at each control point, the velocity and pressure at these points can be determined. Letting t_i be the tangential vector to the surface at each panel, the velocity at each control point is defined as in equation 3.15, where the coefficients $C_{t1,ij}$ and $C_{t2,ij}$ are given in Reference [85]. Here, the summation term represents the tangential velocity at

$$V_i = \frac{\partial}{\partial t_i}\phi(x_i, y_i) = \cos(\Theta_i - \alpha) + \sum_{j=1}^{m} (C_{t1,ij} \cdot \gamma_j + C_{t2,ij} \cdot \gamma_{j+1}) \quad ; \quad i = 1, 2, \cdots, m \tag{3.15}$$

the i^{th} control point induced by the linear vortex distribution on the j^{th} panel. Writing equation 3.15 in a more suitable form for the implementation into a computer code, one

$$V_i = \frac{\partial}{\partial t_i}\phi(x_i, y_i) = \cos(\Theta_i - \alpha) + \sum_{j=1}^{m+1} A_{t,ij} \cdot \gamma_j \quad ; \quad i = 1, 2, \cdots, m \quad , \tag{3.16}$$

$$A_{t,i1} = C_{t1,i1} \quad ; \quad A_{t,im+1} = C_{t2,im} \quad , \tag{3.17}$$

$$A_{t,ij} = C_{t1,ij} + C_{t2,ij-1} \quad ; \quad j = 2, 3, \cdots, m \tag{3.18}$$

obtains equation 3.16, where the tangential influence coefficients $A_{t,ij}$ are defined in equations 3.17 and 3.18.

$$C_{p,i} = \left(\frac{p - p_\infty}{\frac{1}{2}\rho V_\infty^2} \right)_i = 1 - \frac{V_i^2}{V_\infty^2} \tag{3.19}$$

Finally, the pressure coefficient at the i^{th} control point is expressed in equation 3.19 and the following algorithm can be itemized :

1. Computation of the panel geometry according to the given two-dimensional contour and the specified number of points.

2. Computation of the influence coefficients $C_{n,ij}$ and $C_{t,ij}$, as well as the the influence matrices $\mathbf{A_n}$ and $\mathbf{A_t}$, and the vector of the right-hand side **RHS** in equation 3.6.

3. Computation of the nondimensional vortex panel strength vector γ by solving equation 3.6.

4. Computation of the inviscid velocity distribution V_i and the pressure distribution $C_{p,i}$ around the contour using equations 3.16 and 3.19.

Thus, the inviscid outer flow has been obtained and will provide the boundary conditions for the computation of the mean flow profiles which is described in the next section.

3.2 Quasi-three-dimensional Mean Flow Profiles

In this section, a general quasi-three-dimensional geometry and a corresponding body-oriented coordinate system are considered. The coordinate system is described in figure 3.2. In the first subsection, the governing equations will be derived in their nondimensional form. The second subsection then explains the solution method of the nondimensional boundary layer equations in detail.

3.2.1 Governing Equations

Defining a dimensional and steady basic flow $\mathbf{V_0^*}(x_1, x_2, x_3) = \{U_0^*, W_0^*, V_0^*\}^T$, making the boundary layer assumptions and assuming no variations of the basic flow in the spanwise direction, the dimensional boundary layer equations in body-oriented coordinates (equations 3.20 - 3.23) can be derived from the Navier-Stokes equations.

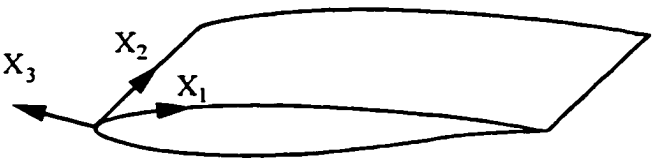

Figure 3.2: Body-oriented coordinate system

$$\frac{\partial U_0}{\partial x_1} + \frac{\partial V_0}{\partial x_3} = 0 \ , \tag{3.20}$$

$$U_0 \frac{\partial U_0}{\partial x_1} + V_0 \frac{\partial U_0}{\partial x_3} = U_e \frac{\partial U_e}{\partial x_1} + \nu \frac{\partial U_0^2}{\partial x_3^2} \ , \tag{3.21}$$

$$U_0 \frac{\partial W_0}{\partial x_1} + V_0 \frac{\partial W_0}{\partial x_3} = \nu \frac{\partial W_0^2}{\partial x_3^2} \ , \tag{3.22}$$

$$U_0 = W_0 = V_0 = 0 \ \text{ at } \ x_3 = 0 \ ; \ U_0 = U_e, \ W_0 = W_\infty = \text{const. at } \ x_3 \to \infty \ . \tag{3.23}$$

Introducing the stream function Φ, the normal coordinate η and the similarity parameter m in equation 3.24, the mean flow components are defined according to equation 3.25.

$$\Phi = \sqrt{\nu^* x_1^* U_e^*}\ f(x_1^*, \eta) \ ; \ \eta = \frac{x_3^*}{\sqrt{\nu^* x_1^* / U_e^*}} \ ; \ m = \frac{x_1^*}{U_e^*} \frac{\partial U_e^*}{\partial x_1^*} \ , \tag{3.24}$$

$$U_0^* = \partial\Phi / \partial x_3^* \ ; \ V_0^* = -\partial\Phi / \partial x_1^* \tag{3.25}$$

Writing the velocity components explicitly in equations 3.26 - 3.28 and substituting these into equations 3.21 and 3.22, one can write the nondimensional version of the quasi-three-dimensional boundary layer equations as in equations 3.29 and 3.30. There,

$$U_0^*(x_1^*, x_3^*) = U_e^*(x_1) \cdot f'(x_1^*, \eta) \quad , \tag{3.26}$$

$$W_0^*(x_1^*, x_3^*) = W_\infty^* \cdot g(x_1^*, \eta) \quad , \tag{3.27}$$

$$V_0^*(x_1^*, x_3^*) = -\sqrt{\frac{U_e^* \cdot \nu^*}{x_1^*}} \left\{ \frac{f}{2} \cdot (1 + m) + x_1^* \cdot \frac{\partial f}{\partial x_1^*} + \frac{\eta}{2} \cdot f' \cdot (m - 1) \right\} \tag{3.28}$$

primes denote differentiation with respect to the normal coordinate η. These equations stand for a first-order approximation to the full Navier-Stokes equations, where the order of approximation is proportional to the small parameter $\epsilon = 1/\sqrt{Re_\infty}$.

$$f''' + \frac{m+1}{2} f \cdot f'' + m \cdot (1 - f'^2) = x_1 \cdot (f' \cdot \frac{\partial f'}{\partial x_1} - f'' \cdot \frac{\partial f}{\partial x_1}) \,, \tag{3.29}$$

$$g'' + \frac{m+1}{2} f \cdot g' = x_1 \cdot (f' \cdot \frac{\partial g}{\partial x_1} - g' \cdot \frac{\partial f}{\partial x_1}) \,, \tag{3.30}$$

$$f = f' = g = 0 \quad \text{at} \quad \eta = 0 \;\; ; \;\; f' = g = 1 \quad \text{at} \quad \eta \to \infty \tag{3.31}$$

3.2.2 Solution Method

In this subsection, the solution method for the quasi-three-dimensional boundary layer equations based on a compact scheme formulation will be derived. The Euler-McLaurin equation 3.32 describes a fourth-order-accurate finite difference approximation

$$\Lambda_k - \Lambda_{k-1} = \frac{h_k}{2} \cdot (\Lambda'_k + \Lambda'_{k-1}) - \frac{h_k^2}{12} \cdot (\Lambda''_k - \Lambda''_{k-1}) \tag{3.32}$$

for functions depending on a single variable, here the wall-normal coordinate at the stations k. The advantage of this scheme is that it achieves fourth-order accuracy with only two grid points. Thus, non-uniform grids can be utilized without the need of Jacobian-matrices, and it is very straightforward to implement the boundary conditions. Applying this scheme to the present problem, one needs to rewrite the non-dimensional boundary layer equations 3.29 - 3.31 as a system of ordinary differential equations (ODE's). This is accomplished by defining new unknown variables. The streamwise equation, equation 3.29, is considered first. In equation 3.33, the new vector of unknowns Λ is introduced. Now, one can rewrite the streamwise equation as a system of ODE's in the matrix equations 3.34 and 3.35.

$$\Lambda = \{f, f', f''\}^T = \{f_0, f_1, f_2\}^T \tag{3.33}$$

$$\begin{Bmatrix} f_1 \\ f_2 \\ f_3 \end{Bmatrix} = \begin{bmatrix} 0 & 1 & 0 \\ 0 & 0 & 1 \\ -f_2\frac{m+1}{2} & m\, f_1 + x_1\frac{\partial f_1}{\partial x_1} & -x_1\frac{\partial f_0}{\partial x_1} \end{bmatrix} \cdot \begin{Bmatrix} f_0 \\ f_1 \\ f_2 \end{Bmatrix} + \begin{Bmatrix} 0 \\ 0 \\ m \end{Bmatrix} \tag{3.34}$$

$$\Lambda_1 = \Lambda' = \{f_1, f_2, f_3\}^T = \mathbf{H_f} \cdot \Lambda + \mathbf{G_f} \tag{3.35}$$

The first streamwise derivative of the vector Λ is written in equation 3.36. Here, a second-order-accurate, three-point upwind finite-difference scheme is used where the coefficients P_1, P_2, P_3 are found from a Lagrangian interpolation.

$$\frac{\partial \Lambda}{\partial x_1} = P_1 \cdot \Lambda_{n-2} + P_2 \cdot \Lambda_{n-1} + P_3 \cdot \Lambda_n \tag{3.36}$$

Applying equation 3.36 to the equation for the third component of Λ_1 (equation 3.34), one can rewrite the latter in terms of the components of Λ in equation 3.37. The first subscript denotes the derivative in the normal direction and the second subscript the derivative in the streamwise direction. Since equation 3.37 represents a nonlinear ODE, the unknowns are also contained in the coefficient matrix $\mathbf{H_f}$ and one has to solve this problem iteratively.

$$f_3 = -\, f_{00} \cdot f_{20} \cdot \frac{m+1}{2} - m \cdot (1 - f_{10}^2) + \tag{3.37}$$

$$x_1 \cdot f_{10} \cdot \{P_1 \cdot f_{12} + P_2 \cdot f_{11} + P_3 \cdot f_{10}\} - x_1 \cdot f_{20} \cdot \{P_1 \cdot f_{02} + P_2 \cdot f_{01} + P_3 \cdot f_{00}\}$$

Now, the Euler-McLaurin formula (equation 3.32) is considered again. Having derived analytical relations for the vectors Λ and Λ_1, one still needs to express the second derivative in the normal coordinate direction. This expression is given in equation 3.38.

$$\Lambda'' = (\Lambda_1')_{\Lambda'=\text{const.}} + \Lambda_1 \cdot \left(\frac{\partial(\Lambda')}{\partial \Lambda}\right)_{\eta=\text{const.}} = \Lambda_{2,\Lambda=\text{const.}} + \Lambda_{2,\eta=\text{const.}} \tag{3.38}$$

Substituting equations 3.35 and 3.38 into the Euler-McLaurin formula, one obtains equation 3.39. Here, h_k is the distance between two consecutive normal points.

$$\Lambda_k - \Lambda_{k-1} = \frac{h_k}{2} \cdot \{\Lambda_{1,k} + \Lambda_{1,k-1}\} - \tag{3.39}$$

$$\frac{h_k^2}{12} \cdot \left\{(\Lambda_{2,\Lambda=\text{const.}} + \Lambda_{2,\eta=\text{const.}})_k - (\Lambda_{2,\Lambda=\text{const.}} + \Lambda_{2,\eta=\text{const.}})_{k-1}\right\}$$

As stated above, the present problem is nonlinear and one has to iterate for the solution starting from an initial guess. Thus, the terms of equation 3.39 are approximated by a one-term Taylor series expansion in equations 3.40 - 3.44, so that the method can iterate on the linear correction $\Delta\Lambda$ to an initial guess Λ^0.

$$\Lambda_k = \Lambda_k^0 + \Delta\Lambda_k \ , \tag{3.40}$$

$$\begin{aligned} \Lambda_{1,k} &= \left(\Lambda_k^0 + \Delta\Lambda_k\right)' = \Lambda_{1,k}^0 + \left(\frac{\partial\Lambda^0}{\partial\Lambda}\right)_k \cdot \Delta\Lambda_k \\ &= \Lambda_{1,k}^0 + L_k \cdot \Delta\Lambda_k \ , \end{aligned} \tag{3.41}$$

$$\begin{aligned} \Lambda_{2,\Lambda=\text{const.},k} &= \Lambda_{2,\Lambda=\text{const.},k}^0 + \left(\frac{\partial\Lambda_{2,\Lambda=\text{const.}}}{\partial\Lambda}\right)_k \cdot \Delta\Lambda_k \\ &= \left(\frac{\partial\Lambda_{2,\Lambda=\text{const.}}}{\partial\Lambda}\right)_k \cdot \Delta\Lambda_k = L_{\Lambda=\text{const.},k} \cdot \Delta\Lambda_k \ , \end{aligned} \tag{3.42}$$

$$\begin{aligned} \Lambda_{2,\eta=\text{const.},k} &= \Lambda_{2,\eta=\text{const.},k}^0 + \left(\frac{\partial\Lambda_{2,\eta=\text{const.}}}{\partial\Lambda}\right)_k \cdot \Delta\Lambda_k \\ &= L_{1,\eta=\text{const.},k} + L_{2,\eta=\text{const.},k} \cdot \Delta\Lambda_k \end{aligned} \tag{3.43}$$

Substituting the above relations 3.40 - 3.43 into equation 3.39, one obtains equation 3.44.

$$\Lambda_k^0 - \Lambda_{k-1}^0 + \Delta\Lambda_k - \Delta\Lambda_{k-1} = \tag{3.44}$$

$$\frac{h_k}{2} \cdot \left\{\Lambda_{1,k}^0 + \Lambda_{1,k-1}^0 + L_k \cdot \Delta\Lambda_k + L_{k-1} \cdot \Delta\Lambda_{k-1}\right\} -$$

$$\frac{h_k^2}{12} \cdot \{L_{\Lambda=\text{const.},k} \cdot \Delta\Lambda_k - L_{\Lambda=\text{const.},k-1} \cdot \Delta\Lambda_{k-1} +$$

$$L_{1,\eta=\text{const.},k} + L_{2,\eta=\text{const.},k} \cdot \Delta\Lambda_k - L_{1,\eta=\text{const.},k-1} + L_{2,\eta=\text{const.},k-1} \cdot \Delta\Lambda_{k-1}\}$$

By collecting terms of $\Delta\Lambda$ in equation 3.44, a matrix equation is derived and written in equation 3.45. Here, **D** is a 3×1 vector, and **A** and **B** are 3×3 coefficient matrices at each normal location. The corresponding boundary conditions for the components of the vector $\Delta\Lambda$ (see equation 3.33) are developed in equations 3.46 - 3.48.

$$\mathbf{A} \cdot \Delta\Lambda_{k-1} + \mathbf{B} \cdot \Delta\Lambda_k = \mathbf{D} \tag{3.45}$$

$$\text{At the wall :} \quad f_0 = \Lambda_1^0 + \Delta\Lambda_1 = \Delta\Lambda_1 = 0 \quad , \ \Delta\Lambda_1 = 0 \tag{3.46}$$

$$f_1 = \Lambda_2^0 + \Delta\Lambda_2 = \Delta\Lambda_2 = 0 \quad , \ \Delta\Lambda_2 = 0 \tag{3.47}$$

$$\text{At freestream :} \quad f_1 = \Lambda_2^0 + \Delta\Lambda_2 = 1 + \Delta\Lambda_2 = 1, \ \Delta\Lambda_2 = 0 \tag{3.48}$$

Implementing the boundary conditions and forming a block-tridiagonal system consisting of the matrix equation 3.45 at each normal location k are the last steps in the formulation of the solution procedure for the streamwise boundary layer equation. Then, initializing the vector Λ^0 with the two-dimensional Hiemenz Flow solution at the stagnation point, one can compute the correction $\Delta\Lambda$ by a Newton-Raphson technique until the maximum component of the vector $\Delta\Lambda$ is less than a prescribed tolerance, typically ϵ=10^{-10}.

For the spanwise component, a similar approach is taken in developing the solution procedure. The derivation is simpler, since the spanwise direction is described by a linear and second-order partial differential equation (PDE) compared to a nonlinear and third-order PDE for the streamwise direction. First, the new vector of unknowns is defined below. Then, rewriting equation 3.30 as a system of ODE's, one obtains the matrix equations 3.50 and 3.51. Here, the second-order upwind scheme (equation 3.36) is directly applied to the streamwise derivatives of the function $g(x_1, \eta)$. In equation 3.50,

$$\Lambda_{\mathbf{g}} = \{g, g'\}^T = \{g_0, g_1\}^T \tag{3.49}$$

$$\begin{Bmatrix} g_1 \\ g_2 \end{Bmatrix} = \begin{bmatrix} 0 & 1 \\ x_1 f_1 P_3 & -f_0 \frac{m+1}{2} - x_1 \frac{\partial f_0}{\partial x_1} \end{bmatrix} \cdot \begin{Bmatrix} g_0 \\ g_1 \end{Bmatrix} + \begin{Bmatrix} 0 \\ x_1 f_1 (P_1 g_{02} + P_2 g_{01}) \end{Bmatrix} \quad (3.50)$$

the values for $\Lambda=\{f_0, f_1, f_2\}^T$ and the streamwise derivative of f_0 are known from the iteration on the streamwise equation, and the subscripts of the Λ_g components stand for the streamwise and spanwise derivatives, respectively. In order to apply the Euler-McLaurin formula, the expressions for the first and second derivatives in the normal direction need to be determined next. From equation 3.50, one can directly write equation 3.51 for the first derivative, where the coefficient matrix $\mathbf{H_g}$ is a 2×2-matrix and $\mathbf{G_g}$ is a 2×1 vector at each normal location k. The expression for the second derivative is derived in equations 3.52 - 3.55.

$$\Lambda_g'(\eta) = \{g_1, g_2\}^T(\eta) = \Lambda_{g,1}(\eta) = \mathbf{H_g}(\eta) \cdot \Lambda_g(\eta) + \mathbf{G_g}(\eta) = \mathbf{F}(\eta, \Lambda_g) \quad (3.51)$$

$$\Lambda_g''(\eta) = \left(\frac{\partial \mathbf{F}}{\partial \eta}\right)_{\Lambda_g=\text{const.}} + \left(\frac{\partial \mathbf{F}}{\partial \Lambda_g}\right)_{\eta=\text{const.}} \cdot \mathbf{F} \quad (3.52)$$

$$\Lambda_g''(\eta) = \left(\frac{\partial \mathbf{H_g}}{\partial \eta}\right)_{\Lambda_g=\text{const.}} \cdot \Lambda_g + \mathbf{H_g} \cdot \left(\frac{\partial \Lambda_g}{\partial \eta}\right)_{\Lambda_g=\text{const.}} + \left(\frac{\partial \mathbf{G_g}}{\partial \eta}\right)_{\Lambda_g=\text{const.}} + \left(\frac{\partial \mathbf{F}}{\partial \Lambda_g}\right)_{\eta=\text{const.}} \cdot \mathbf{F} \quad (3.53)$$

$$\Lambda_g''(\eta) = \left(\frac{\partial \mathbf{H_g}}{\partial \eta}\right)_{\Lambda_g=\text{const.}} \cdot \Lambda_g + \left(\frac{\partial \mathbf{G_g}}{\partial \eta}\right)_{\Lambda_g=\text{const.}} + \left(\frac{\partial \mathbf{F}}{\partial \Lambda_g}\right)_{\eta=\text{const.}} \cdot \mathbf{F} \quad (3.54)$$

$$\Lambda_g''(\eta) = \mathbf{H_{g,1}} \cdot \Lambda_g + \mathbf{G_{g,1}} + \mathbf{F_{\Lambda g}} \cdot \mathbf{F} \quad (3.55)$$

In equations 3.52 - 3.55, the matrices $\mathbf{H_{g,1}}$ and $\mathbf{F_{\Lambda g}}$ are 2×2-matrices, and the vectors $\mathbf{G_{g,1}}$ and $\mathbf{F}$ are 2×1-vectors at each normal location. Substituting the above expressions into the Euler-McLaurin formula, one obtains equation 3.56, and collecting terms in Λ_g yields the matrix equation 3.57 at every normal location k similar to equation 3.45 for the streamwise boundary layer equation. Specifying the two necessary

$$\mathbf{\Lambda_{g,k} - \Lambda_{g,k-1}} = \frac{h}{2}\{\mathbf{H_{g,k} \cdot \Lambda_{g,k} + H_{g,k-1} \cdot \Lambda_{g,k-1} + G_{g,k} + G_{g,k-1}}\} - \tag{3.56}$$

$$\frac{h^2}{12}\{\mathbf{H_{g,1,k} \cdot \Lambda_{g,k} - H_{g,1,k-1} \cdot \Lambda_{g,k-1} + G_{g,1,k} + G_{g,1,k-1} + F_{\Lambda g,k} \cdot F_k - F_{\Lambda g,k-1} \cdot F_{k-1}}\} ,$$

$$\mathbf{A_g \cdot \Lambda_{g,k-1} + B_g \cdot \Lambda_{g,k} = D_g} \tag{3.57}$$

boundary conditions in equations 3.58 and 3.59, implementing these and the matrix equations 3.57 into a block-tridiagonal matrix, the spanwise equation can be solved in one sweep using a block-tridiagonal solver, since all the matrix coefficients are known.

$$\text{At the wall :} \quad g_0 = \Lambda_{g,1} = 0 \tag{3.58}$$

$$\text{At freestream :} \quad g_0 = \Lambda_{g,1} = 1 \tag{3.59}$$

Concluding this subsection, the solution method is summarized as follows :

1. Finding the location of the stagnation point and the streamwise distribution of the similarity parameter m from the outer flow solution.

2. Initializing the vectors $\mathbf{\Lambda^0}$, $\mathbf{\Lambda_g}$ at the stagnation point using the Falkner-Skan-Cooke similarity solution.

3. Marching to the next station, the correction $\Delta\mathbf{\Lambda}$ is computed using a Newton-Raphson technique and the streamwise equation is solved at this location.

4. Solving the spanwise equation in one sweep using a block-tridiagonal solver.

Steps three and four are repeated until the separation point is detected. The method is very effective, since it takes only a few iterations, typically two to three, on $\Delta\mathbf{\Lambda}$ until the streamwise solution converges.

CHAPTER 4

STABILITY OF WALL-BOUNDED FLOWS

4.1 Introduction

The transition process without bypass in a three-dimensional boundary layer flow can be described by five main phases. First, in the receptivity phase, disturbances determined by the outer conditions (surface roughness, freestream turbulence, acoustic noise) are entering the boundary layer. In the region of their introduction, a wide spectrum of disturbances is present. However, many of these initial disturbances decay and only a few are amplified in the downstream flow. Second, the phase of exponential growth sees a slow amplitude growth of the few unstable modes. Due to its linearity, this phase can be well described by following the most unstable disturbance. Third, in the phase of nonlinear interaction, the disturbance amplitudes are large enough to interact nonlinearly, the uniform spanwise flow is modulated by the disturbances, and a disturbance saturation into an equilibrium stage can be observed. The onset of saturation, as well as its amplitude level, are strong functions of the initial conditions of amplitude, frequency and phase, determined by the receptivity mechanism. In this third phase, the mean flow profiles are being distorted, co-rotating crossflow vortices develop within the boundary layer causing a lift of low-speed fluid away from the wall and into the outer flow, and in turn, a pull of high-speed fluid from the outer flow towards the wall. This is seen as a roll-up motion into half-mushroom-like structures that point into the positive spanwise direction (see Subsection 5.3.2). Due to the strong distortion of the boundary layer, inflectional mean flow profiles develop in both the spanwise and the streamwise

direction and one can distinguish a fourth phase, in which the boundary layer becomes unstable to three-dimensional high-frequency disturbances. The frequencies observed in this phase are an order-of-magnitude higher than the primarily unstable ones, and this mechanism is usually referred to as secondary instability. Finally, an explosive growth of these high-frequency modes initiates the fifth phase, the breakdown to turbulence.

The scope of the presented work are the phases two through four. Starting with general remarks on temporal and spatial stability formulations, the derivation of the locally parallel stability theory will be given in Section 4.2. The derivations of the linear and nonlinear PSE formulation are contained in Section 4.3. There, the main focus is on the explanation of the explicit solution method. Section 4.4 introduces the concept of the Floquet theory and its application to the secondary instability of three-dimensional boundary layer flows. In particular, the developed global and local eigenvalue solver that are based on a Newton-Raphson technique and the recently developed Implicitly Restarted Arnoldi Method [1], respectively, will be explained.

4.2 Locally Parallel Theory

Following the formulation of the stability theory given by Mack [35] in 1969, the concepts of spatial and temporal stability theory for three-dimensional boundary layer flows will be introduced in this section, and a solution method based on a Newton-Raphson technique will be presented.

The total incompressible flow quantity $\mathbf{Q}=\{\mathbf{V},P\}^T=\{U,W,V,P\}^T$ can be expressed as the summation of the mean flow $\mathbf{Q_0}=\{\mathbf{V_0},P_0\}^T=\{U_0,W_0,V_0,P_0\}^T$ and the disturbance $\mathbf{q_1}=\{\mathbf{v_1},p_1\}^T=\{u_1,w_1,v_1,p_1\}^T$. Using the body-oriented coordinate system applied in the mean flow computations (figure 3.2), the Navier-Stokes equations for

the disturbances quantities can be written as in equations 4.1 and 4.2. There, the mean flow quantities are known, and homogeneous boundary conditions for the disturbance quantities are enforced at the wall and at the freestream boundary.

$$\nabla \cdot \mathbf{v_1} = 0 \ ; \tag{4.1}$$

$$\frac{\partial \mathbf{v_1}}{\partial t} + (\mathbf{v_1} \cdot \nabla)\mathbf{v_1} + (\mathbf{V_0} \cdot \nabla)\mathbf{v_1} + (\mathbf{v_1} \cdot \nabla)\mathbf{V_0} = - \nabla p_1 + \frac{1}{Re}\nabla^2 \mathbf{v_1} \tag{4.2}$$

In the locally parallel approach to the solution of the stability problem, the following assumptions are made. First, the mean flow quantity $\mathbf{Q_0}$ is considered. Since the variations of the mean flow in the streamwise and in the spanwise directions are much slower than in the normal direction, one assumes that the mean flow quantities only depend on the wall-normal coordinate and a zero normal mean flow component as indicated by :

$$\mathbf{Q_0}(x_1, x_2, x_3, t) = \mathbf{Q_0}(x_3, t) = \{U_0, W_0, 0, P_0\}^T \tag{4.3}$$

Secondly, a normal mode formulation is employed for the disturbance quantities. The disturbance quantities as written in equation 4.4 consist of a complex amplitude vector $\hat{\mathbf{q}}_1$ that depends only on the wall-normal coordinate, and a complex phase θ that allows for periodic variations in the wall-parallel directions and in time. In equations 4.4 and 4.5, α_1 and β_1 are the complex wave numbers in the streamwise and in the spanwise direction, respectively, and ω is the complex frequency of the disturbance. Further, the complex wave vector $\mathbf{k}$ is defined in equation 4.6. It represents the propagation direction

$$\mathbf{q_1}(x_1, x_2, x_3, t) = \hat{\mathbf{q}}_1(x_3)\, e^{i\theta} + \text{c.c.} = \hat{\mathbf{q}}_1(x_3)\, e^{i\alpha_1 + i\beta_1 x_2 - i\omega t} + \text{c.c.} \ ; \tag{4.4}$$

$$\frac{\partial \theta}{\partial t} = \omega \ ; \quad \frac{\partial \theta}{\partial x_1} = \alpha_1 \ ; \quad \frac{\partial \theta}{\partial x_2} = \beta_1 \ ; \tag{4.5}$$

$$\mathbf{k}(x_1, x_2) = \{\alpha_1, \beta_1\}^T = \nabla\theta \tag{4.6}$$

of the disturbance waves in the wall-parallel plane. The wave fronts of the disturbances perpendicular to the wave vector are denoted as constant phase lines.

Substituting equations 4.3 - 4.5 into the Navier-Stokes equations in disturbance form (equations 4.1 and 4.2) and dropping the nonlinear terms, the resulting continuity and momentum equations are given in equations 4.7- 4.11.

$$0 = i\alpha_1\hat{u}_1 + i\beta_1\hat{w}_1 + \frac{\partial\hat{v}_1}{\partial x_3} \tag{4.7}$$

$$0 = \frac{1}{Re}\frac{\partial^2\hat{u}_1}{\partial x_3^2} - \Delta\hat{u}_1 - \frac{\partial U_0}{\partial x_3}\hat{v}_1 - i\alpha_1\hat{p}_1 \tag{4.8}$$

$$0 = \frac{1}{Re}\frac{\partial^2\hat{w}_1}{\partial x_3^2} - \Delta\hat{w}_1 - \frac{\partial W_0}{\partial x_3}\hat{v}_1 - i\beta_1\hat{p}_1 \tag{4.9}$$

$$0 = \frac{1}{Re}(-i\alpha_1\frac{\partial\hat{u}_1}{\partial x_3} - i\beta_1\frac{\partial\hat{w}_1}{\partial x_3}) - \Delta\hat{v}_1 - \frac{\partial\hat{p}_1}{\partial x_3} \tag{4.10}$$

$$\Delta = i\alpha_1 U_0 + i\beta_1 W_0 + \frac{1}{Re}(\alpha_1^2 + \beta_1^2) - i\omega \tag{4.11}$$

This system of ODE's and the corresponding homogeneous boundary conditions at the wall and in the freestream represent an eigenvalue problem that is written in the form of a general dispersion relation for the complex quantities ω, α_1, β_1 in equation 4.12.

$$0 = F(Re, \alpha_1, \beta_1, \omega) \tag{4.12}$$

In the stability theory, it is assumed that disturbances can either grow in time, or in space. Accordingly, two different formulations are distinguished. In the temporal formulation, the wave numbers in the streamwise and in the spanwise direction are assumed to be real, and a unique solution for the complex frequency of the disturbance ($\omega_{real} + i\omega_{imag}$) is obtained by solving the temporal dispersion relation (equation 4.13) for specified values of α_1, β_1 and Re. The temporal growth rate is defined as the positive imaginary part of ω.

$$\omega = F(Re, \alpha_1, \beta_1) \tag{4.13}$$

In the spatial formulation, the disturbance frequency is assumed to be real and the two wave numbers α_1 and β_1 are complex. The resulting spatial dispersion relation is written in equation 4.14. There, the wave number β_1 needs to specified in order to ob-

$$\alpha_1 = \mathrm{F}(\mathrm{Re}, \beta_1, \omega) \tag{4.14}$$

tain a well-posed problem. However, since there is no prior knowledge about the growth of the disturbances in the spanwise direction, an additional condition is required to determine the imaginary part of β_1. This condition was derived from a irrotationality condition on the complex phase θ by Mack [86] in 1977 and leads to the relations for $\alpha_1 = \alpha_1(\mathrm{x}_1)$ given by :

$$\frac{\partial \alpha_1}{\partial \mathrm{x}_2} = \frac{\partial \beta_1}{\partial \mathrm{x}_1} \quad ; \quad \beta_1 = \text{constant.} \quad ; \quad \beta_{1,\mathrm{imag}} = 0 \tag{4.15}$$

That is to say, the disturbances are assumed to grow only in the x_1-direction. In the light of a mean flow that does not depend on the spanwise direction, this is a reasonable consequence. In the spatial formulation, the growth rate σ_1 is defined as the negative imaginary part of the streamwise wave number expressed by :

$$\sigma_1 = -\alpha_{1,\mathrm{imag}} \tag{4.16}$$

In the remainder of this section, the applied Newton-Raphson technique for the solution of the spatial eigenvalue problem is explained. In order to utilize the fourth-order-accurate compact scheme formulation applied for the solution of the boundary layer equations in Chapter 3, a new vector of unknowns is introduced in equation 4.17, and the system of ODE's (equations 4.7- 4.11) is rewritten in equation 4.18.

$$\mathbf{\Lambda_1} = \{\hat{\mathrm{u}}_1, \frac{\partial \hat{\mathrm{u}}_1}{\partial \mathrm{x}_3}, \hat{\mathrm{w}}_3, \frac{\partial \hat{\mathrm{w}}_3}{\partial \mathrm{x}_3}, \hat{\mathrm{v}}_3, \hat{\mathrm{p}}_3\}^{\mathrm{T}} \quad ; \tag{4.17}$$

$$\frac{\partial \mathbf{\Lambda_1}}{\partial \mathrm{x}_3} = \mathbf{A}\mathbf{\Lambda_1} \tag{4.18}$$

Since all the coefficients of the matrix **A** are either functions of the wall-normal coordinate, or constants, the Euler-McLaurin formula in equation 4.19 is applied straightforwardly at each normal location k. In equation 4.19, h_k is the normal distance between

$$\Lambda_{1_k} - \Lambda_{1_{k-1}} = \frac{h_k}{2}(\Lambda'_{1_k} + \Lambda'_{1_{k-1}}) - \frac{h_k^2}{12}(\Lambda''_{1_k} - \Lambda''_{1_{k-1}}) \tag{4.19}$$

two adjacent grid points and the primes denote a differentiation with respect to the wall-normal direction. Substituting equation 4.18 and the not explicitly written relation for the second normal derivative of Λ_1 into equation 4.19, the matrix equation 4.20 is obtained at every normal location except the boundaries. There, the matrices $\mathbf{A_k}$ and $\mathbf{B_k}$ are (6×6) coefficient matrices and the $\mathbf{D_k}$ is the (6×1) vector of the right-hand side.

$$\mathbf{A_k} \cdot \Lambda_{1_{k-1}} + \mathbf{B_k} \cdot \Lambda_{1_k} = \mathbf{D_k} \;\; ; \;\; k = 2, \cdots, N-1 \tag{4.20}$$

Implementing the boundary conditions at the wall in the (3×6) matrix $\mathbf{B_1}$, at the freestream boundary in the (3×6) matrix $\mathbf{A_N}$, and shifting the entire matrix system as shown in figure 4.1 results in a block-tridiagonal system that is written in equation 4.21.

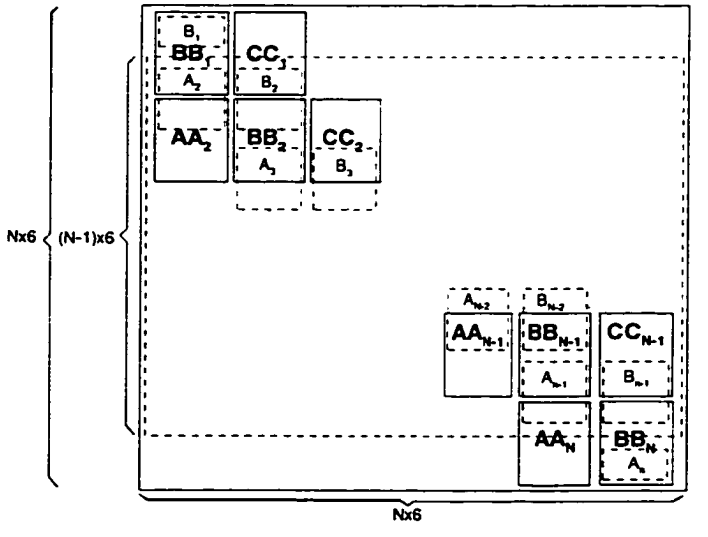

Figure 4.1: Setup of the block-tridiagonal system

Then, exploiting the compact banded structure of the system and using the subroutines ZGBTRF and ZGBTRS of the public-domain software library LAPACK, this system can be solved very efficiently.

$$\mathbf{AA_k} \cdot \mathbf{\Lambda_{1_{k-1}}} + \mathbf{BB_k} \cdot \mathbf{\Lambda_{1_k}} + \mathbf{CC_k} \cdot \mathbf{\Lambda_{1_{k+1}}} = \mathbf{DD_k} \tag{4.21}$$

Dropping one velocity boundary condition at the wall and normalizing the pressure at the wall by specifying the first element of the right-hand side vector **DD** instead, the iteration for the streamwise wave number α_1 starts with an initial guess α_{1_0} that is obtained from a global eigenvalue computation. Expanding the homogeneous wall-boundary condition in a Taylor series for small changes in α_1 (equation 4.22), a Newton-Raphson technique is applied to update the wave number α_1 according to equation 4.23. After each iteration, the dropped boundary condition is evaluated and the iteration pro-

$$u_1(\alpha_{1,\text{old}} + \Delta\alpha) = u_{1_0} + \frac{\partial u_1}{\partial \alpha_1}\Delta\alpha = 0 \;\; ; \;\; \Delta\alpha = -\frac{u_{1_0}}{(\frac{\partial u_1}{\partial \alpha_1})} \;\; ; \tag{4.22}$$

$$\alpha_{1,\text{new}} = \alpha_{1,\text{old}} + \Delta\alpha \tag{4.23}$$

ceeds until the error in the homogeneous boundary condition is less than a prescribed tolerance, typically 10^{-10}. Usually, a converged solution for the eigenvalue of α_1 is obtained within three or four iterations.

4.3 PSE Methods

In the Parabolized Stability Equations approach, one attempts to construct an approximate solution of the Navier-Stokes equations. The concept was introduced by Herbert and Bertolotti [40] in 1987 and has now been well developed and applied to a variety of linear and nonlinear stability problems for two- and three-dimensional, incompressible and compressible boundary layer flows (see Section 2.4).

In contrast to the locally parallel approach explained in the previous section, the central idea of the PSE formulation is to split the disturbance quantities into a shape function that slowly varies in the x_1-direction, and an oscillatory wave part as written in equation 4.24. Here, β_1 is the spanwise wave number, ω is the frequency, α_1 is the wave number in the streamwise direction, and $\hat{\mathbf{q}}_{\mathbf{1}_{mn}}$ is the vector of the shape functions. The indices m and n are the Fourier summation indices, and the subscript mn denotes the mode number. Before substituting this into the Navier-Stokes equations in disturbance

$$\mathbf{q}_1(x_1, x_2, x_3, t) = \sum_{n=-\infty}^{\infty} \sum_{m=-\infty}^{\infty} \hat{\mathbf{q}}_{\mathbf{1}_{mn}}(x_1, x_3) e^{i \int \alpha_{1_{mn}} dx_1 + im\beta_1 x_2 - in\omega t} \tag{4.24}$$

form (equations 4.1, 4.2), the streamwise derivatives of the shape functions are written in equations 4.25 and 4.26. Due to the assumption of a slow variation of the shape func-

$$\frac{\partial \hat{\mathbf{q}}_{\mathbf{1}_{mn}}}{\partial x_1} = \left(i\alpha_{1_{mn}} \hat{\mathbf{q}}_{\mathbf{1}_{mn}} + \frac{\partial \hat{\mathbf{q}}_{\mathbf{1}_{mn}}}{\partial x_1} \right) e^{i\theta_{mn}} \tag{4.25}$$

$$\frac{\partial^2 \hat{\mathbf{q}}_{\mathbf{1}_{mn}}}{\partial x_1^2} = \left(\frac{\partial^2 \hat{\mathbf{q}}_{\mathbf{1}_{mn}}}{\partial x_1^2} + 2i\alpha_{1_{mn}} \frac{\partial \hat{\mathbf{q}}_{\mathbf{1}_{mn}}}{\partial x_1} + \frac{d\alpha_{1_{mn}}}{dx_1} \hat{\mathbf{q}}_{\mathbf{1}_{mn}} - \alpha_{1_{mn}}^2 \hat{\mathbf{q}}_{\mathbf{1}_{mn}} \right) e^{i\theta_{mn}} \tag{4.26}$$

$$\theta_{mn} = i \int \alpha_{1_{mn}} dx_1 + im\beta_1 x_2 - in\omega t \tag{4.27}$$

tions in the x_1-direction, the second derivative in equation 4.26 can be dropped, which enforces the PSE assumption. Now, substituting equations 4.25 and 4.26 into equations 4.1 and 4.2 and collecting terms with the same Fourier coefficients mn, a new system of PDE's is obtained. This system of PDE's is referred to as the Parabolized Stability Equations (PSE) and written in vector form for each Fourier component in eq-

$$\mathbf{A}_{mn} \frac{\partial^2 \hat{\mathbf{q}}_{\mathbf{1}_{mn}}}{\partial x_3^2} + \mathbf{B}_{mn} \frac{\partial \hat{\mathbf{q}}_{\mathbf{1}_{mn}}}{\partial x_3} + \mathbf{C}_{mn} \hat{\mathbf{q}}_{\mathbf{1}_{mn}} = \mathbf{D}_{mn} \frac{\partial \hat{\mathbf{q}}_{\mathbf{1}_{mn}}}{\partial x_1} + \mathbf{E}_{mn} \frac{\partial^2 \hat{\mathbf{q}}_{\mathbf{1}_{mn}}}{\partial x_1 \partial x_3} + \frac{\mathbf{S}_{mn}}{\mathcal{A}_{mn}} \tag{4.28}$$

uation 4.28. There, the vector $\mathbf{S}_{mn}$ represents the Fourier components of the nonlinear term $(\mathbf{v_1} \cdot \nabla)\mathbf{v_1}$, $\mathcal{A}_{mn} = e^{i \int \alpha_{1_{mn}} dx_1}$ denotes the amplitude and phase modulation by

the complex wave number $\alpha_{1_{mn}}$, and $\mathbf{A_{mn}}$, $\mathbf{B_{mn}}$, $\mathbf{C_{mn}}$, $\mathbf{D_{mn}}$, $\mathbf{E_{mn}}$ are (4×4) coefficient matrices.

The major advantage of the PSE is that despite a small elliptic remainder consisting of the streamwise pressure gradient, the system of PDE's is parabolic and its solution can be obtained by a marching-type method. From equation 4.28, it is noted that the linear PSE are obtained by dropping the nonlinear term $\mathbf{S_{mn}}$ and setting the indices m and n to one. Further, assuming that the amplitude part $\hat{\mathbf{q}}_1$ of the disturbance quantity is no longer a function of the streamwise location, but depends only on the normal coordinate, the two remaining terms on the right-hand side of equation 4.28 vanish and one obtains the linear stability equations as discussed in Section 4.2.

In the spatial framework of the PSE, the unknown quantities are the wave numbers α_1, β_1, and the frequency ω in addition to the unknown shape functions $\hat{\mathbf{q}}_1$. Fixing the real frequency ω and the real spanwise wave number β_1, a relation to determine the complex streamwise wave number α_1 is still missing. This forms the main difficulty in the PSE formulation, since both the shape functions and the phase of the disturbance quantities depend on the streamwise coordinate (equation 4.24). In a non-parallel mean flow, the different physical quantities grow at different rates, and thus, one can only determine the growth rate σ_1=-$\alpha_{1,imag}$ from the computed the wave number α_1 based on some quantity (e.g., velocities, pressure, or energy). Usually, the wave number α_1 is computed at the location in the boundary layer where the disturbance quantities, or the disturbance energy become maximal. This location varies slowly in the marching direction.

The procedure to compute α_1 at a streamwise station is described as follows. Starting with an initial solution found from solving the local eigenvalue problem at

$x_1 = x_0$, one marches to the next station $x_1 = x_0 + \Delta x_1$ and solves for the shape functions $\hat{q}_1$ assuming that $\alpha_1(x_1 = x_0 + \Delta x_1) = \alpha_1(x_0)$. Approximating the change in the shape functions with a Taylor series at $x_1 = x_0 + \Delta x$, one can derive equation 4.29 to update α_1 at $x_1 = x_0 + \Delta x_1$ as in equation 4.29, where $\hat{q}_1$ stands for any physical

$$\alpha_{1,new} = \alpha_{1,old} + \frac{1}{i \cdot \hat{q}_1} \left(\frac{\partial \hat{q}_1}{\partial x_1} \right)_{x_3 = x_3(\hat{q}_{1,max})} \tag{4.29}$$

quantity in the flow field. Updating the shape functions and iterating until the change in α_1 is less than a defined tolerance, the solution at this station is obtained and the procedure repeated at the next streamwise station. The PSE method is very efficient, since it takes only a few iterations on α_1 to obtain an accurate solution, provided that the gradients in the flowfield are moderate.

Before the explanation of the implemented solution method for the PSE, an important property of the disturbance quantities needs to be mentioned. Since the Navier-Stokes equations (equations 4.1, 4.2) represent real physical quantities, the total disturbance quantities must be real as well. For the applied Fourier series representation of the disturbance quantities (equation 4.24), this condition is expressed in equation 4.30 and leads to the general symmetry condition for the complex disturbances given in equation 4.31. Here, the asterisk denotes the complex conjugate.

$$\sum_{n=-\infty}^{\infty} \sum_{m=-\infty}^{\infty} \hat{q}_{1_{mn}} e^{i\theta} = \sum_{n=-\infty}^{\infty} \sum_{m=-\infty}^{\infty} \hat{q}^*_{1_{mn}} e^{-i\theta^*} \tag{4.30}$$

$$\hat{q}_{1_{m,n}} = \hat{q}^*_{1_{-m,-n}} \tag{4.31}$$

This symmetry condition can be exploited to reduce the computational effort significantly. For later reference, figures 4.2 - 4.4 show the symmetry conditions for different disturbances in the complex (m,n)-plane.

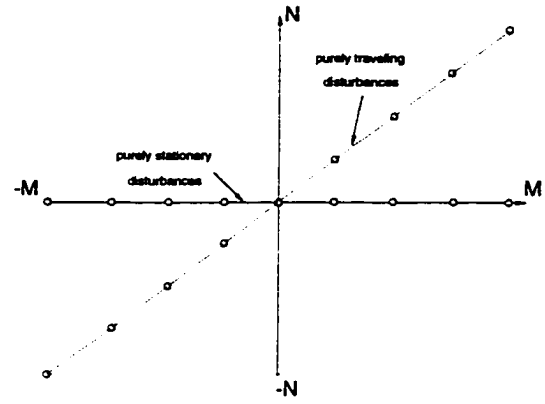

Figure 4.2: Symmetry of purely steady, or purely traveling disturbances (2D and 3D)

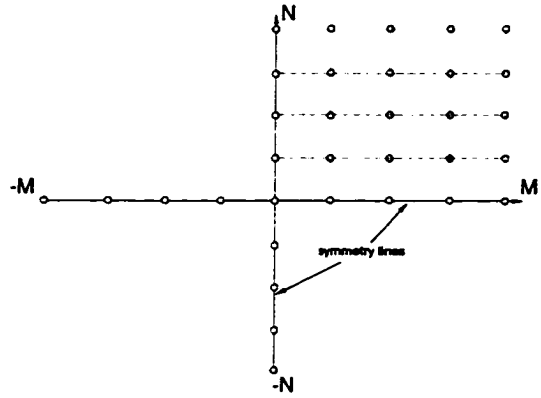

Figure 4.3: Symmetry of interacting symmetric steady and traveling disturbances (2D)

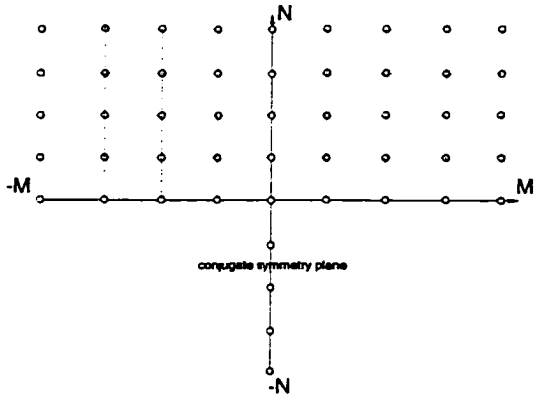

Figure 4.4: Symmetry of interacting steady and traveling disturbances (3D)

In the present formulation, the PSE are expressed in body-oriented coordinates and solved using a fourth-order-accurate compact difference scheme in the wall-normal

direction, a second-order-accurate upwind finite difference scheme in the streamwise direction, and Fast Fourier Transform (FFT)-techniques for the formation of the nonlinear terms. The remainder of this section will explain the applied solution method that treats the nonlinear terms explicitly.

In order to apply the compact scheme formulation in the wall-normal direction, a new vector of unknowns $\Lambda_1=\{\hat{u}_1, \partial\hat{u}_1/\partial x_3, \hat{u}_2, \partial\hat{u}_2/\partial x_3, \hat{u}_3, \hat{p}\}^T$ is introduced. Now, the system of PDE's representing the PSE (equation 4.28) is rewritten as a system of ODE's for each Fourier mode in equation 4.32. The streamwise derivative is discretized

$$\frac{\partial \Lambda_{1_{mn}}}{\partial x_3} = \mathbf{H}_{mn}\Lambda_{1_{mn}} + \mathbf{F}_{mn}\frac{\partial \Lambda_{1_{mn}}}{\partial x_1} + \mathbf{G}_{mn} \tag{4.32}$$

using the second-order-accurate upwind scheme given in equation 4.33, where the coefficients P_1, P_2, P_3 are found from a Lagrangian interpolation.

$$\frac{\partial \Lambda_{1_{mn}}}{\partial x_1} = P_1 \cdot \Lambda_{1_{n-2}} + P_2 \cdot \Lambda_{1_{n-1}} + P_3 \cdot \Lambda_{1_n} \tag{4.33}$$

Substituting equation 4.33 into equation 4.32, the first wall-normal derivative is expressed in a form suitable for the Euler-McLaurin equation (equation 4.19), and with the matrix coefficients of $\overline{\mathbf{H}}_{mn}$ and $\overline{\mathbf{G}}_{mn}$ being functions of the normal coordinate only, the second wall-normal derivative of the new vector of unknowns is written in equations

$$\frac{\partial \Lambda_{1_{mn}}}{\partial x_3} = \overline{\mathbf{H}}_{mn}\Lambda_{1_{mn}} + \overline{\mathbf{G}}_{mn} \tag{4.34}$$

$$\overline{\mathbf{H}}_{mn} = \mathbf{H}_{mn} + \mathbf{F}_{mn} \cdot P_3 \tag{4.35}$$

$$\overline{\mathbf{G}}_{mn} = \mathbf{G}_{mn} + \mathbf{F}_{mn} \cdot (P_1 \cdot \Lambda_{1_{n-2}} + P_2 \cdot \Lambda_{1_{n-1}}) \tag{4.36}$$

$$\frac{\partial^2 \Lambda_{1_{mn}}}{\partial x_3^2} = \left(\overline{\mathbf{H}}_{mn} \cdot \overline{\mathbf{H}}_{mn} + \frac{\partial \overline{\mathbf{H}}_{mn}}{\partial x_3}\right)\Lambda_{1_{mn}} + \left(\overline{\mathbf{H}}_{mn} \cdot \overline{\mathbf{G}}_{mn} + \frac{\partial \overline{\mathbf{G}}_{mn}}{\partial x_3}\right) \tag{4.37}$$

4.34 - 4.37. In equations 4.32 - 4.37, the matrices $\mathbf{H}_{mn}$ and $\overline{\mathbf{H}}_{mn}$ are (6×6) coefficient matrices, and the vectors $\mathbf{F}_{mn}$, $\mathbf{G}_{mn}$ and $\overline{\mathbf{G}}_{mn}$ are (6×1) coefficient vectors. It is further noted that the vector of the nonlinear terms is contained in the vector $\mathbf{G}_{mn}$.

Again utilizing the Euler-McLaurin formula as explained in Section 4.2, the matrix equation 4.38 for any Fourier mode can be formed at every normal location k except the boundaries. The (6×6) coefficient matrices $\mathbf{A}_{mn_k}$ and $\mathbf{B}_{mn_k}$, as well as the

$$\mathbf{A}_{mn_k} \cdot \Lambda_{1_{mn_{k-1}}} + \mathbf{B}_{mn_k} \cdot \Lambda_{1_{mn_k}} = \mathbf{D}_{mn_k} \quad ; \quad k = 2, \cdots, N-1 \tag{4.38}$$

$$\mathbf{A_k} = -\mathbf{I} - \frac{h_k}{2} \cdot \overline{\mathbf{H}}_{k-1} - \left(\overline{\mathbf{H}} \cdot \overline{\mathbf{H}} + \frac{\partial \overline{\mathbf{H}}}{\partial x_3} \right)_{k-1} \tag{4.39}$$

$$\mathbf{B_k} = -\mathbf{I} - \frac{h_k}{2} \cdot \overline{\mathbf{H}}_k + \left(\overline{\mathbf{H}} \cdot \overline{\mathbf{H}} + \frac{\partial \overline{\mathbf{H}}}{\partial x_3} \right)_k \tag{4.40}$$

$$\mathbf{D_k} = \frac{h_k}{2} \left(\overline{\mathbf{G}}_k + \overline{\mathbf{G}}_{k-1} \right) - \frac{h_k^2}{12} \left\{ \left(\overline{\mathbf{HG}} + \frac{\partial \overline{\mathbf{G}}}{\partial x_3} \right)_k - \left(\overline{\mathbf{HG}} + \frac{\partial \overline{\mathbf{G}}}{\partial x_3} \right)_{k-1} \right\} \tag{4.41}$$

(6×1) coefficient vector $\mathbf{D}_{mn_k}$ are formed according to equations 4.39 - 4.41, where **I** represents the unit matrix, h_k is the normal distance between two adjacent grid points, and the indices m and n are dropped for convenience.

The boundary conditions are treated as follows. For all Fourier modes except the mean flow distortion, the three homogeneous boundary conditions for the velocity components at the wall and in the freestream are implemented. For the treatment of the mean flow distortion mode, one drops the spanwise momentum equation, since there is no disturbance growth in that direction, eliminates the elliptic remainder in the streamwise momentum equation consisting of the pressure gradient $\partial p/\partial x_1$, and hence, obtains a parabolic and boundary layer-type system of equations. The only unknowns of that system are $u_{1_{0,0}}$ and $v_{1_{0,0}}$ that can be solved for using the continuity equation and the streamwise momentum equation. In order to determine the mean flow distortion of the pressure, a normalization condition is specified at the wall, and the momentum equation in the wall-normal direction is integrated.

Then, shifting the matrix system, the block-tridiagonal system in equation 4.42 is obtained. This system can be solved efficiently as described in Section 4.2.

$$\mathbf{AA}_{\mathbf{mn_k}} \cdot \mathbf{\Lambda}_{\mathbf{1_{mn_{k-1}}}} + \mathbf{BB}_{\mathbf{mn_k}} \cdot \mathbf{\Lambda}_{\mathbf{1_{mn_k}}} + \mathbf{CC}_{\mathbf{mn_k}} \cdot \mathbf{\Lambda}_{\mathbf{1_{mn_{k+1}}}} = \mathbf{DD}_{\mathbf{mn_k}} \tag{4.42}$$

Before the summary of the explicit solution algorithm, the dealiasing method implemented will be explained for stationary disturbances. The phenomenon of aliasing arises due to the truncation of the applied Fourier series at a finite number of modes. Consider the generic nonlinear term in equation 4.43. Due to the multiplication of the well-resolved phase terms θ_m, higher phase terms θ_{2m} are created that cannot be repre-

$$u^2 = \left(\sum_{m_1=-M}^{M} u_{m_1} \cdot e^{i\theta_{m_1}} \right) \cdot \left(\sum_{m_2=-M}^{M} u_{m_2} \cdot e^{i\theta_{m_2}} \right) = \left(\sum_{m=-2M}^{2M} a_m u_m \cdot e^{i\theta_m} \right) \tag{4.43}$$

sented in the (-M,$\cdots$,M)-Fourier space. Hence, they appear as a high-frequency errors in the solution, if no measures are taken to avoid that. In the present solution method, a double-sized Fourier space (-2M,$\cdots$,2M) is created for the nonlinear terms, where the higher-phase terms arising are set to zero after the evaluation of the nonlinear terms.

Concluding this section, the present explicit solution algorithm for the PSE will be summarized. Starting at $x_1 = x_{1_0}$ with an initial solution for the shape functions of the individual modes $\mathbf{q_{1_{mn}}}$, and with an initial guess for the corresponding streamwise wave numbers $\alpha_{1_{mn}}$, the nonlinear solution method proceeds as follows.

- Nonlinear iteration
  - Form the individual Fourier modes $\mathbf{\Lambda_{1_{mn}}} = \hat{\mathbf{q}}_{\mathbf{1_{mn}}} \cdot e^{i \int \alpha_{1_{mn}} dx_1}$ of the disturbances according to the relevant symmetry conditions in the entire complex (m,n)-plane, and distribute the wave numbers $\alpha_{1_{mn}}$ according to the selected primary disturbances.
  - In order to avoid aliasing errors due to the applied FFT-techniques, create a double-sized complex plane and transform all complex quantities there.

- Transform all Fourier components into the physical space using the FFT.
- Compute all the nonlinear terms contained in $(\mathbf{v_1} \cdot \nabla)\mathbf{v_1}$ in the physical space.
- Using the inverse FFT, transfer the nonlinear terms back to the Fourier space and form the vector $\mathbf{S_{mn}}/\mathcal{A}_{mn}$.
- Transfer all complex quantities back to the normal-sized complex plane and proceed with a wave number iteration loop for the primary disturbances.
- Wave number iteration
  * For the specified primary disturbances, form and solve the block-tridiagonal system for the shape functions according to equations 4.38 - 4.42.
  * Until convergence, compute the new streamwise wave numbers $\alpha_{1_{mn}}$ based on different physical quantities according to equation 4.29 and the procedure described in the present section.
  * Based on the computed primary wave numbers, distribute the wave numbers of the other disturbances algebraically.
- After the wave number iteration converged, check for the convergence of the nonlinear terms.

The iteration on the nonlinear terms continues until the maximal difference in the shape functions of two consecutive iterations is less than, say, $\epsilon=10^{-10}$. For the wave number iteration, a typical tolerance is also given by $\epsilon=10^{-10}$.

In the presented explicit method, convergence problems arise when the nonlinear terms grow to significant amplitude levels. This is due to the lagging of the iteration on all nonlinear terms behind the wave number iteration on just the selected primary disturbances. This observation is discussed in more detail in Chapter 7, where an alternative implicit solution method is presented.

4.4 Secondary Instability Analysis using Floquet Theory

In the last section of this chapter, the focus is on the presentation of the numerical tools for the investigation of the secondary instability mechanism. The first subsection describes the secondary instability according to the findings of previous experimental and computational work. The second subsection contains the derivation of the applied temporal Floquet theory, and the last subsection introduces the recently developed and very efficient Implicitly Restarted Arnoldi Method for the solution of selected regions of the eigenvalue spectrum.

4.4.1 Portrait of the Secondary Instability

In the present work, the secondary instability is defined as the linear instability of a periodic secondary flow. Due to the nonlinear interaction and saturation of primary stationary disturbances, highly inflectional velocity profiles are formed in both the spanwise and the wall-normal direction, and these are the origin of this instability mechanism.

In the review of the previous work on the secondary instability in the Sections 2.3 and 2.4, it was pointed out that the secondary instability originates away from the wall in regions of high vorticity and shear at normal locations of about half the boundary layer thickness. The developing instability structures were then found to travel on the back of the primary stationary crossflow vortices, and their growth was attributed to combined vortex stretching and tilting in the presence of strong flow gradients. Further, the inclination of the secondary instability structures with respect to the constant phase lines was found to be about 50° for three-dimensional boundary layer flows. The secondary instabilities are seen as high-frequency disturbances that grow explosively within

a short streamwise distance. Their frequency is usually in the kHz-range, which is an order-of-magnitude higher than the most amplified primary traveling disturbances. This high frequency is in accordance with the typical local time scale $t^* = \delta^*/U_e^*$ in the region of the nonlinear saturation. Further, the experimentally and numerically observed half-wavelength periodicity is interpreted as an indication of the presence of secondary instabilities in the flow.

An important open question regards the self-sustained growth of the high-frequency disturbances. From this discussion, it is clear how the secondary instability to high-frequency disturbances develops. Rather, the question is related to the route by which the high-frequency disturbances enter the boundary layer before their amplitude is explosively amplified by the strong growth rates typical for the secondary instability. This question is discussed in subsequent chapters.

4.4.2 Floquet Theory

A Floquet system is defined to be a system of linear ODE's whose coefficients are periodic in the independent variables. Floquet Theory was, for example, applied by Herbert [65] in 1983 to explain the nonlinear transition process in two-dimensional boundary layers, as well as by Fischer and Dallmann [67] in 1991 for the DLR-Transition Experiment (see Subsection 2.4.5).

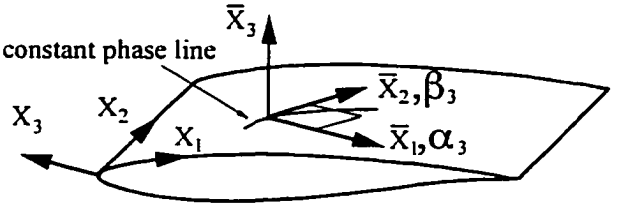

Figure 4.5: Definition of the Galilean coordinate system

In this subsection, the stability of a new mean flow consisting of the original basic flow and the saturated primary disturbance wave is investigated. A new Galilean coordinate system $(\bar{x}_1, \bar{x}_2, \bar{x}_3)$ is defined that travels with the phase velocity in the $\bar{x}_1$-direction. The coordinate $\bar{x}_2$ is aligned with the constant phase lines as shown in figure 4.5 (see also Appendix I for the definition of the different coordinate systems and angles). In this coordinate system, the new mean flow $\mathbf{Q_2} = \{U_2, W_2, V_2, P_2\}^T$ is formed by a superposition of the parallel base flow $\mathbf{Q_0}(\bar{x}_3)$ and the solutions of the primary disturbance quantities obtained from a PSE computation. In equation 4.44, α_3 is the real wave number in the $\bar{x}_1$-direction. Its definition is given in equation 4.45, where Ψ is the wave angle of the primary disturbances. By forming the mean flow $\mathbf{Q_2}$ as described above, the neglect of the mean flow distortion (shape assumption) and the assumption of an arbitrary amplitude of the primary disturbance utilized in previous work [65, 67] are avoided.

$$\mathbf{Q_2}(\bar{x}_1, \bar{x}_3) = \mathbf{Q_0}(\bar{x}_3) + \sum_{m=-\infty}^{\infty} \hat{\mathbf{q}}_{\mathbf{1}_m}(\bar{x}_3) e^{im\alpha_3 \bar{x}_1} \tag{4.44}$$

$$\alpha_3 = \mathrm{sgn}(\Psi)\sqrt{\alpha_{1,\mathrm{real}}^2 + \beta_1^2} \quad ; \quad \Psi = \tan^{-1}\left(\frac{\alpha_{1,\mathrm{real}}}{\beta_1}\right) \tag{4.45}$$

The temporal stability of this mean flow is investigated by seeking a disturbance of the form shown in equation 4.46. There, the new vector of unknowns $\mathbf{q_3}$ consists of the four primitive variables u_3, w_3, v_3 and p_3. Further, the real part of σ_3 measures the growth of the secondary instability, its imaginary part determines the frequency, and β_3 is the real wave number tangential to the constant phase lines.

$$\mathbf{q_3}(\bar{x}_1, \bar{x}_2, \bar{x}_3, t) = e^{\sigma_3 t + i\beta_3 \bar{x}_2} \sum_{m=-\infty}^{\infty} \hat{\mathbf{q}}_{\mathbf{3}_m}(\bar{x}_3) e^{im\alpha_3 \bar{x}_1} \tag{4.46}$$

Substituting equations 4.44 and 4.46 for $\mathbf{V_0}$ and $\mathbf{v_1}$, respectively, into equation 4.2, dropping the nonlinear term $(\mathbf{v_1} \cdot \nabla)\mathbf{v_1}$, and introducing a new vector of

unknowns $\bar{\Lambda}_m=\{\bar{u}_{3_m}, \partial\bar{u}_{3_m}/\partial\bar{x}_3, \bar{w}_{3_m}, \partial\bar{w}_{3_m}/\partial\bar{x}_3, \bar{v}_{3_m}, \bar{p}_{3_m}\}^T$ in a similar way to the approach described in Section 4.3, one obtains a linear system of ODE's for the vector of the secondary disturbance eigenfunctions $\bar{\Lambda}$. The resulting equations for all the Fourier modes are given in equations 4.47 - 4.60, where $\bar{\Lambda}$ is a $\{(2\cdot M+1)\cdot 6\}$-vector at the normal location k .

$$\frac{\partial\bar{\Lambda}_{1_m}}{\partial\bar{x}_3} = \bar{\Lambda}_{2_m} \quad ; \quad \frac{\partial\bar{\Lambda}_{3_m}}{\partial\bar{x}_3} = \bar{\Lambda}_{4_m} \quad ; \tag{4.47}$$

$$\frac{\partial\bar{\Lambda}_{2_m}}{\partial\bar{x}_3} = \{\Delta\bar{\Lambda}_{1_m} + im\alpha_{3_m}\bar{\Lambda}_{6_m} + (\sum_{m_1} U_{2_{m_1}})(\sum_{n_1} in_1\alpha_{3_{n_1}}\bar{\Lambda}_{1_{n_1}}) + \tag{4.48}$$

$$(\sum_{m_1} W_{2_{m_1}})(i\beta_3\sum_{n_1}\bar{\Lambda}_{1_{n_1}}) + (\sum_{m_1} V_{2_{m_1}})(\sum_{n_1}\Lambda_{2_{n_1}}) + \tag{4.49}$$

$$(\sum_{m_1}\bar{\Lambda}_{1_{m_1}})(\sum_{n_1} in_1\alpha_{3_{n_1}} U_{2_{n_1}}) + (\sum_{m_1}\bar{\Lambda}_{5_{m_1}})(\sum_{n_1}\frac{\partial U_{2_{n_1}}}{\partial\bar{x}_3})\}Re \quad ; \tag{4.50}$$

$$\frac{\partial\bar{\Lambda}_{4_m}}{\partial\bar{x}_3} = \{\Delta\bar{\Lambda}_{3_m} + i\beta_3\bar{\Lambda}_{6_m} + (\sum_{m_1} U_{2_{m_1}})(\sum_{n_1} in_1\alpha_{3_{n_1}}\bar{\Lambda}_{3_{m_1}}) + \tag{4.51}$$

$$(\sum_{m_1} W_{2_{m_1}})(i\beta_3\sum_{n_1}\bar{\Lambda}_{3_{n_1}}) + (\sum_{m_1}\Lambda_{4_{m_1}})(\sum_{n_1} V_{2_{n_1}}) + \tag{4.52}$$

$$(\sum_{m_1}\bar{\Lambda}_{1_{m_1}})(\sum_{n_1} in_1\alpha_{3_{n_1}} W_{2_{n_1}}) + (\sum_{m_1}\bar{\Lambda}_{5_{m_1}})(\sum_{n_1}\frac{\partial W_{2_{n_1}}}{\partial\bar{x}_3})\}Re \quad ; \tag{4.53}$$

$$\frac{\partial\bar{\Lambda}_{5_m}}{\partial\bar{x}_3} = -im\alpha_3\bar{\Lambda}_{1_m} - i\beta_3\bar{\Lambda}_{3_m} \quad ; \tag{4.54}$$

$$\frac{\partial\bar{\Lambda}_{6_m}}{\partial\bar{x}_3} = -\Delta\bar{\Lambda}_{5_m} - \frac{1}{Re}(im\alpha_{3_m}\bar{\Lambda}_{2_m} + i\beta_3\bar{\Lambda}_{4_m}) - \tag{4.55}$$

$$(\sum_{m_1} U_{2_{m_1}})(\sum_{n_1} in_1\alpha_{3_{n_1}}\bar{\Lambda}_{5_{n_1}}) - (\sum_{m_1} W_{2_{m_1}})(i\beta_3\sum_{n_1}\bar{\Lambda}_{5_{n_1}}) + \tag{4.56}$$

$$(\sum_{m_1} V_{2_{m_1}})(\sum_{n_1} in_1\alpha_{3_{n_1}}\bar{\Lambda}_{1_{n_1}}) + (\sum_{m_1} V_{2_{m_1}})(i\beta_3\sum_{n_1}\bar{\Lambda}_{3_{n_1}}) - \tag{4.57}$$

$$(\sum_{m_1}\bar{\Lambda}_{1_{m_1}})(\sum_{n_1} in_1\alpha_{3_{n_1}} V_{2_{n_1}}) - (\sum_{m_1}\bar{\Lambda}_{5_{m_1}})(\sum_{n_1}\frac{\partial V_{2_{n_1}}}{\partial\bar{x}_3}) \quad ; \tag{4.58}$$

$$\Delta = \frac{1}{Re}(m^2\alpha_{3_m}^2 + \beta_3^2) + \sigma_3 \quad ; \tag{4.59}$$

$$\frac{\partial\bar{\Lambda}}{\partial\bar{x}_3} = \overline{A}\bar{\Lambda} \tag{4.60}$$

Expanding the summations in m_1 and n_1 from -M$\cdots$M, collecting terms with the same Fourier component, and writing equations 4.47 - 4.59 in the entire wall-normal

domain, a generalized eigenvalue problem of the form given in equation 4.61 is obtained. In fact, the compact scheme formulation applied here yields the non-trivial case of a sin-

$$\overline{\mathbf{A}}\overline{\mathbf{\Lambda}} = \sigma_3\overline{\mathbf{B}}\overline{\mathbf{\Lambda}} \tag{4.61}$$

gular, non-symmetric, and semi-positive-definite generalized eigenvalue problem. It is noted that the leading dimensions of the coefficient matrices $\overline{\mathbf{A}}$ and $\overline{\mathbf{B}}$ in equation 4.61 can easily reach significant orders. Considering a minimal problem size for a satisfactory resolution in both the Fourier space and the wall-normal direction, a leading matrix dimension of 9·6·71=3834 is obtained by distributing 71 points in the normal direction and truncating the Fourier series at M=4. Hence, the need for efficient eigenvalue solvers is obvious. Utilizing the QZ-algorithm that is implemented in the ZGEGV-routine available in the public-domain software library LAPACK proved to be extremely CPU-time intensive for these matrix dimensions. For example, it takes about five CPU-hours on a Sun-Ultra-2 workstation (333 MHz) to compute the entire eigenvalue spectrum of a problem with a leading matrix dimension of 2700.

Therefore, the recently developed Implicitly Restarted Arnoldi Method [1] was adapted to the present problem. This method approximates the eigenvalues and eigenvectors in specified regions of the eigenvalue spectrum. The details of this very efficient solution method are explained in Subsection 4.4.3. Applying this method to a problem size of 5000, the required CPU-time to compute 10 eigenvalues that are located in a selected region of interest amounts to only one minute on the workstation quoted above.

For a confirmation of the eigenvalues obtained from the global solver, a local eigenvalue solver based on a Newton-Raphson technique was developed. The solution method is based on a fourth-order-accurate compact scheme formulation and the solution algorithm is equivalent to the one explained for the solution of the linear spatial

eigenvalue problem in Section 4.2. However, additional iteration options have been implemented in order to account for the presence of (2·M+1) eigenmodes in the coefficient matrices.

Instead of dropping one of the wall boundary conditions as described for the linear spatial eigenvalue problem in Section 4.2, the iteration is performed at the wall-normal location where the most dominant secondary eigenmode has its maximum. There, either one of the momentum equations, or the continuity equation is dropped, the block-tridiagonal system is solved, and the convergence check is performed by evaluating the dropped momentum, or continuity equation. Hence, the developed solution method is capable of iterating on different eigenmodes of the unknowns u_3, w_3 and v_3 at a specified wall-normal location.

$$\Psi_2 = \tan^{-1}\left(\frac{\alpha_3}{\beta_3}\right) \tag{4.62}$$

Finally, and for later reference in Chapters 5 and 6, the wave angle of the secondary disturbances Ψ_2 is defined in equation 4.62 and depicted in figure 4.6.

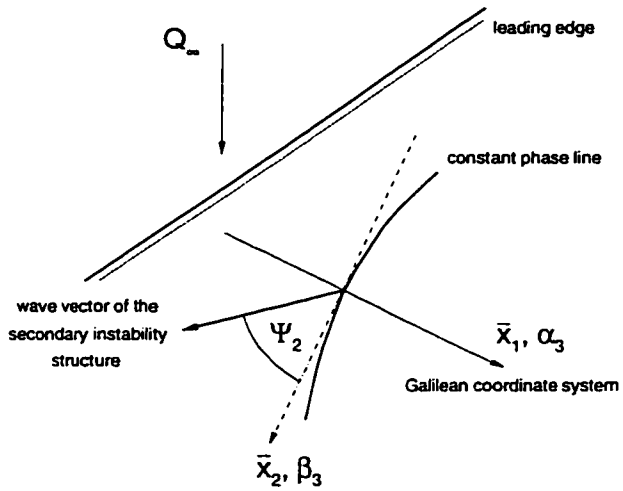

Figure 4.6: Definition of the secondary wave angle

4.4.3 The Implicitly Restarted Arnoldi Method

The original method developed by Arnoldi [87] in 1951 represents an orthogonal projection method for the approximation of a subset of eigenvalues and eigenvectors of a general sparse square matrix. In order to overcome the severe computational and storage requirements for a large number of iteration steps towards a converged Ritz-approximation, Saad [88] introduced the explicitly restarted Arnoldi iteration in 1980. For the sake of improving the starting vector by forcing it into the direction of the desired invariant subspace, Sorensen [89] proposed the Implicitly Restarted Arnoldi Method (IRAM) which is based on Krylov-subspace projection techniques in 1992. Ever since, this method has seen much improvement and automation. In 1995, a public-domain software package called ARPACK was developed by Lehoucq et al. [1]. This package was used for the computations of this work. In the remainder of this subsection, the essentials of this method will be explained.

For the solution of a generalized eigenvalue problem in the form given in equation 4.61, one is faced with a singular and non-symmetric matrix $\overline{\mathbf{A}}$, and with a semi-positive-definite, symmetric matrix $\overline{\mathbf{B}}$. Introducing a complex shift δ such that it is located in the center of a complex cell in which a few eigenvalues are expected, the singularity problem can be bypassed and equation 4.61 is reformulated as in equation 4.63.

$$(\overline{\mathbf{A}} - \delta\overline{\mathbf{B}})\bar{\mathbf{\Lambda}} = (\sigma_3 - \delta)\overline{\mathbf{B}}\bar{\mathbf{\Lambda}} \tag{4.63}$$

$$\kappa\bar{\mathbf{\Lambda}} = (\overline{\mathbf{A}} - \delta\overline{\mathbf{B}})^{-1}\overline{\mathbf{B}}\bar{\mathbf{\Lambda}} \;\; ; \;\; \kappa = \frac{1}{(\sigma_3 - \delta)} \tag{4.64}$$

Defining a matrix operator $\mathbf{M} = (\overline{\mathbf{A}} - \delta\overline{\mathbf{B}})^{-1}\overline{\mathbf{B}}$, the problem is then rewritten in the form of a standard eigenvalue problem (equation 4.65).

$$\kappa\bar{\mathbf{\Lambda}} = \mathbf{M}\bar{\mathbf{\Lambda}} \tag{4.65}$$

The objective of the IRAM is to obtain approximate eigenvalues and eigenvectors of a selected part of the entire eigenvalue spectrum of the matrix **M** in equation 4.65. These approximate eigenvectors and eigenvalues are called Ritz-approximations. Equation 4.66 defines a property for the Ritz-pair (**X**, θ) [1]. The scalar $|\beta_k e_k^T \Gamma|$

$$\|\mathbf{MX} - \mathbf{X}\theta\| = \|(\mathbf{MV_k} - \mathbf{V_k H_k})\| = |\beta_k \mathbf{e_k^T \Gamma}| \tag{4.66}$$

is called the Ritz-estimate for the Ritz-pair (**X**, θ) as an approximate eigenpair for **M**. Ritz-pairs are immediately available from the eigenpairs of the small projected upper Hessenberg matrix **H**. A matrix is called an upper Hessenberg matrix, if its elements $h_{ij}=0$ for $i>j+1$.

Regarding the accuracy of the eventually obtained eigenvalues of the non-Hermitian matrix **M**, the only possible statement is that the residual is small if $|\beta_k e_k^T \Gamma|$ is small [1]. Typically, this is accomplished to an order of $|\beta_k e_k^T \Gamma| < 10^{-15}$.

Put $v_1 = \frac{A}{\|A\|}$; $w = Mv_1$; $\alpha_1 = v_1^H w$;

Put $f_1 \leftarrow w - v_1\alpha_1$; $V \leftarrow v_1$; $H \leftarrow \alpha_1$;

For j=1,k-1

1. $\beta_j = \|f_j\|$; $v_{j+1} \leftarrow f_j/\beta_j$
2. $V_{j+1} \leftarrow (V_j, v_{j+1})$; $\hat{H}_j \leftarrow \begin{pmatrix} H_j \\ \beta_j e_j^T \end{pmatrix}$
3. $z \leftarrow Mv_{j+1}$
4. $h \leftarrow V_{j+1}^T z$; $f_{j+1} \leftarrow z - V_{j+1}h$

   (hereafter, an orthogonalization is done, if necessary)
5. $H_{j+1} \leftarrow (\hat{H}_j, h)$

EndFor

Figure 4.7: Algorithm for a k-step Arnoldi factorization

In order to utilize the property given by equation 4.66, the method starts by building a m-step Arnoldi factorization of the form given in equation 4.67 according to the flow chart in figure 4.7 [1]. There, the columns of $\mathbf{V_k}$ contain the orthonormal so-called Arnoldi vectors, $\mathbf{H_k}$ is an upper Hessenberg matrix, and $f_k e_k^T$ represents the residual. From equation 4.67, the connection to the Ritz-approximation is obvious.

$$\mathbf{M V_m} = \mathbf{V_m H_m} + f_m e_m^T \tag{4.67}$$

Since the information obtained through this process is determined by the chosen starting vector $\mathbf{v_1}$, and since there is no a priori information about the number of required Arnoldi steps until the solutions converge, it is attractive to restart the method with an improved starting vector. This restarting is an essential part of the IRAM. The steps of the method are summarized in figure 4.8 [1]. Starting with a sparse square matrix $\mathbf{M}$ of dimension m, an initial m-step Arnoldi factorization is computed and the implicitly restarted iteration begins. First, the eigenvalues of the $\mathbf{H_m}$-matrix are computed and split into a wanted set k and an unwanted set p, where m=k+p. The unwanted set is then used as shifts μ_j in Step 3 of the algorithm. Here, only p instead of m QR-factorization steps are done, and new matrices $\mathbf{H_m}$ and $\mathbf{V_m}$ are built. Restarting the method is now accomplished in Step 4. The old m-step Arnoldi factorization is post-multiplied by the newly obtained matrices $\mathbf{Q_{1,\cdots,p}}$ that are associated with the shifts μ_j. Because of the Hessenberg-structure of the matrices $\mathbf{Q_j}$, it turns out that the leading k columns of the new factorization remain in an Arnoldi form with an updated residual [1]. It is here where the check for convergence is appropriate for just the k eigenvalues wanted. If convergence was not reached yet, the method proceeds with p additional Arnoldi steps in Step 5 of the algorithm in order to obtain a new m-step Arnoldi factorization that has an updated starting vector.

Have an initial m-step Arnoldi factorization

For l=1,2,$\cdots$, until convergence

1. Compute eigenvalues of $\mathbf{H_m}$ and select p shifts $\mu_1, \mu_2, \cdots, \mu_p$
2. $q^T \leftarrow e_m^T$
3. For j=1,2,$\cdots$,p
   (a) Factor $[\mathbf{Q_j}, \mathbf{R_j}] = qr(\mathbf{H_m} - \mu_j \mathbf{I})$
   (b) $\mathbf{H_m} \leftarrow \mathbf{Q_j^H H_m Q_j}$; $\mathbf{V_m} \leftarrow \mathbf{V_m Q_j}$
   (c) $q \leftarrow q^H \mathbf{Q_j}$

   EndFor
4. $f_k \leftarrow v_{k+1}\hat{\beta}_k + f_m \sigma_k$; $\mathbf{V_k} \leftarrow \mathbf{V_{m(1:n,1:k)}}$; $\mathbf{H_k} \leftarrow \mathbf{H_{m(1:k,1:k)}}$
5. Beginning with the k-step Arnoldi factorization $\mathbf{AV_k} = \mathbf{V_k H_k} + f_k e_k^T$, apply p additional steps of the Arnoldi process to obtain a new m-step Arnoldi factorization $\mathbf{AV_m} = \mathbf{V_m H_m} + f_m e_m^T$.

EndFor

Figure 4.8: Algorithm for the Implicitly Restarted Arnoldi Method (IRAM) [1]

Before the summary of the IRAM advantages, the alternatively mentioned QZ-algorithm will be briefly compared to the conventional Arnoldi method. According to Golub and Van Loan [90], the number of operations necessary to solve for the entire spectrum of the (n×n) eigenvalue problem $\mathbf{Ax}=\sigma\mathbf{Bx}$ amounts to $30n^3$. This estimate is based on two necessary QZ-steps per eigenvalue. In comparison, Saad [91] gives an estimate for the number of operations necessary to perform one step of the conventional

Arnoldi algorithm for linear systems as $(m+3)n + m^2/2$. Here, m is the dimension of the Krylov-subspace and is usually small compared to n. Making an extremely conservative estimate of n necessary Arnoldi steps, the number of operations is still one power less than for the QZ-algorithm.

Finally, a few advantages of the IRAM versus the conventional Arnoldi method will be pointed out that result in a significant savings regarding the number of necessary iterations and the required CPU-time.

- Due to the restarting, the problem of the a priori unknown memory requirement for an unknown number of iteration steps in the conventional method is avoided.
- Only p instead of (k+p)-steps are necessary in each QR-factorization. Even if k is small, the savings are significant when a large number of iterations is necessary for convergence.
- Only k residuals instead of (k+p) residuals need to fulfill the specified convergence criteria in Step 4 of the algorithm.
- Each iteration begins with an improved starting vector that has enhanced components in the wanted directions, whereas the other directions are damped.

CHAPTER 5

SWEPT HIEMENZ FLOW

5.1 Introduction

The stability of incompressible quasi-three-dimensional boundary layers of a similarity type was previously investigated by Mack [22] and Malik et al. [23]. Whereas Mack presented linear stability results for different similarity parameters and documented the influence of the pressure gradient on the stability of these crossflow dominated boundary layers, Malik et al. considered the model problem of Swept Hiemenz flow in more detail and focused on the nonlinear interaction of different disturbances in the flow. Following the work of Malik et al. [23], the mean flow is defined in Section 5.2. Linear and nonlinear results from a primary stability analysis are presented in Section 5.3, and Section 5.4 contains detailed results from a secondary instability analysis of Swept Hiemenz flow using both the PSE and Floquet Theory.

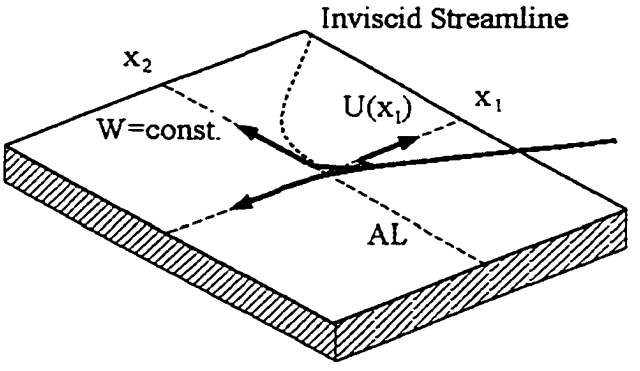

Figure 5.1: Stagnation flow over a swept flat plate

The two-dimensional stagnation flow against a wall is usually referred to as Hiemenz Flow, since it was Hiemenz who found an analytical solution to the problem in 1911 (see Reference [92]). Superposing a constant velocity component in the spanwise direction along the attachment-line (AL) upon this two-dimensional flow, a quasi-three-dimensional mean flow is constructed that represents the stagnation flow against a swept flat plate of infinite extension as shown in figure 5.1. This flow is called Swept Hiemenz flow and can be used to model the leading edge region of a swept wing, where the leading edge extends along the attachment-line. The inviscid velocity distributions are given in equation 5.1. Due to the constant pressure gradient in the flow, the inviscid U^*-compo-

$$U^* = c \cdot x_1^* \;\; ; \;\; V^* = -c \cdot x_3^*; \;\; W^* = W_\infty^* = \text{const.} \tag{5.1}$$

nent develops in the streamwise direction according to equation 5.1, whereas the velocity component W^* along the attachment-line remains constant. The inviscid streamline then experiences a continuous curvature, since its angle is defined as in equation 5.2. As explained in Chapter 1, it is the imbalance of the forces in the boundary layer due to this curvature that causes the Swept Hiemenz flow to be inviscidly unstable.

$$\Theta(x_1^*) = \tan^{-1}\left(\frac{W^*}{U^*(x_1^*)}\right) \tag{5.2}$$

5.2 Mean Flow Computation

According to the definitions for the stream function Φ, the similarity parameter m, the normal coordinate η and the velocity components given in Chapter 3, and further using the inviscid velocity components from equation 5.1, these parameters are written for Swept Hiemenz flow as follows.

$$m \;=\; \frac{x_1^*}{U^*}\frac{\partial U^*}{\partial x_1^*} = 1 \quad , \tag{5.3}$$

$$\Phi = \sqrt{\nu^* x_1^* U^*} f(\eta) = \sqrt{c \cdot \nu^*} \cdot x_1^* \cdot f(\eta) \quad , \tag{5.4}$$

$$\eta = \frac{x_3^*}{\sqrt{\nu^* x_1^* / U^*}} = \frac{x_3^*}{\sqrt{\nu^* / c}} \quad , \tag{5.5}$$

$$U_0^* = c \cdot x_1^* \cdot f'(\eta) \;\; ; \;\; V_0^* = -\sqrt{c \cdot \nu^*} \cdot f(\eta) \;\; ; \;\; W_0^* = W_\infty^* \cdot g(\eta) \tag{5.6}$$

Substituting these expressions into the quasi-three-dimensional boundary layer equations, a set of two homogeneous ordinary differential equations can be derived. It is

$$f''' + f \cdot f'' + (1 - f'^2) = 0 \quad , \tag{5.7}$$

$$g'' + f \cdot g' = 0 \quad , \tag{5.8}$$

$$f = f' = g = 0 \;\; \text{at} \;\; \eta = 0 \;\; ; \;\; f' = g = 1 \;\; \text{at} \;\; \eta \to \infty \tag{5.9}$$

noted that the obtained equations 5.7 - 5.9 are exact solutions to the Navier-Stokes equations. Further, they represent the homogeneous version of the boundary layer equations from Chapter 3 for the similarity parameter m=1. Solving the equations numerically by a Runge-Kutta method yields a solution with the important feature of a constant bound-

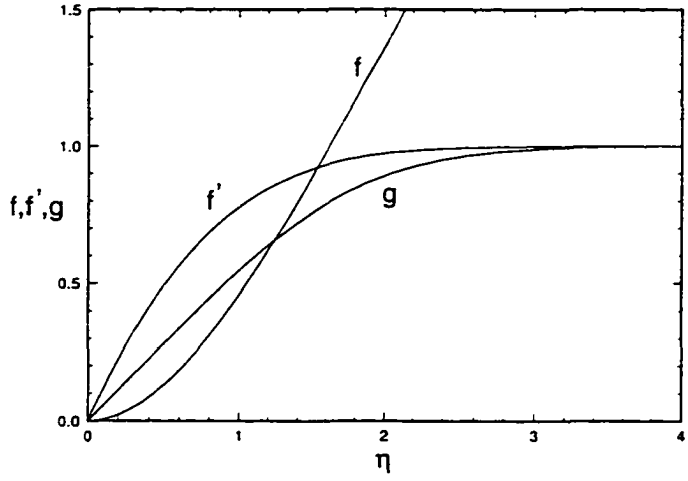

Figure 5.2: Falkner-Skan-Cooke similarity solutions for m=1

ary layer thickness. In figure 5.2, the obtained similarity profiles are plotted versus the wall-normal coordinate.

Next, the velocity and length scales used for the nondimensionalization of the velocities in equation 5.6, and for the streamwise and wall-normal coordinates are defined. For the computations in this chapter, the constant inviscid spanwise velocity component W^*_∞ is used as velocity scale, as well as the constant local length scale given in equation 5.10. One can further define two characteristic Reynolds numbers for the

$$l^* = \sqrt{\frac{\nu^* \cdot x_1^*}{U^*}} = \sqrt{\frac{\nu^*}{dU^*/dx_1^*}} = \sqrt{\frac{\nu^*}{c}} \tag{5.10}$$

stream- and spanwise directions, Re and $\overline{Re}$ respectively, in equation 5.11. Having described the mean flow, the remaining sections of this chapter will deal with the stability analysis of this flow.

$$Re(x_1^*) = \frac{l^* \cdot U^*(x_1^*)}{\nu^*} = \frac{U^*}{\sqrt{\nu^* \cdot c}} \quad ; \quad \overline{Re} = \frac{l^* \cdot W^*_\infty}{\nu^*} = \frac{W^*_\infty}{\sqrt{\nu^* \cdot c}} \tag{5.11}$$

5.3 Primary Stability Analysis

In studying the stability of quasi-three-dimensional boundary layers away from the leading edge of the considered geometry, care must be taken in specifying a flow that is stable along the attachment-line (see Chapter 1). According to recent results by Balakumar [93], the attachment-line of an infinite swept wing is numerically shown to be stable against two-dimensional disturbances for Reynolds numbers less than the critical value of $\overline{Re}_{crit.}$=583. For the results presented in the next sections, a constant spanwise Reynolds number of $\overline{Re}$=500 was chosen, and thus, the attachment-line is assumed to be linearly stable.

Before the detailed presentation of the results from a linear and nonlinear primary stability analysis in the following subsections, the applied computational grid needs

to be described. A typical grid for the primary stability computations consists of 141 points in the wall-normal direction, where the first 71 points are clustered within the boundary layer according to the grid-stretching equation 5.12. In the region of the outer

$$x_{3,i} = \frac{\Delta \cdot \eta_i}{1 + \frac{\Delta}{x_{3,max}} - \eta_i} \tag{5.12}$$

flow, the remaining points were distributed uniformly up to a maximal normal extension of about 10 boundary layer thicknesses. For the marching in the streamwise direction, different step sizes were selected depending on the complexity of the flow. Purely stationary or traveling cases could be run with a step size of ΔRe=7.5, whereas the interaction cases in Subsection 5.3.2 and in Section 5.4 required values of ΔRe=5, or even ΔRe=2.5 for a proper resolution of the steep gradients in the region of nonlinear saturation.

5.3.1 Linear Analysis

In order to investigate the stability characteristics of the prescribed flow, local stability analyses at different streamwise locations are performed first. Thus, the neutral points for stationary and traveling disturbances, as well as the locally most amplified wave numbers and frequencies can be determined. In figure 5.3, the spatial growth rates σ_1 for the stationary disturbances are plotted versus the spanwise wave number β_1. It can be seen that the unstable wave number range begins at $\beta_1 \simeq 0.10$ for all investigated streamwise locations. However, its extension increases rapidly with increasing distance from the neutral point at Re=98.0, where β_1=0.125. The locally most amplified spanwise wave number was found to be β_1=0.32 at Re=300, where the streamwise wave number assumes a value of α_1=(-0.4398,-0.0231). Next, the most amplified spanwise wave number according to its spatial growth in the downstream direction is sought. Therefore, starting at their neutral point, disturbances of different spanwise wave number are intro-

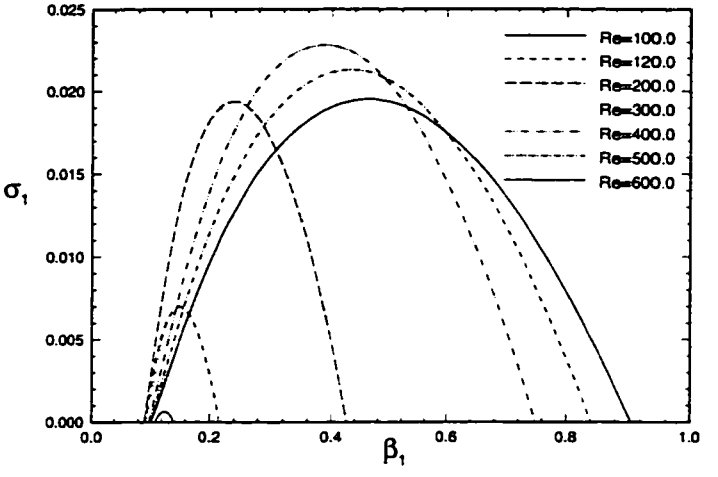

Figure 5.3: Stationary growth rates from local theory

duced and their spatial evolution downstream computed. Figure 5.4 shows the N-factors obtained from a computation incorporating the parallel flow assumption. Obviously, the wave numbers in the range of β_1=0.3 - 0.4 are amplified the most, and for a further investigation of the nonlinear development of the disturbances, these wave numbers need to be considered.

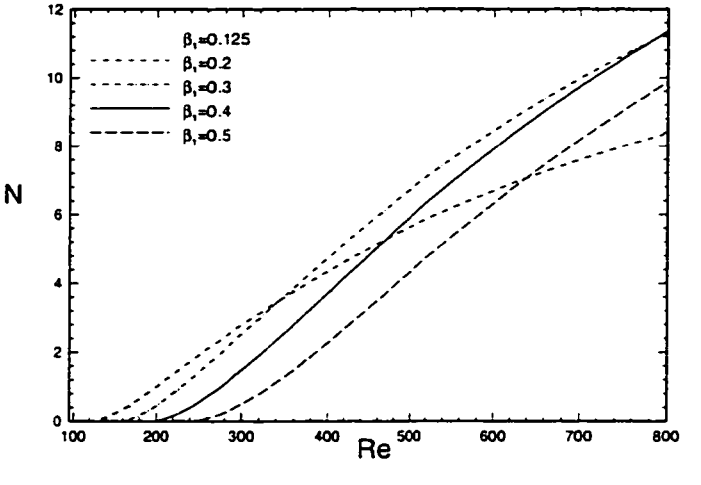

Figure 5.4: N-factors from a locally parallel computation

Having determined the most amplified stationary disturbances, the traveling disturbances will now be considered. Therefore, the nondimensional frequency F is defined in equation 5.13.

$$F = \frac{2\pi \cdot \nu^* \cdot f^*}{(W_\infty^*)^2} \tag{5.13}$$

First, the existence of two unstable families of spanwise wave numbers will be discussed. This observation is due to Mack [22] who investigated the stability of three-dimensional boundary layers with different pressure gradients. It was also reported by Malik et al. [23] from their study of the Swept Hiemenz flow and by Takagi et al. [21] from their experimental work on the rotating-disc flow problem.

a) $F=0.75\cdot10^{-4}$

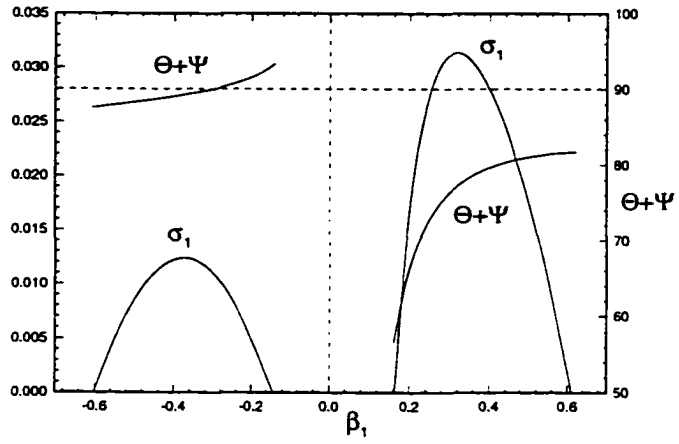

b) $F=1.20\cdot10^{-4}$

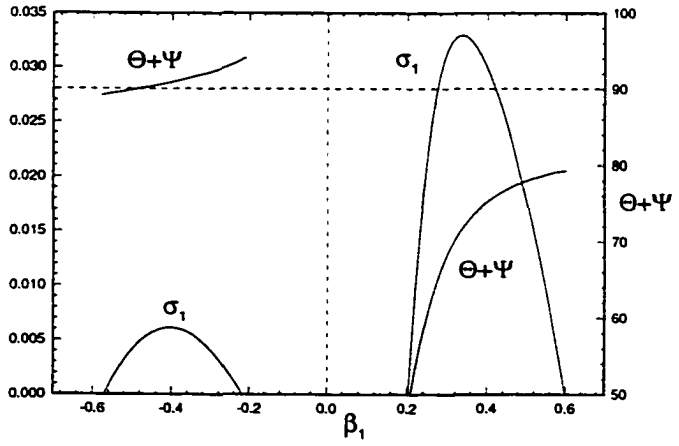

Figure 5.5: Two unstable spanwise wave number families at Re=300

Figure 5.5 shows the growth rates and the angle of inclination with respect to the inviscid streamline Ψ_1 of the two unstable families for the later considered frequency of $F=0.75\cdot10^{-4}$, and for the most unstable frequency of $F=1.2\cdot10^{-4}$ at Re=300.

$$\Theta = \tan^{-1}\left(\frac{\mathrm{Re}}{\overline{\overline{\mathrm{Re}}}}\right) \quad ; \quad \Psi = \tan^{-1}\left|\frac{\alpha_{1,\mathrm{real}}}{\beta_1}\right| \quad ; \quad \Psi_1 = \Theta + \Psi \tag{5.14}$$

The angles of the inviscid streamline Θ and of the wave propagation direction Ψ are defined in equation 5.14 and visualized in figure 5.6. At Re=300, the most amplified spanwise wave numbers of the most amplified frequency $F=1.2\cdot10^{-4}$ (as shown in the subsequent computation) are $\beta_1=0.34$ and $\beta_1=-0.40$ with the corresponding streamwise

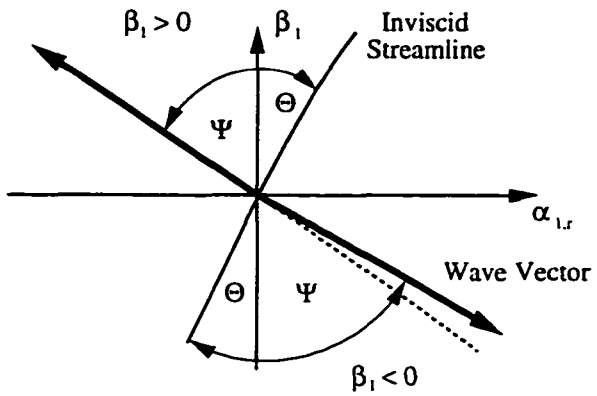

Figure 5.6: Definition of the wave angle and the angle of the inviscid streamline

wave numbers and angles of $\alpha_1=(-0.29609,-0.03294)$ and $\alpha_1=(0.69103,-0.00611)$, as well as $\Psi_1=72.01°$ and $\Psi_1=90.90°$, respectively. Observed is, first, that both families are propagating in opposite directions. Second, the more unstable family is oriented opposite to the direction of the crossflow-component of the mean flow (i.e., it is propagating in the direction of the centrifugal force induced by the streamline curvature).

Next, the dependence of the most amplified spanwise wave numbers on the frequency will be examined. In this computation, the procedure is as follows. Starting from the most amplified spanwise wave number at F=0, the frequency is incremented

and the new eigensolution is found such that it satisfies the condition given below for the most amplified β_1. A Newton-Raphson technique can be implemented to compute a

$$\frac{\partial \sigma_1}{\partial \beta_1}(\beta_1 + \Delta\beta_1) = (\frac{\partial \sigma_1}{\partial \beta_1})_0 + (\frac{\partial^2 \sigma_1}{\partial \beta_1^2}) \cdot d\beta = 0 \tag{5.15}$$

correction $\Delta\beta_1$ until equation 5.15 is satisfied. In figure 5.7, the most amplified spanwise wave number and the wave angle Ψ_1 are plotted versus the nondimensional frequency at Re=300. As discussed earlier in this subsection, the two unstable families of disturbances are distinguished by their propagation direction along the wave vector that is inclined at the wave angle Ψ with respect to the body-fixed coordinate system. Plotting the locally

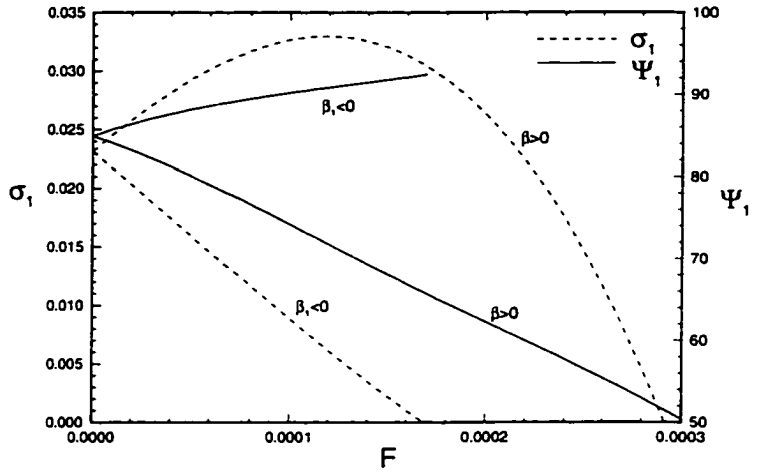

Figure 5.7: Two families of unstable waves at Re=300

most unstable growth rate versus the nondimensional frequency at different streamwise stations in figure 5.8, one observes a decrease of the most amplified frequency in the streamwise direction. Starting with $F=1.6 \cdot 10^{-4}$ at Re=100, the locally most unstable frequency at Re=600 is $F=0.9 \cdot 10^{-4}$. Thus, a wide range of frequencies needs to be investigated using a computation that considers the spatial disturbance growth in the downstream direction for a determination of the most unstable frequency.

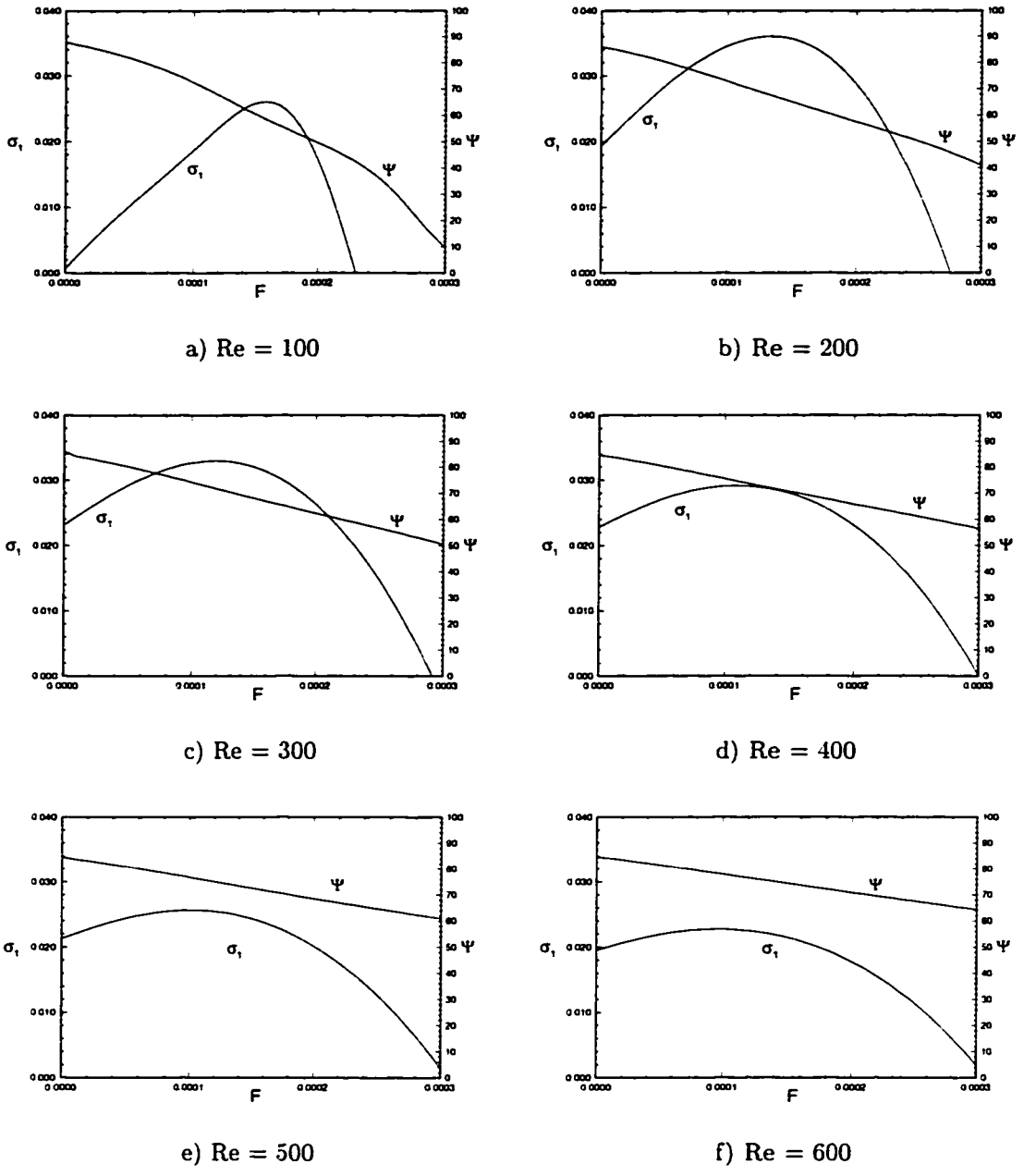

a) Re = 100 b) Re = 200

c) Re = 300 d) Re = 400

e) Re = 500 f) Re = 600

Figure 5.8: Wave angles and most amplified frequencies at different streamwise locations

In table 5.1, the values of the frequency, the spanwise wave number and the wave angle are specified at the locations of the maximal growth rate. In the downstream direction, the locally most amplified disturbances are shifted to lower frequencies and

Table 5.1: Locally most amplified eigenpairs at different streamwise locations

Re	$\sigma_{1,=max.}$	$F_{\sigma_1=max}$	$\beta_{1,\sigma_1=max.}$	$\Psi_{\sigma_1=max.}$
100	0.026	$1.60 \cdot 10^{-4}$	0.237	58.06°
200	0.036	$1.35 \cdot 10^{-4}$	0.289	67.25°
300	0.033	$1.20 \cdot 10^{-4}$	0.335	71.70°
400	0.029	$1.10 \cdot 10^{-4}$	0.378	74.46°
500	0.026	$1.00 \cdot 10^{-4}$	0.410	76.72°
600	0.023	$0.95 \cdot 10^{-4}$	0.434	78.26°

the constant phase lines turn towards the inviscid streamline. The closer alignment of the constant phase lines with the inviscid streamline can be also seen in figure 5.9, where the propagation direction of the steady crossflow vortices is visualized together with corresponding mean flow profiles along the wave vector.

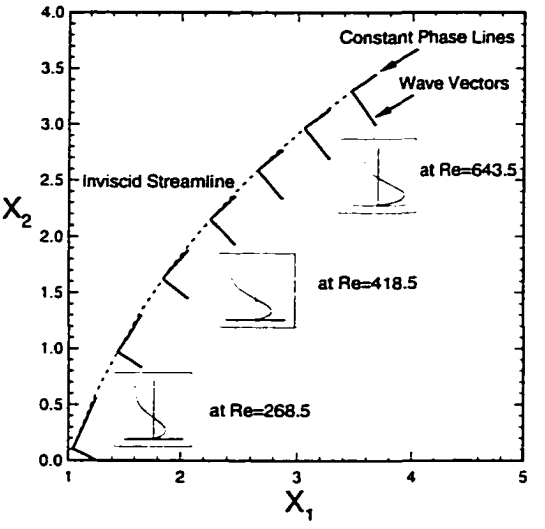

Figure 5.9: Propagation of steady disturbances relative to the inviscid streamline (β_1=0.4)

Considering the data in table 5.1 and the most amplified stationary wave numbers, β_1=0.3 and 0.4, were selected for a computation of the most unstable frequency according to the spatial growth in the x_1-direction. Figure 5.10 shows the N-factors ob-

tained from a computation incorporating the locally parallel flow assumption for different frequencies. Comparing the results of figures 5.4 and 5.10, one concludes the following :

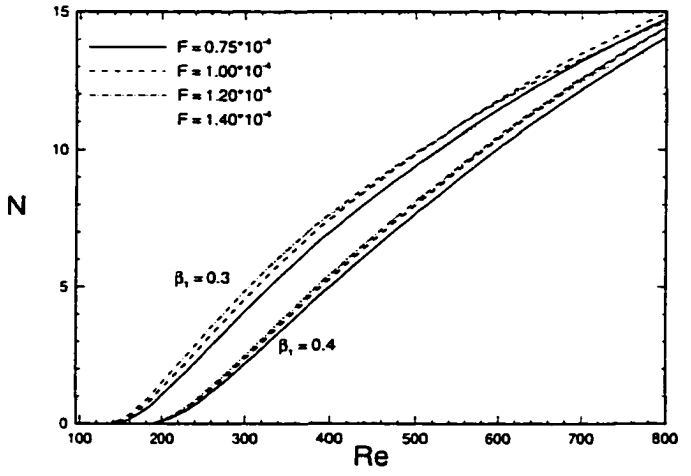

Figure 5.10: N-factors from a locally parallel computation

- The traveling disturbances become unstable at lower Reynolds numbers than the stationary disturbances.
- The traveling disturbances are slightly more unstable than the stationary disturbances ($N_{trav} \simeq 15$, $N_{stat} \simeq 13.5$ at Re=800).
- For Re $\leq$ 800, the spanwise wave number β_1=0.3 is more amplified than β_1=0.4. The difference in the amplification is larger for the traveling disturbances.
- The most unstable frequency for both β_1=0.3 and β_1=0.4 is F=$1.0 \cdot 10^{-4}$.

Concluding this subsection, figures 5.11 and 5.12 show the growth rates and N-factors obtained from a PSE computation in comparison with the results of a locally parallel computation for the most amplified spanwise wave number β_1=0.3 and the most amplified frequency F=$1.0 \cdot 10^{-4}$. The disturbance growth of the different flow quantities predicted by the PSE varies widely in the region immediately behind the neutral point.

Further downstream, the growth rates based on the u_1-component and the disturbance energy tend towards the same value, as well as the v_1- and w_1-components. Comparing the physically most relevant results for the growth rate and the N-factor based on the disturbance energy with the parallel results, one can state that including the non-parallel variation of the mean flow in the computation is destabilizing the flow, where the destabilizing influence is stronger for the traveling disturbances.

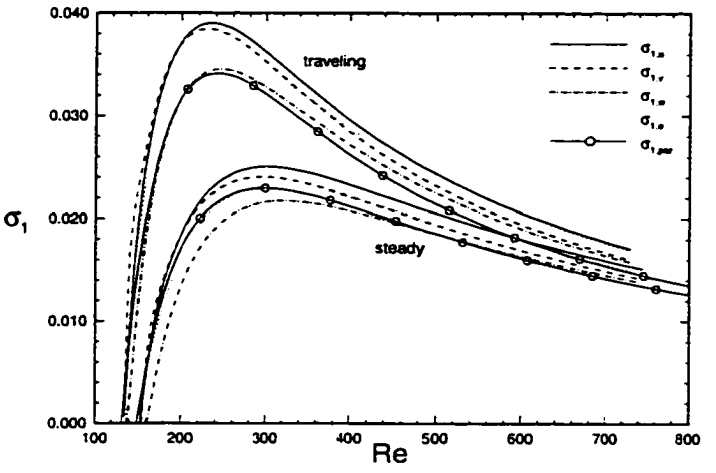

Figure 5.11: Growth rates from locally parallel theory and PSE

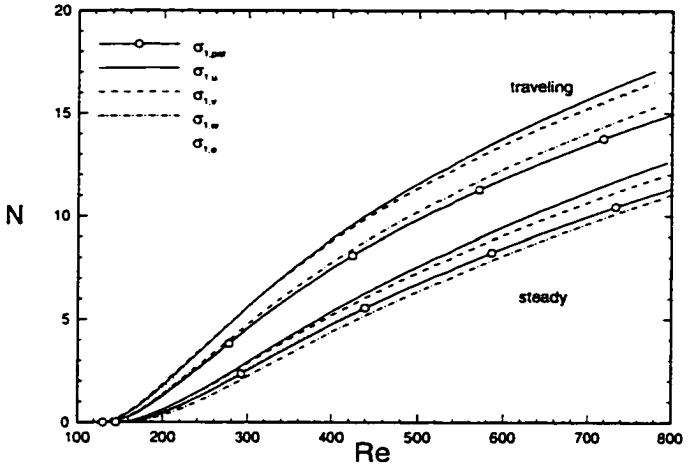

Figure 5.12: N-factors from locally parallel theory and PSE

5.3.2 Nonlinear Analysis

After the extensive study of the linear stability of Swept Hiemenz flow, the nonlinear interaction of the disturbances will be investigated in this subsection. Despite the findings in the previous subsection, where the flow was found to be most unstable against disturbances with a spanwise wave number of β_1=0.3 and a frequency F=$1.0 \cdot 10^{-4}$, disturbances with a spanwise wave number of β_1=0.4 and a frequency F=$0.75 \cdot 10^{-4}$ will be considered in the remainder of this chapter. Thereby, previous work by Malik et al. [23] is followed closely. The main objective of this approach is the validation of the modifications in the nonlinear PSE code that account for three-dimensional disturbances.

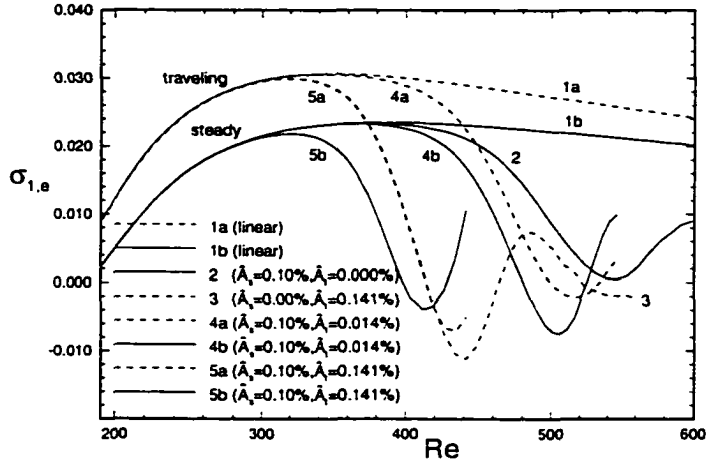

Figure 5.13: Growth rates based on the disturbance-energy

In particular, the interaction of a stationary and a traveling disturbance of similar initial amplitude, as well as the interaction of a stationary disturbance with larger amplitude and a traveling disturbance with smaller amplitude were considered. Figure 5.13 shows the growth rates for different initial amplitude levels Â. The rms amplitude Â is defined in equation 5.16, where $\hat{u}_1$ and $\hat{w}_1$ are the total shape functions in the streamwise and spanwise direction, respectively.

$$\hat{A} = \sqrt{(\hat{u}_1^2 + \hat{w}_1^2)_{max}}/W_\infty^* \tag{5.16}$$

Introducing the initial disturbances at Re=186, the computations were performed including eight modes in the spanwise and frequency domain. The results agree with the work by Malik et al. [23]. It can be seen from figure 5.13 that the interaction of a larger amplitude stationary with a smaller traveling disturbance leads to an earlier saturation of the stationary disturbance. On the other hand, the nonlinear evolution of the traveling disturbance is not affected by the stationary vortex when both initial modes are of similar amplitude.

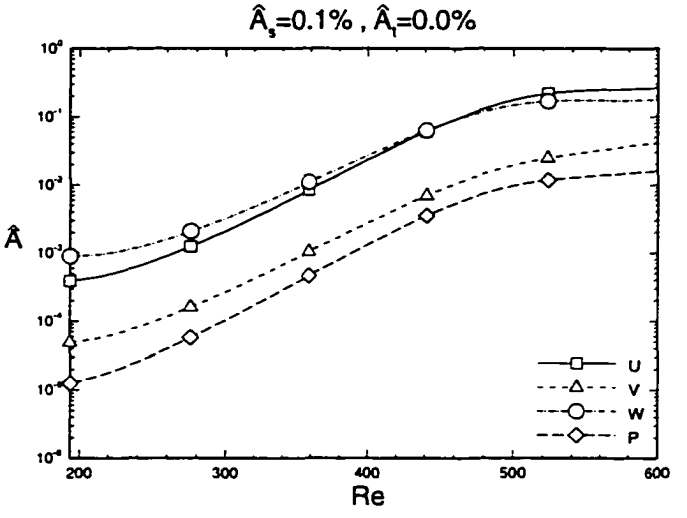

Figure 5.14: Amplitudes of the primary disturbances for the purely stationary case

The influence of including a small amplitude traveling disturbance in the computations is presented in figures 5.14 and 5.15, where the evolution of the stationary and traveling disturbance amplitudes is shown. In figure 5.14, the results for the purely steady case are presented, and figure 5.15 shows the results for a case where a small amplitude traveling disturbance interacts with the stationary vortex. The latter case will be referred to as the "lower-frequency" case from now on. For the purely stationary

case, one observes that both the u_1- and w_1-components are fully saturated at Re $\simeq$ 550, and the saturation amplitude levels are $\hat{A}_s \simeq 24\%$ for the u_1-component and $\hat{A}_s \simeq$ 17% for the w_1-component. For the "lower-frequency" case with a primary frequency of $F=0.75\cdot10^{-4}$, the stationary disturbance saturates at Re $\simeq$ 480 and the amplitude levels are $\hat{A}_s \simeq 10\%$ and $\hat{A}_s \simeq 8\%$ for the u_1- and w_1-components, respectively. Also, since the traveling disturbances grow longer in that case (see Curve 4a in figure 5.13), they reach larger amplitude levels than the stationary disturbances.

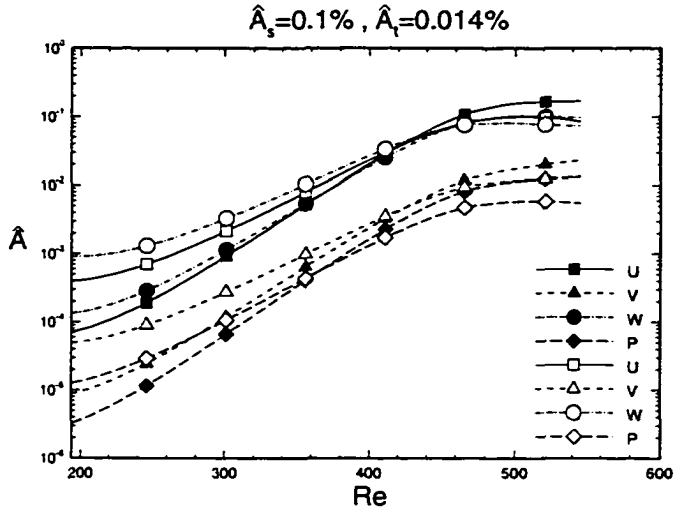

Figure 5.15: Amplitudes of the primary disturbances for the "lower-frequency case" (solid symbols: traveling mode; hollow symbols: steady mode)

Next, the distribution of the velocity profiles for the purely stationary case is presented. In figure 5.16, at the streamwise location where the stationary disturbances are saturated (Re=546), the shapes of the individual modes for the velocity components tangential to the stationary vortex (w_1), and perpendicular to it (u_1) are plotted in the Galilean coordinate system ($\bar{x}_1, \bar{x}_2, \bar{x}_3$) as defined in Appendix I. Obviously, the first seven modes of the component along the vortex contain important information, and thus, it is necessary to include at least eight modes in the computation. One also observes that the fundamental mode β_1 along the stationary vortex is very large at this

Reynolds number ($\hat{A} \simeq 30\%$) and shows the typical double peak structure observed in the experiments just before the secondary instability mechanism causes transition. At

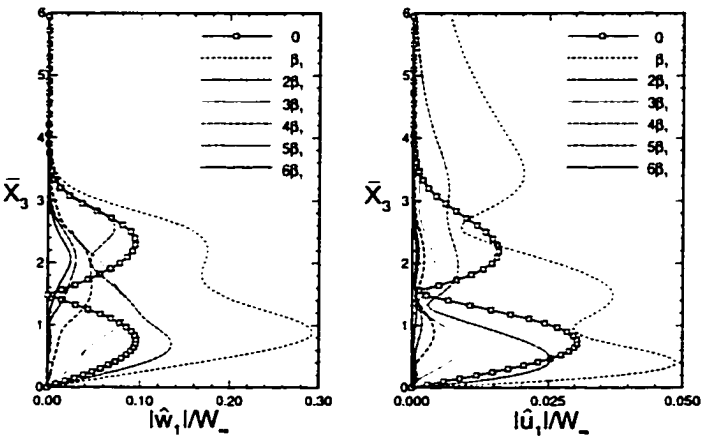

Figure 5.16: Shape functions of individual modes at Re=546

the same streamwise station, the total velocity component along the stationary vortex is shown at four different locations within one wavelength perpendicular to the vortex in figure 5.17. Here, α_3 is a new wave number perpendicular to the vortex (see Section 5.4). The inflectional character of the profiles is clearly observed. These strongly inflectional profiles are the origin of the secondary instability that will be studied in the next section.

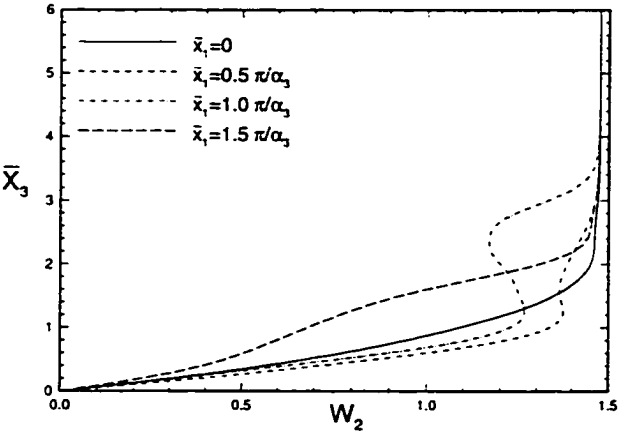

Figure 5.17: Total flow quantity at different spanwise stations for Re=546

For the purpose of a more detailed description of the present flow and in order to further explain the onset of the secondary instability, certain features of the purely stationary crossflow vortex will be visualized next. First, the spatially developing stationary crossflow vortex is shown at different streamwise stations in figure 5.18. The developing distortion of the boundary layer in the spanwise direction and the roll-up of the crossflow vortices in the positive spanwise direction are clearly seen. The spanwise variation of the boundary layer thickness is about two at Re $\simeq$ 400, where the vortices start to roll over. At Re $\simeq$ 600, however, the spanwise difference in the wall-normal locations where the flow reaches the freestream value is about four. The structure of these velocity contours explains the varying inflectional profiles observed at different spanwise positions in figure 5.17. Combining these observations, it can be stated that a strong mechanism is present in the flow that moves low-speed fluid away from the wall into the outer flow and high-speed fluid from the outer flow towards the wall. It is this exchange of fluid that causes the redistribution of vorticity in the spanwise direction.

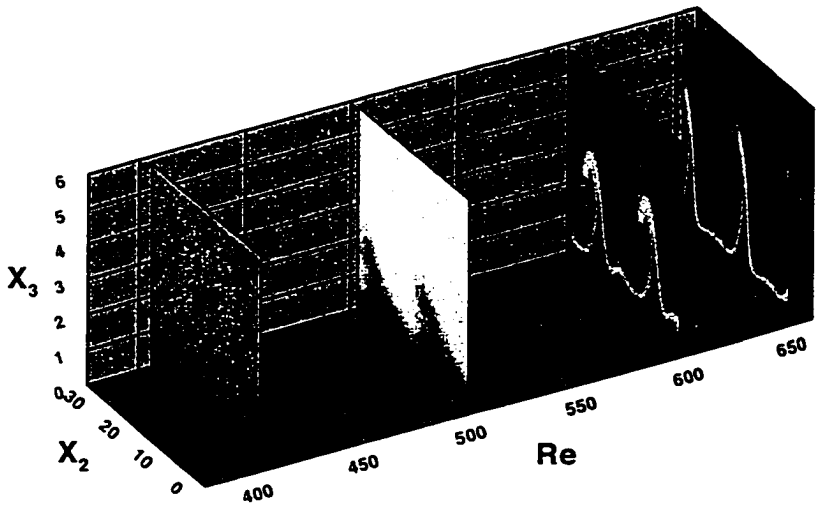

Figure 5.18: Contours of the total U_2-component of the stationary crossflow vortex

In order to further document the structure of the distorted boundary layer, two components of the total modified mean flow are shown at different normal positions and streamwise locations in figure 5.19. Plotted in the Galilean coordinate system

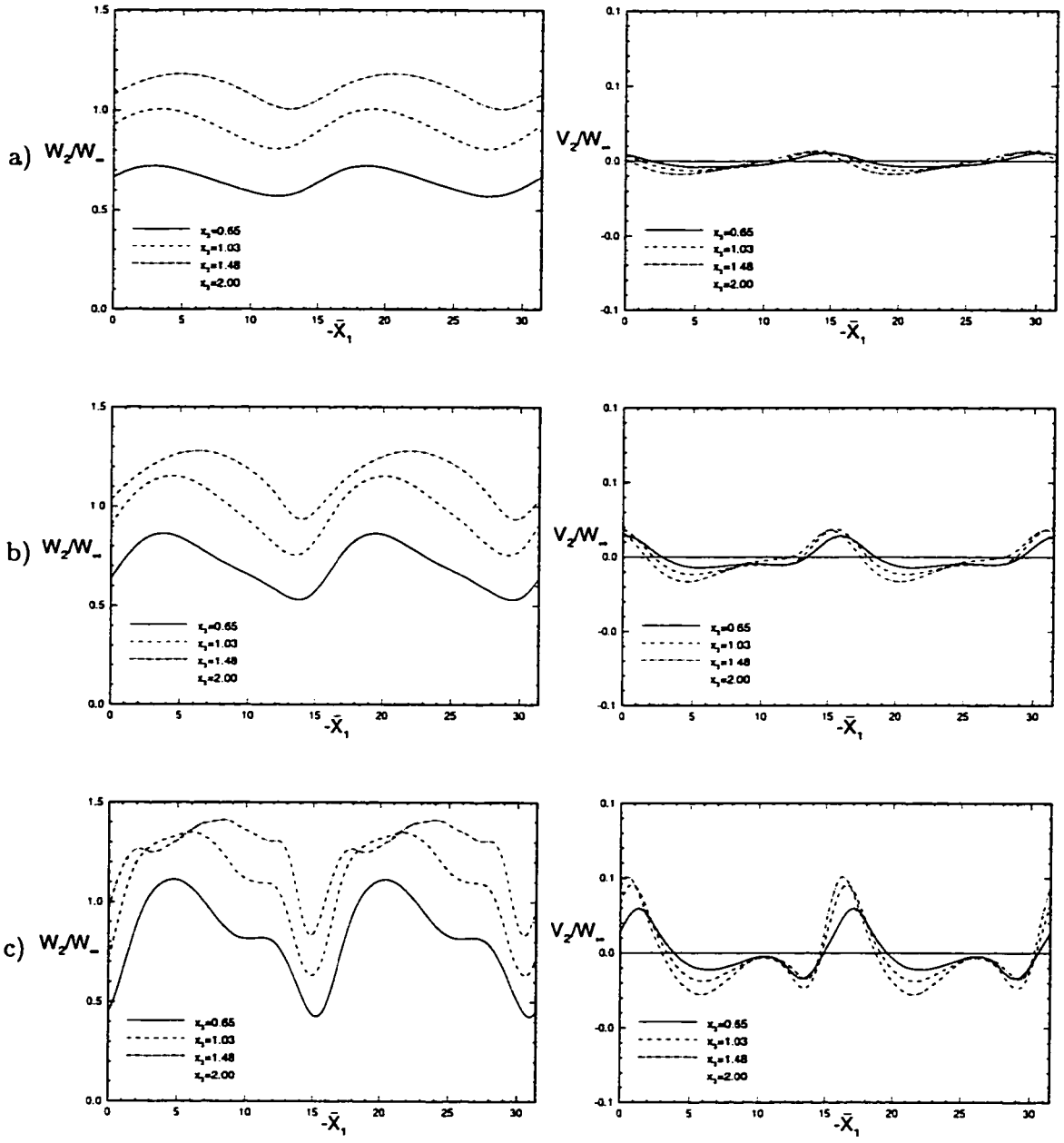

Figure 5.19: Total modified mean flow at different normal and streamwise locations; a) Re=448.5, b) Re=486.0, c) Re=546

are the components in the streamwise and normal direction, W_2 and V_2, respectively, for two spanwise wavelengths. Also, table 5.2 lists the rms-amplitudes for the different disturbance components at the corresponding streamwise locations. At the first shown streamwise location of Re=448.5, a moderate distortion of the boundary layer in

Table 5.2: Amplitudes at different streamwise locations [%]

Re	$\hat{A}_{s,u}$	$\hat{A}_{s,v}$	$\hat{A}_{s,w}$
448.5	7	1	7
486.0	14	2	13
546.0	24	3	17

the spanwise direction is observed. The variation of both plotted components is sinusoidal, where the spanwise change in the normal component is very small. At the next streamwise location of Re=486.0, the peak and valley structure of the W_2-component is developed more distinct, and the development of stronger spanwise gradients in the normal velocity component is observed as well. At the last shown streamwise location of Re=546, a very complex spanwise variation of both plotted velocity components is observed. The increased inflectional character of the spanwise velocity profiles corresponds to the growing instability of the flow. Also, the presence of the strong vertical mechanism mentioned above is seen in the positive and negative peaks of the normal velocity component.

At Re=643.5, where the stationary vortex is fully saturated, the redistribution of vorticity is shown from another perspective in figure 5.20. There, the velocity vectors that result from a superposition of the normal velocity and the total velocity component along the stationary vortex are plotted in the $\bar{x}_1, \bar{x}_3$-plane. Note that the negative $\bar{x}_1$-direction in the Galilean coordinate system corresponds to a positive x_2-direction in the body-fixed coordinate system. Visualizing two streamlines starting close to the wall at

$\bar{x}_3$=0.05 and away from the wall at $\bar{x}_3$=2 reveals the existence of two counter-rotating vortices at this streamwise location. The primary crossflow vortex extends far into the outer flow, whereas the secondary crossflow vortex remains close to the wall.

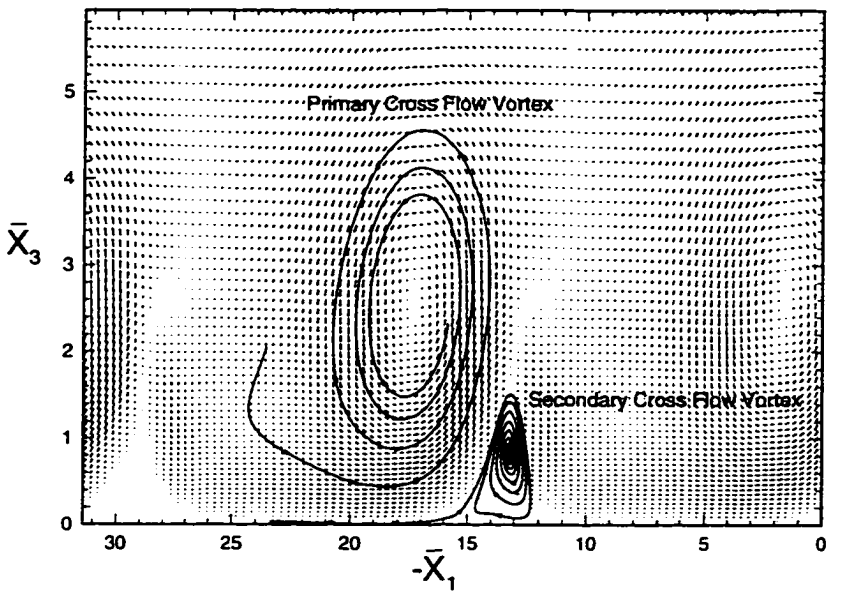

Figure 5.20: Velocity vectors of the stationary crossflow vortex at Re=643.5

$$\omega = |\Omega_{\text{total}}| - |\Omega_{\text{meanflow}}| \quad , \tag{5.17}$$

$$\omega = \sqrt{\left(\frac{\partial W_2}{\partial x_3}\right)^2 + \left(\frac{\partial V_2}{\partial x_2}\right)^2 + \left(\frac{\partial W_2}{\partial x_1}\right)^2 + \left(\frac{\partial U_2}{\partial x_2}\right)^2 + \left(\frac{\partial V_2}{\partial x_1}\right)^2 + \left(\frac{\partial U_2}{\partial x_3}\right)^2} - \sqrt{\left(\frac{\partial W_0}{\partial x_3}\right)^2 + \left(\frac{\partial V_0}{\partial x_2}\right)^2 + \left(\frac{\partial W_0}{\partial x_1}\right)^2 + \left(\frac{\partial U_0}{\partial x_2}\right)^2 + \left(\frac{\partial V_0}{\partial x_1}\right)^2 + \left(\frac{\partial U_0}{\partial x_3}\right)^2} \tag{5.18}$$

This secondary vortex is also seen in figures 5.21 and 5.22 where the spatial distribution of the vorticity is shown for the disturbance component and for the total vorticity. The vorticity was computed by evaluating total and mean flow vorticity according to equations 5.17 and 5.18. In figure 5.21, the footprint of the secondary vortex can be seen as a region of high negative vorticity between the λ-shaped structure of the primary vortex close to the wall. Also observed are concave structures of negative

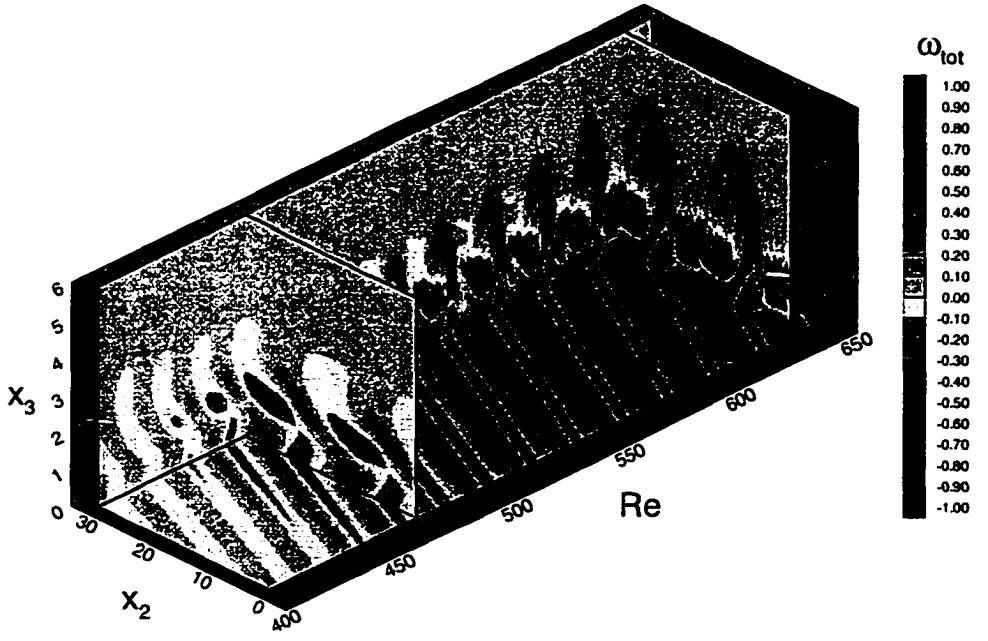

Figure 5.21: Disturbance vorticity in the presence of a stationary crossflow vortex

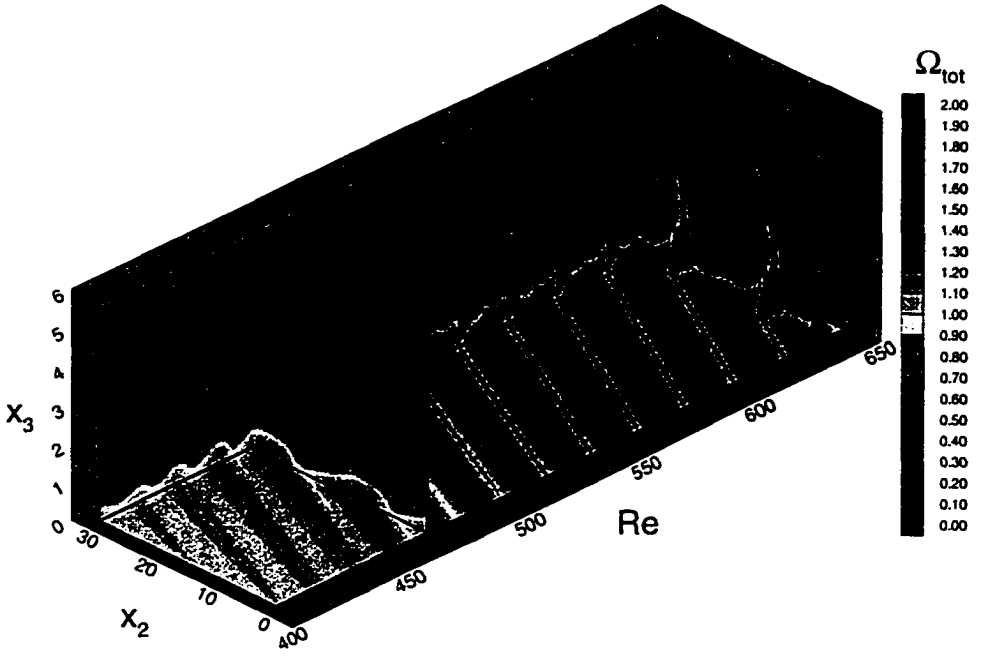

Figure 5.22: Total vorticity in the presence of a stationary crossflow vortex

vorticity away from the wall at $x_3 \simeq 1$. All these features start to develop at a streamwise position of Re=480, where the amplitudes of the stationary disturbances are $\hat{A}_s$=13% and $\hat{A}_s$=11% for the u_1- and w_1-components, respectively. Further noteworthy is the changing inclination of the primary vortex structures in the streamwise direction. While growing along the streamwise direction, they straighten more and more up and start leaning in into the streamwise direction at Re $\simeq$ 480.

Finally, figure 5.23 shows the computed disturbance vorticity pattern at the wall in the presence of a stationary crossflow vortex. As reported from oil-visualizations in experiments (see Chapter 6), a streaky footprint of the stationary vortices is seen, where the curvature of the streak lines decreases with growing distance from the attachment line according to the variation of the wave angle.

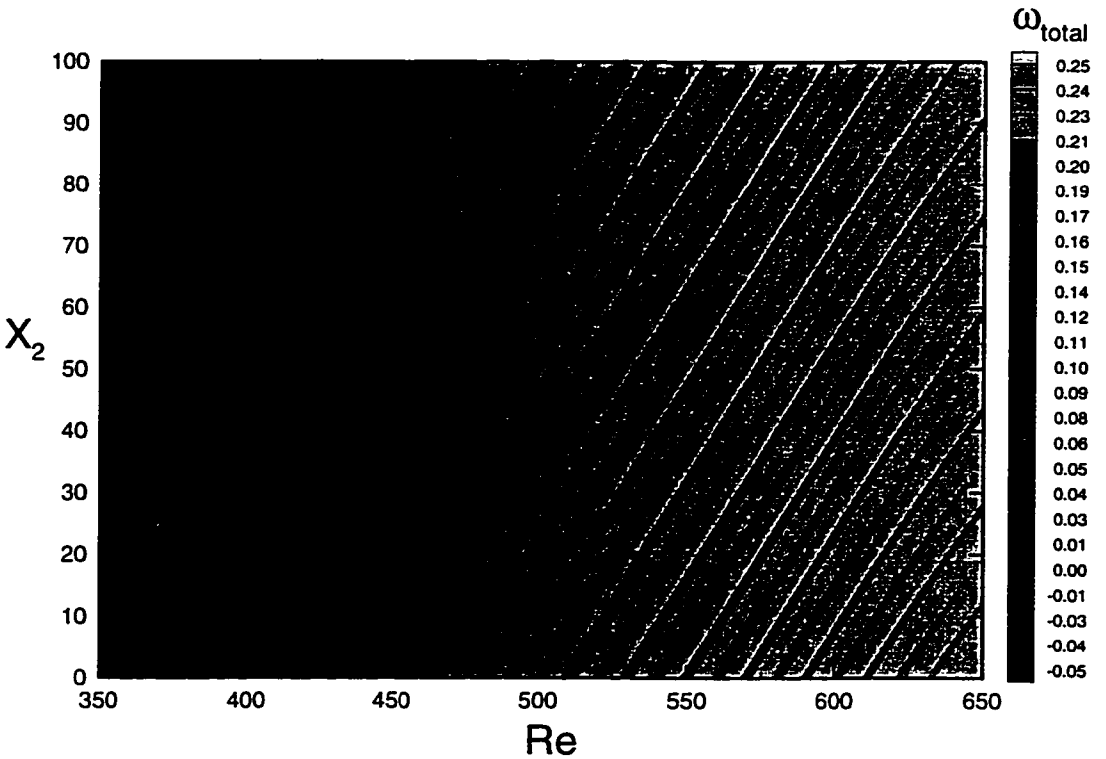

Figure 5.23: Computed wall vorticity pattern caused by a stationary crossflow vortex

5.4 Secondary Stability Analysis

The interpretation of the observed physical features in the previous section, where a crossflow instability dominated mean flow is modified by the presence of a stationary vortex, predicts the onset of a secondary instability. This section will investigate this instability mechanism further. For a detailed definition of the secondary instability, the reader is referred to Chapter 4. First, however, a summary of the observed results from the previous section will be given that explains the onset of the secondary instability.

- A necessary condition for the onset of a secondary instability is the existence of a strong saturated stationary disturbance.
- Particularly the strong fundamental, first and mean flow distortion modes, having maximal amplitudes of $\hat{A} = 30\%$, $\hat{A} = 13\%$ and $\hat{A} = 10\%$ for the presented case, respectively, cause strongly inflectional profiles in the directions tangential and perpendicular to the constant phase lines of the stationary disturbance (see figures 5.16, 5.17, and 5.19).
- The disturbances are periodic in the spanwise direction and cause the inflectional profiles to differ largely in shape within a wavelength perpendicular to the direction of the constant phase lines (see figure 5.17).
- The different magnitude of the disturbances in the spanwise direction also causes vertical and horizontal gradients in the flow that appear as crossflow vortices.
- The existence of these gradients in the flow explains the experimental observations of well-defined streaks on the body-surface that are the footprint of the crossflow vortices.

- Physically interpreted, the previous items represent a strong mechanism in the flow that moves low-speed fluid away from the wall, and high-speed fluid from the outer flow towards the wall, thus distorting the boundary layer and redistributing vorticity in both the spanwise and streamwise directions.

Provided that a modified mean flow like described in the summary above exists, the secondary instability sets in once the disturbances reached a threshold amplitude and the inflectional character of the profiles along the crossflow vortex originates an inviscid instability. In the first subsection of this section, a temporal investigation of the secondary instability mechanism is described that uses Floquet Theory and the solution method explained in Chapter 4. Utilizing the results of this temporal approach, an attempt to capture the essential features of the secondary instability with a PSE computation will be documented in the second subsection.

5.4.1 Temporal Analysis using Floquet Theory

Following the method described in Section 4.4, the temporal investigation of the secondary instability is started at the streamwise location where Re=546. At this location, the stationary disturbance of an initial amplitude $\hat{A}_s$=0.1% has fully saturated and reached an amplitude level of $\hat{A}_s$ = 24% for the u_1-component. The computations presented here were limited to a maximal number of eight modes (n = -8,$\cdots$,8) in the Fourier approximation. However, Malik et al. [23] showed that a consideration of 16 modes does not change the results qualitatively. Further, the results presented consider the fundamental type of secondary disturbances only. This restriction of the work is supported by the findings of Balachandar et al. [69] for the three-dimensional boundary layer of a rotating-disc flow where they did not find a qualitative difference between the behavior of fundamental and subharmonic secondary disturbances.

The computational grid applied in the present computations is described as follows. For the same computational domain as in Section 5.3, where the freestream boundary conditions were enforced at a normal extension of about 10 boundary layer thicknesses, the total number of points is decreased from 141 to 81. Also, the grid is now stretched in the entire domain such that the number of points within the boundary layer is 50. For the local solution method, the iteration can be performed on either the continuity equation, or one of the momentum equations. Additionally, the disturbance mode to be iterated on can be specified. Table 5.3 presents the findings from a grid refinement study. Shown are results from the local method for different grids and iteration options. The guess values from the second-order-accurate global method for the two different numbers of points are given by σ_3=(0.0267,-1.2043) for 71 points, and σ_3=(0.0262,-1.2073) for 81 points. The results of the fourth-order-accurate local method vary only in the fourth decimal place, and thus, the grid resolution is considered satisfactory.

Table 5.3: Grid study at Re=546, α_3=-0.508, β_3=0.9, Mode=-1

Δ-Grid	Points	Equation	$\bar{x}_{3,max}$	σ_3
3	71	continuity	44	(0.021652,-1.212607)
3	71	x_3 − mom.	44	(0.021652,-1.212607)
5	71	continuity	44	(0.021779,-1.212359)
5	71	x_3 − mom.	44	(0.021779,-1.212359)
3	81	continuity	55	(0.021715,-1.212264)
5	81	continuity	55	(0.021729,-1.212671)

In general, there will be several unstable eigenmodes for a given wave number at a streamwise location. Thus, a scan of the complex σ_3-plane for a wave number of β_3=0.8 is performed first. Here, the global and local solver are used as explained in Section 4.4. All eigenvalues that were found within the scanned domain are plotted in figure 5.24. Even though they appear clustered around σ_3=(0.,-1.), there is no obvious connection between the positive (unstable) real parts. For the chosen parameters, this

isolated appearance indicates that there are no multiple eigenvalues present in the flow, and thus no absolute instability. The five detected unstable eigenvalues are given in the order of increasing frequency $-\sigma_{3,\text{imag}}$ in table 5.4. It is seen that all the detected unstable secondary frequencies are an order-of-magnitude higher than the most amplified frequency found from the nonlinear analysis in the previous section (F=$1.0 \cdot 10^{-4}$). The

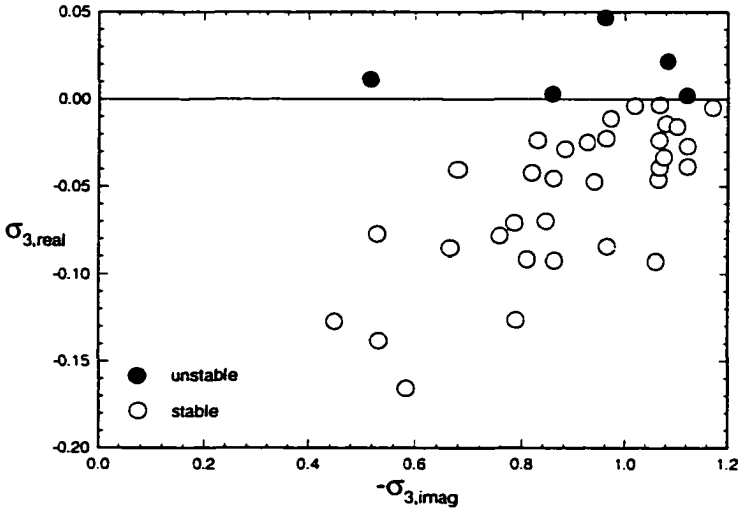

Figure 5.24: Temporal eigenvalue spectrum at Re=546

Table 5.4: Unstable eigenvalues Re=546, α_3=-0.508, β_3=0.8

Mode	σ_3	F=$-\sigma_{3,\text{imag}}/\overline{\text{Re}}$
1	(0.0113,-0.5160)	$1.03 \cdot 10^{-3}$
2	(0.0030,-0.8566)	$1.71 \cdot 10^{-3}$
3	(0.0467,-0.9595)	$1.92 \cdot 10^{-3}$
4	(0.0218,-1.0838)	$2.16 \cdot 10^{-3}$
5	(0.0021,-1.1205)	$2.24 \cdot 10^{-3}$

shape functions of the five unstable modes are shown in figure 5.25. Plotted is the summation of eight modes of the wave number α_3 in the Galilean coordinate system. Observed is that the shape functions of the different modes vary widely in features like the location of the maximum in the normal direction, the largest disturbance component,

the magnitude, the presence of multiple peaks, and the extension into the outer flow. Of special interest are Modes 4 and 5, as well as the most unstable Mode 3. Because of their

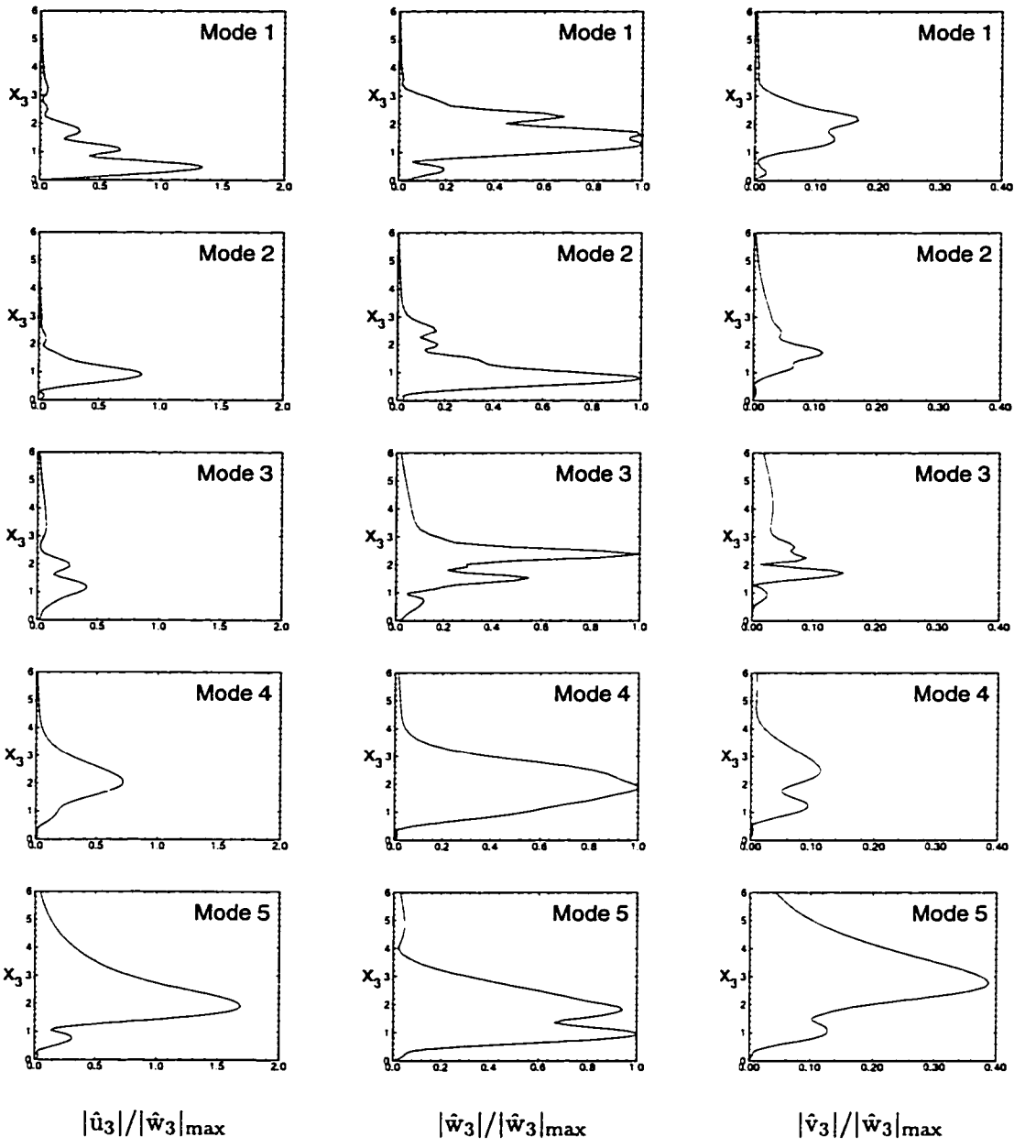

Figure 5.25: Total shape functions for unstable modes at Re=546, α_3=-0.508, β_3=0.8

full shape profiles, Modes 4 and 5 might be easier detected in experiments than the other three modes that show a more narrow and fluctuating shape. For Mode 4, in particular,

it is noted that the component tangential to the constant phase lines has a shape that is very similar to the experimentally and numerically observed profile in the DLR Transition experiment at x_1/c=0.80 [67]. For that reason, the following study where the spatial development of the temporally unstable modes is investigated, considers Mode 4. In figure 5.26, the shape functions of the individual Fourier components are given for Mode 4. Plotted are the normalized quantities for the first seven modes. In contrast to the

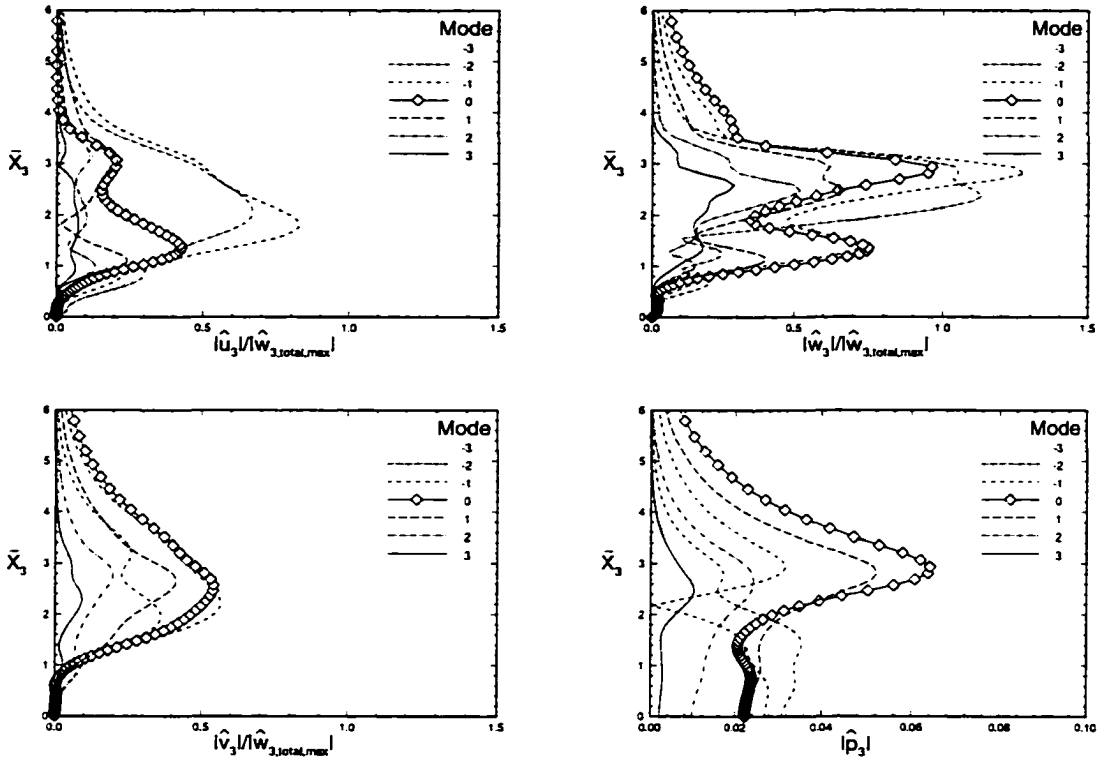

Figure 5.26: Shapes of the secondary instability eigenfunctions for Mode 4 at Re=546

primary stability analysis, where the transformation of a physical (real) quantity into the Fourier space yields a symmetry condition for the individual modes ($q_{1,m,n}=q^*_{1,-m,-n}$, the asterisk denotes the complex conjugate), one observes non-symmetric mode shapes for the presented secondary eigenfunctions. This is due to the missing complex conjugate of the secondary disturbance in the formulation of this linear analysis (see Section 4.4).

Also, it is observed that the disturbance mode tangential to the constant phase lines (0-Mode) shows a double peak structure for both disturbance quantities parallel to the wall. The maximal disturbance quantity is found for the $\hat{w}_3$-component tangential to the constant phase lines at $\bar{x}_3 \simeq 3$, where its normalized value $|\hat{w}_{3,0}|/|\hat{w}_{3,total}|_{max} \simeq 1$.

While studying the origin of the secondary instability, another important issue is whether there exists a link between the eigenmodes of the undisturbed mean flow, investigated by the linear stability theory, and the unstable secondary eigenmodes, investigated by Floquet Theory. Also, which is the threshold amplitude where the secondary disturbances become unstable ? In order to investigate this problem, the amplitude of the stationary disturbances obtained from the nonlinear stability analysis in the previous section is set to A=1.0 for the given Reynolds number. Then, by gradually decreasing A to zero, the variation of the eigenvalues is monitored. During the computations, the evolution of the shape functions is followed in order to assure that no jumps to different eigenvalues occur. A typical step size in the amplitude is $\Delta A=0.01$. The computations are continued until the local method ceases to converge.

For a Reynolds number of Re=546, a value of A=1 corresponds to amplitudes of $\hat{A}_s$=24%, $\hat{A}_s$=17% and $\hat{A}_s$=1% for the u_1-, w_1- and v_1-disturbance components of the primary stationary vortex, respectively. In figure 5.27, the variation of the eigenvalues $\sigma_3=(\sigma_{3,real}, \sigma_{3,imag})$ versus a decreasing amplitude A is shown for the five unstable eigenvalues at A=1. Additionally, the eigenvalues of the undisturbed parallel mean flow $Q_0(\bar{x}_3)$ are shown in the relevant σ_3-range. It turns out that only one of the five unstable eigenvalues at Re=546 has a link to the eigenvalue spectrum of the undisturbed mean flow. This connection could be established for Mode 1, the mode with the lowest unstable secondary frequency ($F=1.03\cdot10^{-3}$).

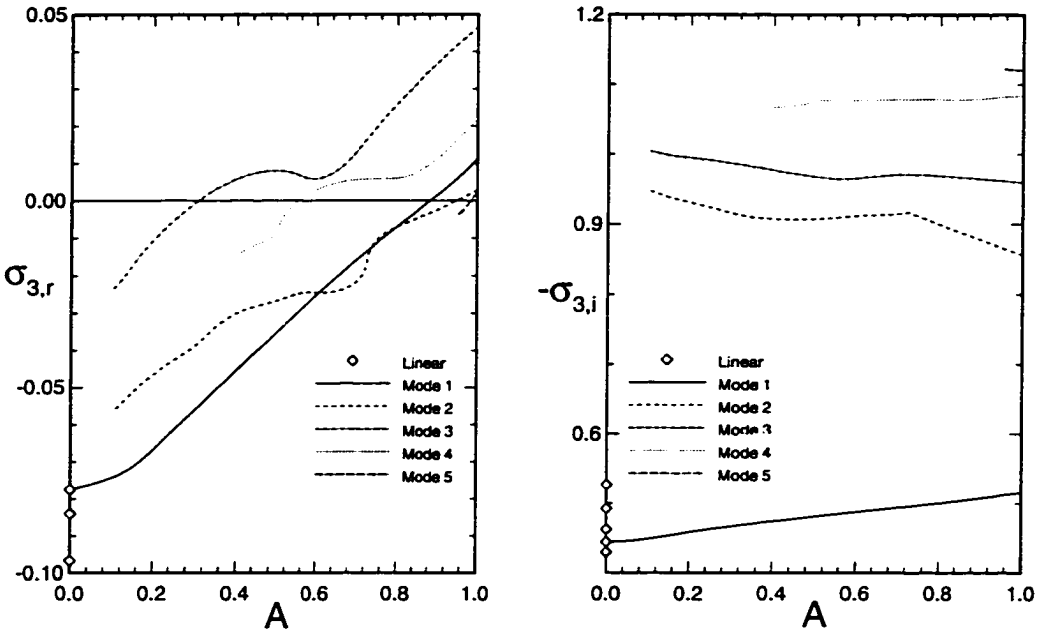

Figure 5.27: Growth rates and frequencies of the secondary disturbances as functions of the amplitude A (Re=546, α_3=-0.508, β_3=0.8)

As seen in figure 5.27, the variation of the eigenvalues with decreasing amplitude A takes very different routes. For example, the highest frequency mode (Mode 5) becomes stable at a threshold amplitude of A_{thres}=0.98. Shortly thereafter, the iteration for an eigenvalue ceases to converge. On the other hand, Modes 2 and 3 could be followed further until A≃0.1. The threshold amplitudes for Modes 1-4, respectively, are A_{thres}=0.88, A_{thres}=0.95, A_{thres}=0.31, A_{thres}=0.55. Thus, this analysis predicts the onset of a secondary instability due to Mode 3 already for stationary disturbance amplitudes of $\hat{A}_s$=0.31·24%=7.5% and $\hat{A}_s$=0.31·17%=5% for the u_1- and w_1-components, respectively. The corresponding values for Mode 4 are $\hat{A}_s$=0.55·24%=13% and $\hat{A}_s$=0.55·17%=9%.

In order to investigate the eigenmode-variation in the amplitude range where the eigenvalue computation stops converging, the next study examines the decay of the

individual disturbance components at the freestream boundary. Thereby, it can be determined whether the convergence problems are due to an insufficient grid resolution, or if they are part of the physics of the investigated problem. In the present stability formulation, a complex eigenvalue reaches the continuous spectrum when the corresponding eigenfunction does not decay in the freestream and is of rather oscillatory nature [51]. In the following, the method of the investigation is described, and results are presented for the Modes 1 and 4.

In Floquet Theory, one seeks a solution to the linear eigenvalue problem that can be written as in equation 5.19 (see Section 4.4), where the elements of the coefficient

$$\Lambda' = \mathbf{A} \cdot \Lambda \tag{5.19}$$

matrix $\mathbf{A}$ are determined from a nonlinear PSE computation. Since the coefficients of the matrix are not constant in the entire domain, one usually solves the eigenvalue problem using a Newton-Raphson technique as described in Section 4.4. Here, however, the focus is on the eigenvalues of $\mathbf{A}$ at the freestream boundary where the primary disturbance quantities are zero, and thus, the coefficients of the matrix $\mathbf{A}$ are constant. Therefore, the behavior of the secondary disturbances at the freestream boundary can be investigated by finding the eigenvalues of the submatrix $\mathbf{A_n}$ at the maximal normal extension of the computational domain. The dimension of the submatrix $\mathbf{A_n}$ depends on the number of considered Fourier modes in the Floquet analysis and is determined to $(2 \cdot N_{mode} + 1) \cdot 6$ for the six components of the vector of unknowns (see Section 4.4). Considering eight Fourier modes in the analysis, the complex and non-symmetric coefficient matrix $\mathbf{A_n}$ consists of 102×102 elements. If the eigenvalue problem to be solved is well-posed, one obtains 51 positive and 51 negative eigenvalues which are distributed almost symmetrically about the imaginary axis. In figure 5.28, the eigenvalue spectrum at the freestream boundary

of Mode 4 is shown for an amplitude of A=1. In that case, none of the eigenvalues has a zero real part, the secondary disturbances decay in the freestream, and the iteration for an eigenvalue of the entire problem converges.

Table 5.5: Eigenvalue characteristics at the freestream boundary for Mode 4

A	1.0	0.8	0.6	0.4	0.38	0.36	0.34
$\#of\lambda_{real,i} > 0$	51	51	51	51	51	51	53
$\#of\lambda_{real,i} < 0$	51	51	51	51	51	51	49
$(\lambda_{real,i})_{min}$	0.8	0.8	0.8	-0.16	-0.078	-0.011	0.0066

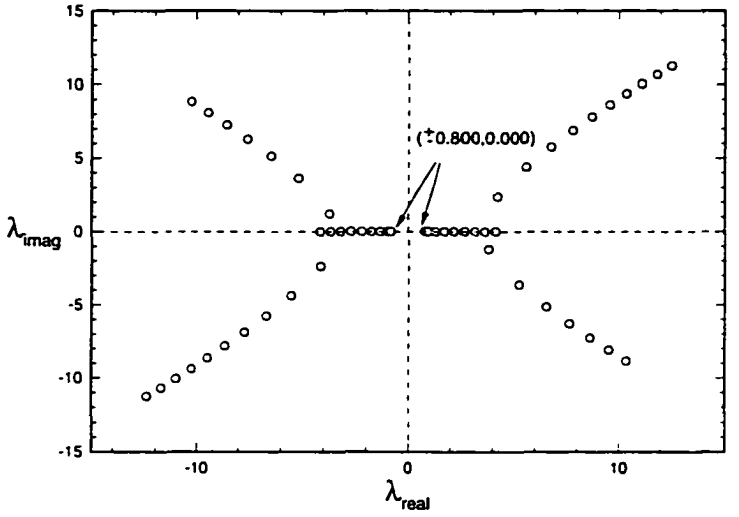

Figure 5.28: Eigenvalue spectrum at the freestream boundary (Mode 4, A=1)

In the approach the continuous spectrum, however, the real part of the eigenvalue closest to the imaginary axis tends towards zero, and the well-posedness of the eigenvalue problem is violated by an imbalance of the eigenvalues with a positive and negative part. This is seen in figure 5.29, where the eigenvalue spectrum at the freestream boundary of Mode 4 is shown for an amplitude of A≃0.34. There are two eigenvalues close to the imaginary axis which indicates that the disturbances will not decay in the freestream.

Further, tables 5.5 and 5.6 list the number of eigenvalues in the spectrum with positive and negative real parts, as well as the magnitude of the eigenvalues closest to the imaginary axis for Modes 1 and 4 depending on the amplitude A. It is seen that the eigenvalues of Mode 4 join the continuous spectrum at an amplitude of A=0.34, whereas the eigenvalues of Mode 1 indeed reaches the linear eigenvalue spectrum.

Table 5.6: Eigenvalue characteristics at the freestream boundary for Mode 1

A	1.0	0.8	0.6	0.4	0.2	0.1	0.01
$\#of\lambda_{real,i} > 0$	51	51	51	51	51	51	51
$\#of\lambda_{real,i} < 0$	51	51	51	51	51	51	51
$(\lambda_{real,i})_{min}$	0.8	0.8	0.8	0.8	0.8	0.8	0.8

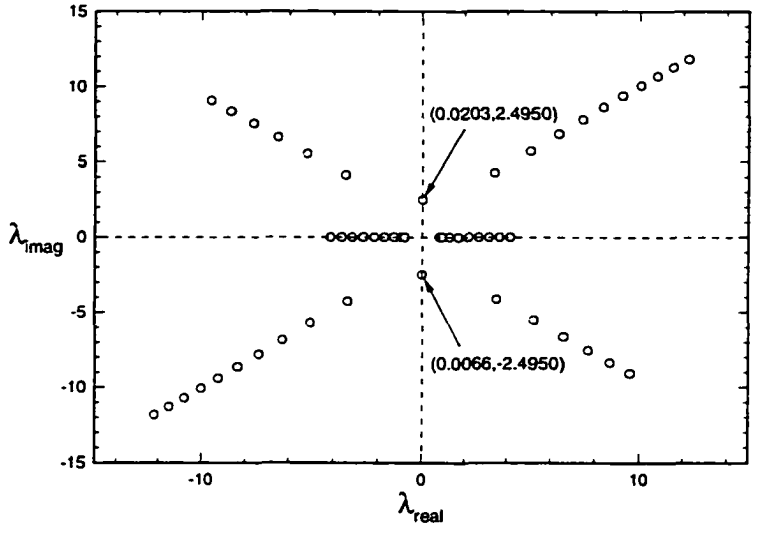

Figure 5.29: Eigenvalue spectrum at the freestream boundary (Mode 4, A=0.34)

Referring back to figure 5.27, a peculiar behavior in the limit of $A \rightarrow 0$ is noted for Mode 1. From figure 5.27, a clear tendency towards the linear eigenvalue at A=0 is observed. However, starting at A=0.10, the dominant (-1) Fourier component starts to decay and the (0) Mode becomes the prevailing component. At A=0.01, all Fourier components are negligible, except the (0) Mode. The fact that the corresponding linear

eigenvalue of σ_3=(-0.07725,-0.44443) at A=0 is obtained for a wave number of α_3=0 is consistent with that observation. In figure 5.30, the normalized total shape functions of

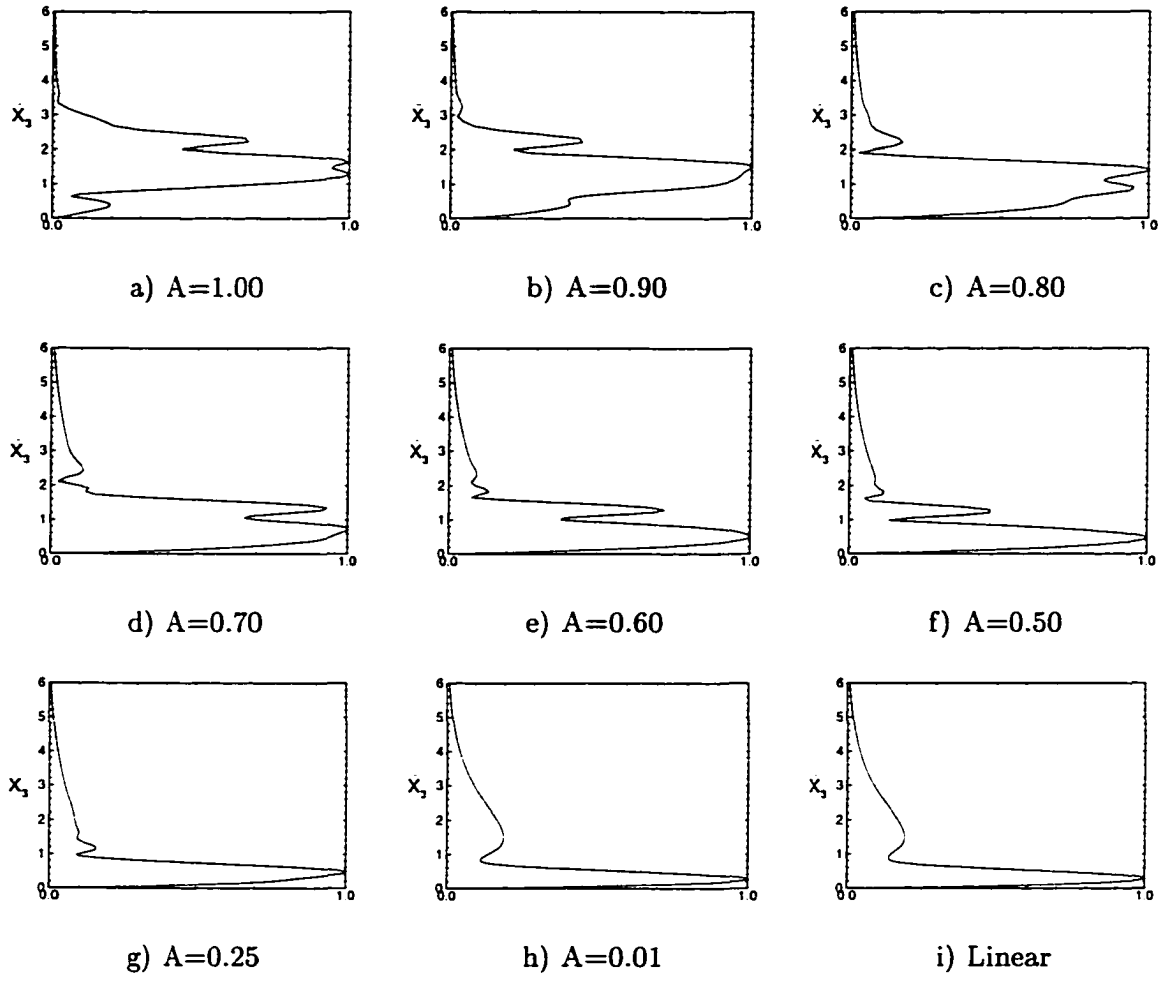

a) A=1.00 b) A=0.90 c) A=0.80

d) A=0.70 e) A=0.60 f) A=0.50

g) A=0.25 h) A=0.01 i) Linear

Figure 5.30: Shape functions $|\hat{w}_3|/|\hat{w}_{3,max}|$ of the linear eigenmode and of Mode 1 for different amplitudes A

the w_3-component of Mode 1 are given for different amplitudes. It is seen that the shape functions for the different amplitudes indeed belong to the same family of eigenmodes. Comparing the linear shape function with the nonlinear shape function at A=0.01, it is obvious that nonlinear and linear results merge in the limit of A $\rightarrow$ 0.

Next, the eigenvalues σ_3 for the different unstable modes are computed as functions of the wave number tangential to the stationary vortex at Re=546. In particular,

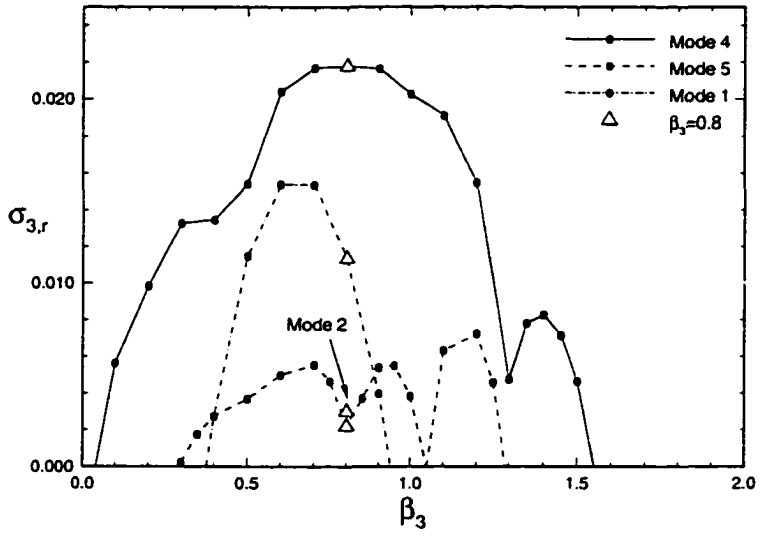

Figure 5.31: Secondary growth rates at Re=546

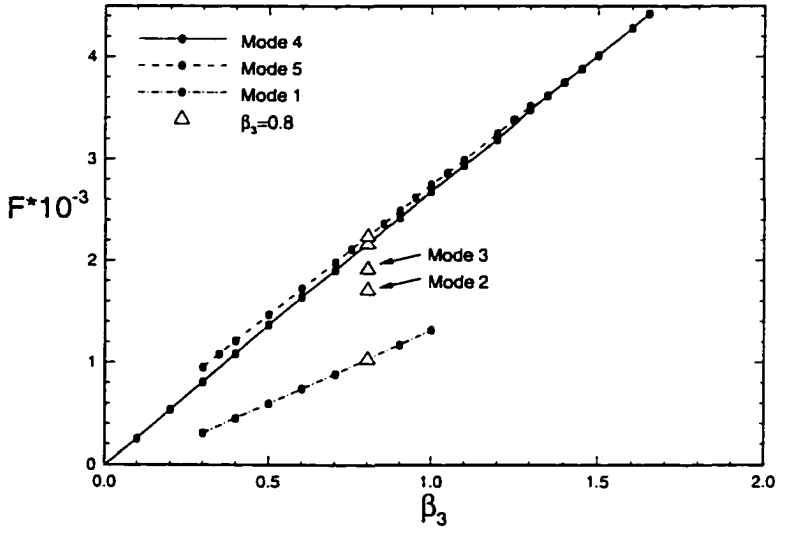

Figure 5.32: Secondary frequencies at Re=546

three of the five unstable eigenmodes at β_3=0.8 are traced through their unstable wave number range. Figures 5.31 and 5.32 show the growth rate and frequency development,

respectively, that was obtained by closely watching the evolution of the eigenfunctions with changing wave numbers. Thereby, it is assured that the curves for the different modes in figure 5.31 indeed belong to the specified modes (see Section 4.4). Moreover, the wave angle of the secondary disturbances Ψ_2 is given as a function of the wave number β_3 in table 5.7, where Ψ_2 is determined according to its definition in Section 4.4.

Table 5.7: Wave angle of secondary disturbances at Re=546 (α_3=-0.508)

β_3	0.25	0.5	0.8	1.0	1.5
Ψ_2	-63.8°	-45.5°	-32.4°	-26.9°	-18.7°

The following observations can be made from figures 5.31 and 5.32 :

- A wide range of unstable secondary wave numbers is present at the investigated Reynolds number.
- Starting at β_3=0, which corresponds to an alignment with the primary wave vector, the disturbances turn towards the direction of the constant phase lines with a growing wave number tangential to the stationary vortex.
- The dependence of the frequency on the wave number β_3 is approximately linear.
- An intricate structure of the high-frequency/low-growth rate Mode 5 is observed. The growth rate behaves in a periodic manner versus the wave number β_3.
- The most unstable disturbances of Modes 4 and 5 are found in the wave number range of β_3=0.6 - 0.9. This corresponds to an inclination of the secondary structure of Ψ_2=-30° $\cdots$ -40° with respect to the direction of the constant phase lines.
- Modes 4 and 5 have very similar frequencies; however, the frequency curves never cross each other.

- Even though the curves for the real parts (growth rates) of the different modes do cross each other, their eigenvalues $\sigma_3=(\sigma_{3,real}, \sigma_{3,imag})$ do not coincide because of the missing corresponding crossovers of the imaginary parts (frequencies).

- Thus, multiple eigenvalues were not detected at the investigated location and the flow seems to be subject to a convective type of instability.

Completing the investigation of the secondary instability at Re=546, figure 5.33 shows the temporal eigenfunctions superimposed on the modified mean flow. Plotted are contours of the velocity components along the stationary crossflow vortex. The eigenfunctions are computed for the most amplified spanwise wave number β_3=0.8 at this streamwise location. The secondary instability structure appears riding on top of the largest boundary layer distortion caused by the primary crossflow vortex. Also, it is completely lifted away from the wall, having its maximal magnitude at $\bar{x}_3 \simeq 2.75$.

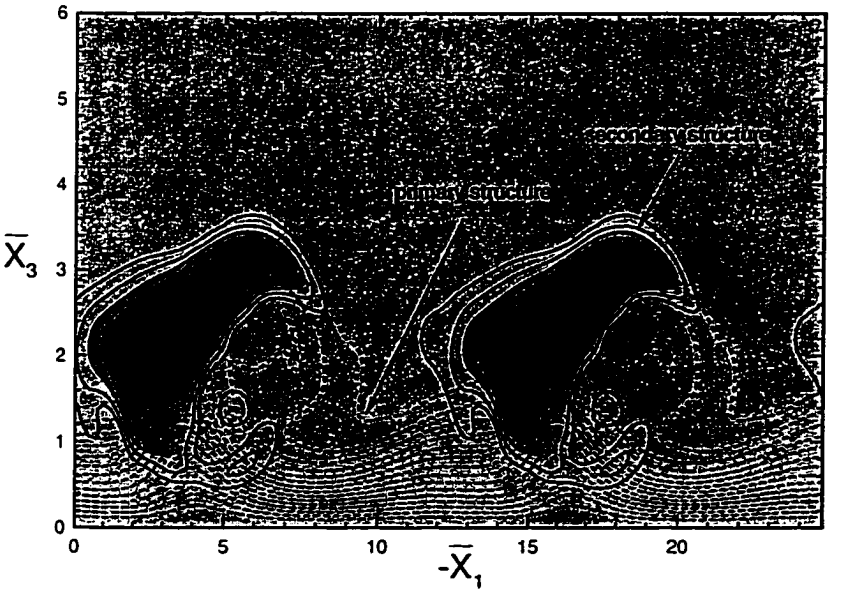

Figure 5.33: $|w_3|$-eigenfunctions and the modified mean flow at Re=546

Next, in order to gain some first insight into the spatial development of the secondary instability, a temporal analysis at eight different streamwise positions is performed. This investigation is also aimed at providing data of unstable frequencies to be used in the PSE analysis of the secondary instability in the next subsection. Thus, choosing Mode 4 at Re=546 and decreasing the Reynolds number, this mode is traced back to its onset at Re≃475. At this Reynolds number, both the u_1- and the w_1-components have reached an amplitude level of $\hat{A}$=11%. Figure 5.34 shows the secondary growth rates at the different streamwise positions. It can be seen that the unstable spanwise wave numbers align more closely with the direction of the wave vector $\mathbf{k}_{real}$ for a decreasing Reynolds number. In figure 5.35, the most amplified secondary growth rates are plotted together with the primary growth rates. The most unstable secondary frequencies are

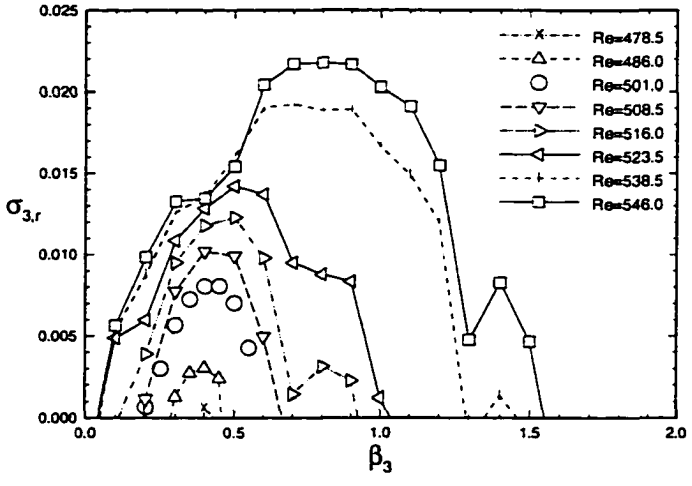

Figure 5.34: Secondary growth rates at different streamwise stations

found in the range of $F=1.0\cdot10^{-3}$-$2.0\cdot10^{-3}$, which is an order-of-magnitude higher than the most amplified primary frequency of $F=1.0\cdot10^{-4}$ (see Section 5.3). Also, a linear development of the temporal growth rate $\sigma_{3,real}$ is observed. Another interesting feature in figure 5.35 is the development of primary and secondary growth rates. At Re≃510,

the primary and secondary growth rates are of the same order. At Re=546, however, the primary growth rates are about to become stable, whereas the temporal theory predicts a continued steep growth of the high-frequency disturbances. Looking again at

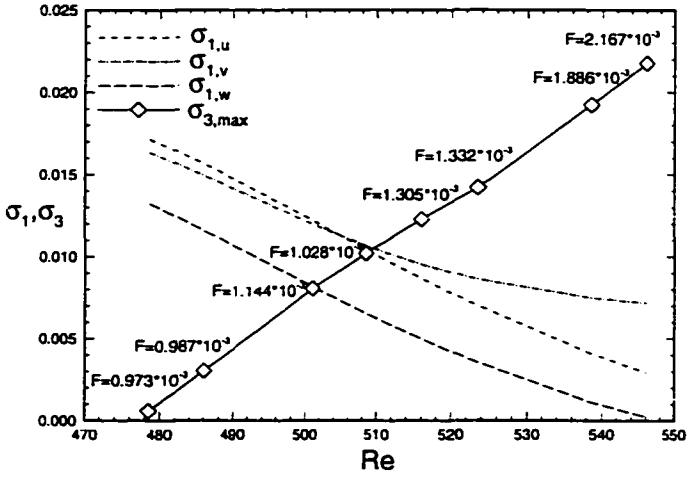

Figure 5.35: Trace-back of the secondary instability

figure 5.14 where the amplitude evolution of the stationary disturbances was plotted, one notes that the onset of the secondary instability according to the temporal theory occurs in the region where the stationary disturbances saturate.

Having gathered quantitative information about the wave number structure and frequency spectrum of the secondary instability originating from a purely stationary crossflow vortex, the next subsection will describe an attempt to utilize this information in a PSE computation.

5.4.2 Spatial Analysis using the PSE

After the discussion of the temporal approach in the previous subsection, the focus here will be on an attempt to capture the high-frequency secondary instability with a spatial analysis. Since the physical evolution of the disturbance is more appropriately

modeled by a spatial approach, one expects to obtain the flow features of the secondary stability in a more straightforward manner than by a temporal computation. Ideally, one would like to capture the large growth rates and spike-like amplitude evolution typical for the secondary instability in agreement with the prediction by the Floquet Theory and with an unchanged steady crossflow vortex. To pursue that idea, the initial disturbances to be included in the PSE analysis need to be specified such that they resemble the wave number structure and frequency spectrum determined in the temporal analysis as closely as possible.

The wave number range is considered first. Since the PSE computations are performed in the body-fixed reference frame, the wave numbers β_3 found from the temporal analysis for each Fourier mode are transformed from the Galilean to the body-fixed coordinate system using equation 5.20.

$$\beta_{1,n} = -n\ \alpha_{3,n}\ \sin|\Psi| + \beta_3\ \cos\Psi \quad ; \quad \Psi = \tan^{-1}\frac{\beta_1}{\alpha_{1,real}} \tag{5.20}$$

This transformation is done at each streamwise location that was investigated in the previous subsection. It is found that for a spanwise wave number of β_3=0.6, which is in the unstable range for Re$\geq$500 and close to the most unstable wave number for Re$\geq$520 according to figure 5.34, multiples of the spanwise wave number for the primary stationary disturbance β_1=0.4 closely represent the values of β_3 in the body-fixed coordinate system. Specifically, the transformed spanwise wave numbers for each Fourier mode took values from $\beta_{1,-8}$=-2.83 to $\beta_{1,8}$=3.58 at Re=523.5. This is a range that can be almost covered by specifying eight modes in the spanwise direction for the chosen primary wave number of β_1=0.4.

The next important parameter is the primary frequency of the traveling mode to be included in the PSE analysis. In order to reproduce the behavior of the secondary

instability as predicted by the temporal analysis, one tries to cluster the available number of frequency modes as densely as possible up to the predicted unstable frequency. For β_3=0.6, this unstable frequency is about F=1.6·10^{-3} (see figure 5.35). Thus, a primary frequency of F=2·10^{-4} and eight modes for the discretization of the frequency domain are selected.

Finally, the last parameter to be considered while shaping the primary input for the PSE is the initial amplitude of the traveling disturbance. Due to the nonlinear interaction of traveling and stationary disturbances, the stationary disturbance is modified as mentioned in Subsection 5.3.2. Keeping the intention of maintaining a mostly unmodified mean flow in mind, cases for three different initial amplitudes were run (see table 5.8). It turns out that the behavior of the high-frequency modes is very sensitive to the initial amplitude $\hat{A}_t$. Figures 5.36 - 5.38 show the growth rates based on the energy-component, the amplitudes of the individual modes and the amplitudes of the primary disturbances for the three cases. For comparison, the plots of the growth rates also show the curve of the purely stationary disturbance.

Table 5.8: Secondary analysis using PSE ($\overline{Re}$=500, β_1=0.4, $\hat{A}_s$=0.1%, F=2.0 ·10^{-4})

	$\hat{A}_{t,initial}$	Modes in β_1-domain	Modes in ω_1-domain
Case 1	0.0014%	8	8
Case 2	0.0075%	8	8
Case 3	0.0141%	4	8

In Case 1, it is observed that the steady primary disturbance remains largely unaffected by the small amplitude traveling disturbance, since the traveling modes do not grow large enough to interact nonlinearly with the steady modes. Thus, one essentially maintains the same new mean flow as investigated in the previous subsection using the temporal approach. However, for this very small initial traveling amplitude, the

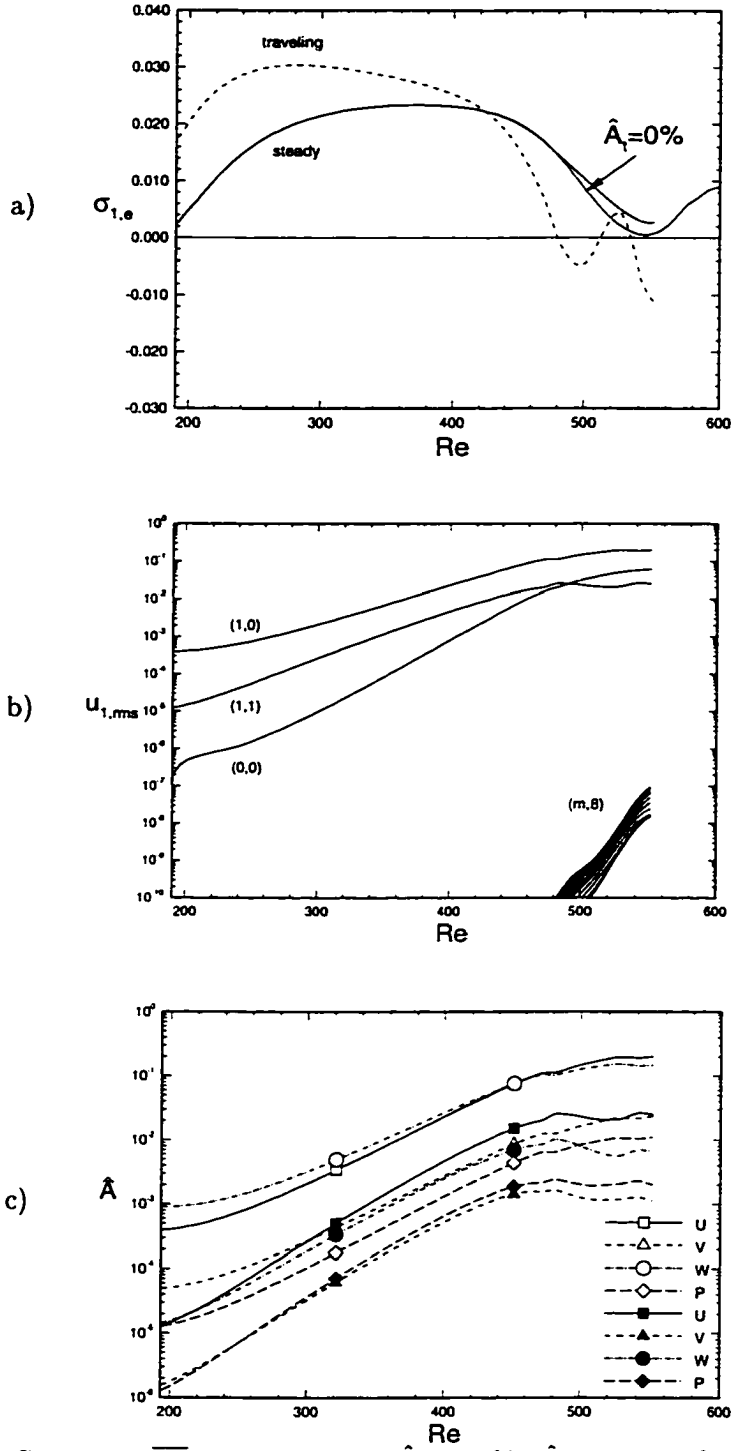

Figure 5.36: Case 1 : $\overline{Re}$=500, β_1=0.4, $\hat{A}_s$=0.1%, $\hat{A}_t$=0.00141%, F=2.0·10^{-3}, 8×8 modes; a) Growth rates, b) Amplitudes of individual modes, c) Amplitudes of primary disturbances; (hollow symbols : stationary disturbances; solid symbols : traveling disturbances)

high-frequency modes remain negligible throughout the investigated region and start saturating at a Reynolds number of Re≃550 where the temporal theory predicts a large growth rate for these modes. Consequently, the initial amplitude of the traveling mode is increased by one order-of-magnitude and the computation repeated (see Case 3). There, the steady primary disturbance is strongly affected by the nonlinear interaction with the traveling disturbance. This was expected from the nonlinear PSE analysis for the primary instability (see figures 5.14 and 5.15). However, this now different new mean flow gives rise to new physical features in the flow, as shown in figure 5.38. One observes an explosive disturbance-energy growth of even the low-frequency primary mode starting at Re=480 (figure 5.38(a)), and a very strong amplitude growth of the high-frequency modes (figure 5.38(b)). The highest frequency mode ($F=1.6 \cdot 10^{-3}$) experiences an amplitude growth of more than five orders-of-magnitude during a Reynolds number change from Re≃420 until Re≃500. Further, the amplitude of the mean flow distortion shows a sharp rise at Re≃480 after an earlier saturation onset at Re≃460 (figure 5.38(c)). The oscillations in the steady growth rate curve are thought to be caused by physical features in the flow, rather than by numerical oscillations. Continuing the computations further into the transition region exceeded the available computational resources, since it took several hundreds of iterations on the nonlinear terms per station for the solution to converge in the presence of these steep gradients in the flow. Case 3 will be also referred to as the "higher-frequency" case from now on.

Considering the final Case 2, it was attempted to obtain similar results as in Case 3 with a less modified new mean flow. Also, this last case was aimed at gaining more information about an existing threshold amplitude for a self-sustained growth of the secondary disturbances in the investigated flow. From the plots for Case 2 in figure 5.37,

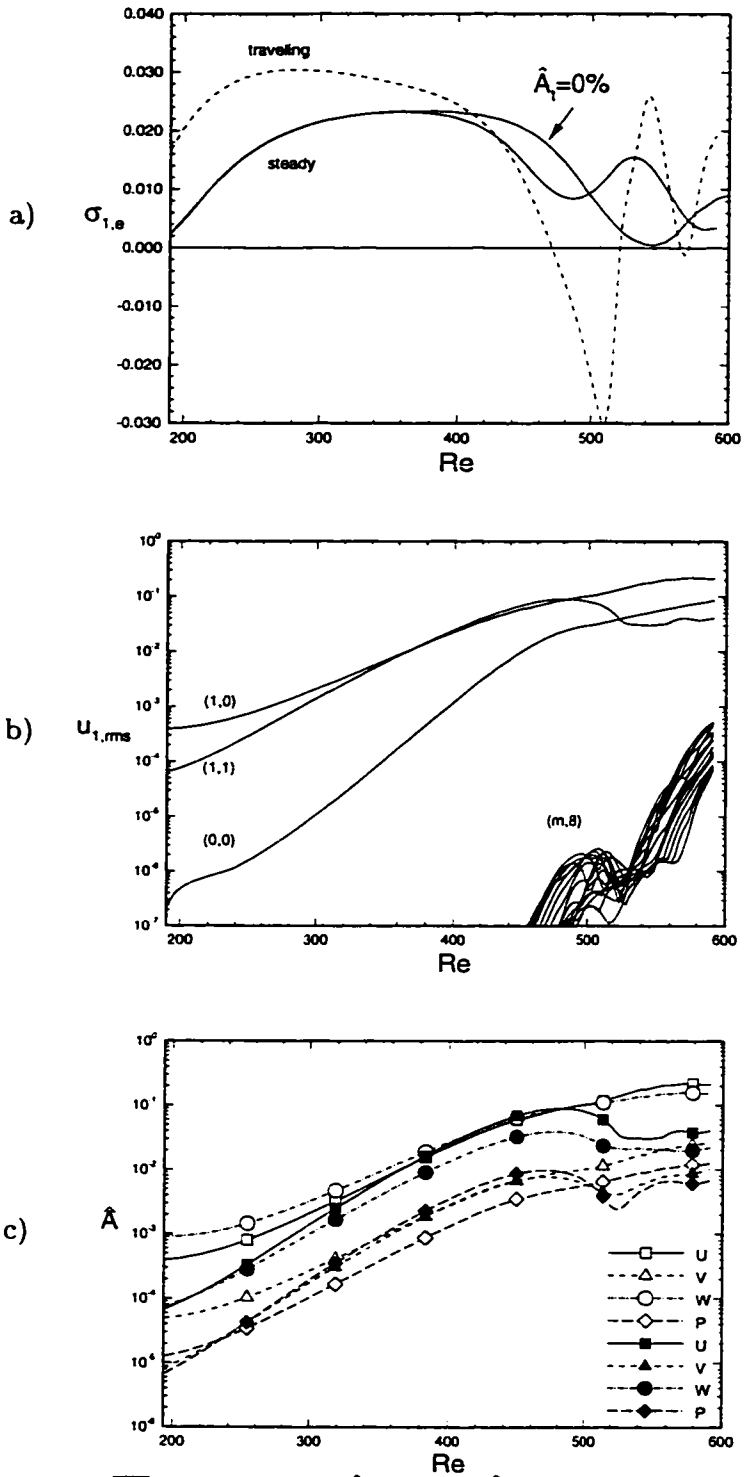

Figure 5.37: Case 2 : $\overline{Re}$=500, β_l=0.4, $\hat{A}_s$=0.1%, $\hat{A}_t$=0.0075%, F=2.0·10^{-3}, 8×8modes; a) Growth rates, b) Amplitudes of individual modes, c) Amplitudes of primary disturbances; (hollow symbols : stationary disturbances; solid symbols : traveling disturbances)

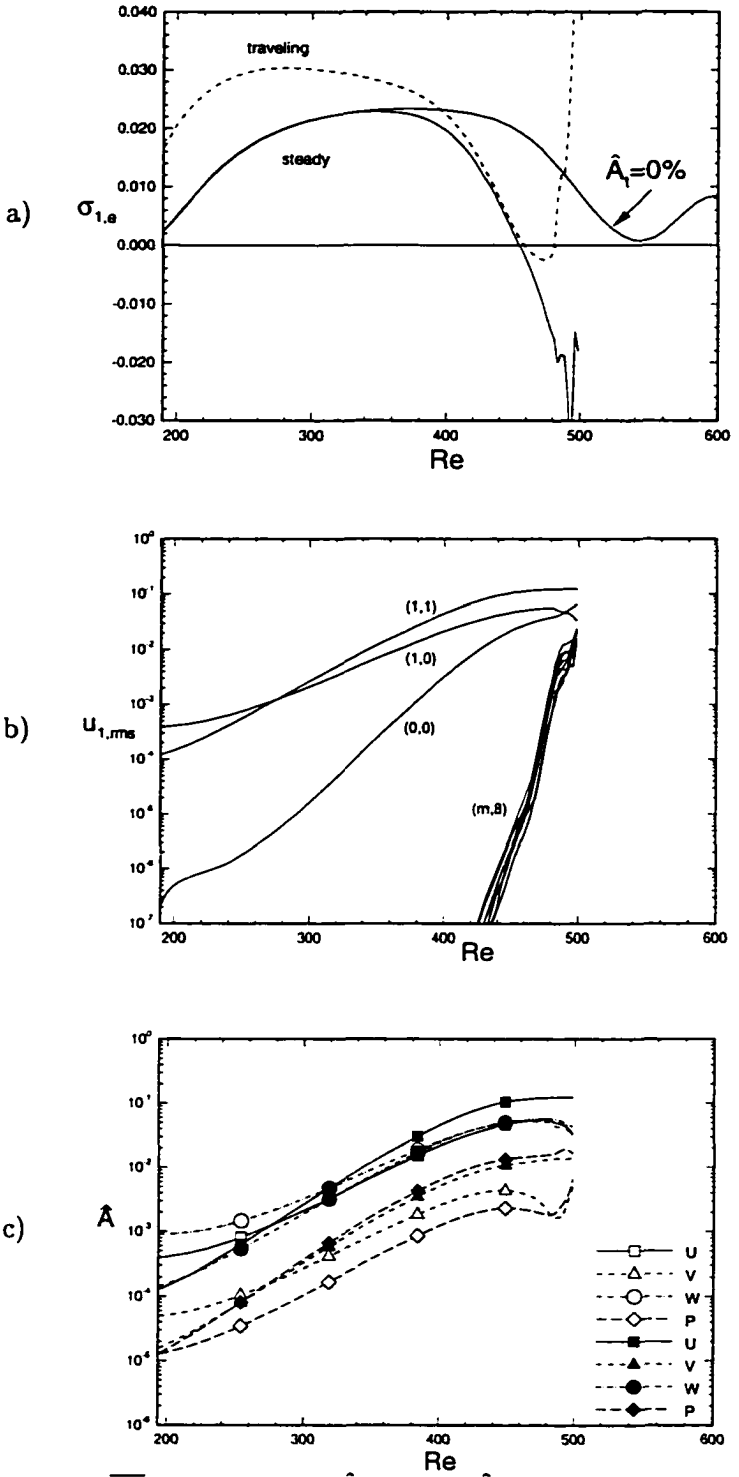

Figure 5.38: Case 3 : $\overline{Re}$=500, β_1=0.4, $\hat{A}_s$=0.1%, $\hat{A}_t$=0.0141%, F=2.0·10^{-3}, 4×8modes; a) Growth rates, b) Amplitudes of individual modes, c) Amplitudes of primary disturbances; (hollow symbols : stationary disturbances; solid symbols : traveling disturbances)

one can see that the modification of the steady primary disturbance is weaker than in Case 3, but there are still features of a weak secondary instability to be noted. In particular, the steep gradients in the temporal growth rate are still present, and both the amplitudes of the mean flow distortion and the primary traveling disturbance show a secondary growth at a Reynolds number of Re≃500 after an earlier saturation onset. Further, the high-frequency modes grow significantly and reach an amplitude level of $\hat{A}_t \simeq 0.0005$, but their growth is much slower than in Case 3 and a tendency towards saturation at the highest computed Reynolds number of Re=591 is observed.

The saturation amplitudes for the u_1- and w_1-components of the primary stationary and traveling disturbances for Cases 1-3 are given in table 5.9. It is noted that in Case 2, where the high-frequency disturbances do not grow as explosively as in Case 3, the saturation amplitude of the stationary u_1-component is of the same order as for the purely stationary case. In contrast, for Case 3 where the explosive secondary growth of the high-frequency disturbances is observed, the saturation amplitude of the stationary u_1-component is much lower than observed in the purely stationary case. A detailed discussion of these observations will be given in the summary at the end of this subsection.

Table 5.9: Saturation amplitudes for the primary disturbance components

	$\hat{A}_s$[%], u_1	$\hat{A}_s$[%], w_1	$\hat{A}_t$[%], u_1	$\hat{A}_t$[%], w_1
"Purely-steady" Case	24	17	-	-
Case 1	20	15	3	1
Case 2	22	16	9	4
Case 3	6	5	12	6
"Lower-frequency" Case	10	8	17	10

For the purpose of illustrating the observations in Case 3, contours of the disturbance component and of the total flow quantity tangential to the constant phase lines

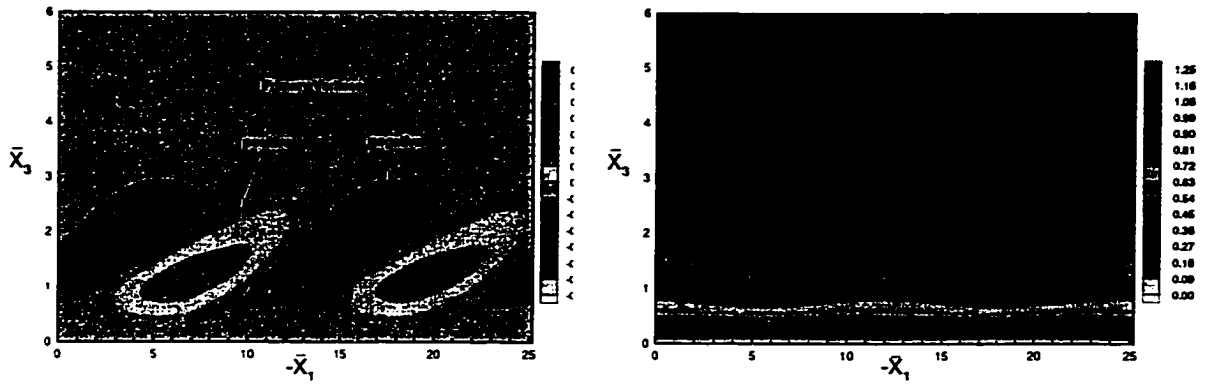

a) Disturbance component (Re=448.5)

b) Total component (Re=448.5)

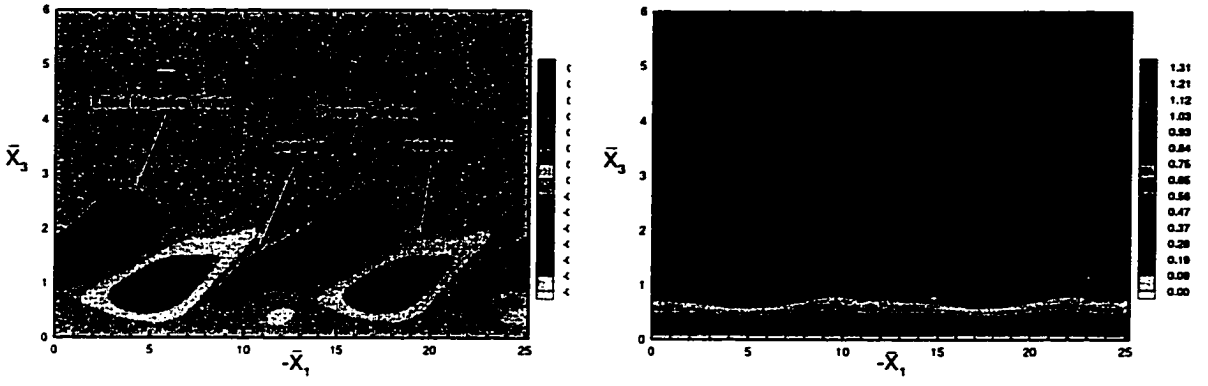

c) Disturbance component (Re=486)

d) Total component (Re=486)

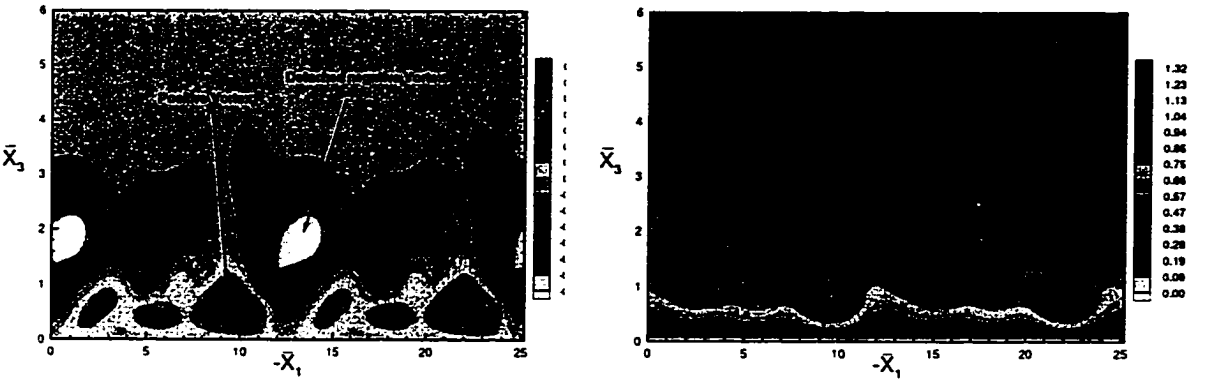

e) Disturbance component (Re=498.5)

f) Total component (Re=498.5)

Figure 5.39: Formation of secondary structures for the velocity component tangential to the constant phase lines (Case 3, T=18)

are plotted at the time T=18 at three different streamwise locations in the Galilean coordinate system in figure 5.39. The chosen Reynolds numbers represent the region where the high-frequency modes experience an explosive growth. It is noted that a negative $\bar{x}_1$-direction corresponds to a positive x_2-direction (see Section 4.4), and hence, the roll-over of the crossflow vortices in the negative $\bar{x}_1$-direction (see figure 5.39(b)) agrees with the previous observations for a purely stationary crossflow vortex (see figure 5.18). At Re=448.5, the high-frequency modes with a frequency of $F=1.6 \cdot 10^{-3}$ have not yet reached any significant amplitude level ($\hat{A} \simeq 0.1\%$ for the w_1-component). Thus, it can be seen from figure 5.39(a) that the co-rotating crossflow vortices are arranged as known from a primary stability analysis. In contrast, at Re=486 where $\hat{A} \simeq 1\%$, the regions of a negative w_1-component show two separated vortices. The locations of the primary vortices can still be distinguished; however, a large negative vortex structure is being lifted away from the wall and above the regions of a positive w_1-component. Finally in figure 5.39(c), where the high-frequency modes have reached an amplitude level of $\hat{A} \simeq 3\%$ at Re=498.5, two separated regions of a positive and a negative u_1-component are observed. Both regions are characterized by the existence of vortex cores at a smaller spanwise spacing than at the previous stations. In particular, a strong positive vortex is located near the wall at $\bar{x}_1 \simeq -10$, and a strong negative vortex adjacent to it at $\bar{x}_1 \simeq -13$ and $\bar{x}_3 \simeq 1.5$. From the plots of the total quantities at these three Reynolds number stations, it can be seen that the degree of the boundary layer distortion is much smaller than for the purely stationary disturbance (see figure 5.18 in Section 5.3). This is due to the earlier saturation of the stationary disturbance at lower amplitude levels in the "higher-frequency" case. On the other hand, the wave number spectrum of the disturbance in the "higher-frequency" case is much fuller than in the purely steady case.

Whereas the fundamental wavelength clearly dominates the observed vortex pattern in the steady case (see figure 5.18), it is still present in the "higher-frequency" case, but modulated by the wavelength of the traveling disturbances (see figure 5.39(f)).

Further documenting the observed secondary instability features caused by the interaction of traveling and disturbances with the stationary vortex in Case 3, figure 5.40

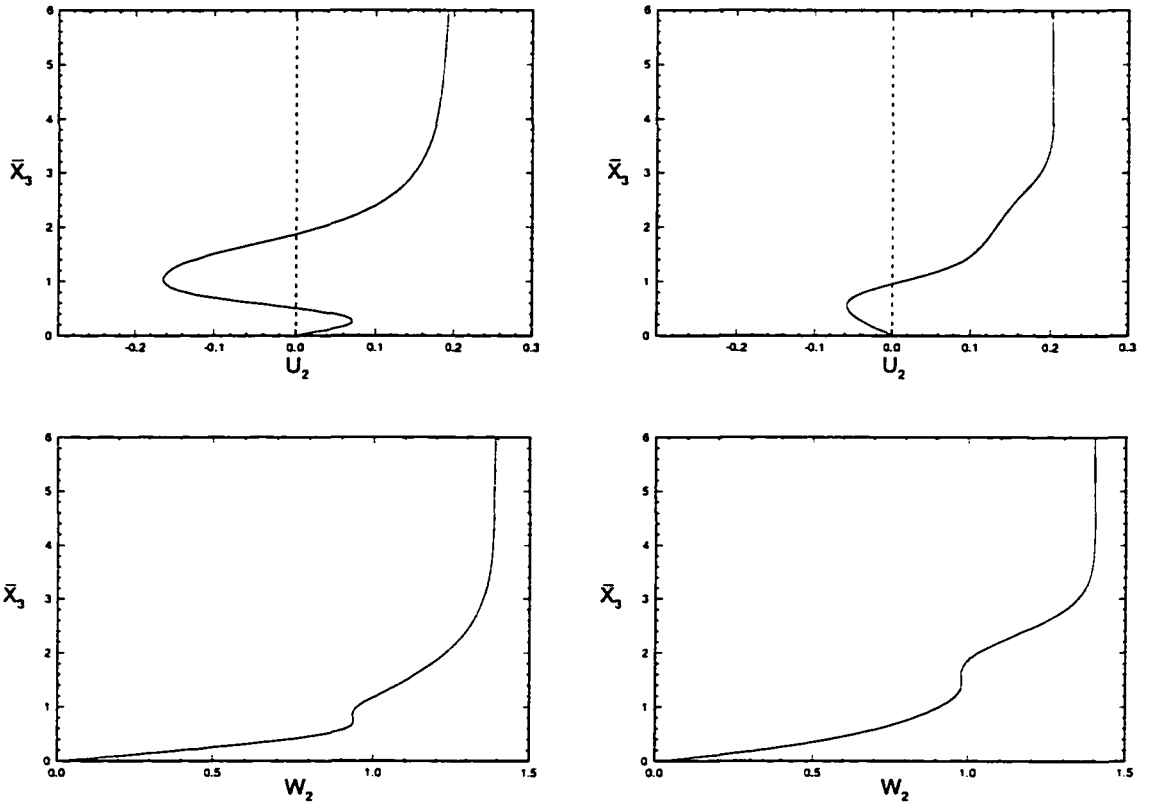

a) $\bar{x}_1$=-9.57 b) $\bar{x}_1$=-13.1

Figure 5.40: Total mean flow components at locations of a maximal/minimal disturbance component tangential to the constant phase lines (Re=498.5)

shows the primary disturbances superimposed on the mean flow in the Galilean coordinate system. Plotted are the modified mean flow components perpendicular and tangential to the constant phase lines, U_2 and W_2, respectively, at the locations where the positive and negative disturbance components tangential to the constant phase lines are

maximal. From figure 5.39(e), these locations are determined as $\bar{x}_1 \simeq$ -9.5 for the positive maximum of the w_1-component, and as $\bar{x}_1 \simeq$ -13.0 for its negative maximum. It is seen in figure 5.40 that at the two selected locations both total velocity components show multiple inflection points. It is this inflectional character of both wall-parallel velocity profiles that documents the presence of a strong inviscid secondary instability.

Investigating the observed lift-up of regions where the disturbance component in the direction tangential to the constant phase lines is negative from a different perspective, figure 5.41 shows streamlines of the total flow quantity in the plane perpendicular to the constant phase lines. Plotted are the velocity vectors and streamlines for two wavelengths $\lambda_{\bar{x}_1} = 2\pi/\alpha_3$ at the same time instant and Reynolds number locations as in figure 5.39. At a Reynolds number of Re=448.5, where the primary vortices were seen to be dominant (figure 5.39(a)), the classical cat's-eye pattern of the primary crossflow vortices is obtained in figure 5.41(a), and the presence of secondary instability features is not yet observed. Here, the normal location of the vortices is $\bar{x}_3 \simeq 1.5$. At Re=486.0, the basic cat's-eye structure of the streamlines is still preserved. However, the vortex observed at the previous Reynolds number location has now split into two weaker vortices that are contained within one "cat's-eye" (see figure 5.41(b)). The normal location of the vortices still remains at $\bar{x}_3 \simeq 1.5$. In contrast, a qualitative change in the streamline traces is observed at Re=498.5. Here, the cat's-eye structure has dissolved into three clockwise rotating vortices that are embedded in a large scale vortex structure covering the entire boundary layer thickness. Part of this vortex structure is a very strong lift-up mechanism located between $\bar{x}_1$=-12 and $\bar{x}_1$=-14 (figure 5.41(c)). Another qualitative difference to the previous two Reynolds number locations is the presence of a counter-clockwise rotating vortex close to the wall at $\bar{x}_1 \simeq$ -10. In figure 5.41(c), it is seen that

a) Re=448.5

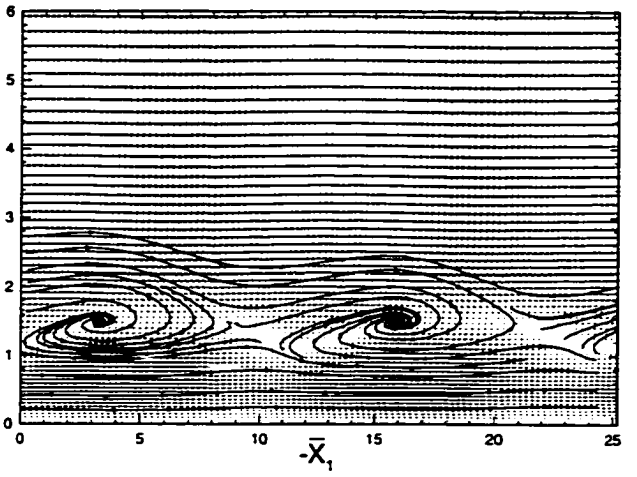

b) Re=486.0

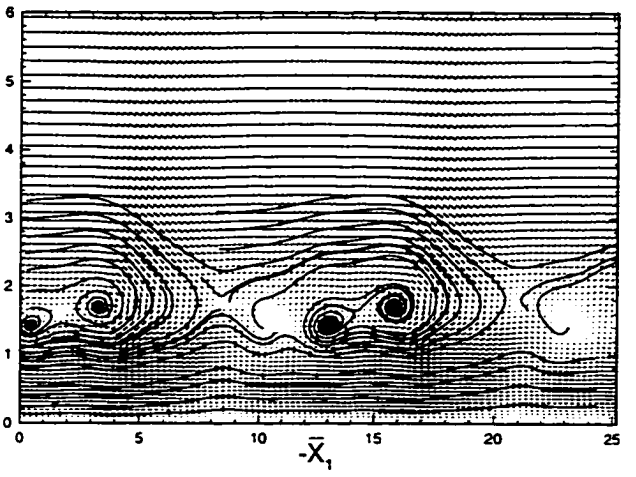

c) Re=498.5

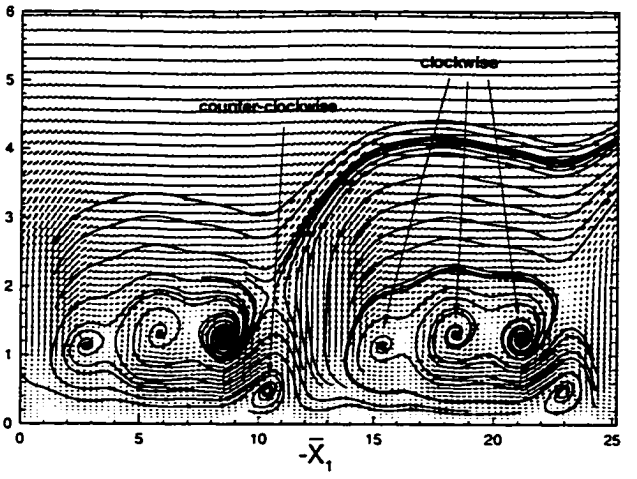

Figure 5.41: Vortex structures perpendicular to the constant phase lines

two counter-rotating vortices exist almost on top of each other at $\bar{x}_1 \simeq$ -9.0 and $\bar{x}_1 \simeq$ -10. The combination the two above observations at Re=498.5 confirms the existence of the earlier mentioned mechanism that moves lower speed fluid on top of higher speed fluid (see figure 5.39(e)).

During the computations, another observation was made with respect to the time-dependence of the lifting process of lower speed fluid on top of higher speed fluid. The assumption of periodicity in time, part of the PSE formulation, causes the described lifting mechanism to be periodic in time and in space. That is to say, the observed horizontal separation of positive and negative layers of disturbance velocity layers is not present at all times, and additionally, the first streamwise occurrence of this phenomenon varies as well.

The observed features of vortex-splitting are interpreted as a confirmation of the previously stated wavelength modulation of the stationary vortex by the presence of high-frequency traveling disturbances. This was also found by Fischer and Dallmann in [16] and [67], where they superimposed primary and secondary disturbances, determined by solving linear eigenvalue problems, on a parallel base flow. The phenomenon of a half-wavelength periodicity has also been observed experimentally by Saric and Yeates [24] and by Kohama et al. [27].

In a last attempt to visualize the mechanism of the secondary instability in this section, figure 5.42 shows two components of the total modified mean flow at different normal and streamwise locations in the Galilean coordinate system for Case 3. Comparing figure 5.42 with the similar figure 5.19 for the purely stationary case, the following is noted. Starting with the same sinusoidal spanwise variation at Re=448.5, the spanwise variation of the plotted velocity components tangential to the constant phase lines and

normal to the wall, W_2 and V_2, respectively, is more complex at the other two Reynolds number stations in Case 3. In particular, the modulation of the primary spanwise wavelength is observed, as pointed out above. Also, at Re=498.5, the fluctuations in the wall-normal component are about twice as large as at Re=546 in the purely stationary case. This again indicates the presence of strong vertical mechanisms in Case 3.

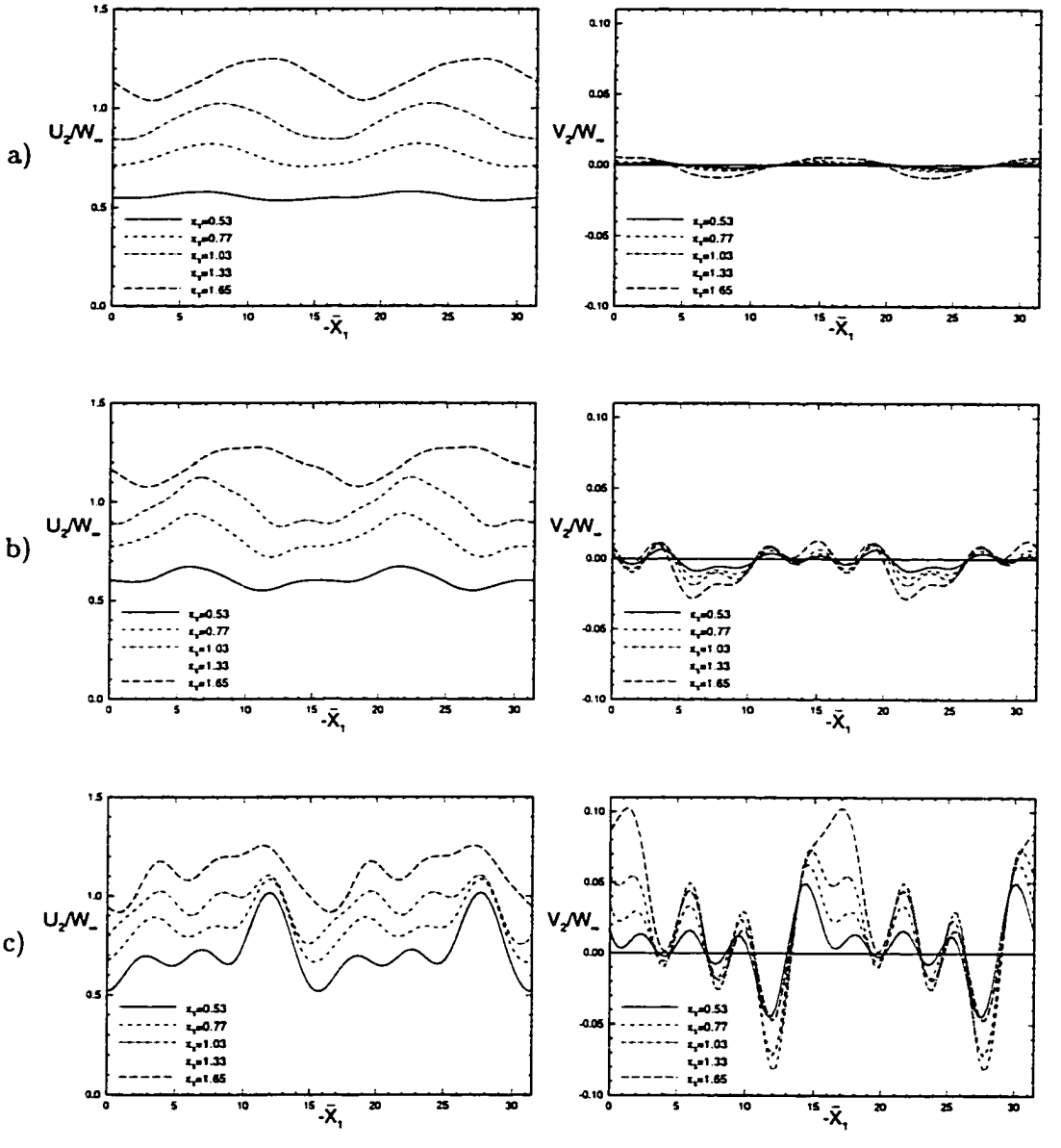

Figure 5.42: Total modified mean flow at different normal and streamwise locations a) Re=448.5, b) Re=486.0, c) Re=498.5

In order to further investigate the role of the stationary disturbance in the interaction process with the traveling disturbance, the traveling disturbance is considered separately in the next study. For the same initial amplitude as in Case 3, the results of the purely traveling case are shown in figures 5.43 and 5.44. Figure 5.43(a) shows the growth rates based on the disturbance energy. Plotted are the curves for the purely stationary case ($\hat{A}_t$=0), for the purely traveling case ($\hat{A}_s$=0), and for the "higher-frequency" case. It can be seen that the purely traveling disturbance saturates slightly later than the traveling disturbance in the "higher-frequency" case at Re≃470. This corresponds to the previously made observations regarding the influence of the interaction of stationary and traveling disturbances.

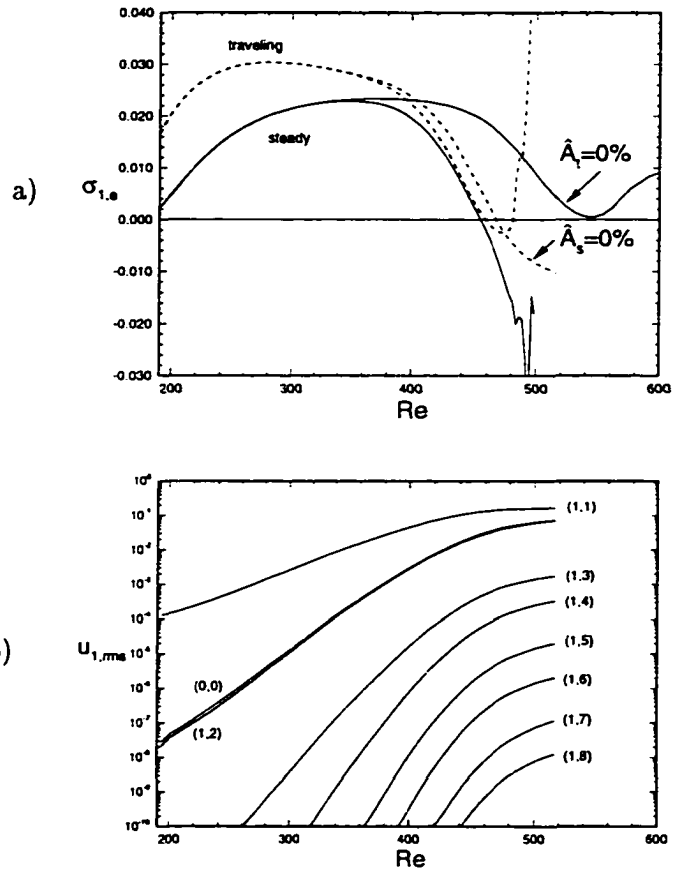

Figure 5.43: Purely traveling case : $\overline{Re}$=500, β_1=0.4, $\hat{A}_s$=0.%, $\hat{A}_t$=0.0141%, F=2.0·10^{-3}, a) Growth rates, b) Amplitudes of individual modes

However, the growth rate of the purely traveling disturbance does not show the strong secondary increase as observed for the "higher-frequency" case. Figure 5.43(b) shows the amplitude evolution of the individual traveling modes. The qualitative difference to the "higher-frequency" case in figure 5.38(b) is obvious. Even though the disturbances cover the same frequency range as in the "higher-frequency" case, all the traveling modes saturate at different amplitude levels, and no secondary growth is detected. From this, it can be concluded that the secondary instability features observed in Case 3 must be attributed to the presence of both a saturated stationary crossflow disturbance and a traveling disturbance of smaller initial amplitude, as well as to the nonlinear interaction of the two disturbances.

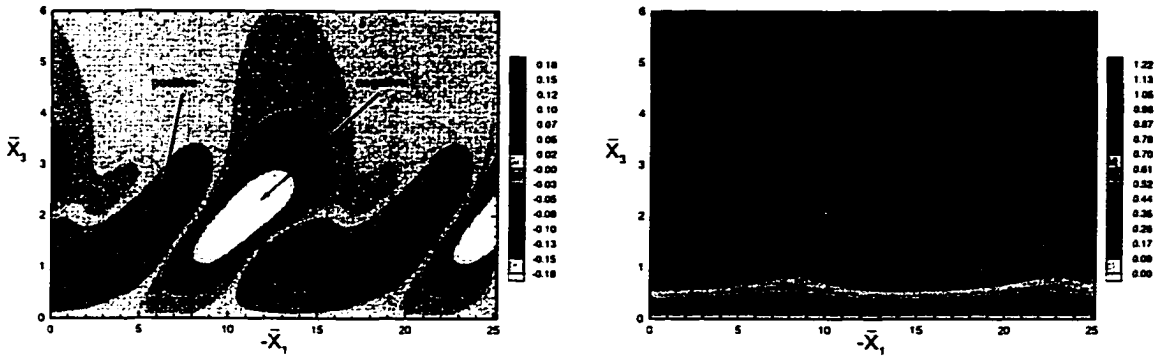

a) Disturbance component (Re=486) b) Total component (Re=486)

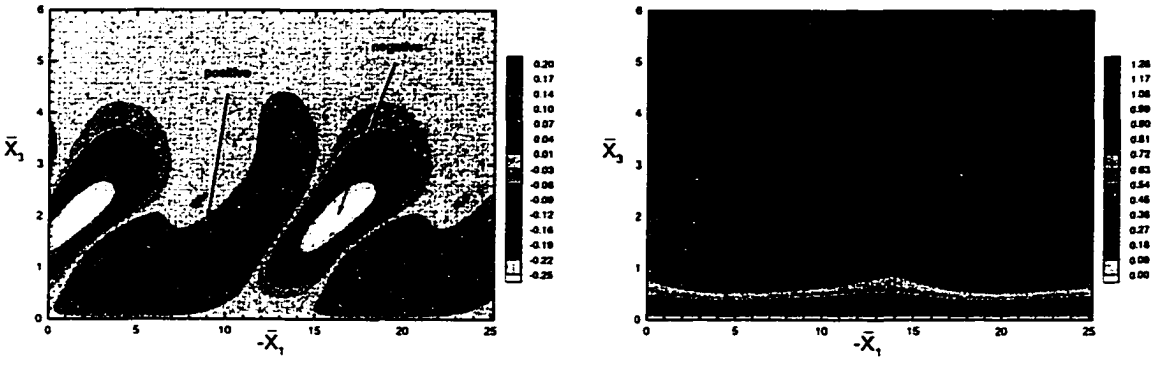

c) Disturbance component (Re=501) d) Total component (Re=501)

Figure 5.44: Velocity components tangential to the constant phase lines for the purely traveling case (T=18)

Further evidence for this statement is found from figure 5.44. There, contours of the velocity component tangential to the constant phase lines are plotted for the disturbance and the total quantity at two Reynolds numbers in the same streamwise region and at the same time as shown in figure 5.39 for the "higher-frequency" case. Comparing figures 5.39(c)-(f) with figures 5.44(a)-(d), one observes that the typical primary vortex structure is obtained in the purely traveling case. The traveling crossflow vortices stretch far into the outer flow and the fundamental wavelength is clearly dominant. There is no indication for the presence of the wavelength modulation and the lifting of low-speed fluid on top of high-speed fluid, as noted in the "higher-frequency" case.

As the last topic in this subsection, the "lower-frequency" case from the nonlinear stability analysis in Section 5.3 will be reconsidered and compared with the "higher-frequency" case from this section. In particular, the following two questions are intended to be answered by this study :

- Is there indeed a qualitative difference between the supposedly primary stability investigation in the "lower-frequency" case and the attempt of modeling the secondary instability in the "higher-frequency" case ?

- Of which order should the initial amplitude of the stationary disturbance be in order to allow for the downstream development of a secondary instability ?

First, the relevant parameters for both cases are given again in table 5.10. The main difference between the input for the two cases is in the specified primary frequency. There is a factor of 2.5 between the maximal frequencies for the "higher-frequency" case and the "lower-frequency" case. Additionally, the "lower-frequency" case covers a wider spanwise wave number range. This, however, is of minor importance for the interpretation of the results.

Table 5.10: Parameters for the "lower-frequency" case and the "higher-frequency" case

	"Lower-frequency" case	"Higher-frequency" case
Modes in β_1-domain	8	4
Modes in ω_1-domain	8	8
β_1	0.4	0.4
$\beta_{1,max}$	3.2	1.6
F_1	$0.75 \cdot 10^{-4}$	$2.0 \cdot 10^{-4}$
F_{max}	$0.6 \cdot 10^{-3}$	$1.6 \cdot 10^{-3}$
$A_{s,initial}$	0.100%	0.100%
$A_{t,initial}$	0.014%	0.014%

In figure 5.45, the growth rates based on the disturbance energy and the amplitude evolution of the individual modes are plotted for the two cases. From the plots of

"Lower-frequency" Case "Higher-frequency" Case

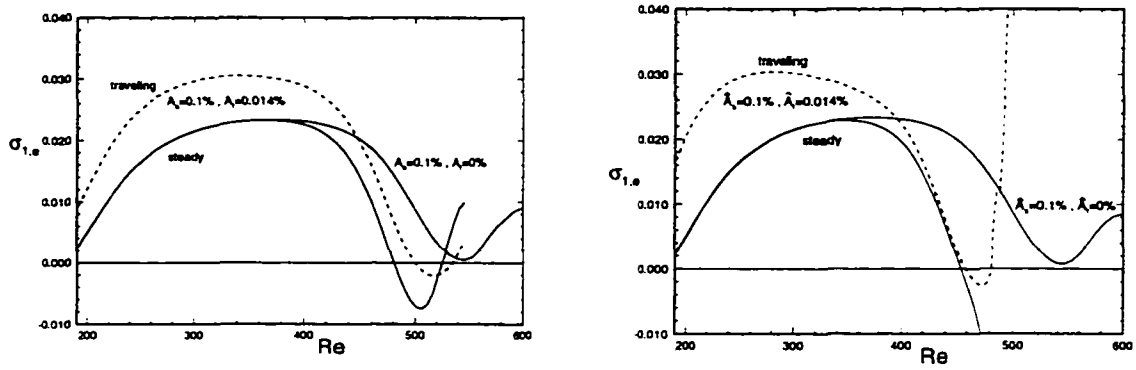

Growth rates based on the disturbance energy

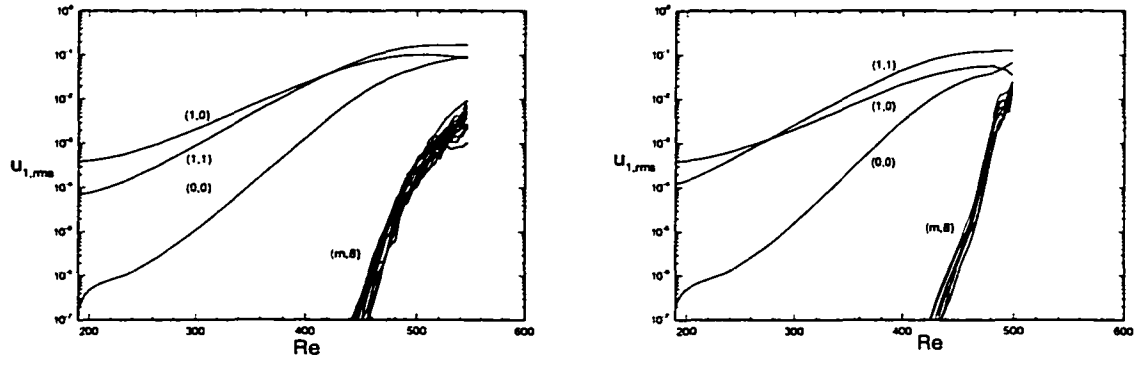

Amplitudes of the individual modes

Figure 5.45: Comparison of the "lower-frequency" case with the "higher-frequency" case

the growth rates, it can be seen that the initial growth rate of the traveling disturbance is much higher in the "higher-frequency" case. Comparing the growth rates of the steady disturbances for both cases with the curve for the purely stationary disturbance, one notes that the steady disturbance is less modified in the "lower-frequency" case. It is the slower growth of the lower-frequency disturbance in this case that allows for a longer growth of both traveling and stationary disturbances. In the "lower-frequency" case, a saturation of the steady primary disturbance is observed at Re$\simeq$480, and the traveling primary disturbance saturates at Re$\simeq$500. In the "higher-frequency" case, however, both the traveling and stationary disturbance saturate at Re$\simeq$460. Also, both primary disturbances show a moderate secondary growth after saturation in the "lower-frequency" case, whereas the traveling disturbances experience an explosive secondary growth in the "higher-frequency" case.

The same features can be viewed from a different perspective in the plots of the amplitude evolution of the individual modes. Due to their longer growth in the "lower-frequency" case, both the traveling and stationary primary disturbances reach larger saturation amplitudes in this case. However, the main difference between the results for the two cases is seen in the growth of the highest frequency modes. Whereas the modes with $F=0.6\cdot10^{-3}$ in the "lower-frequency" case tend towards saturation after a steep growth beyond Re=440, the modes with $F=0.6\cdot10^{-3}$ in the "higher-frequency" case show the spike-like growth that was discussed earlier.

Thus, the questions raised earlier are answered as follows. There is qualitative difference between the two investigated cases that is embodied in the different growth of the high-frequency modes in the region of the nonlinear saturation of the stationary disturbance. Thus, the "higher-frequency" case can indeed be referred to as a case

where secondary instability features are captured. Regarding the second question, it can be stated that in both cases the initial amplitude of the stationary disturbance was too small to allow for saturation amplitudes of about $\hat{A} \simeq 20\%$, as observed for the purely stationary case. Thus, the obtained saturation amplitude levels for the stationary u_1-disturbance component of $\hat{A}=6\%$ and $\hat{A}=10\%$ for the "higher-frequency" case and "lower-frequency" case, respectively, are too low to allow for the development of a self-sustained secondary instability. As stated earlier, the observed features are attributed to the nonlinear interaction of stationary and high-frequency traveling disturbances.

Summarizing the results of this subsection, one can conclude the following :

- A certain amplitude level of the primary traveling disturbance and the interaction of steady and traveling disturbances are required to cause the large growth rates of the high-frequency disturbances. The information about the initial amplitude of the traveling disturbance cannot be obtained from the temporal analysis, since it does not consider the spatial evolution of the nonlinearly interacting disturbances.

- If the initial amplitude of the traveling disturbance is far below a threshold amplitude, say $\hat{A}_s/\hat{A}_t \sim O(100)$, a primary stability analysis is performed (Case 1).

- If the initial amplitude of the primary traveling disturbance is slightly below a threshold value, say $\hat{A}_s/\hat{A}_t \sim O(10)$, the secondary instability is present in the flow, but does not grow large enough to severely modify the flow structure and cause an eventual transition to turbulence (see Case 2).

- If the initial amplitude of the traveling disturbance is larger than the threshold amplitude, a PSE analysis can capture typical features of the secondary instability (see Case 3).

- In order to model the secondary instability further into transition, one might need to incorporate more modes in both the frequency and the spanwise domain, cluster the frequency modes closer and up to a higher frequency than predicted by temporal theory. Also, the initial stationary amplitude might need to be increased in order to obtain a higher saturation amplitude of the stationary disturbance.

- A temporal investigation of the secondary instability using a local Floquet Theory misses essential features of the development of the high-frequency disturbances, like spatial amplitude growth due to nonlinear interaction between the disturbances and the presence of a threshold amplitude for self-sustained growth of the secondary disturbances. However, it can serve as a tool for a prediction of an existing instability to high-frequency disturbance in the flow.

5.5 Summary

In the preceding chapter, the model problem of Swept Hiemenz flow was studied using the linear and nonlinear PSE, as well as Floquet Theory. A detailed qualitative description of the mechanisms leading to the onset of a secondary instability was given, and quantitative results of temporal and spatial investigations of the secondary instability were presented. In summary, the following findings need to be pointed out.

Primary Stability Analysis

- The most amplified stationary and traveling disturbances determined using linear theory were found for β_1=0.3 and F=$1.0 \cdot 10^{-4}$.

- The nonlinear evolution of both stationary and traveling disturbances, as well as their interaction was investigated. Considered were disturbances close to the most amplified ones (β_1=0.4 and F=$0.75 \cdot 10^{-4}$).

- A detailed description of the modifications of the mean flow by the nonlinearly developing disturbances was presented. In particular, the evolution of a purely stationary disturbance was investigated.

- For the presence of a purely stationary crossflow vortex, features that indicate the onset of a secondary instability in the flow were observed beyond Re=480 for rms-amplitudes of $\hat{A}_s$=13% and $\hat{A}_s$=11% for the u_1- and w_1-disturbance components, respectively.

Temporal Secondary Stability Analysis

- Investigating a mean flow that is modified by a purely stationary disturbance using Floquet Theory, several unstable eigenvalues were found in the region of nonlinear saturation of the stationary disturbances. The frequencies of these eigenvalues are an order-of-magnitude higher than the most unstable primary frequency.

- For the investigated station at Re=546, no multiple eigenvalues were detected. Thus, the dominant instability is of a convective type, rather than of the absolute type.

- Applying the local solution method and artificially decreasing the amplitude of the primary disturbances, the existence of a link between the unstable secondary eigenvalues and the eigenvalue spectrum of the undisturbed mean flow was examined. For the chosen Reynolds number of Re=546, a connection could be established for one particular mode (Mode 1).

- Decreasing the amplitude of Modes 2-4 showed that these eigenmodes join the continuous spectrum at different values of the imposed amplitude A.

- The unstable Mode 4 at Re=546 was traced back to its neutral point by gradually decreasing the Reynolds number. The onset of this secondary instability was found at Re $\simeq$ 475 in a region where the primary stationary disturbances are about to saturate. The amplitudes of both the u_1- and w_1-disturbance components of the stationary crossflow vortex are $\hat{A}$ = 11%, which is in agreement with the observations from the primary stability analysis.

- From the observations of a link of unstable secondary eigenvalues to both the linear eigenvalue spectrum and the continuous spectrum, and from the onset of an inviscid high-frequency instability due to the highly inflectional character of all modified mean flow profiles in the region of a saturated stationary crossflow vortex, the following can be concluded. There exist at least three different mechanisms in the region of nonlinear saturation that cause the onset of a high-frequency secondary instability that leads to transition. First, due to the action of the growing nonlinear disturbances, stable linear eigenmodes are modified such that they develop into unstable secondary eigenmodes. Second, from the highly inflectional character of the modified mean flow profiles originates an inviscid high-frequency instability. Third, due to a not yet investigated receptivity mechanism, disturbances from the continuous spectrum present in the outer flow enter the boundary layer and cause high-frequency disturbances. This corresponds to observations by Choudhari et al. in [39], where they allocate the receptivity mechanism to regions of a strong variation in the boundary layer thickness. However, it is understood that the second mechanism represents the dominant path to the transition in a crossflow instability dominated boundary layer.

Spatial Secondary Stability Analysis

- Using the quantitative information about the wave number structure and the frequency spectrum of the secondary instability obtained from the temporal theory, a spatial computation using the PSE was performed in order to capture secondary instability features of the flow in a more straightforward and physical way (see Case 3).

- It was was found that for a careful selection of the initial parameters for the primary stationary and traveling disturbances, it is possible to model the secondary instability using the PSE. The captured secondary instability is attributed to the presence of both stationary and traveling disturbances, and to their nonlinear interaction. Evidence for the existence of a self-sustained secondary instability could not be found.

- The secondary instability features captured for a specification of the initial stationary and traveling amplitudes as $\hat{A}_s$=0.1% and $\hat{A}_t$=0.014%, respectively, as well as for a primary frequency of F=$2.0 \cdot 10^{-4}$ and a fundamental spanwise wave number of β_1=0.4 are described as an explosive growth of the disturbance energy, a spike-like amplitude growth of the high-frequency modes, and a strong secondary rise of the mean flow distortion in the region of the nonlinear saturation of the primary disturbances (see figure 5.38).

- In the region of the spike-like amplitude growth, a mechanism was distinguished that lifts lower speed fluid away from the wall and on top of the higher speed fluid. This mechanism is periodic in time according to the PSE formulation.

- In agreement with a temporal DNS computation by Wintergerste and Kleiser [78] for the DLR Transition experiment, the existence of a counter-clockwise rotating secondary vortex close to the wall was observed in the region where the high-frequency disturbances experience a steep growth (see figure 5.41). Also in accordance with the observations in [78], the existence of several weaker vortices in the region where the nonlinear interaction of the high-frequency disturbances with the stationary crossflow vortex dominates the flow was observed. The development of these vortices eventually leads to the breakdown of the crossflow vortex [78].

- The observed modulation of the primary stationary wavelength by the traveling high-frequency disturbances (see figures 5.39 and 5.42) agrees with the half-wavelength periodicity observed theoretically by Fischer and Dallmann [67] and experimentally by Kohama et al. [27].

CHAPTER 6

DLR TRANSITION EXPERIMENT

6.1 Introduction

The variety of wind tunnel tests that is usually referred to as the DLR Transition experiment began in the mid-eighties at the German aerodynamic test and research facility located in Göttingen. Under supervision of Bippes, Nitschke-Kowsky [13] conducted the first experiments on a swept flat plate on which a pressure gradient was imposed by a suitable aerodynamic displacement body. A generic version of the experimental setup is shown in figure 6.1. Using endplates, infinite wing conditions were simulated

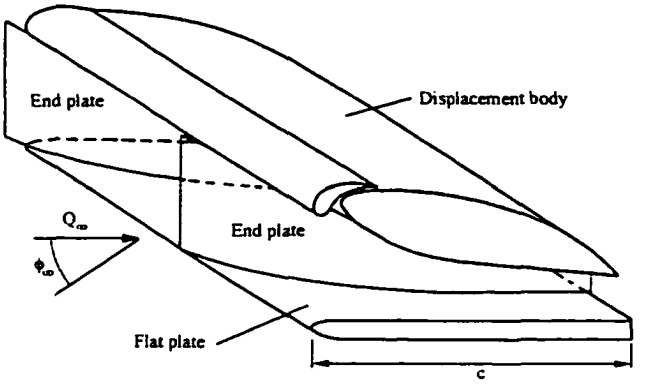

Figure 6.1: Experimental setup for the DLR Transition experiment (from [2])

such that there was no variation of the mean flow in the spanwise direction. Due to the presence of a displacement body, the obtained mean flow experiences a favorable pressure gradient over the entire chord length of the model, and hence, the transition in the boundary layer is dominated by a purely crossflow-type instability (see Chapter 1). A detailed discussion of the numerous experiments performed in different environments

like in a water towing tank, and under various freestream turbulence levels is given by Deyhle and Bippes in [2]. The conducted experiments were aimed at studying the receptivity and transition mechanisms in a crossflow instability dominated boundary layer. In particular, they examined the receptivity of the disturbances to surface roughness, to sound waves, as well as to freestream turbulence, and established a data base for a variety of initial conditions. For the reason of its very good documentation, the DLR experiment is of high value for the validation of computational methods and for further investigation of observed phenomena in the experiments using numerical approaches.

The turbulence level during the experiments considered in this chapter is specified as Tu=0.15% at a speed of Q^*_∞=19 m/s [2]. Even though this value represents a fairly benign environment, it is still high in comparison to the turbulence level present in the experiments performed by Saric et al. [4,29] for which a value of Tu=0.04% at a speed of Q^*_∞=20 m/s is given by Chapman et al. [31]. Thus, in the DLR experiment, traveling modes are present in the flow and need to be considered in the computations when compared with the experimental results. Also, the initial presence of traveling modes complicates the isolation of the physical mechanisms considerably.

In the present chapter, the focus will be on the linear and nonlinear evolution of stationary and traveling disturbances, as well as on the secondary instability originating from a purely stationary crossflow vortex. Two different experiments will be considered, the details of which are given in relevant sections. According to the experimental observations by Deyhle and Bippes [2], transition to turbulent flow occurred only for freestream velocities of $Q_\infty > 27$ m/s. The experiments which are investigated in this work were performed at lower freestream velocities, and thus, the considered flows are transitional, but not turbulent.

In particular, Section 6.2 will describe the mean flow computation, Section 6.3 presents the linear and nonlinear results from the primary stability analysis, Section 6.4 discusses the findings from a secondary stability analysis using Floquet Theory, and Section 6.5 summarizes this chapter.

6.2 Mean Flow Computation

The experiments were performed for a freestream velocity of Q^*_∞=19 m/s, a sweep angle of ϕ_∞=45°, and a model chord length of c^*=0.5m. In order to compensate for blockage effects and problems with the simulation of infinite swept wing conditions using end plates, Deyhle and Bippes [2] suggest the use of Q^*_∞=20.5 m/s and ϕ_∞=43.5° instead. The computations presented here are done for the latter parameters. Figure 6.2 shows the measured outer velocity distribution in the chordwise direction that was obtained by courtesy of the DLR. Noted is the existence of a stagnation point at the plate-fixed streamwise position of x_c/c=0.01.

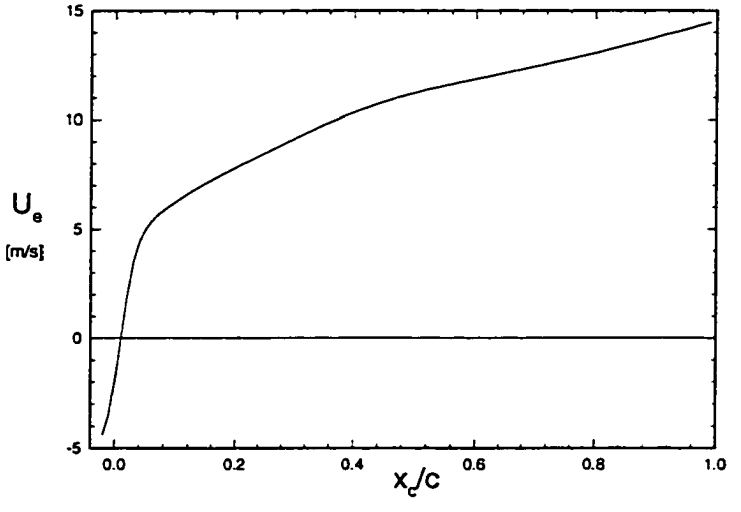

Figure 6.2: Measured outer velocity distribution in the plate-fixed coordinate system

Previous stability analyses of the DLR experiment [2, 3, 18, 71, 78, 94] modeled the measured mean flow with an approximate Falkner-Skan-Cooke (FSC)-type solution. Since this FSC-approximation will be referred to frequently in this chapter, a brief explanation of the essential assumptions will be given first, following the formulation by Wagner [94]. Using the similarity solution to the boundary layer equations for the flow across a wedge of an enclosed angle $\beta_h \cdot \pi$ to locally approximate the experimentally observed outer flow distribution along the chordwise coordinate x_1^*, one can write equation 6.1. The parameter β_h is also referred to as Hartree-Parameter and can be expressed

$$U_e^*(x_1^*) \sim (x_1^*)^m \quad , \quad m = \frac{\beta_h}{2 - \beta_h} \; . \tag{6.1}$$

in terms of the pressure coefficient C_p as in equation 6.2. For a different experiment than considered in this chapter, the chordwise dependence of the measured pressure distribution can be approximated by a straight line (see equation 6.2). Further using the

$$\beta_h = \left[0.5 - \frac{1 - C_p}{x_1 \cdot \frac{dC_p}{dx_1}} \right]^{-1} \quad , \quad C_p(x_1/c) = 0.941 - 0.845 \cdot x_1/c \tag{6.2}$$

similarity coordinate $d^* = (\nu^* \cdot x_1^*/U_e^*)^{1/2}$, the boundary layer equations can be transformed into a system of two ODE's and be solved using a Runge-Kutta method. This approach yields a base flow that depends only on the local angle of the inviscid streamline $\Theta = \tan^{-1}[\tan \phi_\infty / \sqrt{1 - C_p})]$ and on the Hartree-Parameter β_h. The advantage of this method is that it allows for a systematic investigation of the influence of the parameters β_h and Θ on the crossflow instability. The disadvantage is; however, that it neglects the existence of a stagnation point at the leading edge of the swept flat plate.

In the present work and in contrast to the above approximate approach, the mean flow profiles are computed directly from the experimental data. Starting at the stagnation point, a computational grid of 200×300 points in the x_1- and the x_3-directions,

respectively, is constructed. Both the chordwise and the normal coordinate are uniformly spaced up to a normal extension of x_3=15 which corresponds to about twice the maximum boundary layer thickness. For the nondimensionalization of the mean flow parameters, $U^*_{e,0}$ and $l^*_0=(\nu^* \cdot x^*_{1,0}/U^*_{e,0})^{1/2}$ are used as the velocity and length-scales, respectively, where $x^*_{1,0}$ is the streamwise coordinate, and $U^*_{e,0}$ is the freestream velocity in the x_1-direction at the location where the disturbances are introduced.

In the experiment that will be considered first (experiment I), small roughness elements were glued to the surface at x^*_1/c=0.08. These cylindrical elements with a height of 10 μm and a diameter of 3.3 mm are spaced 12 mm apart in the spanwise direction in order to stimulate the most amplified disturbances. The influence of the roughness elements on the mean flow is negligible. Their impact on the downstream evolution of the disturbances, however, will be accounted for in the nonlinear PSE computations in Subsection 6.3.2.

Table 6.1: Freestream conditions for experiment I

Chord length c	0.5 m
Freestream velocity Q^*_∞	20.5 m/s
Reynolds number $Re_\infty = Q^*_\infty \cdot x^*_1/\nu^*$	683,000
Sweep angle ϕ_∞	43.5°
Kinematic viscosity ν	$15.007 \cdot 10^{-6}$ m^2/s

Figure 6.3 shows the most important mean flow properties for the freestream conditions listed in table 6.1. From the distribution of the outer flow given in figure 6.3(c), the angle of the inviscid streamline Θ, the pressure distribution C_p, the Reynolds number $Re=(U^*_e \cdot x^*_1/\nu^*)^{1/2}$, and the similarity parameter $m=\frac{x^*_1}{U^*_e} \cdot \frac{dU^*_e}{dx^*_1}$ are computed. The boundary layer thickness shown in figure 6.3(e) is defined at a location where the velocity component tangential to the inviscid streamline U^*_t reaches a value of 99.9% of the outer velocity $U^*_{t,e}$.

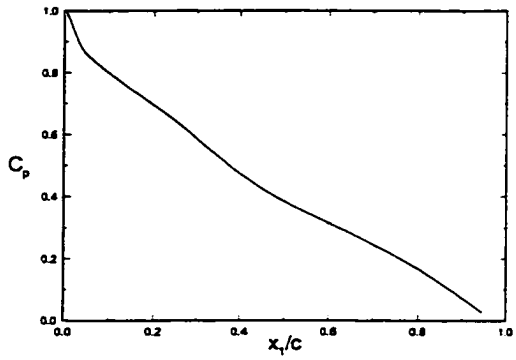

a) Measured pressure distribution

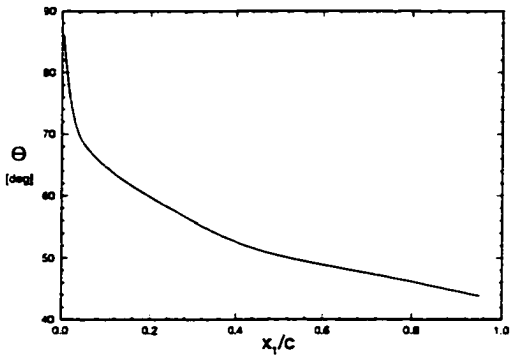

b) Measured angle of inviscid streamline

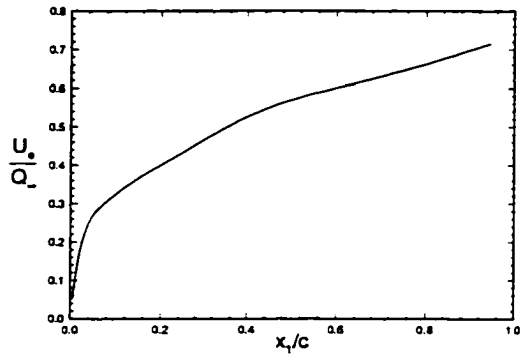

c) Measured outer velocity along the chord

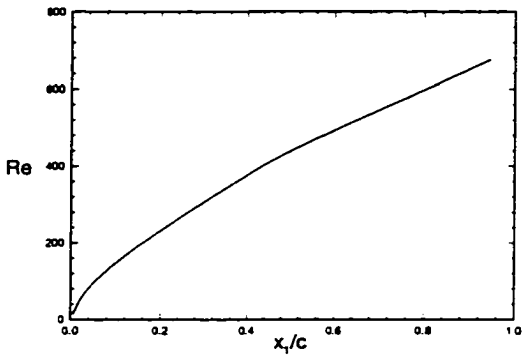

d) Reynolds number

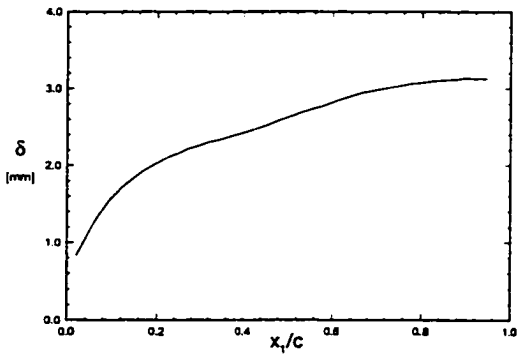

e) Boundary layer thickness

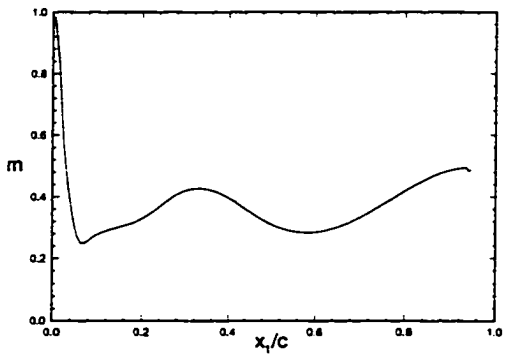

f) Computed similarity parameter

Figure 6.3: Mean Flow properties from experiment and computation

For the purpose of a qualitative comparison of the present approach and the FSC-similarity assumption, figure 6.4 shows the similarity and Hartree-parameters obtained from both methods. A direct comparison of the different results is not possible, since the linear approximation of the pressure distribution applies to a different experiment. However, the qualitative differences are especially seen in the region close to the stagnation point of the swept flat plate, and in the inflectional variation of β_h and m in the results of the present computation. This variation is due to the chordwise development of the measured pressure distribution that is not linear.

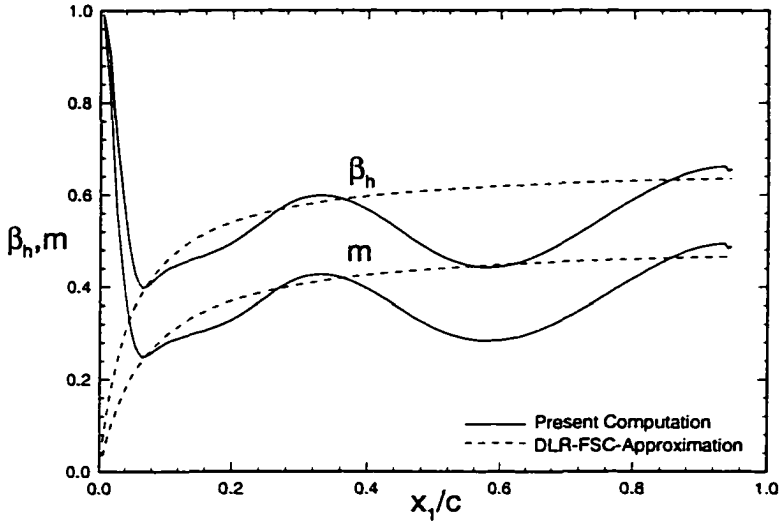

Figure 6.4: Similarity parameter from the FSC-assumption and the present computation

Next, the mean flow profiles obtained from the present mean flow computation are shown at different chordwise positions in figures 6.5 and 6.6. Plotted are the velocity profiles tangential and perpendicular to the inviscid streamline, U_t and U_c, respectively. It is seen that the maximum of the crossflow component reaches values between 4% and 8.5% of the freestream velocity. Also, the crossflow component never changes sign, and hence, the stability of the mean flow is dominated by a purely crossflow-type mechanism (see Chapter 1).

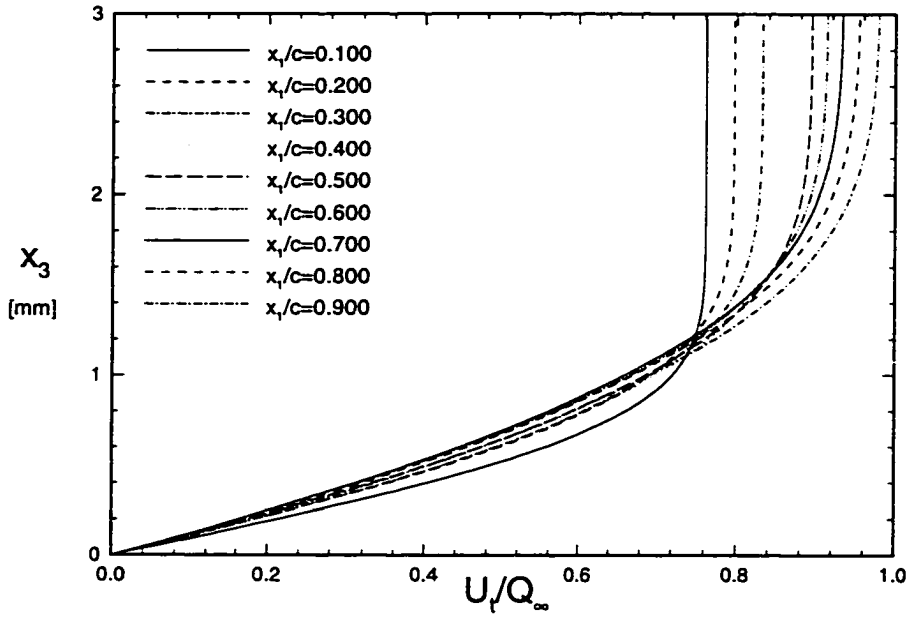

Figure 6.5: Mean flow profiles tangential to the inviscid streamline

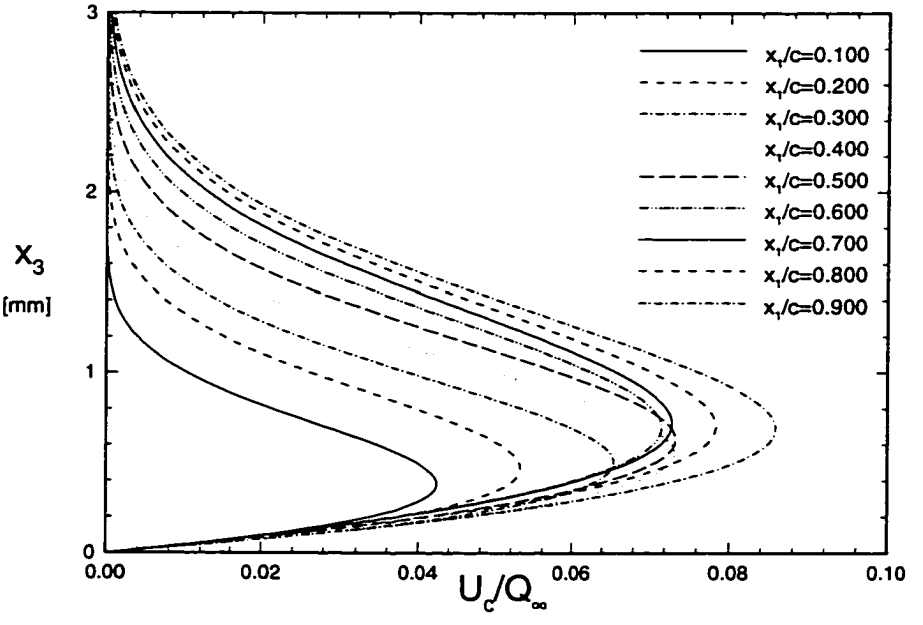

Figure 6.6: Mean flow profiles perpendicular to the inviscid streamline

Finally, figure 6.7 shows a comparison of the computed mean flow profiles from the present approach and from the Falkner-Skan-Cooke similarity assumption with the measured profiles. The agreement of the computed with the experimental data is good.

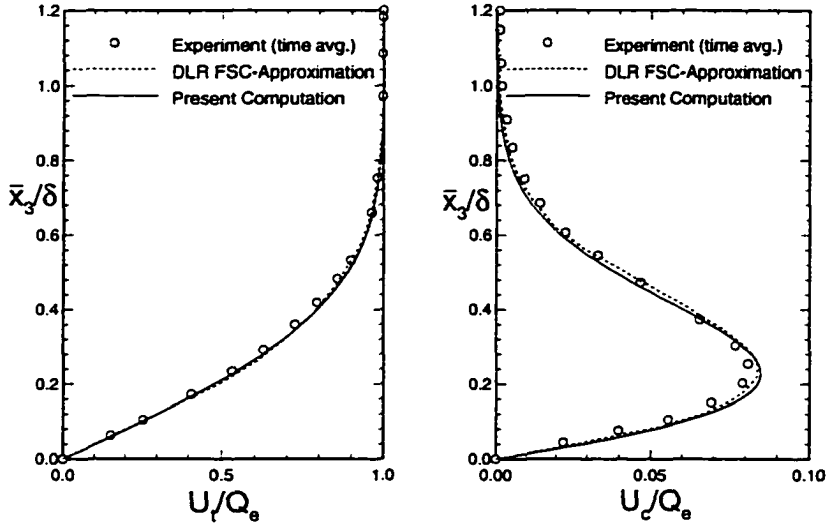

Figure 6.7: Mean flow profiles at x_1/c=0.4 (experimental and FSC-data from [2])

6.3 Primary Stability Analysis

Since the outer velocity distribution shows a stagnation point at the leading edge of the swept flat plate, it is necessary to investigate the stability of the attachment line first. The flow along the attachment line must be stable in order to exclude the existence of a leading edge contamination that would cause an early transition due to this mechanism. Using the local length scale close to the stagnation point $l^* = \sqrt{\nu^*/(dU_e^*/dx_1^*)}$=0.2mm and the constant outer velocity component in the spanwise direction $W_\infty^*=Q_\infty^* \cdot \sin\phi_\infty$=14.11 m/s, the Reynolds number in the spanwise direction is determined as $\overline{Re}=W_\infty^* \cdot l^*/\nu^*$=188, which is far below the numerically critical value of $\overline{Re}$=583 [93]. Also, Deyhle and Bippes [2] show that the experimentally obtained

maximal Reynolds number based on the displacement thickness for the present pressure gradient is well below the critical value for the existence of a Tollmien-Schlichting instability mechanism in the flow. Hence, another two arguments are found which indicate that the obtained mean flow is indeed subject to a purely crossflow-type instability.

Before the presentation of the results, the computational grid needs to be described. A typical grid configuration for the primary stability analysis consists of 141 points in the wall-normal direction, where the first 71 points are clustered within the boundary layer according to the grid-stretching equation 5.12. In the region of the outer flow, the remaining points are distributed uniformly up to a maximum normal extension of about 20 boundary layer thicknesses. For the marching in the streamwise direction, a step-size of $\Delta x_1=0.005$ is usually applied. Here the chordwise coordinate x_1 starts at the location of the stagnation point, and the specified step size corresponds to a discretization of the chordwise direction using 200 points.

6.3.1 Linear Analysis

For completeness, the wave angle Ψ and the angle of the inviscid streamline Θ are defined in figure 6.8. The wave angle represents the angle between the wave

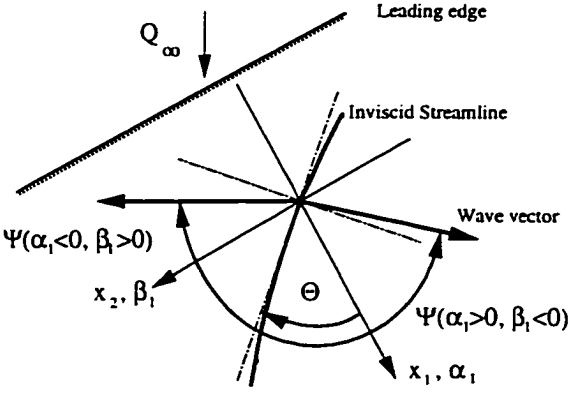

Figure 6.8: Definition of the wave angle and the angle of the inviscid streamline

vector $\mathbf{k_{real}}$ and the inviscid streamline. As for Swept Hiemenz flow, two families of unstable disturbances are distinguished that propagate in opposite directions. Next, and following the procedure performed in the investigation of the Swept Hiemenz flow problem, a local stability analysis of both stationary and traveling disturbances is conducted first. Thereby, the neutral points and the locally most amplified steady and traveling disturbances are determined.

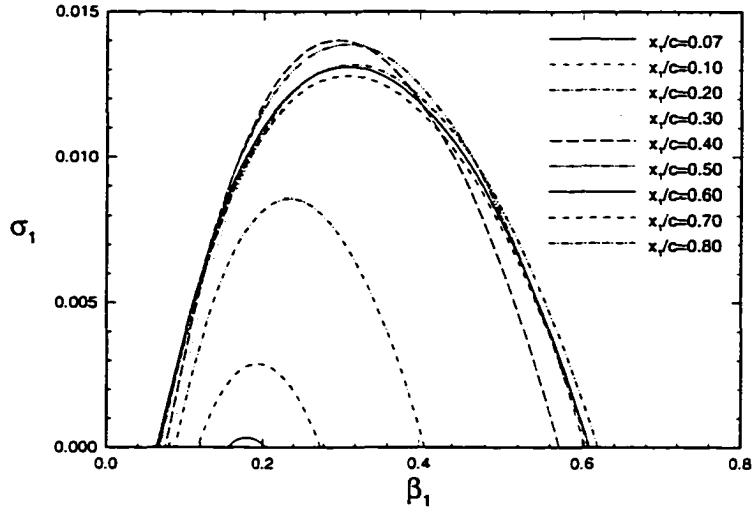

Figure 6.9: Stationary growth rates from a local analysis

In figure 6.9, the nondimensional growth rates σ_1 for stationary disturbances are plotted versus the spanwise wave number β_1 at different chordwise positions. Nondimensionalization is performed using the local length scale $l_0^* = \sqrt{\nu^* \cdot x_{1,0}^*/U_{e,0}^*}$ at the investigated chordwise stations. It can be seen that the unstable wave number range begins at $\beta_1 \simeq 0.08$ for $x_1/c > 0.20$. This wave number is equivalent to a spanwise wavelength of $\lambda_{x_2} \simeq 4$mm. As observed for the Swept Hiemenz flow problem, the local theory predicts an increase of the unstable spanwise wave number range in the downstream direction for the stationary distur-

bances is found at x_1/c=0.067 for β_1=0.174 (λ_{x_2}=10.5mm). The locally most amplified wave number is determined as β_1=0.295 at x_1/c=0.40, where the chordwise wave number is α_1=(-0.33509,-0.01401). Table 6.2 contains the locally most amplified spanwise wave numbers, as well as the corresponding growth rates, dimensional spanwise wavelengths

Table 6.2: Locally most amplified eigenpairs at different chordwise locations (f=0 Hz)

x_1/c	σ_1 = max.	$\lambda_{x_2,\sigma_1=\max}$[mm]	$\beta_{1,\sigma_1=\max.}$	$\Psi_{\sigma_1=\max.}$
0.07	0.00033	10.43	0.177	87.60°
0.10	0.00289	10.92	0.193	87.45°
0.20	0.00858	11.46	0.234	86.89°
0.30	0.01209	11.31	0.269	86.28°
0.40	0.01401	11.23	0.295	86.09°
0.50	0.01387	11.57	0.308	85.70°
0.60	0.01310	12.27	0.309	86.54°
0.70	0.01279	13.02	0.308	86.48°
0.80	0.01317	13.32	0.313	86.18°

and wave angles. It is observed that the wave angle of the most amplified stationary disturbances remains almost constant in the chordwise direction. The constant phase lines of the most unstable stationary disturbances are inclined at angles less than five degrees with respect to the inviscid streamline.

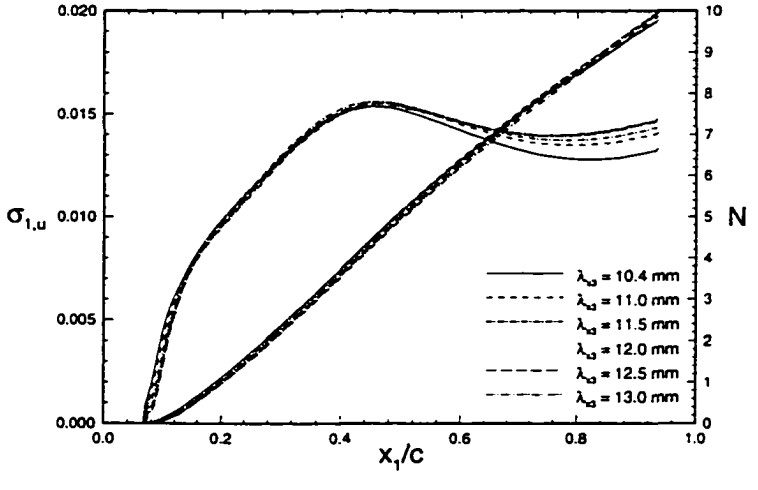

Figure 6.10: Stationary growth rates and N-factors from a PSE computation

Next, the most amplified spanwise wave number according to its spatial growth in the downstream direction is sought. Therefore, starting at x_1/c=0.07, disturbances of a different spanwise wave number are introduced and their spatial evolution downstream computed. Figure 6.10 shows the growth rates and N-factors based on the u_1-component obtained from a linear PSE computation. The maximal N-factors for the different wavelengths are given in table 6.3. The wavelengths in the range of λ_{x_2}=11.5 - 12.0 mm are amplified the most, and for a further investigation of the nonlinear development of the disturbances, these wave numbers need to be considered.

Table 6.3: N-factors of the most amplified stationary disturbances at $x_1/c = 0.935$

λ_{x_2}[mm]	10.4	11.0	11.5	12.0	12.5
N_{max}	9.773	9.962	9.984	9.980	9.936

Defining the nondimensional frequency F in equation 6.3, the locally most amplified traveling disturbance is determined next. In this computation, the procedure

$$F = \frac{2\pi \cdot \nu^* \cdot f^*}{(U_\infty^*)^2} \tag{6.3}$$

described in Subsection 5.3.1 is repeated. Starting from the most amplified spanwise wave number at f=0 Hz, the frequency is incremented and the new wave number β_1 computed such that the growth rate σ_1 is maximal for the specified frequency. The resulting growth rates and wave angles at different chordwise locations are plotted versus the dimensional frequency in figures 6.11 and 6.12. In table 6.4, the values of the frequency, the wave angle, the spanwise wavelength and wave number are given at the locations of the maximal growth rate. Also, the unstable frequency range becomes narrower in the downstream direction in the DLR experiment, which is in contrast to the observations for Swept Hiemenz flow. Finally, it is noted that the locally most unstable wavelengths lie within the same range as the wavelengths of locally most unstable

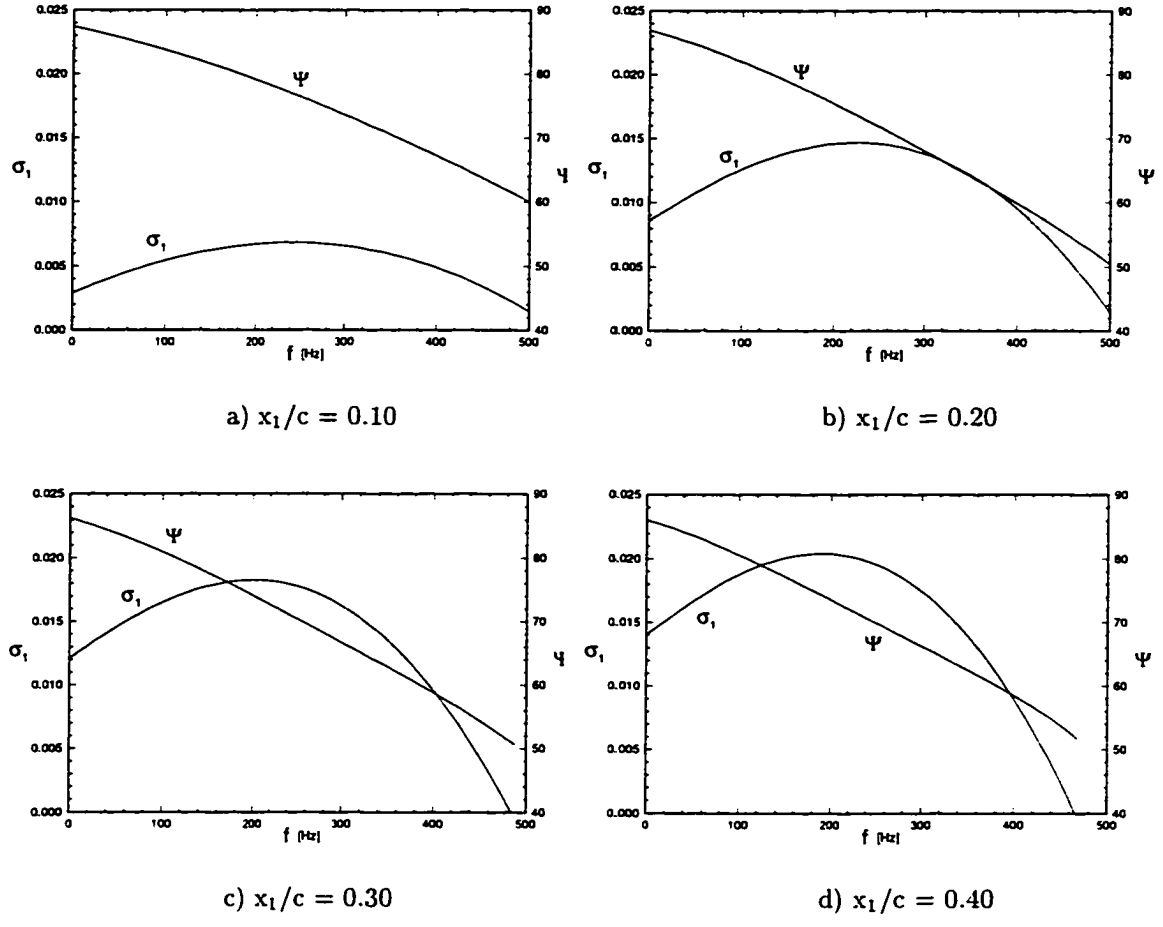

Figure 6.11: Wave angles and most amplified frequencies at different streamwise locations

stationary disturbances. They cover the narrow band from $\lambda_{x_2} \simeq 10$ mm to $\lambda_{x_2} \simeq 15$ mm, with an increasing trend in the downstream direction. The locally most unstable frequency range, on the other hand, covers the fairly wide range from f=125 Hz to f=242 Hz. In agreement with the observations for the Swept Hiemenz flow problem, the locally most amplified frequency decreases in the chordwise direction. However, the development of the unstable frequency range and the wave angle of the most amplified traveling disturbances is different. In contrast to the closer alignment of the locally most unstable traveling disturbances with the constant phase lines observed for the Swept Hiemenz

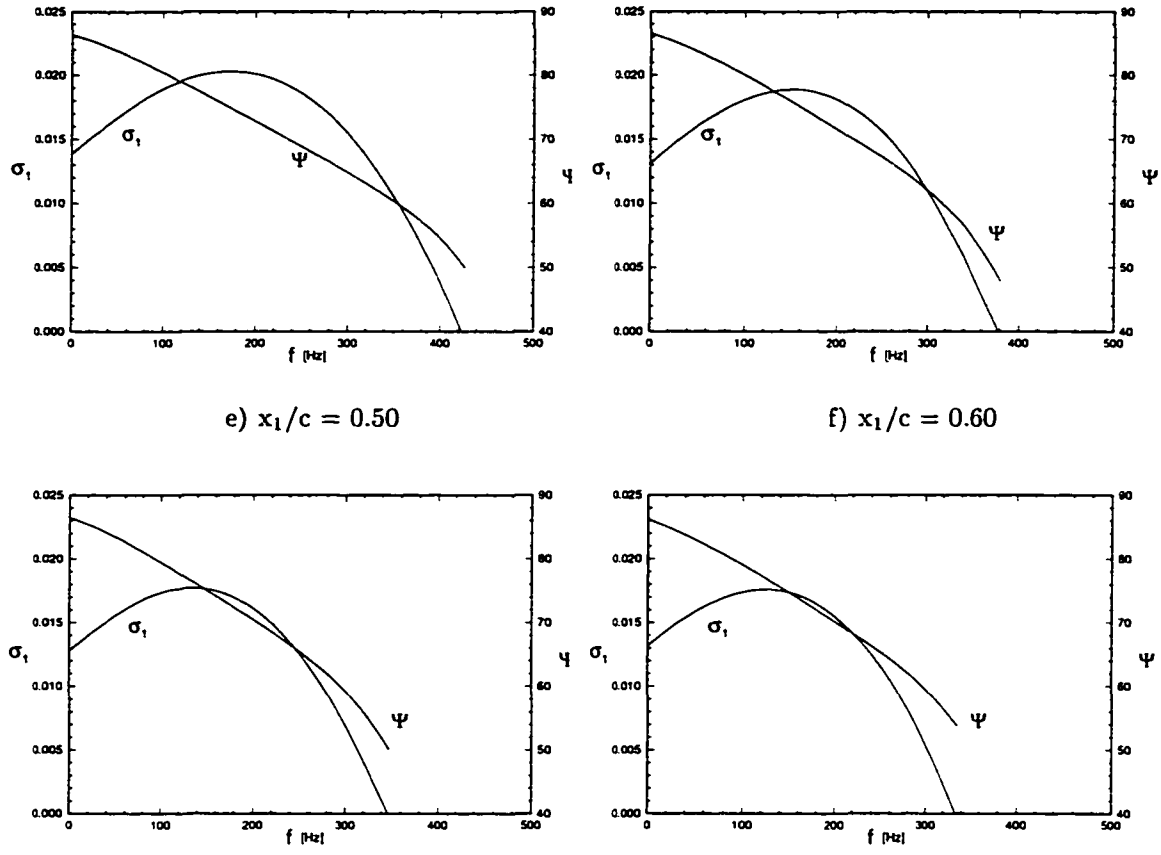

e) $x_1/c = 0.50$ f) $x_1/c = 0.60$

g) $x_1/c = 0.70$ h) $x_1/c = 0.80$

Figure 6.12: Wave angles and most amplified frequencies at different streamwise locations

flow problem, the wave angle of the most amplified disturbances in the DLR experiment remains almost constant in the chordwise direction at values of $\Psi \simeq 75°$.

Table 6.4: Locally most amplified eigenpairs at different streamwise locations (f>0 Hz)

x_1/c	σ_1 = max.	$f_{\sigma_1=max}$[Hz]	$\beta_{1,\sigma_1=max.}$	λ_{x_2} [mm]	$\Psi_{\sigma_1=max.}$
0.10	0.00685	242	0.20826	10.11	76.82°
0.20	0.01467	224	0.23356	11.49	73.70°
0.30	0.01825	200	0.25900	11.76	74.04°
0.40	0.02041	188	0.27512	12.04	74.40°
0.50	0.02027	172	0.27321	13.03	74.84°
0.60	0.01888	150	0.26681	14.23	75.79°
0.70	0.01773	132	0.26754	14.97	76.59°
0.80	0.01759	125	0.27767	15.04	76.86°

The neutral point of the traveling disturbances is found between x_1/c=0.050 and x_1/c=0.055 for a spanwise wavelength of λ_{x_2}=8.43 mm and a frequency of f=268 Hz. In order to determine the most amplified traveling disturbance according to its spatial growth in the downstream direction, the behavior of the locally most unstable frequencies is investigated with a linear PSE computation. Therefore, disturbances of different frequencies and wavelengths are introduced separately at x_1/c=0.05, and their evolution downstream is computed. The wavelengths for this analysis are chosen corresponding to the results for the most amplified stationary disturbances.

Table 6.5 shows the maximal N-factors based on the u_1-component for disturbances of different wavelengths and frequencies. Since the growth of the stationary and traveling disturbances with the wave lengths of λ_{x_2}=11.5 mm, 12.0 mm and 12.5 mm, as

Table 6.5: Maximal N-factors of the most unstable traveling disturbances

	f=160 Hz	f=170 Hz	f=176 Hz	f=178 Hz	f=180 Hz	f=190 Hz
λ_{x_2}=11.5 mm	15.258	15.296	15.314	15.317	15.318	15.301
λ_{x_2}=12.0 mm	15.440	15.468	15.480	15.481	15.479	15.460
λ_{x_2}=12.5 mm	15.493	15.532	15.535	15.532	15.527	15.473

well as with frequencies in the range of f=176 - 180 Hz is very similar, the disturbances with λ_{x_2}=12.0 mm and f=178 Hz will be specified as the most amplified disturbances from now on. This choice is in agreement with the experimentally observed values (see Bertolotti [61]).

Comparing the linear evolution of the most amplified stationary and traveling disturbances in figure 6.13, it is seen that the traveling disturbances are much more unstable. The maximal N-factor for the stationary disturbances is N$\simeq$10 compared to N$\simeq$16 for the most unstable traveling disturbance. Further, the maximal growth rate is about 60% higher for the traveling disturbance.

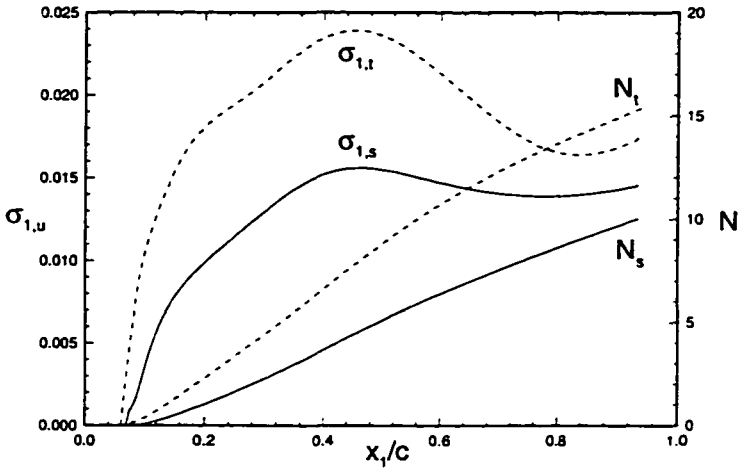

Figure 6.13: Growth rates and N-factors for the most unstable disturbances from a PSE computation

Next, a linear PSE computation is performed for the most amplified stationary wavelength of λ_{x_2}=12.0 mm. Figure 6.14 shows a comparison of the computational results with measured data of Deyhle and Bippes [2]. The results are presented for the velocity components in the directions tangential and perpendicular to the inviscid streamline. Both the locally parallel and linear PSE computation capture the essential features of the measured disturbance profiles like the triple peak structure and the

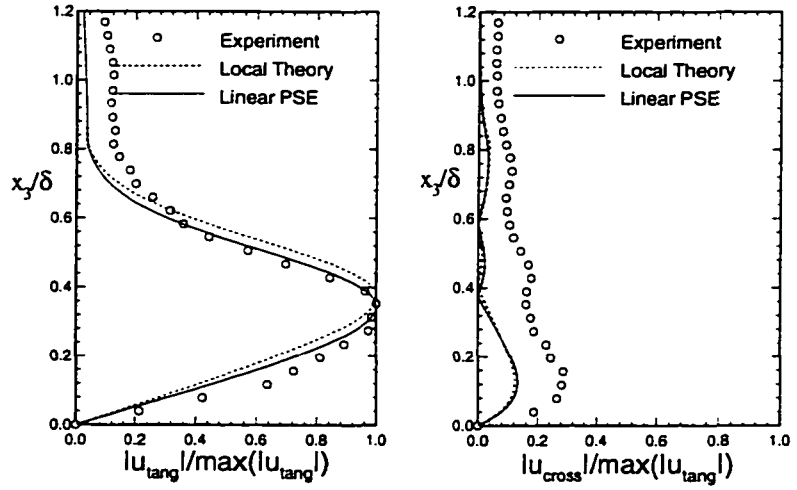

Figure 6.14: Stationary disturbance profiles from experiment and computation at x_1/c=0.60

maximum location of the cross flow component very well. Despite the good qualitative agreement of the computed crossflow component with the experimental results, one notes that the magnitudes obtained from measurement and computation differ by a factor of two. This was also reported by Deyhle and Bippes and is attributed to measurement uncertainties because of the existence of spanwise velocity gradients in the crossflow component of the mean flow [2]. Further, the local theory is predicting a slightly too high peak location of the tangential component, whereas the linear PSE matches the experimental data better.

Concluding the linear stability analysis, results from a local analysis are compared with experimental data by Deyhle et al. [18]. Their experiment (experiment II) was performed for the same experimental setup and outer flow distribution as described for experiment I, but for a different Reynolds number and without the use of roughness elements near the leading edge. The freestream conditions are listed in table 6.6.

Table 6.6: Freestream conditions for experiment II

Chord length c	0.5 m
Freestream velocity Q^*_∞	20.5 m/s
Reynolds number Re_∞	630,000
Sweep angle ϕ_∞	43.5^o
Kinematic viscosity ν	$16.270 \cdot 10^{-6}$ m^2/s

This experiment was mainly motivated by the need of experimental data for a comparison of the disturbance propagation direction with the results of the linear theory. Therefore, they mounted a rotatable insert holding an array of 10 hotfilms at a streamwise location of x_1/c=0.70 into the swept flat plate and measured the wave angle, the wavelength, the phase speed and group velocity, as well as the direction of the group velocity for disturbances of three different frequencies. For details of the experimental setup and the measurement techniques, the reader is referred to [18].

The relevant mean flow parameters at x_1/c=0.7 are Re=527.1, Θ=47.5° and U_e^*=12.91 m/s for the Reynolds number in the chordwise direction, the angle of the inviscid streamline and the chordwise outer velocity component, respectively. In the performed local stability analysis, the wave angle, the wavelength and the phase speed are computed by solving the spatial eigenvalue problem. Considering the temporal eigenvalue problem, the group velocity is computed. The quantities are determined according to the definition in equations 6.4, 6.5 and 6.6, or as in figure 6.8 for the wave angle Ψ. The generally complex vector of the group velocity is real at points of maximal amplification [22] and consists of the components given in equation 6.5. In the following, the procedure to determine the group velocity will be described. First, an eigenpair ω_0,

$$\lambda = \frac{2\pi}{\sqrt{\alpha_{1,\text{real}}^2 + \beta_1^2}} = \frac{2\pi}{|\mathbf{k}_{\text{real}}|}\,,\quad C_{\text{ph}} = \frac{\omega}{|\mathbf{k}_{\text{real}}|} \tag{6.4}$$

$$\mathbf{C_{gr}} = \left\{ \left(\frac{\partial \omega}{\partial \alpha_{1,\text{real}}} \right)_{\beta_1=\text{const.}}, \left(\frac{\partial \omega}{\partial \beta_1} \right)_{\alpha_{1,\text{real}}=\text{const.}} \right\}^T \tag{6.5}$$

$$C_{gr} = |\mathbf{C_{gr}}| = \sqrt{\left(\frac{\partial \omega}{\partial \alpha_{1,\text{real}}} \right)^2_{\beta_1=\text{const.}} + \left(\frac{\partial \omega}{\partial \beta_1} \right)^2_{\alpha_{1,\text{real}}=\text{const.}}} \tag{6.6}$$

$\beta_{1,0}$ and $\alpha_{1,0}$ is determined such that the growth rate is maximal. For this first step, the spatial eigenvalue problem is solved. Second, $\alpha_{1,0}$ is incremented and a new eigenpair ω_1, $\beta_{1,0}$ and $\alpha_{1,1}$ is found from the temporal approach. Third, $\beta_{1,0}$ is incremented and another eigenpair ω_2, $\beta_{1,1}$ and $\alpha_{1,0}$ is determined from the temporal eigenvalue problem. Now, the components of the real group velocity vector can be computed from the results of steps two and three, and the locus of the group velocity is formed according to equation 6.6.

In figure 6.15, the wave angle Ψ relative to the angle of the inviscid streamline, the phase speed C_{ph} and the group velocity C_{gr} are plotted for both unstable disturbance families. The symbols denote different experimental runs and the numbers of the hotfilms

(HF) the plotted data points were measured with. The results are presented for the most unstable wave at a fixed frequency. Between the two modes with positive and negative β_1, the mode with a positive spanwise wave number has the largest growth rate. It is this family with a positive β_1 that seems to match the experimental results reasonably well. The results obtained by the spatial eigenvalue problem show a better agreement with the experiment than for the temporal group velocity results. However, Deyhle et al. [18] report experimental uncertainties in determining the group velocity, which might also account for the deviations in these results.

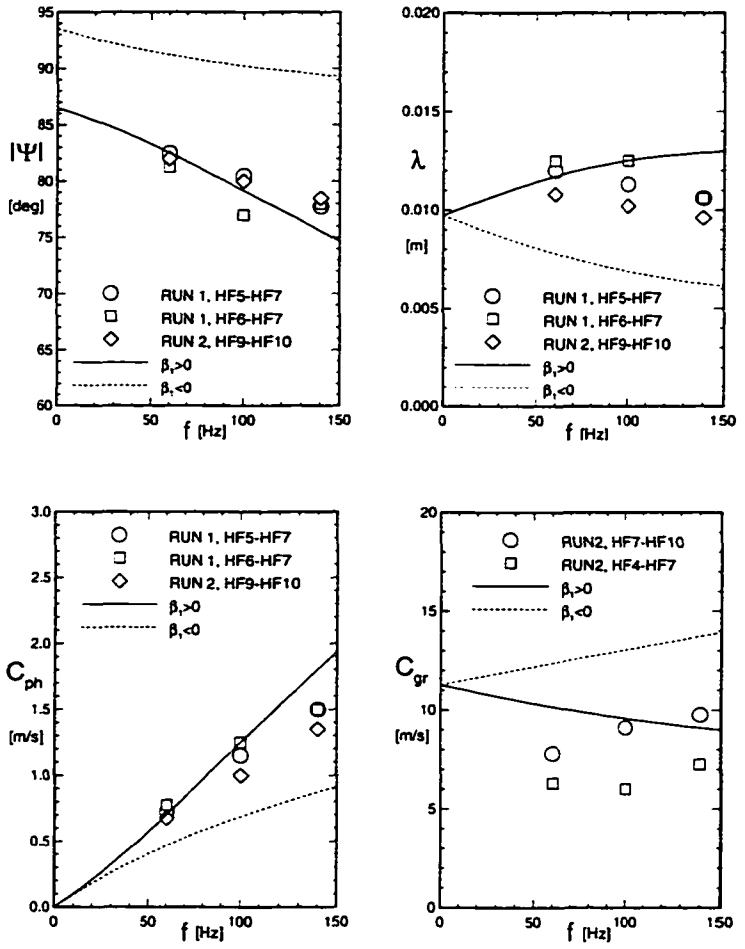

Figure 6.15: Wave angle, wavelength, phase speed and group velocity from a local analysis and the experiment at x_1/c=0.70

6.3.2 Nonlinear Analysis

In this subsection, experiment I will be reconsidered. Having determined the most amplified stationary and traveling disturbances from a detailed linear stability analysis in the previous subsection, the nonlinear interaction of these disturbances will be investigated next. Since the present PSE formulation does not include the receptivity to freestream turbulence or surface roughness, the initial amplitudes of the disturbances are matched with those given by Bertolotti [61] at x_1/c=0.1 in order to account for the presence of the roughness elements. Here, the amplitude is defined as $A = |u_1|_{max}/U_\infty$. For a choice of $A_{s,u} = 0.04\%$ at the location where the disturbances are introduced, the same value for the averaged disturbance component along the inviscid streamline $u_{tang,avg} = (u_{tang,max} - u_{tang,min})/2$ at x_1/c=0.1, as shown by Bertolotti [61], is obtained. The subscripts max and min stand for the maximum and minimum value of an average in the spanwise direction. Figure 6.16 shows both the calculated linear and nonlinear

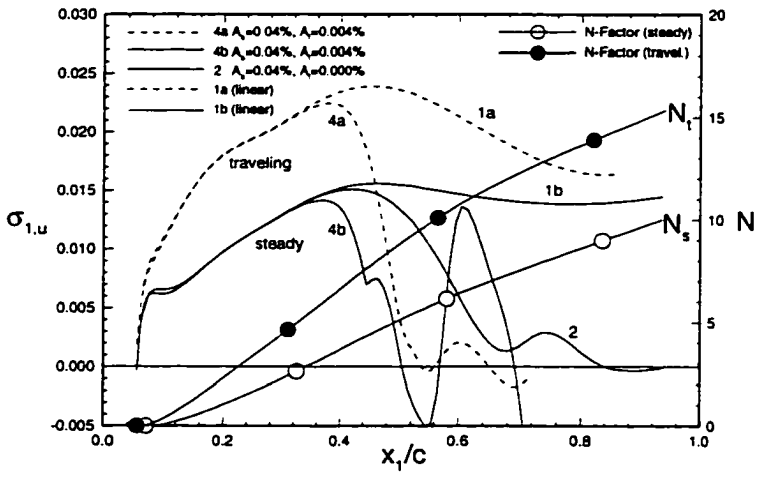

Figure 6.16: Linear and nonlinear growth rates and N-factors (λ_{x_2}=12 mm, f=178 Hz)

growth rates, as well as the N-factors for the most amplified modes. The obtained values for the most amplified spanwise wavelength λ_{x_2}=12 mm, the most amplified frequency

f=178 Hz, and the maximum N-factor of N≃16 for the traveling disturbance agree with previous work [61]. For the nonlinear computations in this section, eight modes in the spanwise direction and four modes for the frequency are included. Shown in figure 6.17 are the measured and computed evolution of the disturbance amplitudes along the

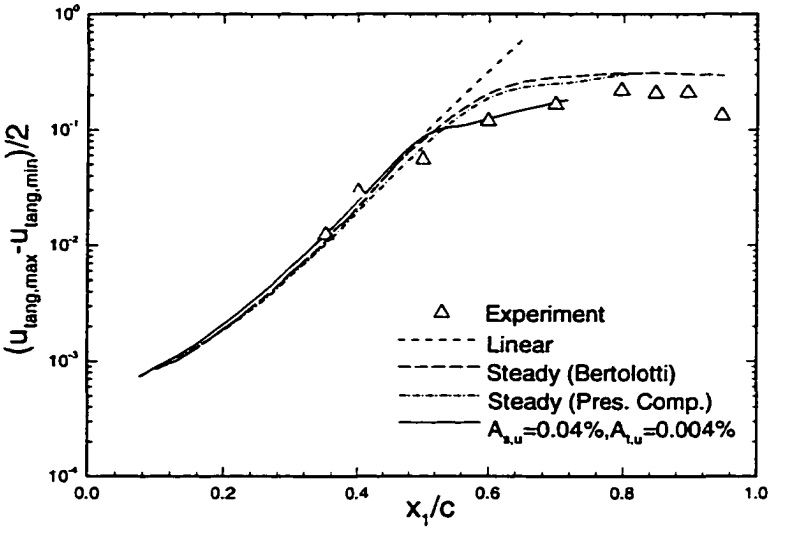

Figure 6.17: Amplitude growth from experiment and computation

chord. As reported by Bertolotti [61] and previously in Section 5.3, it is seen from figure 6.17 that the purely stationary disturbance saturates at a higher amplitude level and a later streamwise location than in the experiment. Therefore, a small amplitude traveling disturbance with the most amplified frequency of f=178 Hz is included in the computations ($A_{t,u}$=0.004%). It is observed that the saturation onset is now predicted slightly late, but the experimental saturation amplitude is matched well. Also, a strong secondary growth of the stationary disturbance in the case where stationary and traveling disturbances interact is seen in curve 4b of figure 6.16. This secondary growth also shows in the amplitude evolution in figure 6.17 and seems to be evident in the experimental data as well.

Next, the spatial development of the crossflow vortices is described. Figure 6.18 shows the u_1-disturbance component at x_1/c=0.5, 0.6, and 0.7 for both the purely sta-

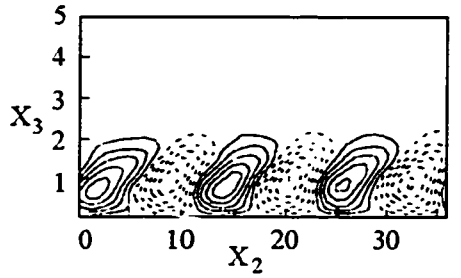

Experimental result at x_1/c=0.60 (dashed lines are negative, from [61])

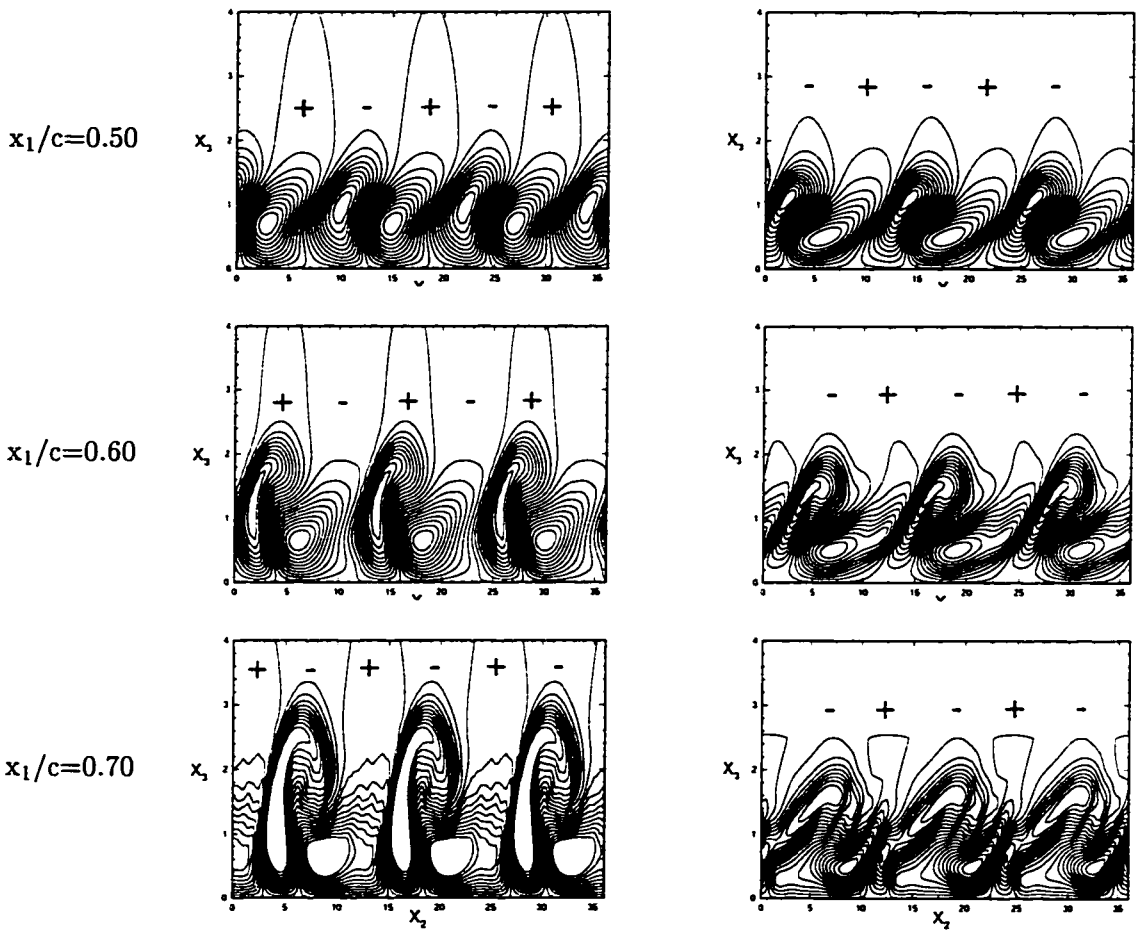

Figure 6.18: Chordwise disturbance quantity u_1 from experiment and computation

tionary and the interaction case, as well as the experimental data at x_1/c=0.6. It can be seen that the purely stationary vortices from the computation at x_1/c=0.6 are further developed than the measured vortices. Both their extension in the normal direction and their degree of distortion are over-predicted. In the interaction case, however, the normal extension of the vortices has decreased to the experimental value, but the structure of the vortices is more distorted than shown in the experimental results. This difference may be attributed to the longer growth of the disturbances in the computation that results into an earlier roll-over of positive and negative disturbance components.

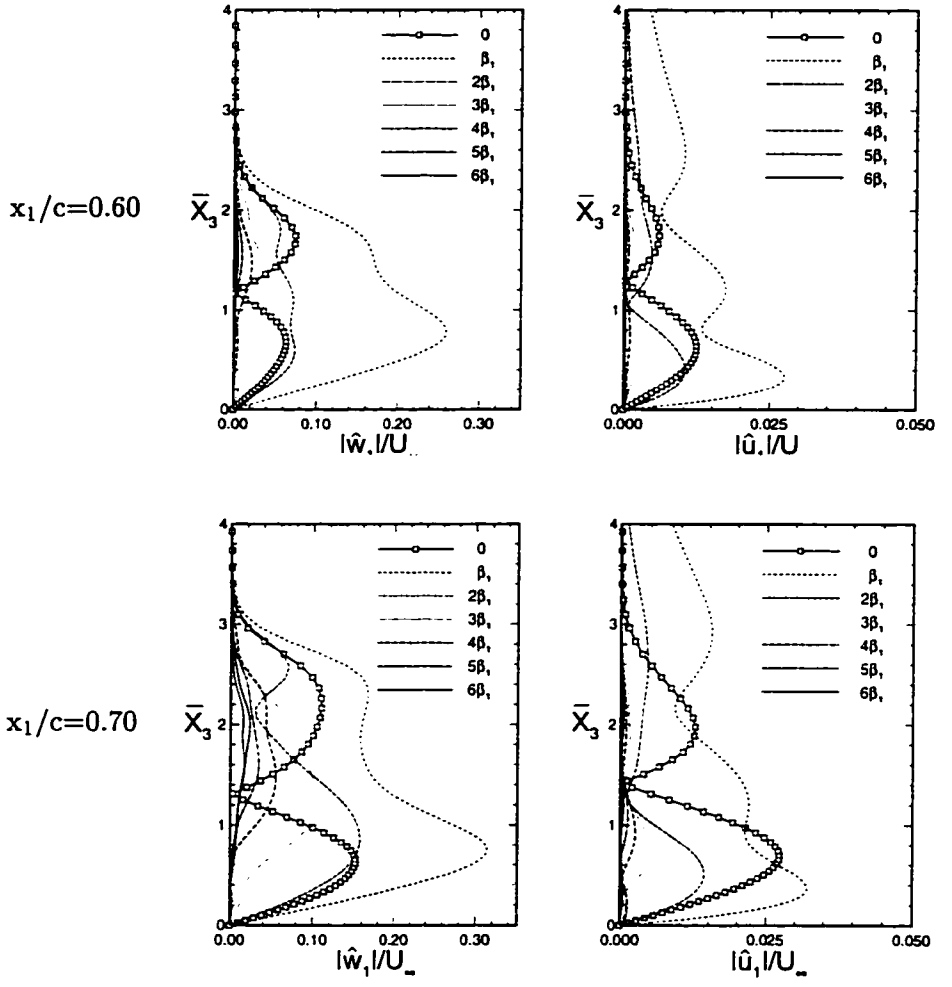

Figure 6.19: Shape functions of the individual modes at two streamwise locations

In order to further describe the purely stationary vortex that will be investigated for its instability to three-dimensional high-frequency secondary disturbances in the next section of this chapter, the shape functions of the individual modes and the total velocity component tangential to the stationary vortex are shown at different spanwise positions in figures 6.19 and 6.20, respectively. There, u_1 and w_1 are the velocity components in the Galilean coordinate system, oriented perpendicular and tangential to the constant phase lines. For the two selected streamwise positions, it can be seen in figure 6.17 that the stationary disturbances are about to saturate at $x_1/c=0.6$ where they reach

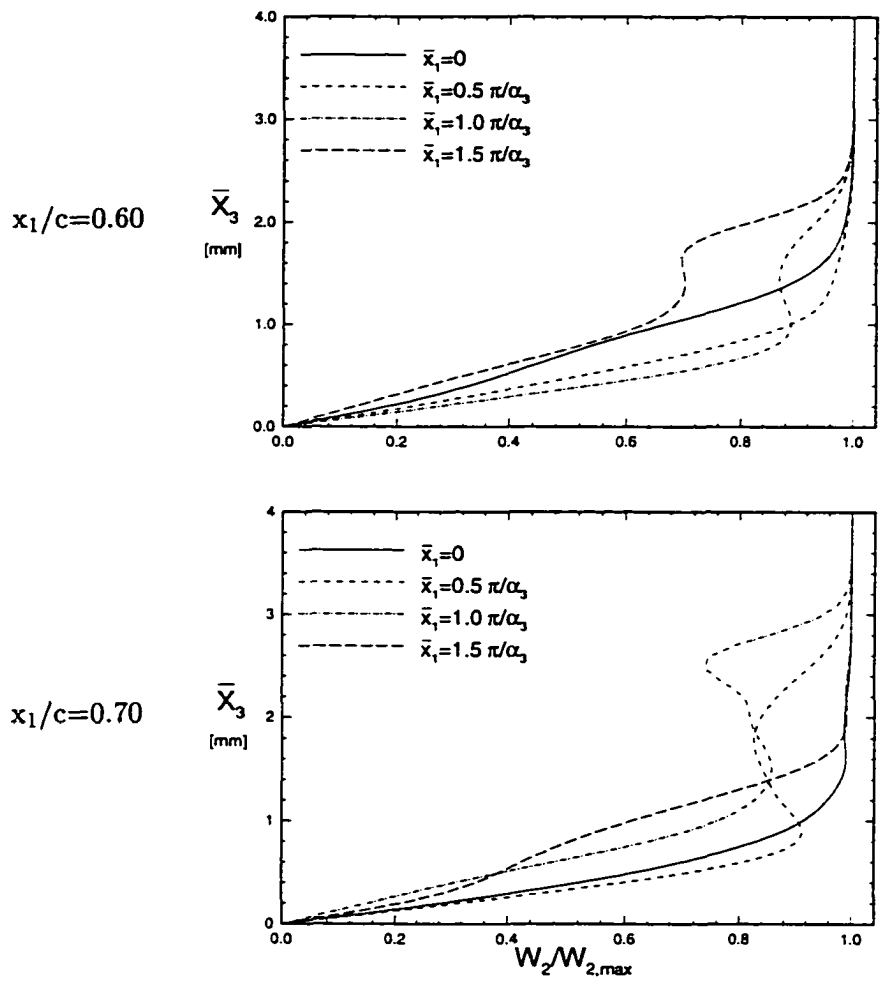

Figure 6.20: Total flow quantity tangential to the constant phase lines

amplitude levels of $A_{s,u} \simeq 20\%$. At x_1/c=0.7, however, they are fully saturated at an amplitude level of $A_{s,u} \simeq 30\%$. As also observed for Swept Hiemenz Flow in Section 5.3, figure 6.20 shows that highly inflectional profiles are present at both streamwise locations. Comparing the results presented in figure 6.19 with the shape functions for Swept Hiemenz Flow in figure 5.16, one notes the very similar shape and even magnitude of the individual shape functions in this region of nonlinear saturation of the stationary crossflow vortex.

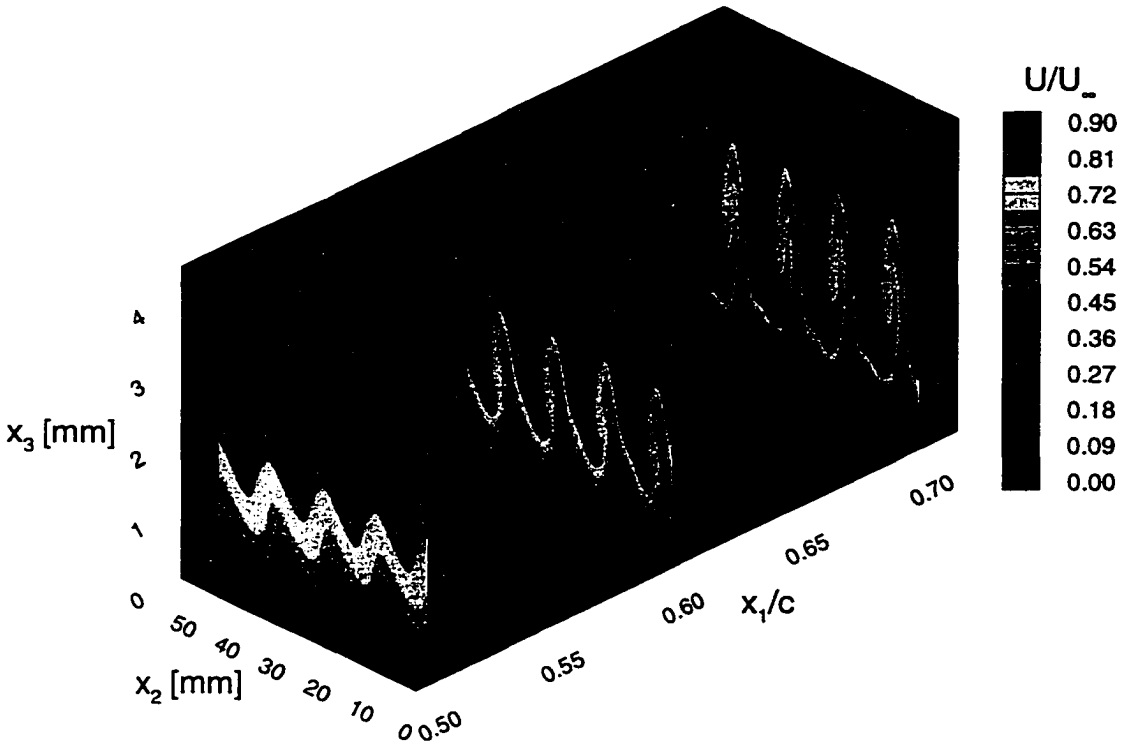

Figure 6.21: Evolution of crossflow vortices (Stationary vortex)

Summarizing the previous plots and visualizing the spatial development of the flow in the region of nonlinear saturation, the development of the crossflow vortices for both the purely stationary and the interaction case is plotted in figures 6.21 and 6.22. Shown are the contours of the total velocity component in the chordwise direction in

the region between 50% and 70% chord length, where the nonlinear interaction of the disturbance components dominates the physics of the flow. Clearly observed are the developing distortion of the boundary layer at x_1/c=0.50, and the roll-up of the vortices in the positive spanwise direction in the purely stationary case.

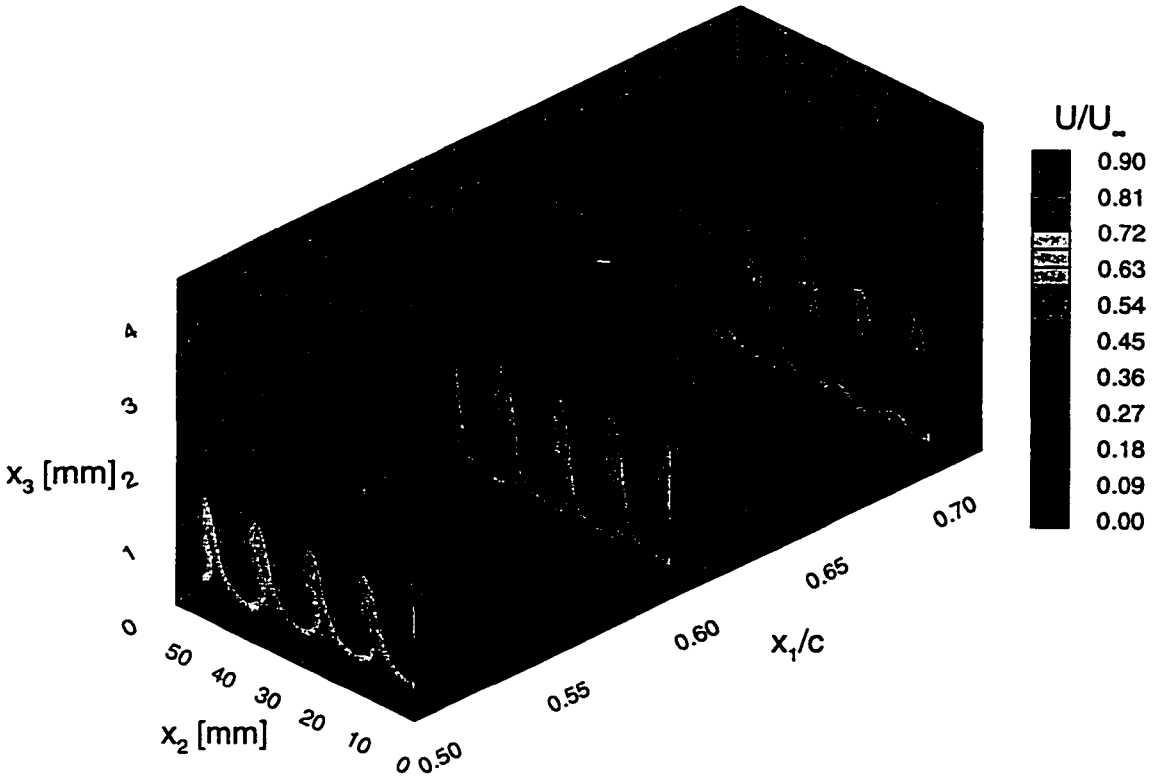

Figure 6.22: Evolution of crossflow vortices (Interaction case at T=0)

Finally, the footprint of the crossflow instability on the surface of the swept flat plate is visualized in figure 6.23. Shown is the experimental result obtained using an oil flow-visualization technique in comparison with the numerical result. In figure 6.23, the plotted disturbance vorticity pattern at the wall caused by a stationary crossflow vortex is obtained using equation 5.18. Even though there is some fine detail missing in the computational results for the later chordwise positions, the experimentally observed spacing and alignment of the vortex streaks are captured very well.

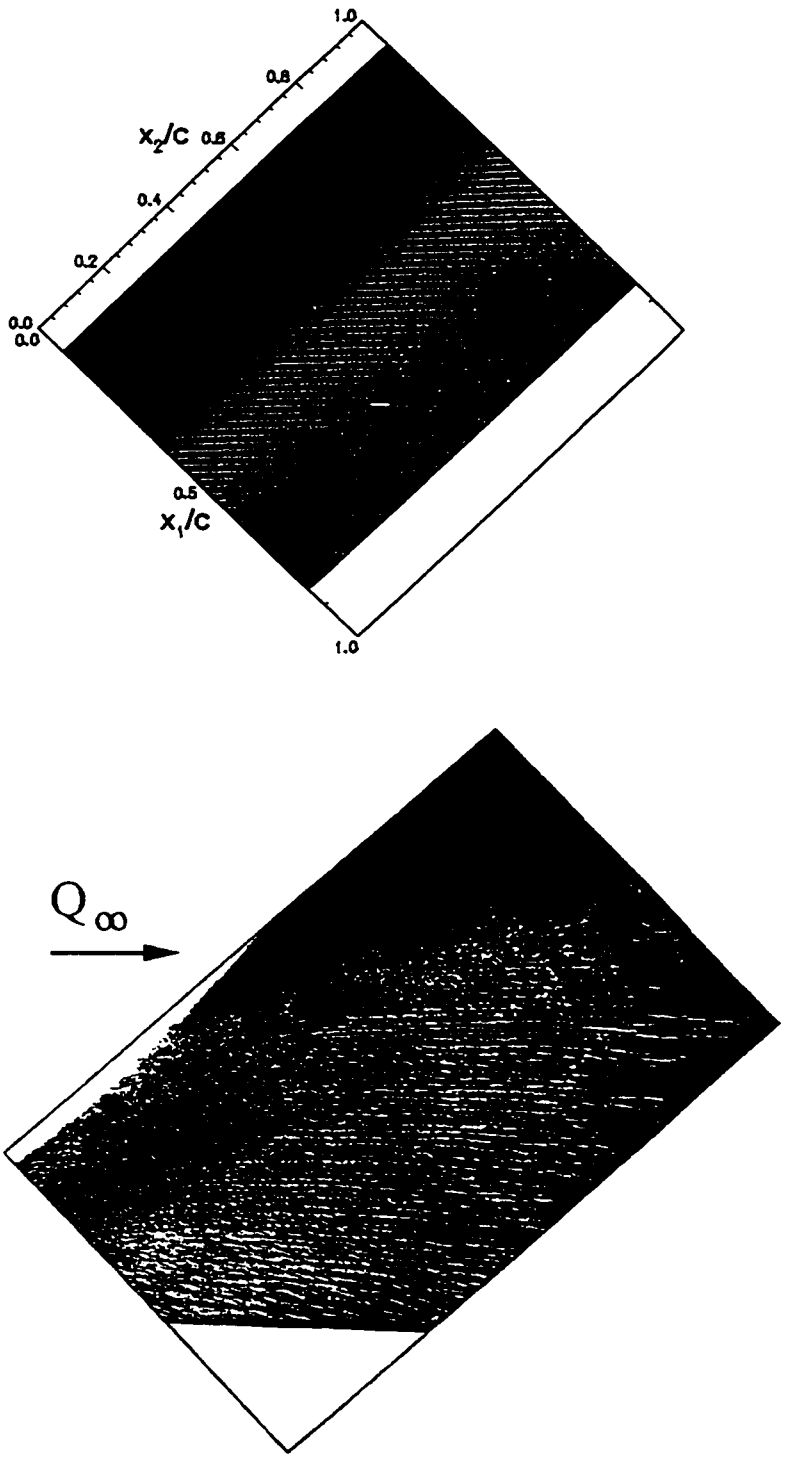

Figure 6.23: Oil flow-visualization of the crossflow instability in the DLR Transition experiment (from [3]) and the computed wall vorticity pattern

6.4 Secondary Stability Analysis

This section presents the results from a secondary instability analysis of a basic flow that is modified by the existence of a stationary crossflow vortex. In particular, the purely stationary case of the experiment I studied in the previous section will be reconsidered. Temporal analyses using Floquet Theory are performed at the two chordwise locations x_l/c=0.6 and x_l/c=0.7. At x_l/c=0.6, the averaged stationary disturbance component tangential to the inviscid streamline $u_{tang,avg}$ with an initial amplitude of $A_{s,u} \simeq 0.1\%$ at x_l/c=0.1 has reached an amplitude level of $A_{s,u} = 20\%$ and is almost saturated. Even though some moderate secondary growth of the purely stationary disturbance is observed beyond x_l/c=0.7 (see curve 2 in figure 6.16), $u_{tang,avg}$ is considered fully saturated at x_l/c=0.7 at an amplitude level of $A_{s,u} = 25\%$.

Special attention will be directed towards the existence of multiple eigenvalues in the considered region of nonlinear saturation. Deyhle and Bippes [2] report from their experiments in a water towing tank an almost explosive growth of unsteady modes that immediately leads to transition. In [2], they compare this explosive growth to a bursting of individual stationary vortices. Additionally, they mention the appearance of high-frequency disturbances riding on the primary disturbances from the measurements in the experiment considered here (experiment I). The measured frequency of these traveling disturbances is specified as f=2100 Hz.

The computational grid for these computations is similar to the grid used in the Swept Hiemenz flow analysis. The boundary conditions are enforced at about seven boundary layer thicknesses, and a total number of 81 points is distributed in the domain according to grid stretching equation 5.12. Table 6.7 shows the results of a grid refinement study at x_l/c=0.6. The results for the temporal wave number σ_3 obtained

for different iteration options vary only in the fourth decimal place, and thus, the grid resolution is considered satisfactory.

Table 6.7: Grid study at x_1/c=0.6, α_3=-0.201, β_3=0.35, Mode=1

Δ-Grid	Points	Equation	$\bar{x}_{3,max}$	Mode	σ_3
8	71	continuity	44	-1	(0.018000,-0.919902)
6	71	continuity	42	-1	(0.018152,-0.919944)
10	71	continuity	46	-1	(0.018299,-0.919952)
8	81	continuity	45	-3	(0.018195,-0.919669)
6	81	continuity	43	-3	(0.018187,-0.919800)
8	81	continuity	45	-1	(0.018195,-0.919669)
6	81	continuity	43	-1	(0.018187,-0.919800)

Pursuing the sequence of global and local eigenvalue computations as described in Section 4.4, the chordwise location of x_1/c=0.6 is examined first. It turns out that there exist more unstable eigenvalues at this location than found for Swept Hiemenz flow. The unstable eigenvalues appear densely clustered in the wave number range between β_3=0.1 and β_3=0.4 corresponding to the wide frequency range of f=500 Hz up to f=4000 Hz. The results for the secondary growth rates and frequencies of three selected modes are plotted in figures 6.24 and 6.25. The development of the eigenfunctions with a varying wave number tangential to the constant phase lines β_3 was followed closely in order to assure that the plotted eigenvalues indeed belong to the same family of unstable secondary eigenmodes. In contrast to the Swept Hiemenz Flow problem, where neither multiple eigenvalues, nor crossing growth rate curves could be found at the investigated locations, it can be seen in figure 6.24 that the given growth rate curves of the different modes cross. This indicates that the absolutely unstable modes found by Koch [68] for Blasius boundary layer flow might be also present in this three-dimensional boundary layer flow. Table 6.8 lists the secondary growth rates, the wave numbers β_3, the wave angles of the secondary disturbances according to the definition in Section 4.4, as well as the dimensional frequencies at the points of maximal amplification for the considered

modes. Here, α_3 denotes the wave number in the $\bar{x}_1$-direction of the Galilean coordinate system (see Chapter 4.4). It is observed that the wave angles of the most amplified secondary disturbances agree with the results for Swept Hiemenz flow.

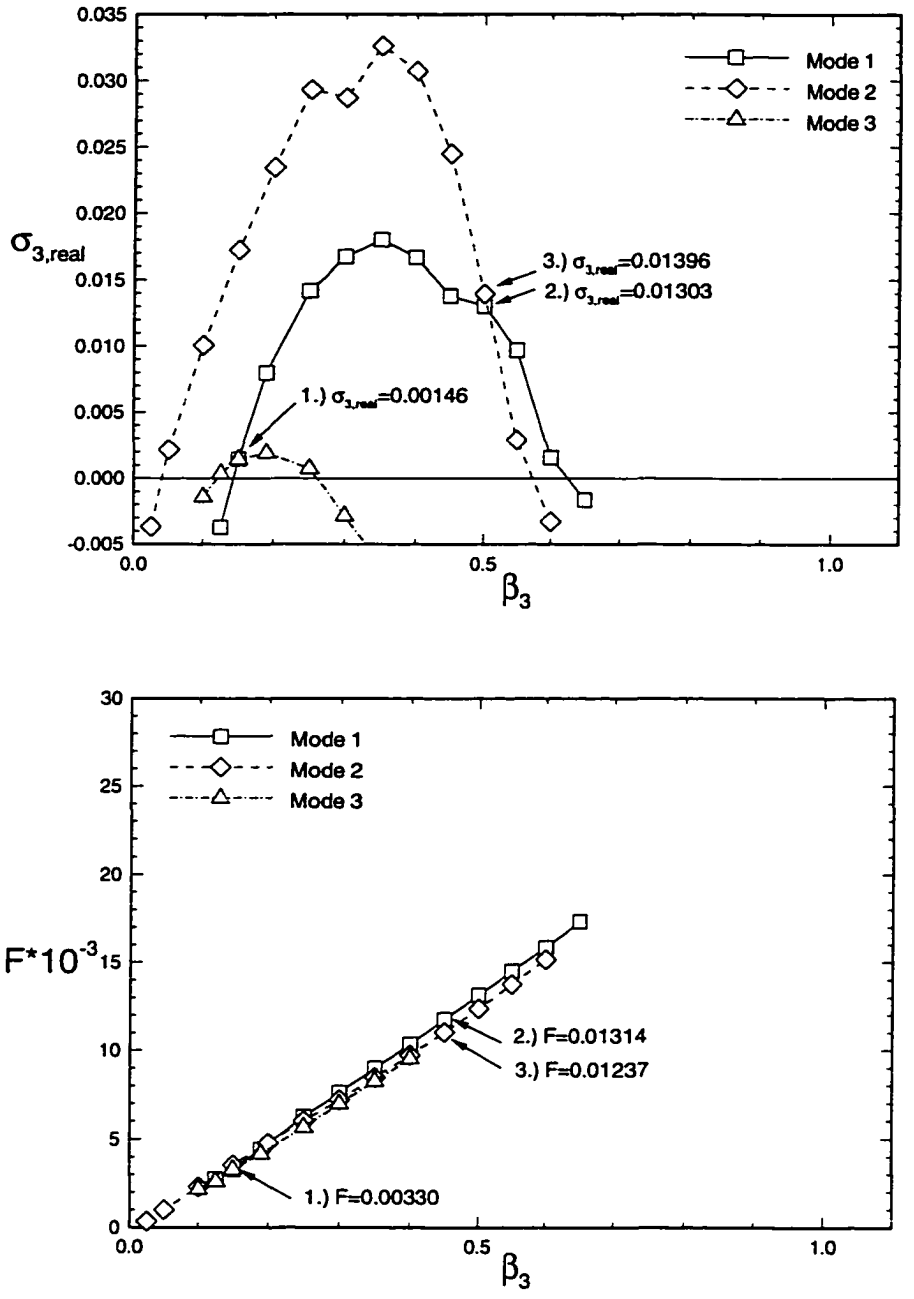

Figure 6.25: Secondary frequencies at x_1/c=0.6

Table 6.8: Parameters for the most unstable modes at x_1/c=0.6, (α_3=-0.201)

	$\sigma_{3,max}$	$\beta_{3,\sigma_3=max}$	$\Psi_{2,\sigma_3=max}$	$f_{\sigma_3=max}$ [Hz]
Mode 1	0.018001	0.35	-29.9°	3117
Mode 2	0.032616	0.35	-29.9°	2933
Mode 3	0.001906	0.19	-46.6°	1451

Further, figure 6.26 shows the total shape functions of the most unstable secondary modes at x_1/c=0.6. Plotted are the normalized shape functions of the disturbance velocity components for the most amplified wave numbers β_3. Comparing the shape functions of the unstable modes in the Swept Hiemenz flow problem at Re=546 and β_3=0.8 (see figure 5.25) with the shape functions shown in figure 6.26, the following is noted. First, the shape functions at Re=546 are fuller than the profiles obtained here.

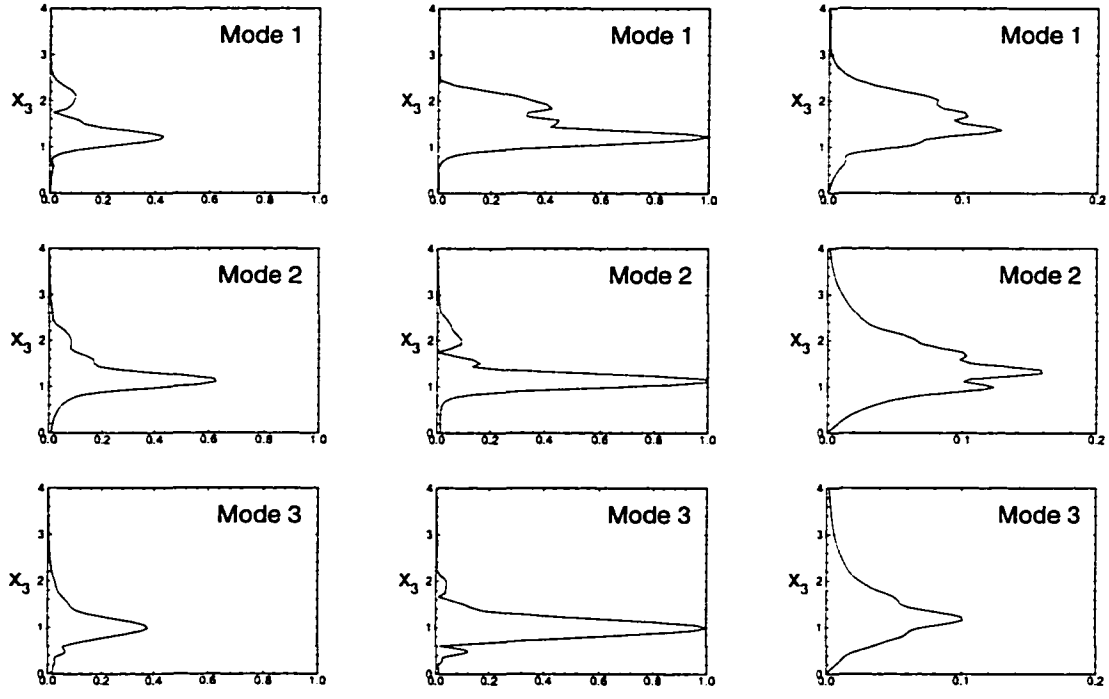

Figure 6.26: Total shape functions of the most unstable modes at x_1/c=0.6, (α_3=-0.201, normal axis in millimeters)

This is attributed to the higher amplitude level of the stationary disturbances in the Swept Hiemenz flow problem ($\hat{A}_{s,u}$=24% at Re=546; $A_{s,u}$=20% at x_1/c=0.6). Second, all the shape functions at x_1/c=0.6 show a strong maximum at a height of $\bar{x}_3 \simeq 1$ mm, which is equivalent to about 30% of the boundary layer thickness at this location and can be interpreted as a formation of shear layers near $\bar{x}_3 \simeq 1$ mm.

From figure 6.25 and as observed for Swept Hiemenz flow, it appears that a linear frequency dependence on the wavenumber β_3 can serve as a first guess for a distinction of the different modes. For closely clustered eigensolutions, however, only an additional comparison of the eigenfunctions can be a conclusive test. It is also noted from figure 6.25 that the frequency curves of Modes 1 and 3 cross at the same wave number $\beta_3 = 0.15$ as the corresponding growth rate curves in figure 6.24 (see Point 1.). Hence, the existence of a multiple eigenvalue at this wave number needs further investigation. The temporal wave number at the location where Modes 1 and 3 cross is σ_3=(0.00146,-0.33792). This corresponds to a dimensional frequency of f=1145 Hz, which is about six times the most amplified frequency. In contrast, the dimensional frequencies at the σ_3-locations where Modes 1 and 2 cross at $\beta_3 = 0.5$ are f=4561 Hz and f=4291 Hz for Mode 1 and 2, respectively. Even though the growth rates are similar at this wave number, the difference in the frequency is considered too large to suspect a multiple root there.

In figures 6.27 - 6.29, the eigenfunctions of the two crossing Modes 1 and 3 of figure 6.24 are plotted at three wave numbers at and near the point of their crossover. It is seen that the shape functions of all disturbance quantities are very similar close to the crossover location at β_3=0.15. Further, the development of the shape functions of both modes with an increasing wave number tangential to the constant phase lines indicates

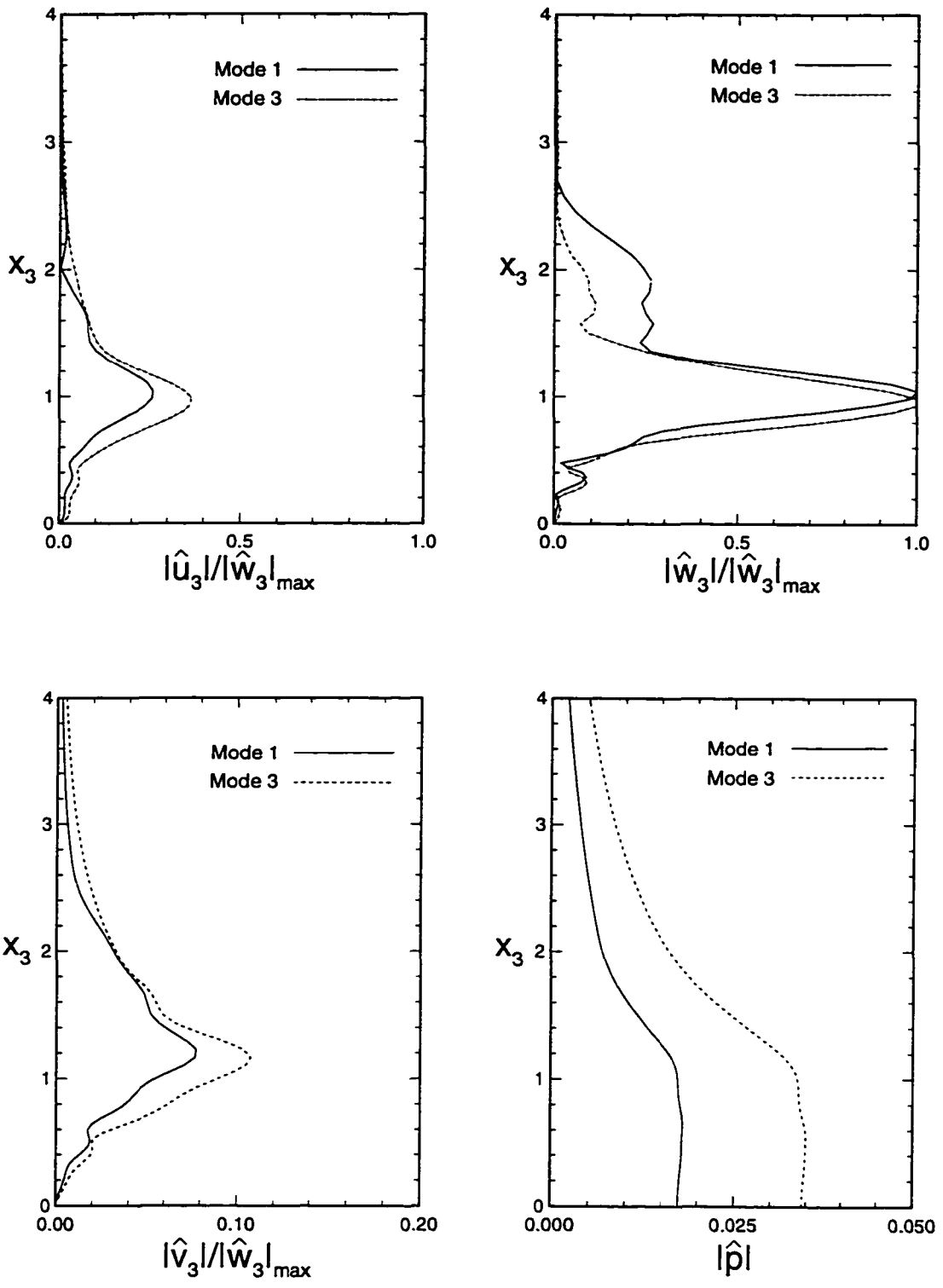

Figure 6.27: Total shape functions near the multiple eigenvalue at x_1/c=0.6, (α_3=-0.201, β_3=0.125, normal axis in millimeters)

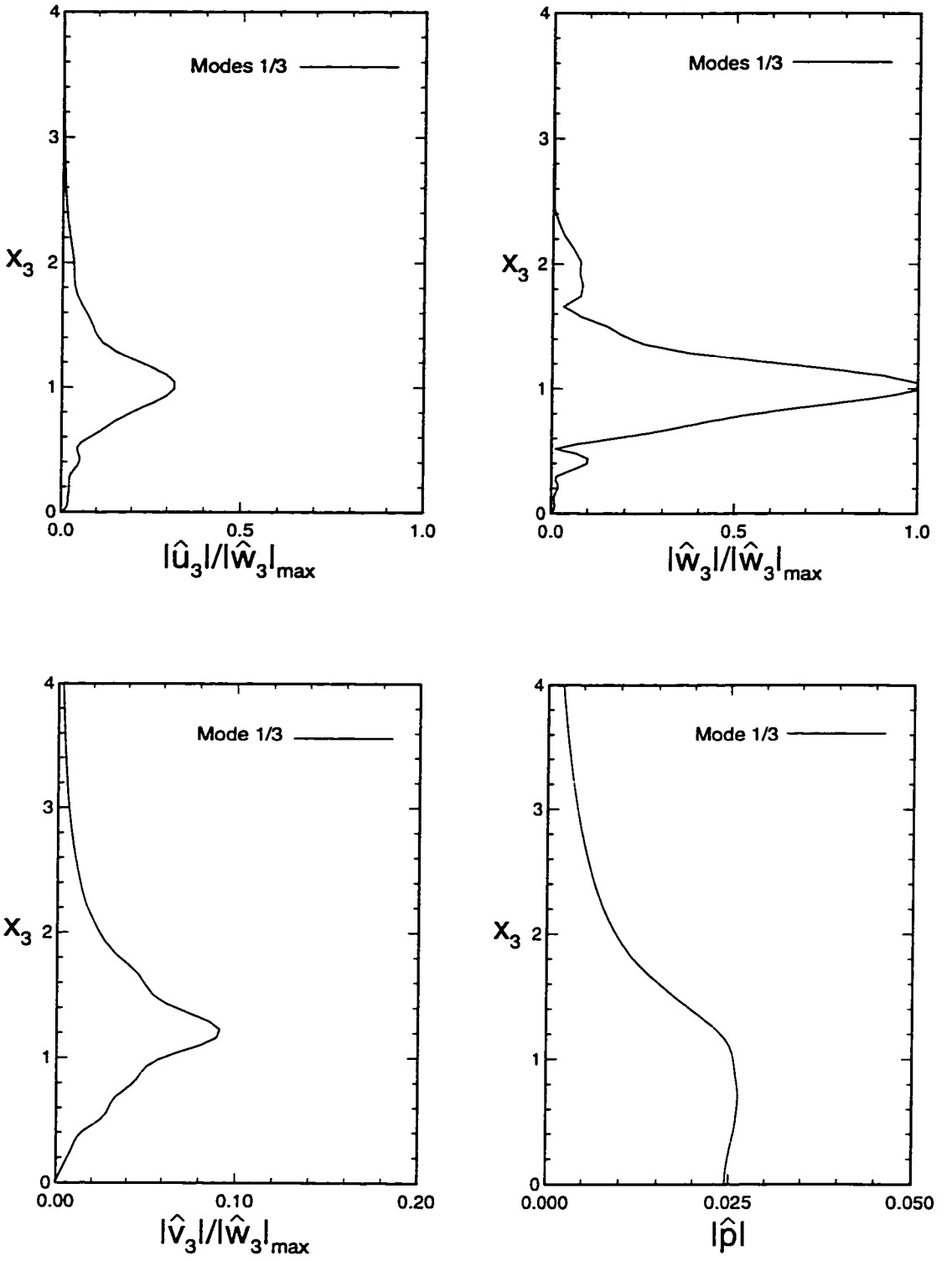

Figure 6.28: Total shape functions of the multiple eigenvalue at x_1/c=0.6, (α_3=-0.201, β_3=0.150, normal axis in millimeters)

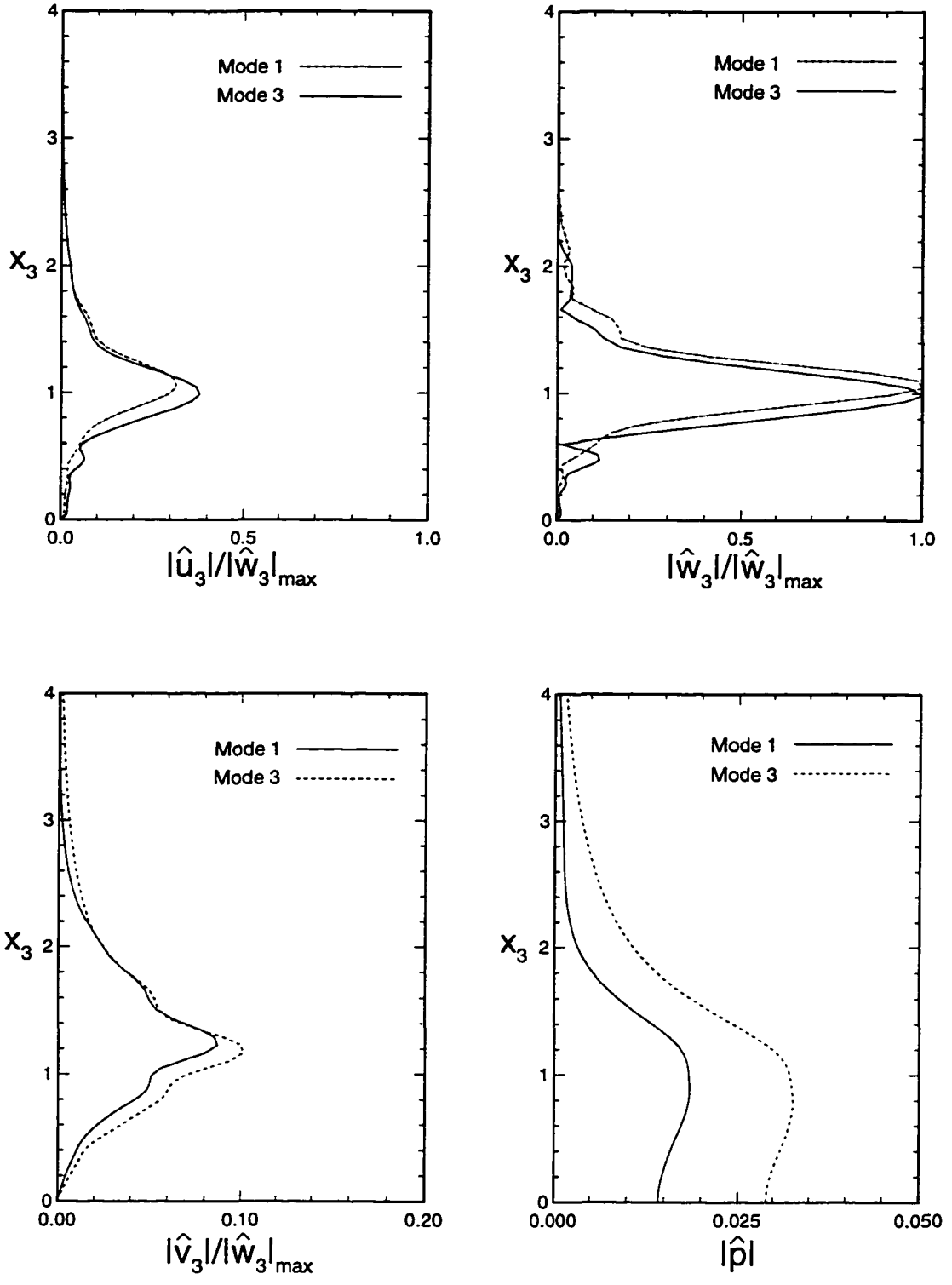

Figure 6.29: Total shape functions near the multiple eigenvalue at x_1/c=0.6, (α_3=-0.201, β_3=0.190, normal axis in millimeters)

that the two modes indeed coincide. Hence, the existence of a multiple eigenvalue at $x_1/c=0.6$ can be concluded. The experimentally observed time-dependent occurrences of an explosive growth of traveling disturbances might be related to this result. Obviously, the current investigation of a crossflow vortex that originates from a purely stationary disturbances does not fully capture the quantitative features of the experimentally obtained mean flow, since it over-predicts the saturation amplitude (see Section 6.3). However, the same qualitative features as in the previously computed interaction case that matched the experiment well, like a strong spanwise and streamwise distortion of the boundary layer in the studied saturation region, are also present in the purely stationary case.

In order to also examine other points in the flow for the existence of multiple eigenvalues, the chordwise location $x_1/c=0.7$ will be considered next. Investigating the

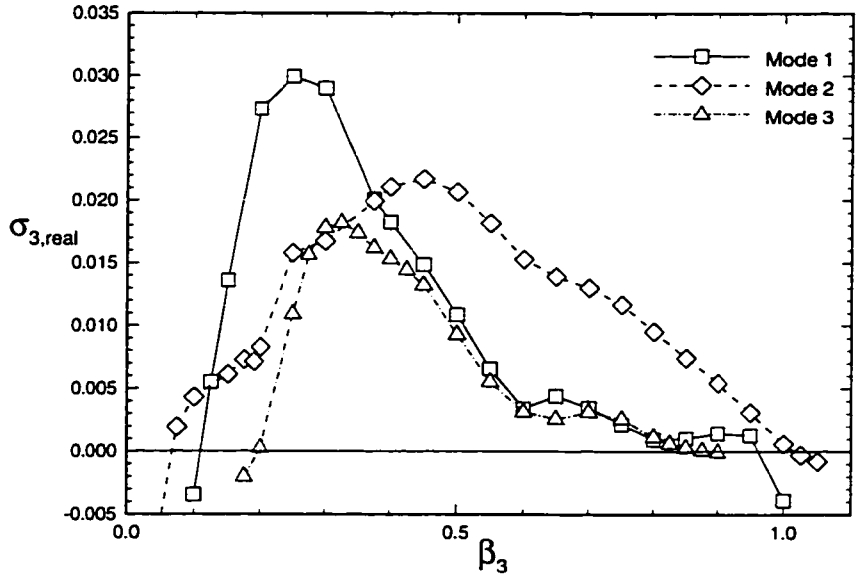

Figure 6.30: Secondary growth rates at $x_1/c=0.7$

same frequency range as at $x_1/c=0.6$, several unstable modes are determined. Out of these, three modes will be examined more closely. Figures 6.30 and 6.31 show the growth

rates and frequencies of those modes. It can be seen that the unstable wave number range increased significantly in comparison to the previously investigated location. On the other hand, the obtained growth rates at $x_1/c=0.7$ are of the same magnitude as

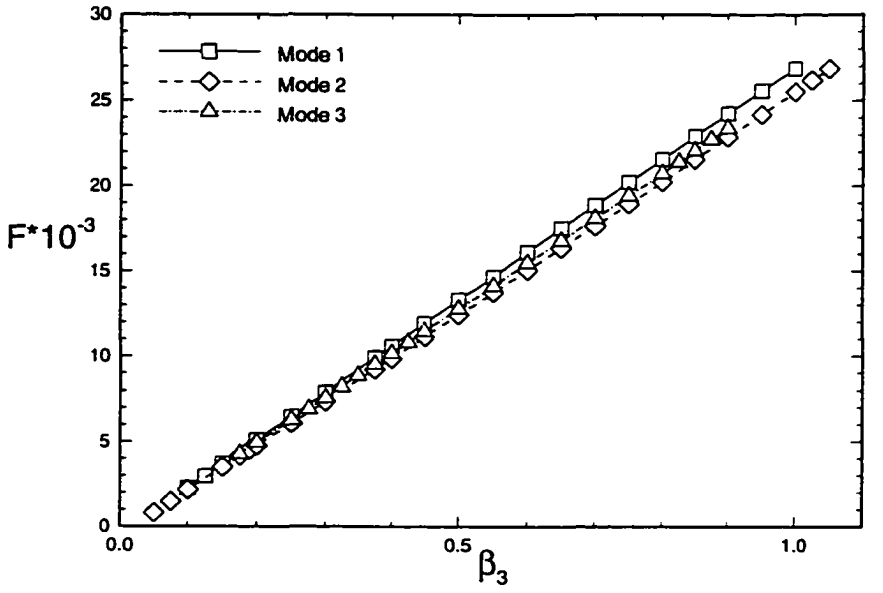

Figure 6.31: Secondary frequencies at $x_1/c=0.7$

the growth rates at $x_1/c=0.6$. This is in contrast to the observed linear growth of the secondary disturbances in the Swept Hiemenz flow problem. However, since there are several unstable eigenmodes present at this chordwise location, the modes considered at

Table 6.9: Parameters for the most unstable modes at $x_1/c=0.7$, (α_3=-0.200)

	$\sigma_{3,max}$	$\beta_{3,\sigma_3=max}$	$\Psi_{2,\sigma_3=max}$	$f_{\sigma_3=max}$ [Hz]
Mode 1	0.029947	0.250	-38.7°	2250
Mode 2	0.021711	0.450	-24.0°	3865
Mode 3	0.018223	0.325	-48.0°	2856

$x_1/c=0.6$ and at $x_1/c=0.7$ might not belong to the same families. Table 6.9 shows the maximal secondary growth rates, the wave numbers β_3, the wave angles of the secondary

disturbances and the dimensional frequencies for the considered modes. As observed at x_1/c=0.6, it is seen that the wave angles of the most amplified secondary disturbances agree with the results for Swept Hiemenz flow. Moreover, the frequency of f=2250 Hz for the most unstable wave number β_3 of Mode 1 is close to the measured frequency of the secondary instability in the experiment (f=2100 Hz) [2].

Next, the total shape functions of the most unstable wave numbers tangential to the constant phase lines at x_1/c=0.7 are shown in figure 6.32. Plotted are the normalized shape functions of the disturbance velocity components. Noted is a strong qualitative

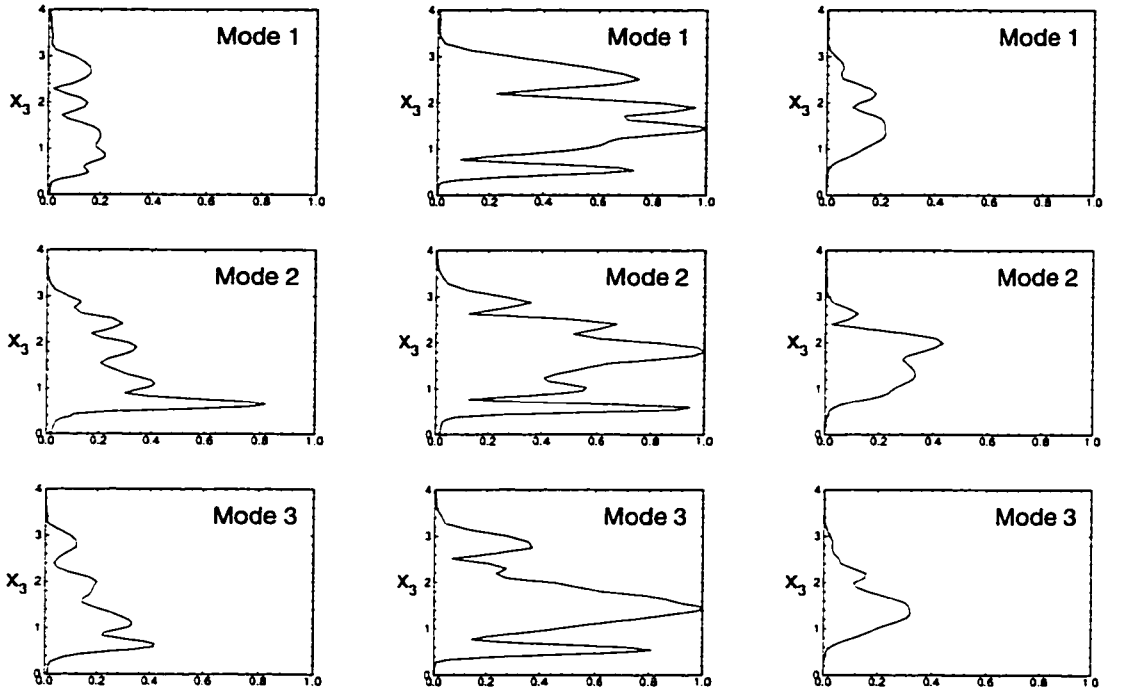

Figure 6.32: Total shape functions of the most unstable modes at x_1/c=0.7, (α_3=-0.200, normal axis in millimeters)

difference between the shape functions at x_1/c=0.6 and at x_1/c=0.7. First of all, the shapes are much fuller at x_1/c=0.7, which might be due to the higher amplitude level of the stationary disturbance at this location. Second, the shapes are much more oscillatory

at x_1/c=0.7. In order to ensure that the obtained results are not due to numerical oscillations, various runs for different grids were performed. It turns out that the plotted shape functions indeed represent grid-independent solutions. Third, the disturbance component of the normal velocity (v_3) is now of the same order as the the disturbance velocity component perpendicular to the stationary crossflow vortex (u_3). A discussion of this qualitative difference between the results for similar modified mean flows for the Swept Hiemenz flow problem and the present investigation is given in the summary of this chapter in Section 6.5.

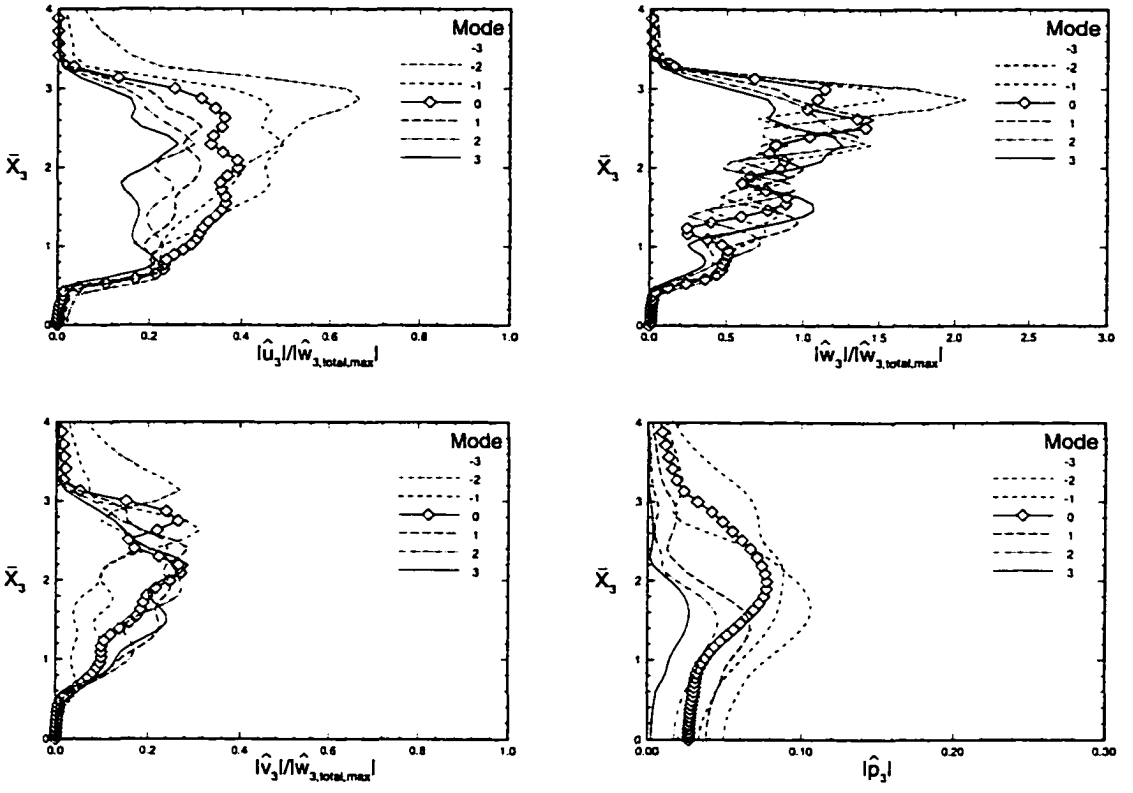

Figure 6.33: Shapes of the secondary instability eigenfunctions for Mode 1 at x_1/c=0.7 (β_3 = 0.25, normal axis in millimeters)

In order to complete the portrait of the most unstable secondary disturbance found at x_1/c=0.7, figure 6.33 shows the shape functions of the individual Fourier com-

ponents for Mode 1 at β_3=0.25. It is seen that the dominant (-2) and (-3) Fourier modes of the wall-parallel disturbance components u_3 and w_3 reach their maximal values at $\bar{x}_3 \simeq 3$ mm, which corresponds to the boundary layer thickness at this chordwise location. Further, particularly the $\hat{w}_3$-disturbance component consists of very oscillatory Fourier components.

Since the growth rate curves of the investigated modes at x_1/c=0.7 show similar crossovers as observed at x_1/c=0.6 (compare figures 6.24 and 6.30), the existence of multiple eigenvalues at the chordwise location of x_1/c=0.7 will be investigated next. As seen from figure 6.30, the growth rate curves of Modes 1 and 2 cross at β_3=0.125 and β_3=0.375, and the curves of Modes 2 and 3 in the range of $\beta_3 \simeq 0.3$. Further, the growth rates of Modes 1 and 3 are similar at $\beta_3 > 0.5$.

However, since the frequency curves are close to each other only for $\beta_3 < 0.4$ (see figure 6.31), the investigation will be restricted to the above three crossover locations. Table 6.10 shows the values of the temporal wave number σ_3 for the relevant modes and wave numbers. The corresponding total shape functions of the disturbance components tangential and perpendicular to the constant phase lines are plotted in figure 6.34.

Table 6.10: Temporal wave numbers σ_3 at crossover points (x_1/c=0.7)

β_3	0.125	0.275	0.375
Mode 1	(0.005516,-0.303645)	-	(0.020089,-1.014967)
Mode 2	(0.005322,-0.292697)	(0.0166478,-0.688554)	(0.019954,-0.944205)
Mode 3	-	(0.0156597,-0.708947)	-

From figure 6.34, it can be seen that the eigenfunctions of the different modes at the crossover points are similar, but there are still qualitative differences. It is concluded that in contrast to the previously investigated chordwise location, no multiple eigenvalues were found at x_1/c=0.70.

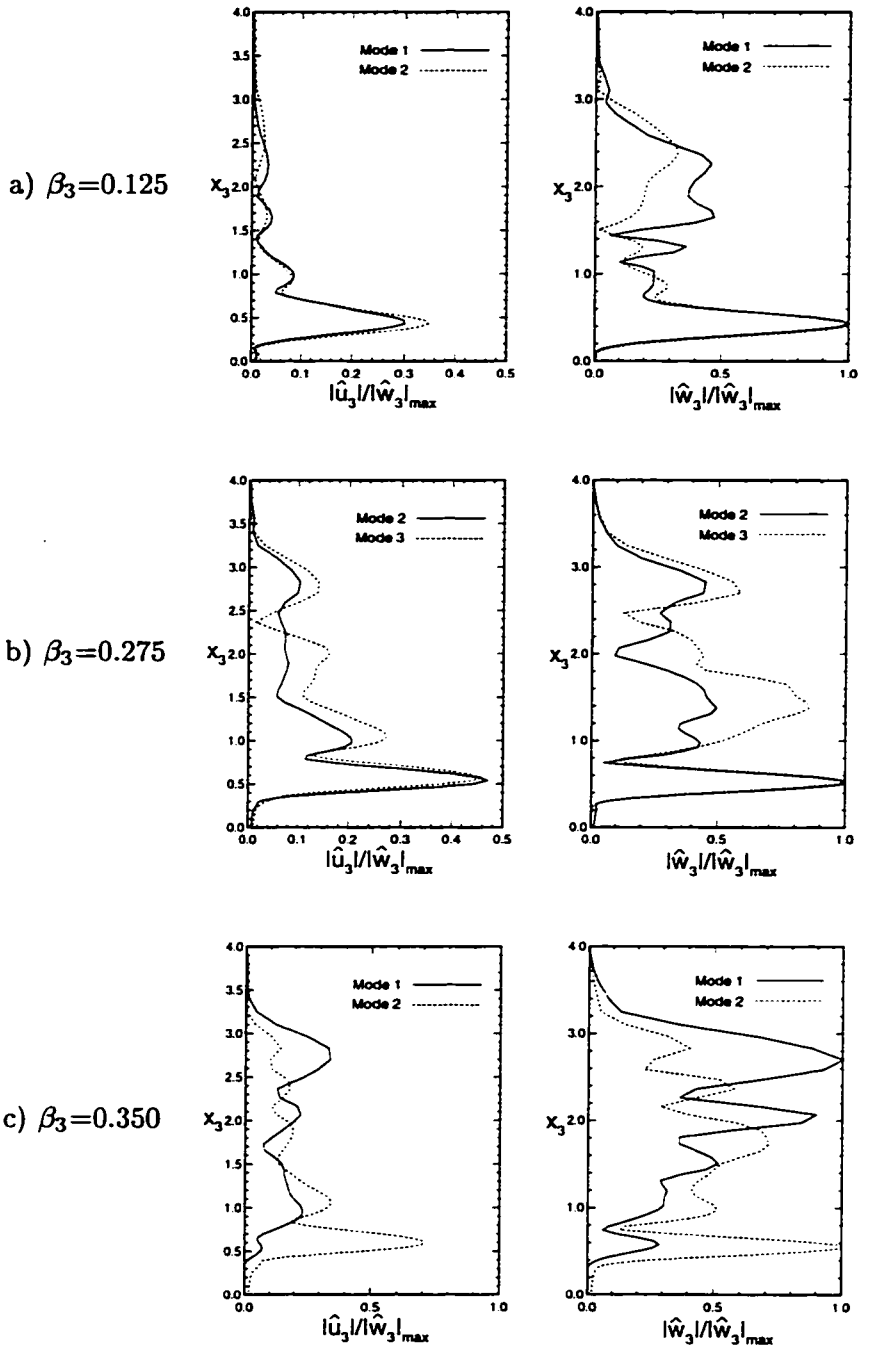

Figure 6.34: Total shape functions at crossover points of the growth rate curves (x_1/c=0.7, normal axis in millimeters)

Concluding the secondary instability analysis of the DLR Transition experiment, the structure of the secondary instability at $x_1/c=0.60$ will be examined. Considering the mode with the highest frequency at that chordwise location (Mode 1), figure 6.35 shows contours of the amplitude of the secondary eigenfunction tangential to the constant phase lines $|w_3|$ for the most amplified wave number $\beta_3=0.35$, and iso-lines of the modified mean flow component in that direction in the Galilean coordinate system. The temporal analysis of the isolated frequency f=3117 Hz of Mode 1 predicts a

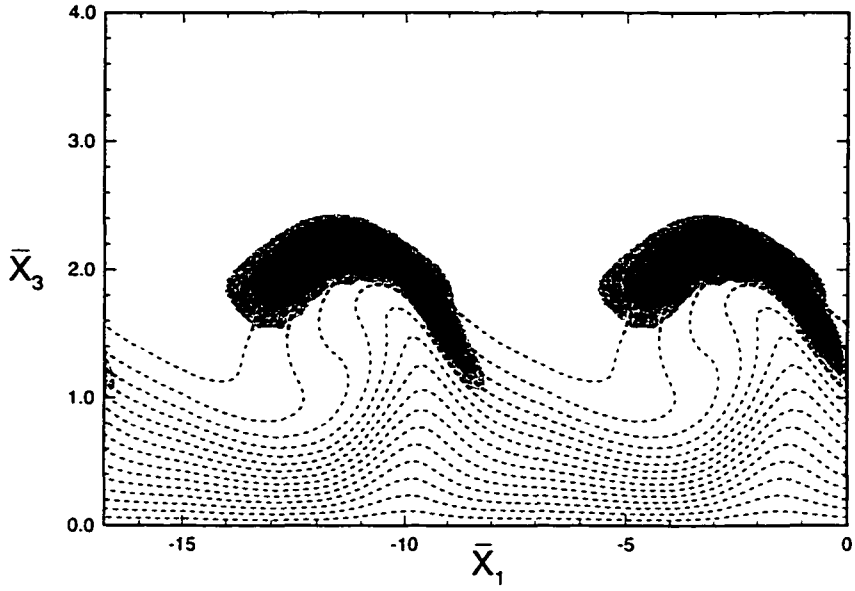

Figure 6.35: Contours of $|w_3|$ and W_2 at $x_1/c=0.6$ (axis in mm)

structure that is completely detached from the wall. The secondary instability rather rides on top of the primary crossflow vortex having two maxima at $\bar{x}_3 \simeq 1.8$ and $\bar{x}_3 \simeq 2.2$. This observation is in full agreement with the results of the temporal secondary instability analysis for Swept Hiemenz flow (see figure 5.33). Taking a cut in the horizontal $(\bar{x}_1,\bar{x}_2)$-plane at the normal location of $\bar{x}_3=2.2$, the secondary instability structure is viewed from the top in figure 6.36. Here, the point ($\bar{x}_1=0$, $\bar{x}_2=0$) coincides with the

chordwise location of x_1/c=0.6. Plotted for two periods in the $\bar{x}_1$- and the $\bar{x}_2$-directions are contours of the real part of the secondary disturbance component w_3. Further, the wave angle $\Psi_2 = \tan^{-1}(\alpha_3/\beta_3)$ of the secondary structure is shown. The secondary structure is of an elongated shape that aligns with the angle of secondary disturbance waves.

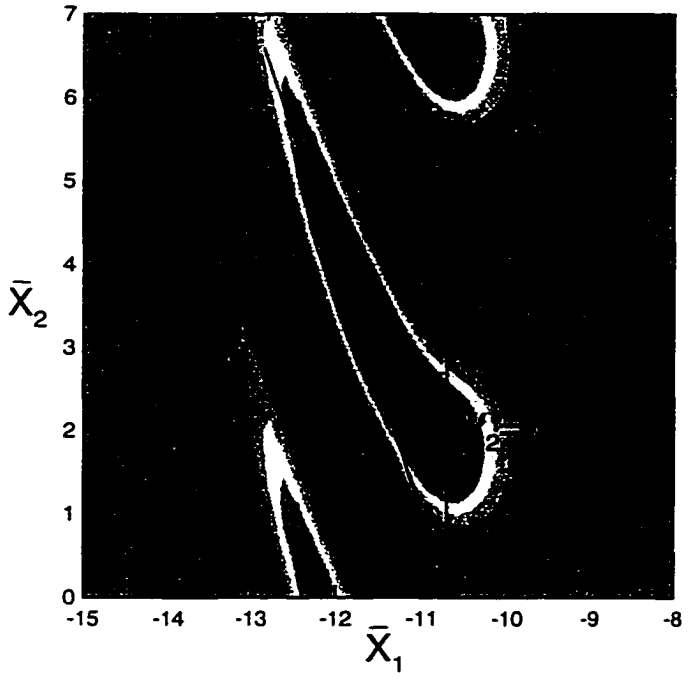

Figure 6.36: Contours of w_3 at x_1/c=0.6 and $\bar{x}_3$=2.2mm (α_3=-0.201, β_3=0.35)

Superimposing the secondary structure on a modified mean flow component W_2 that is assumed to be constant in the $\bar{x}_1$-direction, the total flow component tangential to the constant phase lines $W_3 = W_2 + w_3$ is obtained. Shown in figure 6.37 is a top view of W_3 contours at the same normal location of $\bar{x}_3$=2.2 as in figure 6.36, where the secondary structure is assigned an amplitude of 1%. The dark patches correspond to lower-speed fluid traveling on the crest of the primary crossflow vortices in

the $\bar{x}_2$-direction. Depending on their assigned amplitude, these secondary structures can severely modify the ordered primary structure of the stationary crossflow vortex.

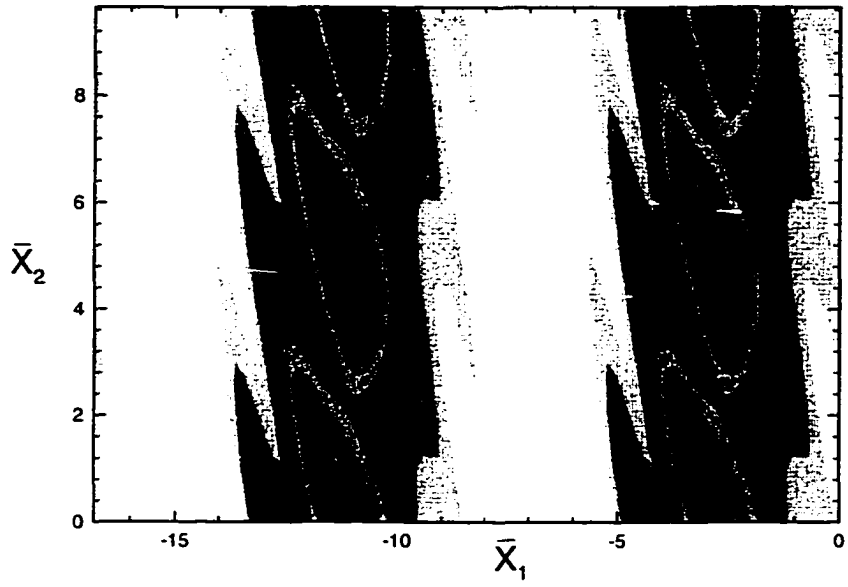

Figure 6.37: Contours of W_3 at x_1/c=0.6 and $\bar{x}_3$=2.2mm

From the observations in figures 6.35 - 6.36, it seems that the structure of a single-frequency secondary instability is well defined and might be detected in experiments, if care is taken as to where the measurements are performed in the boundary layer. However, the results from the secondary instability investigation of the Swept Hiemenz flow problem using the PSE indicate that the secondary instability structures might be more intricate in the presence of more than one unstable high frequency (see figure 5.39).

6.5 Summary

In the present chapter, two different experiments out of the test series known as the DLR Transition experiment were investigated using the linear and nonlinear PSE,

as well as Floquet Theory. Computing the mean flow directly from the measured outer velocity distribution, the results from both the performed detailed linear stability analysis, as well as from the nonlinear computations are found in good agreement with the experiment. In summary, the following points need to be emphasized.

Primary Stability Analysis

- The most unstable disturbances found from a linear PSE computation have a wavelength between λ_{x_2}=11.5 mm and λ_{x_2}=12.5 mm and are in the frequency range of f=176 - 180 Hz. These values are in excellent agreement with the experimental results.

- In contrast to the Swept Hiemenz flow problem, the wave angle of the most amplified disturbances found from a local analysis remains almost constant for both the stationary and the traveling disturbances at Ψ=86° and Ψ=75°, respectively.

- Also in contrast to the results for Swept Hiemenz flow, the range of the unstable frequencies becomes narrower in the downstream direction. Close to the neutral point of the traveling disturbances, the unstable range covers the frequencies from f=0 Hz up to f≃500 Hz. At the chordwise location of x_1/c=0.80, it has shrunk to a range from f=0 Hz to f≃330 Hz.

- A good agreement of the disturbance profiles obtained from the linear PSE analysis with the measured disturbance profiles was found at x_1/c=0.60.

- The results from a local spatial stability analysis at x_1/c=0.70 compare well to the experimental data for the wave angle, the wavelength and the phase speed of the disturbances by Deyhle et al. [18]. The discrepancies in the temporal stability results for the group velocities might be attributed to experimental uncertainties [18].

- As in the Swept Hiemenz flow investigation, including a small amplitude traveling disturbance in the nonlinear PSE computation and allowing for the nonlinear interaction of stationary and traveling disturbances decreases the saturation amplitude in comparison with a purely stationary case. The results of this computation are in good agreement with the experimental results for the disturbance amplitudes.

Temporal Secondary Stability Analysis

The results from the temporal secondary stability analysis in the region of the nonlinear saturation of a purely stationary disturbance performed for Swept Hiemenz flow and the DLR Transition experiment show both similarities and qualitative differences. Summarizing the results of the Floquet analysis for DLR experiment first, a comparison of the two considered problems will be given at the end of this section.

- At the chordwise location of x_1/c=0.60 in the DLR experiment (experiment I), several unstable eigenvalues were found. Out of these, three mode families were investigated closer.

- The maximal growth rate of the examined secondary disturbances was determined as $\sigma_{3,real}$=0.0326 for a wave number tangential to the stationary vortex of β_3=0.35 and a frequency of f=2933 Hz. This secondary growth rate compares to a maximal primary growth rate of σ_1=0.0225 for the traveling disturbance in the case where stationary and traveling disturbances interact nonlinearly (see curve 4a in figure 6.16).

- The existence of a multiple eigenvalue at x_1/c=0.60 was confirmed. This observation might explain the experimentally observed phenomena of a time-dependent explosive growth of the traveling modes [2].

- At the chordwise location of x_1/c=0.70 and for the same frequency range as at x_1/c=0.60, several unstable eigenvalues were determined. Again, three out of these modes were investigated in detail.

- The shape functions of the most unstable disturbances at x_1/c=0.70 are qualitatively different from the results at x_1/c=0.60. This difference is especially attributed to the following observation. The experimentally measured saturation amplitude is largely over-predicted by a purely stationary computation. Therefore, the results of the Floquet analysis at x_1/c=0.70 are assumed to over-predict the secondary instability. This over-prediction also shows in the obtained shape functions at this location which represent almost turbulent features, as the magnitudes of the wall-normal and wall-parallel disturbance velocity components are of the same order, and the profiles are very oscillatory. In contrast, the experimental observations [2] show that no transition to turbulence was detected for the here considered freestream velocity.

- At both investigated chordwise locations, the wave angles of the most unstable secondary disturbances closely correspond to the results from the investigation of the Swept Hiemenz flow. The most amplified secondary structures are inclined at angles between Ψ_2=-24° and Ψ_2=-48° with respect to the direction of the constant phase lines.

The differences in the results of the temporal secondary instability analysis for the Swept Hiemenz flow problem and the DLR Transition experiment are found in the existence of an absolute instability in the DLR experiment only, and in the qualitatively different shape functions of the secondary eigenmodes at Re=546 and x_1/c=0.70. Discussing these differences, a comparison of the two mean flows is provided first. A char-

acteristic parameter for the strength of the crossflow instability mechanism is given by the Crossflow-Reynolds number defined in equation 6.7. There, $|U_c^*|_{max}$ is the maximum

$$Re_{cf} = |U_c^*|_{max} \cdot \delta_{0.1}^*/\nu^* \tag{6.7}$$

of the crossflow mean flow component, and $\delta_{0.1}^*$ is the normal coordinate where the crossflow velocity has dropped to 10% of its maximal value. From figure 6.38 can be seen that the Crossflow-Reynolds numbers obtained in the DLR experiment are lower than for the Swept Hiemenz flow problem at the streamwise locations of interest. A value of Re_{cf}=151 at x_1/c=0.70 for the DLR experiment compares to Re_{cf}=175 at Re=550 for the Swept Hiemenz flow. Hence, it can be stated that the crossflow instability mechanism present in the Swept Hiemenz flow problem is slightly stronger than in the DLR experiment.

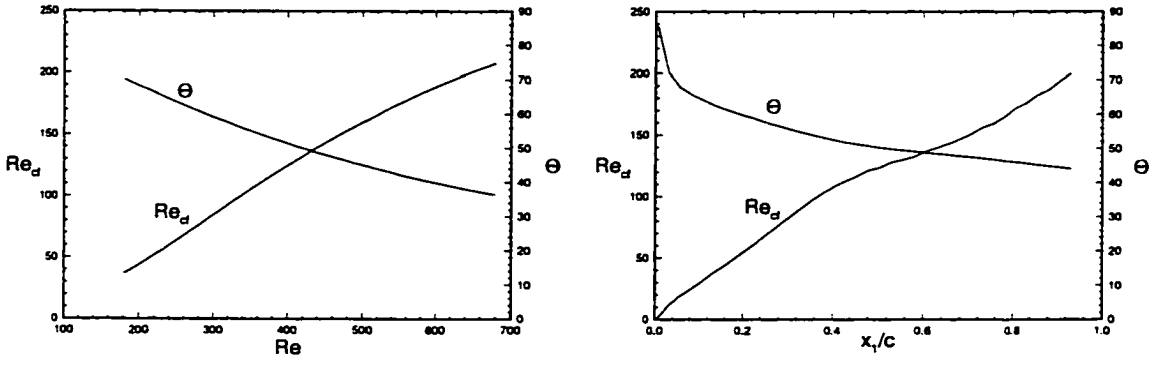

a) Swept Hiemenz flow b) DLR Transition experiment

Figure 6.38: Crossflow-Reynolds numbers of the basic flow

Second, other differences between the two considered cases are found in the wave number perpendicular to the constant phase lines α_3. For the Swept Hiemenz flow problem, the wave number α_3 at Re=546 takes a value of α_3=-0.508, whereas its value at x_1/c=0.70 is α_3=-0.200 in the DLR experiment. However, the inclination of the most

amplified secondary disturbances with respect to the constant phase lines is of the same order for both problems (see values of Ψ_2 above).

a) x_1/c=0.60

b) x_1/c=0.70

c) Re=546

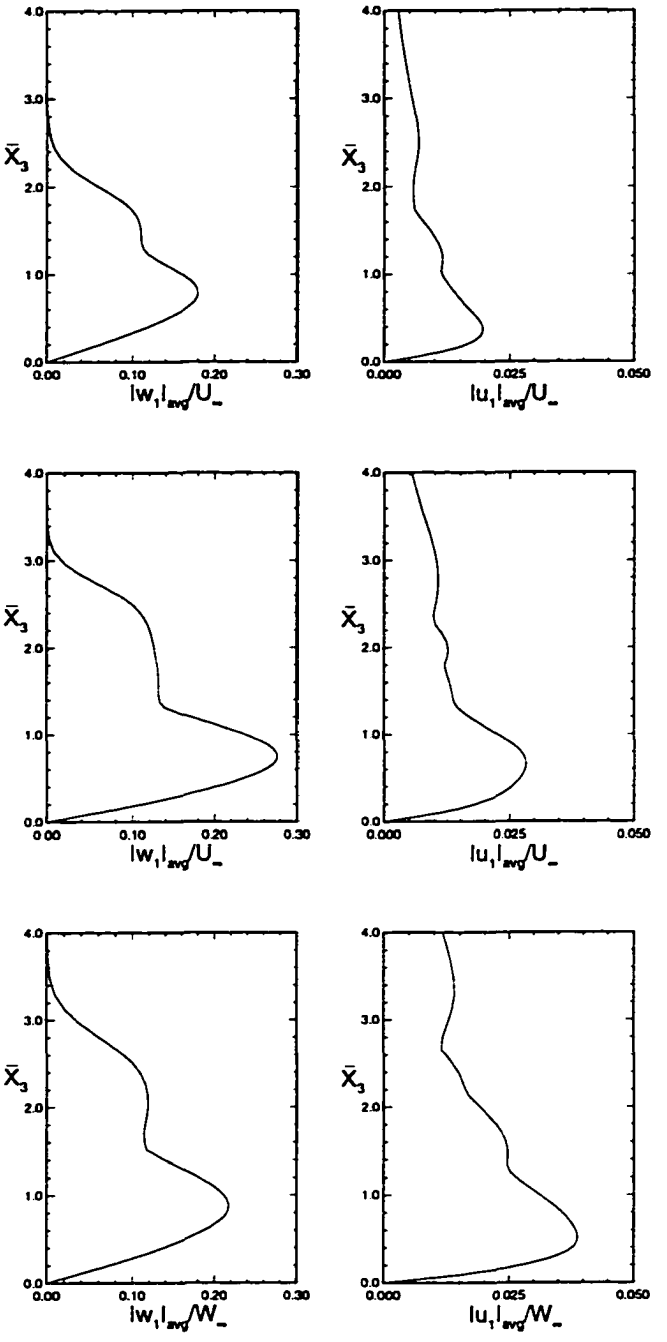

Figure 6.39: Normalized total shape functions from the DLR experiment and Swept Hiemenz flow

Third, the eigenfunctions for the two problems are compared at the chordwise locations of interest. Sampling 100 disturbance profiles over one wavelength in the $\bar{x}_1$-direction, an average of the absolute value of the total disturbance quantities in the Galilean coordinate system obtained from a nonlinear PSE computation is taken. The figures 6.39 (a-c) show the results for the disturbance components tangential and perpendicular to the stationary vortex, $\hat{w}_1$ and $\hat{u}_1$, respectively. Despite the different magnitudes of the disturbance profiles at x_1/c=0.60 and x_1/c=0.70, no qualitative difference between the plotted profiles is noted. Particularly similar are the disturbance profiles at x_1/c=0.70 and Re=546, which are the two locations where the differences in the results for the shape functions were found.

Thus, no strong statement about the origin of the observed differences between the temporal secondary instability results at Re=546 for the Swept Hiemenz flow problem and at x_1/c=0.70 for the DLR Transition experiment can be made. Some hints about their origin are seen in the different Crossflow-Reynolds numbers for the two problems and the much stronger curvature of the inviscid streamline present in the DLR experiment. The fact that there were no multiple eigenvalues found at the studied locations of the Swept Hiemenz flow problem might be explained in a recent linear stability analysis by Lingwood [56]. There, Lingwood determined a critical Reynolds number for the development of an absolute chordwise instability as $\overline{Re}$=545, which is above the specified value in the present work.

CHAPTER 7

IMPLICIT SOLUTION OF THE NONLINEAR PSE

7.1 Introduction

The explicit solution method as presented in Chapter 4 has been shown to be very accurate and efficient in flow regions where the nonlinearity is not yet strongly developed, and hence, the gradients in the flow field are still moderate. In these regions, it typically takes three to five iterations on the streamwise wave number, and two to four iterations on the nonlinear terms per station to obtain a converged solution.

However, once the disturbances have grown to significant amplitude levels and nonlinearity becomes a dominant feature of the flow, the number of iterations increases drastically and the solution eventually ceases to converge. In fact, only an implemented successive under-relaxation (SUR) for the iteration on the nonlinear terms allows for convergence in the later region of nonlinear disturbance growth. There, and for typical SUR-parameters of 0.25 and 0.125, it takes up to 200 iterations on the nonlinear terms until the solution converges at a particular streamwise location.

There are two possible reasons for the convergence problems of the explicit solution method in the highly nonlinear region. First, the iteration on the streamwise wave number might not converge due to very rapid changes in both the wave number phase and its amplitude part. This implies that the PSE assumption of a small amplitude variation in the streamwise direction is violated, and hence, the convergence problems are due to the physics of the flow. Second, the iteration on the nonlinear terms might not converge. In the highly nonlinear region, the different disturbances do not grow

linearly on their own, but their growth is more dominantly influenced by their nonlinear interaction. The lagging between the iteration on the specified primary disturbance and the subsequent update of all other nonlinear terms applied in the explicit iteration method (see Chapter 4) disrupts that nonlinear interaction and is the reason for the convergence problems. In that case, an implicit solution method that computes all the nonlinear terms simultaneously would improve the convergence of the nonlinear iteration.

The present chapter presents an implicit approach to the solution of the PSE. The details of this recently developed and very robust solution method are explained in Section 7.2. An application to Swept Hiemenz flow and a comparison of the efficiency and robustness of the two solution methods will be presented in Section 7.3.

7.2 Solution Method

The solution method was developed by Balakumar in 1997 and is documented in Referecne [95]. For simplicity, and since the investigation of the passive laminar flow control using leading edge roughness assumes that the stationary modes are dominating the traveling disturbances, the derivations in this section will be restricted to the steady case.

As a starting point, consider the nonlinear PSE for each Fourier mode in matrix form as derived in Chapter 4 (equation 7.1). However, in contrast to the explicit method

$$\mathbf{A_m}\frac{\partial^2 \hat{\mathbf{q}}_{\mathbf{1_m}}}{\partial x_3^2} + \mathbf{B_m}\frac{\partial \hat{\mathbf{q}}_{\mathbf{1_m}}}{\partial x_3} + \mathbf{C_m}\hat{\mathbf{q}}_{\mathbf{1_m}} = \mathbf{D_m}\frac{\partial \hat{\mathbf{q}}_{\mathbf{1_m}}}{\partial x_1} + \mathbf{E_m}\frac{\partial^2 \hat{\mathbf{q}}_{\mathbf{1_m}}}{\partial x_1 \partial x_3} + \frac{\mathbf{S_m}}{\mathcal{A}_m} \qquad (7.1)$$

where the vector of the nonlinear terms $\mathbf{S_m}$ is obtained from a computed FFT, it is here determined by performing a summation of all the Fourier modes and collecting only the contributions to the m^{th}-mode. Expressing the x_1-component of vector S as in equation 7.2, the terms contributing to the m^{th}-Fourier mode are written in equation 7.3.

$$S_1 = \left(\sum_{m_1=-M}^{M} \hat{u}_{1_{m_1}} e^{i\int \alpha_{1_{m_1}} dx_1}\right) \cdot \left(\sum_{m_2=-M}^{M} \frac{\partial \hat{u}_{1_{m_2}}}{\partial x_1} e^{i\int \alpha_{1_{m_2}} dx_1}\right) + \left(\sum_{m_1=-M}^{M} \hat{w}_{1_{m_1}} e^{i\int \alpha_{1_{m_1}} dx_1}\right) \cdot \left(\sum_{m_2=-M}^{M} \frac{\partial \hat{u}_{1_{m_2}}}{\partial x_2} e^{i\int \alpha_{1_{m_2}} dx_1}\right) + \left(\sum_{m_1=-M}^{M} \hat{v}_{1_{m_1}} e^{i\int \alpha_{1_{m_1}} dx_1}\right) \cdot \left(\sum_{m_2=-M}^{M} \frac{\partial \hat{u}_{1_{m_2}}}{\partial x_3} e^{i\int \alpha_{1_{m_2}} dx_1}\right) \quad ; \tag{7.2}$$

$$S_{1_m} = \sum_{m_1=-M}^{M} \left(\hat{u}_{1_{m_1}} \frac{\partial \hat{u}_{1_{m-m_1}}}{\partial x_1} + \hat{w}_{1_{m_1}} \frac{\partial \hat{u}_{1_{m-m_1}}}{\partial x_2} + \hat{v}_{1_{m_1}} \frac{\partial \hat{u}_{1_{m-m_1}}}{\partial x_3}\right) \cdot e^{i\int \alpha_{1_{m-m_1}} + \alpha_{1_{m_1}} dx_1} \tag{7.3}$$

Writing the other components of S similarly, the nonlinear system (equation 7.1) is solved using the two-point fourth-order-accurate compact scheme. In order to utilize the Euler-McLaurin formula (equation 4.19), the system of nonlinear PDE's needs to be rewritten as a system of linear ODE's. This is accomplished by linearizing the system over a one-term expansion, as explained in the following.

Considering a new vector of unknowns $\bar{q}_m$ as in equation 7.4, the nonlinear system (equation 7.1) can be rewritten for each normal location k as in equation 7.5. In the present stationary case, $\bar{q}$ and F are $\{6\times(2\cdot M+1)\}$ column vectors. From equation 7.5, the second derivative with respect to the wall-normal coordinate is written in equation 7.6. Substituting equations 7.5 and 7.6 into the Euler-McLaurin formula (equation 4.19), one obtains equation 7.7 for the Fourier mode m at each normal location.

$$\bar{q}_m = \{\hat{u}_{1_m}, \frac{\partial \hat{u}_{1_m}}{\partial x_3}, \hat{w}_{3_m}, \frac{\partial \hat{w}_{3_m}}{\partial x_3}, \hat{v}_{3_m}, \hat{p}_{3_m}\}^T \quad ; \quad m = -M, \cdots, M \tag{7.4}$$

$$\bar{q}'_m = F_m(\bar{q}_m, x_3) \tag{7.5}$$

$$\bar{q}''_m = \frac{\partial F_m}{\partial x_3} + \frac{\partial F_m}{\partial \bar{q}} F \quad ; \quad F = \{F_{-M}^T, \cdots, F_M^T\}^T \tag{7.6}$$

Next, this nonlinear system of ODE's is transformed into a system of linear ODE's using the one-term expansion of the vector $\bar{q}_m$ in equation 7.8. Substituting equation 7.8 into

$$\bar{q}_{m_k} - \bar{q}_{m_{k-1}} = \frac{h_k}{2}(F_{m_k} + F_{m_{k-1}}) - \frac{h_k^2}{12}\left(F'_k - F'_{k-1} + \left(\frac{\partial F_m}{\partial \bar{q}}\right)_k F_k - \left(\frac{\partial F_m}{\partial \bar{q}}\right)_{k-1} F_{k-1}\right) \tag{7.7}$$

$$\bar{q}_m = \bar{q}_{0_m} + \Delta\bar{q}_m \tag{7.8}$$

equation 7.7 and linearizing in $\Delta\bar{q}_m$, one can write equation 7.9. Finally, collecting terms of $\Delta\bar{q}_m$, the obtained linear system (equation 7.9) is rewritten in the familiar ma-

$$\begin{aligned}
&\bar{q}_{0_{m_k}} + \Delta\bar{q}_{m_k} - \bar{q}_{0_{m_{k-1}}} - \Delta\bar{q}_{m_{k-1}} = \\
&\frac{h_k}{2}\left(F_{0_{m_k}} + F_{0_{m_{k-1}}} + \left(\frac{\partial F_{0_m}}{\partial \bar{q}}\right)_k \Delta\bar{q}_k + \left(\frac{\partial F_{0_m}}{\partial \bar{q}}\right)_{k-1} \Delta\bar{q}_{k-1}\right) - \\
&\frac{h_k^2}{12}\{F'_{0_{m_k}} + \left(\frac{\partial F'_{0_m}}{\partial \bar{q}}\right)_k \Delta\bar{q}_k + \left(\frac{\partial F_{0_m}}{\partial \bar{q}}\right)_k F_{0_k} + \\
&\left(\frac{\partial F_{0_m}}{\partial \bar{q}}\right)_k \left(\frac{\partial F_{0_m}}{\partial \bar{q}}\right)_k \Delta\bar{q}_k + \left(\frac{\partial^2 F_{0_m}}{\partial \bar{q}^2}\right)_k F_{0_k}\Delta\bar{q}_k - \\
&F'_{0_{m_{k-1}}} - \left(\frac{\partial F'_{0_m}}{\partial \bar{q}}\right)_{k-1} \Delta\bar{q}_{k-1} - \left(\frac{\partial F_{0_m}}{\partial \bar{q}}\right)_{k-1} F_{0_{k-1}} \\
&\left(\frac{\partial F_{0_m}}{\partial \bar{q}}\right)_{k-1} \left(\frac{\partial F_{0_m}}{\partial \bar{q}}\right)_{k-1} \Delta\bar{q}_{k-1} - \left(\frac{\partial^2 F_{0_m}}{\partial \bar{q}^2}\right)_{k-1} F_{0_{k-1}}\Delta\bar{q}_{k-1}\}
\end{aligned} \tag{7.9}$$

trix form in equation 7.10 for each Fourier mode m at the normal location k. Combining the equations for all the Fourier modes at a normal location k into a single matrix equa-

$$A_{m_k} \cdot \Delta\bar{q}_{m_{k-1}} + B_{m_k} \cdot \Delta\bar{q}_{m_k} = D_{m_k} \tag{7.10}$$

tion, considering all points in the wall-normal direction, incorporating the homogeneous boundary conditions at the wall and in the freestream, as well as shifting the individual matrices according to the procedure explained in Chapter 4, a block-tridiagonal system is obtained (equation 7.11). There, the dimensions of the complex coefficient matrices AA,

BB and **CC**, and of the complex right-hand side vector **DD** are 6·(2·M+1)×6·(2·M+1) and 6·(2·M+1)×1, respectively, considering the six elements of the vector of unknowns

$$\mathbf{AA_k} \cdot \Delta\bar{\mathbf{q}}_{\mathbf{k-1}} + \mathbf{BB_k} \cdot \Delta\bar{\mathbf{q}}_{\mathbf{k}} + \mathbf{CC_k} \cdot \Delta\bar{\mathbf{q}}_{\mathbf{k+1}} = \mathbf{DD_k} \quad ; \quad k = 2, \cdots, N-1 \qquad (7.11)$$

$\Delta\bar{\mathbf{q}}_{\mathbf{k}}$. Exploiting the block-tridiagonal structure of the system and writing it in a compact storage format, a complex coefficient matrix $\mathbf{C_{tridiag}}$ with the dimensions {4·6·(2·M+1)}×{N·6·(2·M+1)} is obtained. This rearranged system is written in equation 7.12.

$$\mathbf{C_{tridiag}} \cdot \Delta\bar{\mathbf{q}} = \mathbf{DD} \qquad (7.12)$$

Since the still significant amount of memory necessary to store the complex coefficients of $\mathbf{C_{tridiag}}$ constitutes a major problem for an application of the implicit solution method (especially for the case where steady and traveling disturbances interact nonlinearly), an algorithm that drastically reduces the required memory by utilizing the symmetry and the block-tridiagonal structure of the linear system will be described next.

First of all, the amount of memory that needs to be allocated for storing the complex matrix $\mathbf{C_{tridiag}}$ is considered. In order to solve the linear system (equation 7.12) for the (N-1)·(2·M+1) complex unknowns $\Delta\bar{\mathbf{q}}_{\mathbf{m}}$, one needs to consider the entire complex plane. This corresponds to the above problem size of {4·6·(2·M+1)}×{N·6·(2·M+1)} and will be taken as the baseline for the following comparisons. However, according to Chapter 4, the symmetry of the problem can be exploited. To accomplish that without neglecting the necessary number of equations from the conjugate half of the complex plane, the complex matrix coefficients are split into their real and imaginary parts, as explained in the following.

Consider the Euler-McLaurin formula for Mode (m) at the normal location k (equation 7.11). Adding the corresponding equation for Mode (-m) and utilizing the

symmetry condition $\Delta\bar{q}_{1_m} = \Delta\bar{q}^*_{1_{-m}}$, one obtains equation 7.13. Here, the asterisk denotes the complex conjugate. Now, expanding the complex coefficients and vector ele-

$$\mathbf{A_{m,k-1}} \cdot \Delta\bar{\mathbf{q}}_{\mathbf{m,k-1}} + \mathbf{B_{m,k}} \cdot \Delta\bar{\mathbf{q}}_{\mathbf{m,k}} + \mathbf{A^*_{-m,k-1}} \cdot \Delta\bar{\mathbf{q}}_{\mathbf{m,k-1}} + \mathbf{B^*_{-m,k}} \cdot \Delta\bar{\mathbf{q}}_{\mathbf{m,k}}$$

$$= \mathbf{D_{m,k}} + \mathbf{D^*_{-m,k}} \tag{7.13}$$

ments, and collecting the real and imaginary terms yields equation 7.14 for the real parts and equation 7.15 for the imaginary parts. There, the subscripts r and i denote the real and imaginary parts of the complex quantities, and the subscripts k and k-1 are omitted for simplicity. Using these two equations, the complex coefficient matrices for each mode,

$$\Delta\bar{q}_{r_m} \cdot \left(a_{r_m} + a^*_{r_{-m}} + b_{r_m} + b^*_{r_{-m}}\right) + \Delta\bar{q}_{i_m} \cdot \left(a^*_{i_{-m}} - a_{i_m} + b^*_{i_{-m}} - b_{i_m}\right) = d_{r_m} + d^*_{r_{-m}} \tag{7.14}$$

$$\Delta\bar{q}_{r_m} \cdot \left(a_{i_m} + a^*_{i_{-m}} + b_{i_m} + b^*_{i_{-m}}\right) + \Delta\bar{q}_{i_m} \cdot \left(a_{r_m} - a^*_{r_{-m}} + b_{r_m} - b^*_{r_{-m}}\right) = d_{i_m} + d^*_{i_{-m}} \tag{7.15}$$

each component of the vector $\Delta\bar{\mathbf{q}}$, and at each normal location are restructured, and the resulting new structure of the coefficient matrices $\overline{\mathbf{A}}$ and $\overline{\mathbf{B}}$ is shown in figure 7.1. Taking

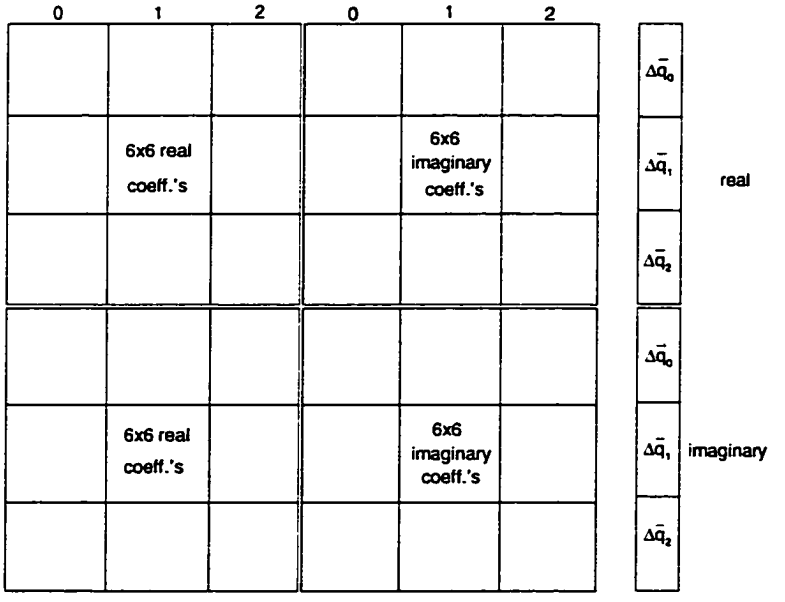

Figure 7.1: Matrix structure utilizing symmetry and purely real coefficients (M=2)

the described approach, real $\{2\cdot(M+1)\cdot 6\}\times\{2\cdot(M+1)\cdot 6\}$ block matrices are obtained instead of complex $\{(2\cdot M+1)\cdot 6\}\times\{(2\cdot M+1)\cdot 6\}$ block matrices at each normal location. Hence, utilizing the symmetric properties of the system and splitting the complex quantities into their real and imaginary parts results in a decrease of the required memory by about 50% compared to the base line value in the case of a purely steady disturbance.

The second system property exploited in the current solution method is the block-tridiagonal structure of the now real coefficient matrix $\overline{\mathbf{C}}_{\mathbf{tridiag}}$. Instead of storing the entire matrix $\overline{\mathbf{C}}_{\mathbf{tridiag}}$ and solving the matrix equation 7.12 directly at each iteration step, a Gaussian elimination is performed line by line using efficient computational libraries that are available in the public domain (LAPACK). Inverting the block-matrix $\overline{\mathbf{BB}}_{\mathbf{1}}$ (see figure 7.2), the first row of the equation 7.12 can be solved for $\Delta\bar{\mathbf{q}}_{\mathbf{1}}$. The solution $\Delta\bar{\mathbf{q}}_{\mathbf{1}}$ is then substituted into the second row and the Gaussian elimination proceeds.

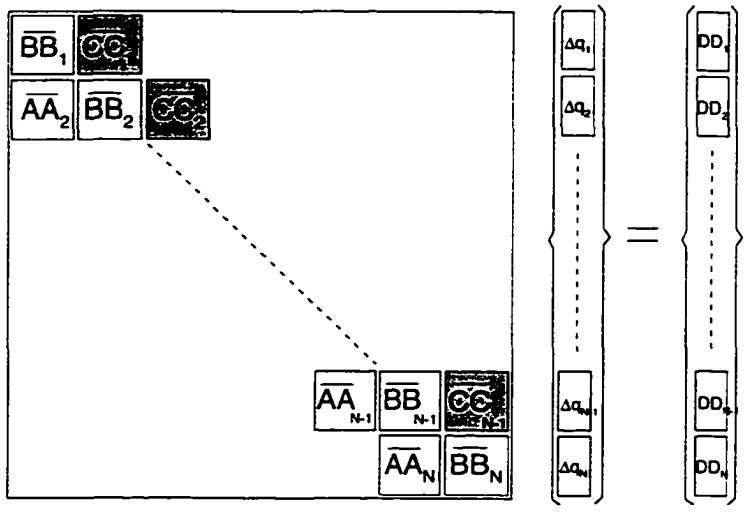

Figure 7.2: Structure of the real block-tridiagonal matrix $\overline{\mathbf{C}}_{\mathbf{tridiag}}$

The main advantage of this algorithm is that the real coefficient matrices $\overline{\mathbf{AA}}_{\mathbf{n}}$ and $\overline{\mathbf{BB}}_{\mathbf{n}}$ can be overwritten after solving the system at a particular line, and only the

newly obtained matrices $\overline{\overline{\mathbf{C}}}_{\mathbf{n}}$ need to be stored for the back-substitution (see figure 7.2). Thus, utilizing the block-tridiagonal structure of $\overline{\mathbf{C}}_{\mathbf{tridiag}}$, this algorithm results in a decrease of the required memory by 66% compared to storing the entire matrix $\overline{\mathbf{C}}_{\mathbf{tridiag}}$. Combined with the decrease obtained by utilizing the symmetry of the problem, the required memory is therefore decreased by 50%+66% $\simeq$ 80%. Even though the presented approach increases the computational work due to the rewriting of the coefficient matrices, the extensive amount of book-keeping involved, and the slower solution of the block-tridiagonal matrix compared to the application of an efficient block-tridiagonal solver, it is only due to this drastic decrease in the required memory that the presented implicit solution method is applicable for problems of interest.

Concluding this section, the implicit solution method will be summarized. Starting from an initial guess for $\bar{\mathbf{q}}_0$ at x_{l_0}, the algorithm proceeds as follows :

1. Nonlinear iteration

   - At each normal location k :
     - Form the complex matrices $\mathbf{A_k}$ and $\mathbf{B_k}$, as well as the vector $\mathbf{D_k}$.
     - Split the complex matrices and vectors into their real and imaginary parts according to equations 7.14, 7.15 and form the real coefficient matrices $\overline{\mathbf{A}}_\mathbf{k}$ and $\overline{\mathbf{B}}_\mathbf{k}$, as well the real vector $\overline{\mathbf{D}}_\mathbf{k}$.
     - Shift the two coefficient matrices into the matrices $\overline{\overline{\mathbf{AA}}}_\mathbf{k}$, $\overline{\overline{\mathbf{BB}}}_\mathbf{k}$ and $\overline{\overline{\mathbf{CC}}}_\mathbf{k}$.
     - Perform a Gaussian elimination step for the current row.
   - Perform the back-substitution in the entire wall-normal domain and determine the vector of the corrections to the initial guess $\Delta\bar{\mathbf{q}}$.
   - Update the shape functions : $\bar{\mathbf{q}}_{\mathbf{new}} = \bar{\mathbf{q}}_{\mathbf{old}} + \Delta\bar{\mathbf{q}}$.

- If $|\Delta\bar{q}_{max}| < \epsilon_1$, then proceed with the wave number computation, else continue the nonlinear iteration with updated shape functions.

2. Wave number computation

   - According to the chosen method, compute the number of specified wave numbers α_1 after equation 4.29 and distribute the remaining wave numbers algebraically.
   - If $|\alpha_{1,new} - \alpha_{1,old}| < \epsilon_2$, then continue with the next streamwise station, else go back to the nonlinear iteration.

Regarding the convergence rates of the implicit method, it is first observed that the convergence rate of the nonlinear iteration is almost quadratic. Second, in the wave number computation, the maximal deviation obtained for an iteration on just the primary wave number typically drops by four orders-of-magnitude within two or three iterations. This rapid convergence is slightly decreased; however, when the convergence of the wave number iteration is based the on maximal deviation of several computed wave numbers.

Finally, an important advantage of the implicit method versus the explicit method needs to be pointed out. Since all the shape functions of the different modes are computed at the same time, the computation of the individual wave numbers is very straightforward and requires no extra iteration on the nonlinear terms.

7.3 Computational Efficiency

In order to discuss the efficiency and robustness of the implicit solution method in comparison with the explicit method, this section will show results from an application of both methods to the Swept Hiemenz flow problem. For a Reynolds number in the spanwise direction of $\overline{Re}$=500, a steady disturbance with a spanwise wave number

of β_1=0.4 and an initial amplitude of A=0.1% (see Section 5.3) is introduced at the streamwise position of Re_0=150.

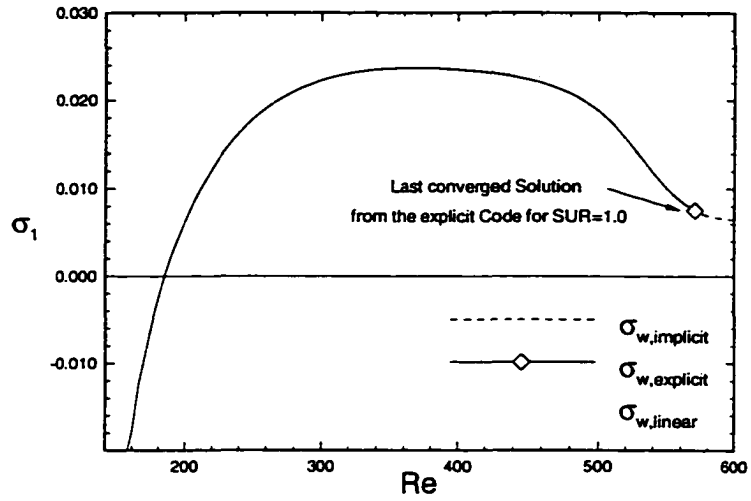

Figure 7.3: Growth rates and regions of convergence for the explicit and the implicit methods

Figure 7.3 shows the growth rates σ_1 based on the disturbance component in the spanwise direction that are obtained from the explicit and the implicit method. Additionally, the linear growth rates are plotted. Besides the perfect agreement of the

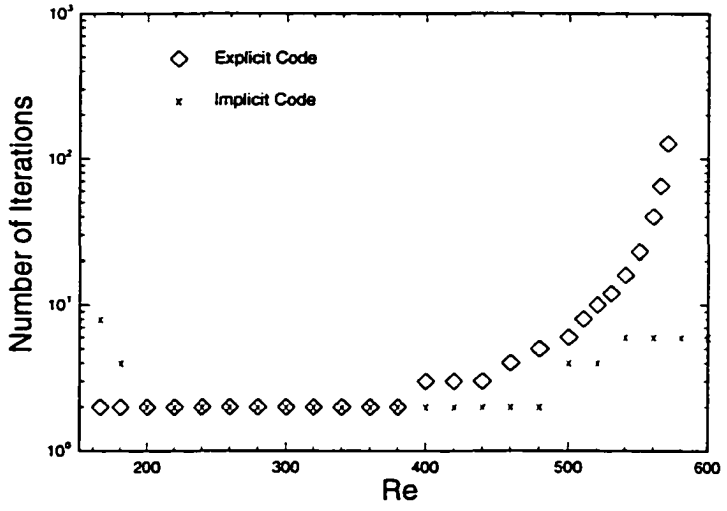

Figure 7.4: Number of iterations on the nonlinear terms (SUR=1.0)

results obtained from the different methods, it is noted that the nonlinear effects modify the growth rate starting at a Reynolds number of Re=400. It is further seen that the explicit method ceases to converge at Re=570 for an SUR-parameter of 1.0, whereas the implicit method continues to converge well beyond the plotted region. From the previous computations for the same mean flow parameters in Section 5.3, it is recalled that a Reynolds number of Re=570 corresponds to the region where the stationary disturbances saturate, and hence, the nonlinear effects are indeed strong at the point where the explicit method stops converging for an SUR-parameter of 1.0.

The number of iterations on the nonlinear terms necessary to obtain a converged solution, and the convergence history at Re=570 are shown in figures 7.4 and 7.5, respectively. There, the residue is defined as the maximal difference in the shape functions of the primary disturbance obtained in two consecutive iterations. The extremely rapid convergence of the implicit method is visualized in figure 7.5 and shows the superiority of the implicit method in the developed nonlinear region. The kinks in the curve are caused by the restart of the nonlinear iteration after every wave number computation.

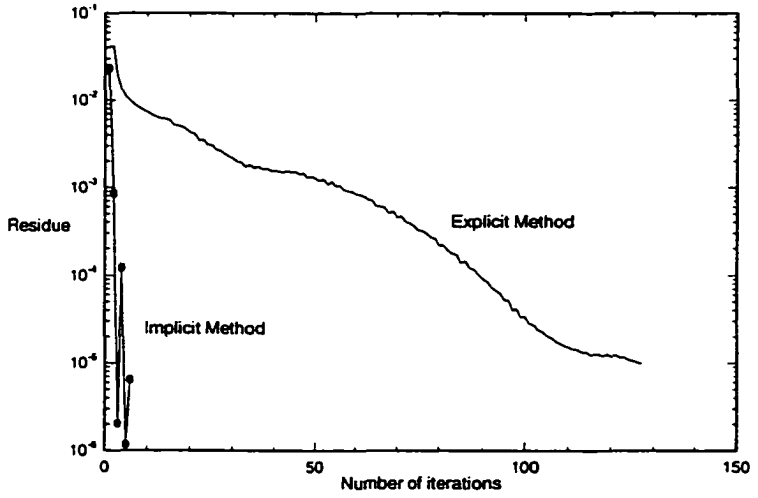

Figure 7.5: Convergence history for the explicit and the implicit methods at Re=570 (SUR=1.0)

Two observations can be made from these above plots. First, in the region of linear disturbance growth (Re<400), the explicit method needs as many iterations on the nonlinear terms as the implicit method. Since the explicit method iterates just on the primary disturbance, whereas the implicit method computes all disturbances simultaneously, the explicit method is expected to be much more efficient in that region. With an increasing effect of the nonlinear terms for Re>400, however, this similar performance of the two methods is altered significantly. The number of iterations on the nonlinear terms using the explicit method increases exponentially, whereas the performance of the explicit code basically remains unchanged.

For a fair comparison of the two methods, the necessary CPU-time needs to be documented. Both methods were run on a one processor Sun-Ultra-II workstation (333 MHz), and the required CPU-times for the two methods are listed in table 7.1. As expected, it turns out that the explicit method is more efficient for the computations performed in a domain that is in large parts representing the region of linear disturbance growth. In fact, the implicit method takes about 50% more CPU-time to compute the solutions at the considered 85 streamwise stations.

Table 7.1: CPU-time for the explicit and the implicit methods (85 stations)

Explicit Method	Implicit Method
2:55:11	4:29:41

However, figures 7.4 and 7.5 also show the limitations of the explicit method. Obviously, the CPU-time balance would drastically change when the computations were continued further into the nonlinear region by specifying a SUR-parameter less than 1.0.

At the end of this chapter, it is concluded that the presented implicit method represents a powerful tool to conduct nonlinear PSE computations in the regions of highly

nonlinear disturbance growth. The most effective technique in applying the developed algorithms is seen in combining the explicit and implicit methods by starting the computations with the explicit method, and once a critical number of nonlinear iterations is reached, by continuing with the implicit method.

CHAPTER 8

TRANSITION CONTROL USING ROUGHNESS ELEMENTS

8.1 Introduction

Recent results by Saric et al. [4] from an experimental investigation of the crossflow dominated boundary layer on an infinite swept wing document observations of a passive transition control mechanism that originates from roughness elements near the leading edge.

The intention of the study presented in this chapter is to investigate the physical mechanisms observed in the ASU experiment in more detail. With a numerical simulation using the nonlinear PSE and an implicit solution method, it will be shown that the growth of the most amplified disturbance in a crossflow dominated boundary layer can be effectively decreased by forcing disturbances with a spanwise wavelength smaller than the most amplified wavelength. Thereby, the growth of the total disturbance quantities is delayed, which is an observation that might be a useful passive technique for laminar flow control.

Since it was not possible to obtain the experimental data and the wing geometry of the ASU experiment on time for a consideration in this work, the ONERA D-wing experiment performed by Arnal et al. [10] was chosen instead. In Section 8.2, the observations of different experimental runs in the ASU experiment will be described in detail. Section 8.3 contains an investigation of the passive control mechanism for the ONERA D-wing experiment. Selecting a case where the flow is purely crossflow dom-

inated (α=-8°, ϕ=40°, see figure 8.4), the mean flow computation is presented in the first subsection. In the second subsection, a linear stability analysis for stationary disturbances is conducted in order to determine the most amplified stationary disturbance. The results from a nonlinear PSE computation are presented in the third subsection. There, the qualitative observations of the ASU experiment are successfully reproduced. Concluding this chapter, a summary is given in Section 8.4.

8.2 The ASU Swept Wing Experiment

In the experiments, Saric et al. [4] used the natural laminar flow airfoil NLF (2)-0415 with a hand-polished aluminium surface. The experimental conditions for the considered test case are given in table 8.1. The profile geometry and the pressure distribution for the given freestream conditions are depicted in figure 8.1.

Table 8.1: Freestream conditions for the ASU experiment

Chord length c	1.83 m
Freestream velocity Q^*_∞	~20 m/s
Reynolds number Re_∞	2,400,000
Sweep angle ϕ	45°
Angle of attack α	-4°

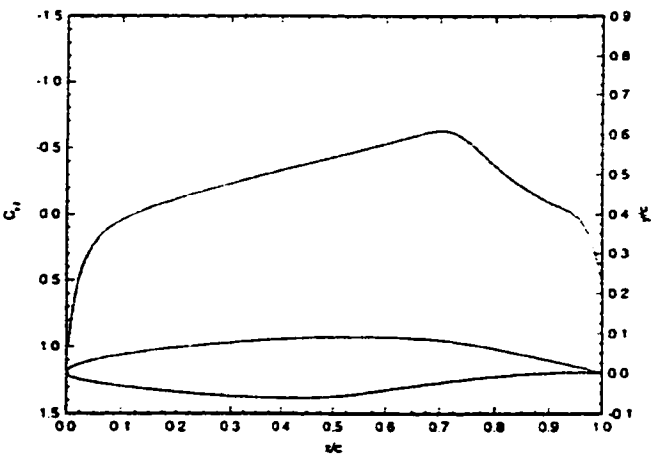

Figure 8.1: Airfoil geometry and C_p-distribution for the ASU experiment (from [4])

Studying the natural transition case without roughness elements first, they determined the most amplified spanwise wavelength as λ_{x_2}=12mm. Transition occured closely before the location of the pressure minimum of the outer flow at $x_1/c \simeq 0.71$ in that case. Next, they forced disturbances of equal, or larger wavelength than the most amplified spanwise wavelength by putting roughness elements at distances of 12mm, 18mm and 36mm near the leading edge at x_1/c=0.023. The ratio of the roughness height of the elements (k_{rough}=6μm), and the distributed roughness height of the hand-polished aluminium surface (k_{rough}=0.25μm) was 24. The Reynolds number based on the height of the roughness elements was specified as $Re_k \simeq 0.1$ [4] which is of negligible influence on the undisturbed mean flow.

By forcing the most amplified disturbances with λ_{x_2}=12mm, they found that transition moved forward to $x_1/c \simeq 0.52$. Forcing the initially stable disturbances with λ_{x_2}=18mm, they observed that neither the 12mm, nor the 36mm modes were amplified in the downstream direction. However, a strong initial growth of the disturbances with λ_{x_2}=9mm was measured. Varying the roughness height, they further noted a weak dependence of the saturation amplitude of the total disturbance on the roughness height. For values of k_{rough}=6,12, and 18μm, the saturation amplitude at x_1/c=0.45 remained almost constant at levels of A$\simeq$14%.

Most interestingly, however, Saric et al. [4] were able to delay transition beyond the location of the pressure minimum to $x_1/c \simeq 0.80$ by forcing disturbances with a wavelength smaller than the most amplified spanwise wavelength. To accomplish that, they placed roughness elements at a spanwise distance of λ_{x_2}=8mm near the leading edge. Interpreting the detailed measurements, they attributed the transition delay to the strong early growth of the 8mm disturbances that suppressed the very unstable

higher wavelengths λ_{x_2}=9mm and λ_{x_2}=12mm initially. The saturation and decay of the 8mm disturbances beyond $x_1/c \simeq 0.30$ then gave rise to the growth of longer wavelength disturbances that eventually lead to transition. However, this succesful transition delay could be accomplished for the Reynolds number of Re=2,400,000 only. Increasing the Reynolds number slightly to Re=2,600,00, or to Re=2,800,000 moved the transition forward to locations of x_1/c=0.59 and x_1/c=0.50, respectively.

8.3 The ONERA D-Wing Experiment

As reviewed in Section 2.3, a series of transition experiments on infinite swept wing models was performed at the French research institution ONERA/CERT between 1984 and 1997. A significant number of these tests was performed on a symmetric airfoil especially designed for the investigation of laminar flow phenomena on infinite swept wings - the ONERA D-airfoil. In figures 8.2 and 8.3, the experimental setup and the

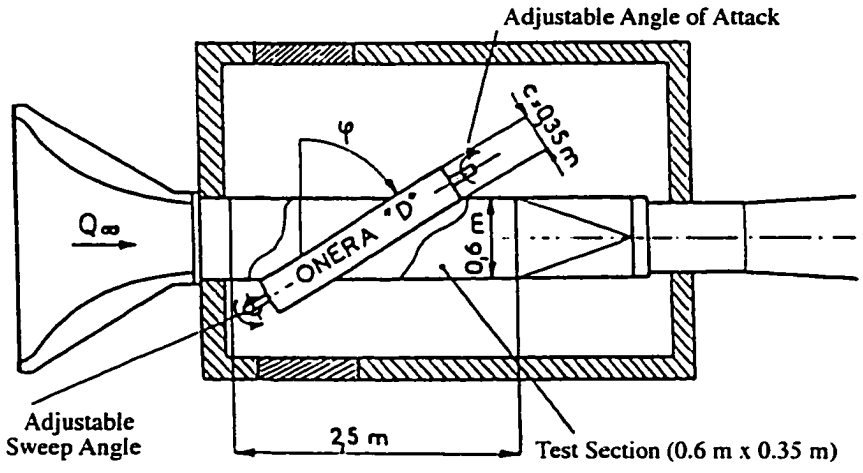

Figure 8.2: Experimental setup for the ONERA D-wing experiment (from [5])

airfoil geometry are shown. The relations for the airfoil geometry are given in Appendix II. The main objectives of these experiments were to develop data bases and empirical

correlations for fast transition prediction methods, as well as to gain more insight into the transition physics of swept wing flows. Therefore, a number of cases for different angles of attack α and sweep angles ϕ was investigated.

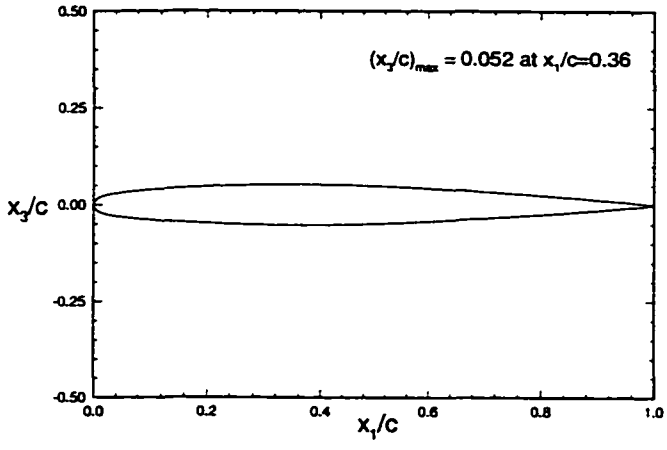

Figure 8.3: ONERA D-airfoil geometry

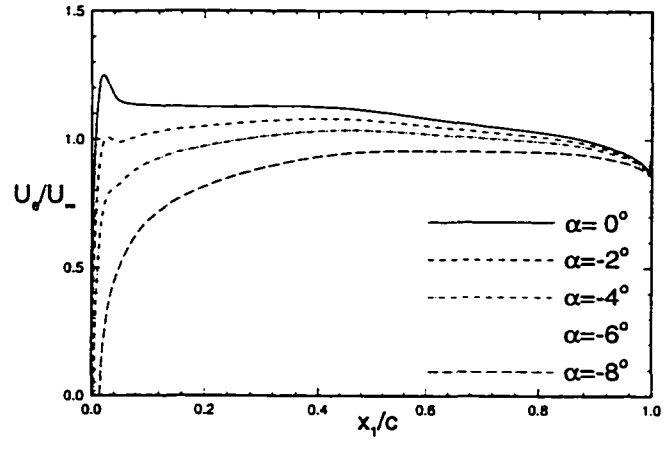

Figure 8.4: Outer velocity distributions for different angles of attack

For different angles of attack, figure 8.4 shows the outer velocity distributions on the upper wing surface. Clearly seen is the vanishing suction peak in the leading edge region with decreasing angles of attack. According to the explanation of the crossflow basics in Section 1.1, it is the adverse pressure gradient near the leading edge that

introduces flow physics which are not purely crossflow dominated. For that reason, the study in this chapter was performed for an outer flow that has a favorable pressure gradient over a large region of the chord.

8.3.1 Mean Flow Computation

Given the freestream conditions as in table 8.2, the outer flow distribution was obtained using the panel method as described in Section 3.1. In table 8.2, the Reynolds number is defined as $Re_\infty = Q^*_\infty \cdot c^*/\nu^*$. The mean flow profiles along the chord were

Table 8.2: Freestream conditions for the ONERA D-wing experiment

Chord length c	0.35 m
Freestream velocity Q^*_∞	80 m/s
Reynolds number Re_∞	1,840,000
Kinematic viscosity ν	$15.217 \cdot 10^{-6}$ m^2/s
Sweep angle ϕ	40°
Angle of attack α	-8°

computed using the solution method for the boundary layer equations that was derived in Section 3.2. For the directions tangential and perpendicular to the inviscid streamline, they are plotted at different streamwise locations in figures 8.5 and 8.6, respectively. It

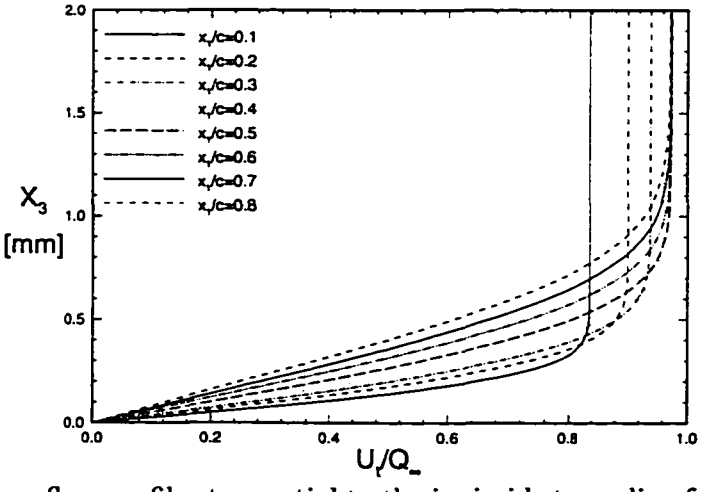

Figure 8.5: Mean flow profiles tangential to the inviscid streamline for α=-8° and ϕ=40°

is noted that the crossflow component U_c remains positive over the entire chord length, and thus, the present mean flow is purely crossflow dominated.

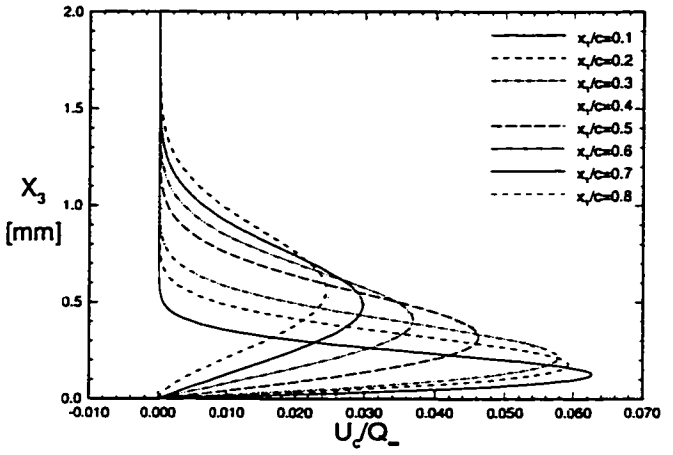

Figure 8.6: Mean crossflow profiles for α=-8° and ϕ=40°

For the boundary layer computations, a computational grid of 400 × 300 points was constructed in the x_1- and the x_3-direction, respectively. Starting at the stagnation point, both the chordwise and the normal coordinates were uniformly spaced up to a normal extension of x_3=15 which corresponds to about twice the maximum boundary layer thickness. For the chosen angle of attack, the stagnation point was found at x_1/c=0.014. Starting a new coordinate system at this point, the separation point of the flow was determined at x_1/c=0.89.

Characteristic parameters of the mean flow are shown in figure 8.7. Plotted are the outer pressure distribution, the Reynolds number in the chordwise direction $Re_x = (U_e^* \cdot x_1^*/\nu^*)^{1/2}$, the angle of the inviscid streamline Θ, the dimensional boundary layer and displacement thickness along the inviscid streamline, the similarity parameter $m=\frac{x_1^*}{U_e^*} \cdot \frac{dU_e^*}{dx_1^*}$, and the curvature term h_1. The boundary layer thickness shown in figure 8.7(d) is defined at a location where the velocity component tangential to the inviscid streamline U_t^* reaches a value of 99.9% of the outer velocity $U_{t,e}^*$.

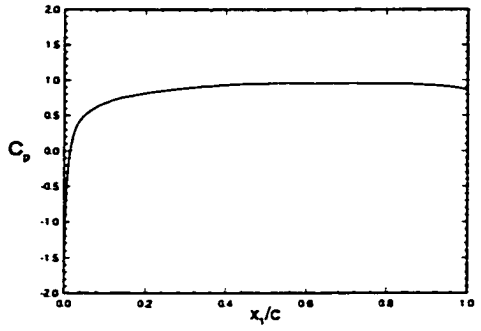

a) Pressure Distribution

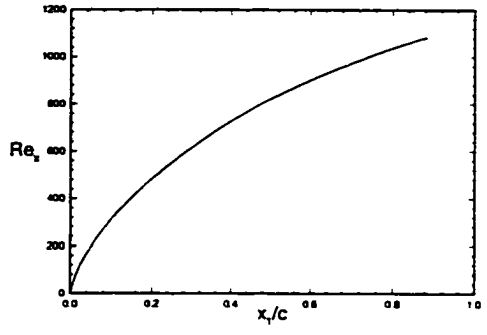

b) Reynolds number

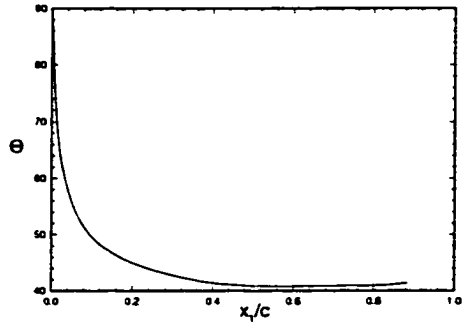

c) Angle of inviscid streamline

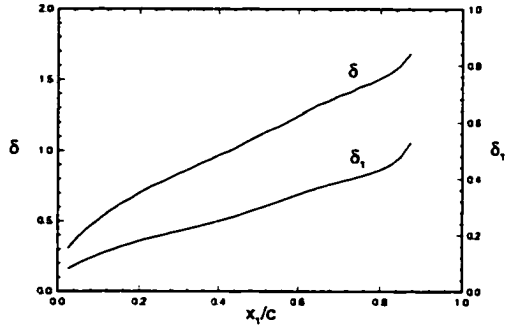

d) δ and δ_1 along inviscid streamline [mm]

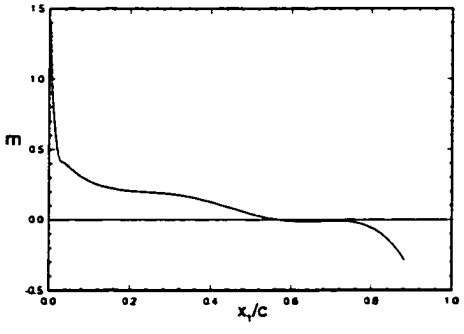

e) Similarity parameter

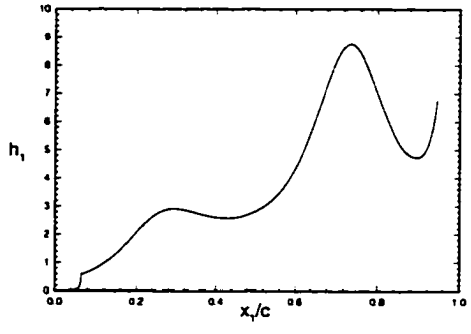

f) Chordwise curvature term

Figure 8.7: Mean flow parameters

8.3.2 Linear Stability Analysis

As in the previously investigated problems of Swept Hiemenz flow and the DLR Transition experiment, the stability of the attachment-line needs to be investigated prior

to any subsequent stability analysis. Using the local length scale close to the stagnation point $l^* = \sqrt{\nu^*/(dU_e^*/dx_1^*)}$=0.07mm and the constant outer velocity component in the spanwise direction $W_\infty^*=Q_\infty^* \cdot \sin \phi_\infty$=50.92 m/s, the Reynolds number in the spanwise direction is determined as $\overline{Re}=W_\infty^* \cdot l^*/\nu^*$=224.5, which is far below the numerically critical value of $\overline{Re}$=583 [93]. Hence, the attachment-line is assumed to be linearly stable.

Before the presentation of the results of the linear stability analysis, the applied computational grid for both the linear and nonlinear stability computations is described. The chordwise direction was devided into 200 points which corresponds to a step-size of Δx_1=0.005. In the normal direction, a grid of 51 points was distributed according to equation 8.1 up to a normal extension of x_3=15. Beyond that extension, another 51 points were spaced uniformly up to a maximum extension of x_3=75, which corresponds to about six to eight boundary layer thicknesses.

$$x_{3,i} = \frac{\Delta \cdot \eta_i}{1 + \frac{\Delta}{x_{3,max}} - \eta_i} \quad ; \quad \Delta = 3 \tag{8.1}$$

Since the purpose of this study is to investigate the nonlinear interaction of purely stationary disturbances, the linear stability analysis will be restricted to steady disturbances. First, a local analysis is performed in order to determine the neutral point of the stationary disturbances and the locally most amplified modes. Figure 8.8 shows the nondimensional spatial growth rates σ_1 based on the chordwise velocity component for stationary disturbances versus the spanwise wave number β_1 at different chordwise positions. At the investigated chordwise stations, the nondimensionalization is performed using the local length scale $l_0^* = \sqrt{\nu^* \cdot x_{1,0}^*/U_{e,0}^*}$. It can be seen that the unstable wave number band width increases in the chordwise direction, which is in agreement with the observations for Swept Hiemenz flow and in the DLR experiment. The neutral point for

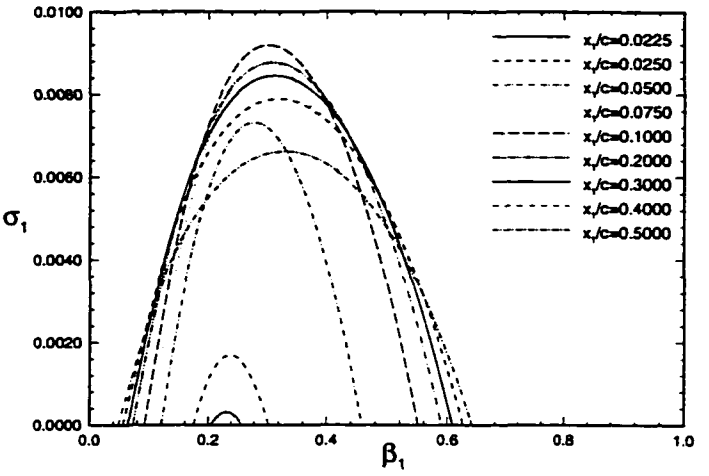

Figure 8.8: Spatial growth rates for steady disturbances from a local analysis

the stationary disturbances is found at $x_1/c \simeq 0.022$ for $\beta_1=0.225$ ($\lambda_{x_2}=1.9$mm). The locally most amplified wave number is determined as $\beta_1=0.302$ at $x_1/c=0.10$, where the chordwise wave number is $\alpha_1=(-0.31545,-0.00919)$. Table 8.3 contains the locally most amplified spanwise wave numbers, as well as the corresponding spatial growth rates, dimensional spanwise wavelengths and wave angles. As in Chapters 5 and 6, the wave angle represents the angle between the wave vector $\mathbf{k_{real}}$ and the angle of the inviscid

Table 8.3: Locally most amplified eigenpairs at different chordwise locations

x_1/c	σ_1 = max.	$\lambda_{x_2,\sigma_1=\max}$[mm]	$\beta_{1,\sigma_1=\max.}$	$\Psi_{\sigma_1=\max.}$
0.0225	0.00031	1.90	0.2288	86.58°
0.0250	0.00169	1.89	0.2361	86.58°
0.0500	0.00732	1.97	0.2790	86.74°
0.1000	0.00919	2.30	0.3020	86.66°
0.2000	0.00877	2.94	0.3085	87.11°
0.3000	0.00845	3.41	0.3137	87.31°
0.4000	0.00789	3.82	0.3159	87.62°
0.5000	0.00662	4.09	0.3271	88.14°

streamline. It is again observed that the wave angle of the most amplified stationary disturbances remains almost constant in the chordwise direction. The constant phase

lines of the most unstable stationary disturbances are inclined at angles less than five degrees with respect to the inviscid streamline and the vector of the most amplified wave points towards the convex side of the inviscid streamline.

Next, the most amplified spanwise wave number according to its spatial growth in the downstream direction is sought. Therefore, disturbances of a different spanwise wave number are introduced at x_1/c=0.02 and their spatial evolution downstream computed using the linear PSE. Figures 8.9 and 8.10 show the spatial growth rates ba-

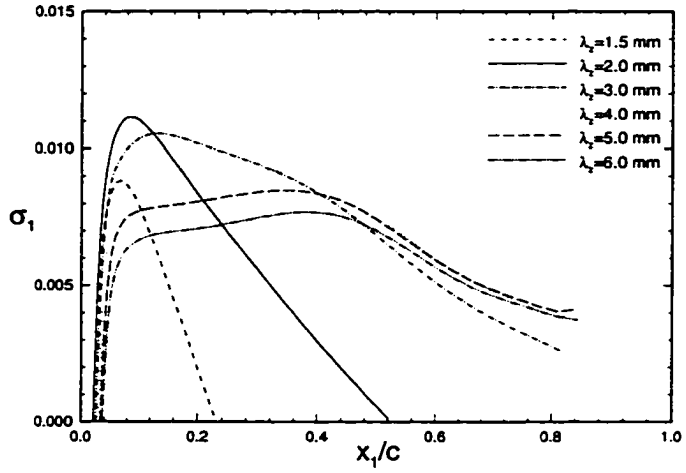

Figure 8.9: Spatial growth rates for steady disturbances from a PSE computation

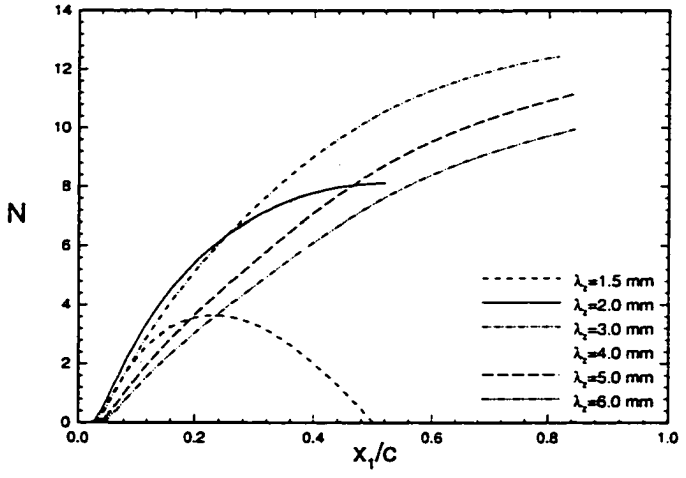

Figure 8.10: N-factors based on u_1 from a PSE computation

sed on the chordwise velocity component and the corresponding N-factors, respectively, that are obtained from a linear PSE computation. From figure 8.9, it is noted that the most amplified disturbance (λ_{max}=3mm) and its subharmonics with λ_{x_2}=1.5mm and λ_{x_2}=2mm behave according to the observations in the ASU experiment. A strong initial growth of the subharmonics (especially of the 2mm mode) is immediately followed by fast decay. Even though the wavelength of λ_{x_2} = 2 mm shows a strong initial amplification, the largest N-factor at x_1/c=0.80 is obtained for the disturbance with a spanwise wavelength of λ_{x_2} = 3 mm. This wavelength will be denoted as λ_{max} from now on. The maximal N-factors for the different wavelengths are given in table 8.4.

Table 8.4: N-factors of the most amplified stationary disturbances at $x_1/c = 0.80$

λ_{x_2}[mm]	3.0	4.0	5.0	6.0
N_{max}	12.35	12.00	10.97	9.77

For completeness, the stabilizing influence of considering the surface curvature in the computations is documented in figure 8.11. Plotted are the N-factors based on the

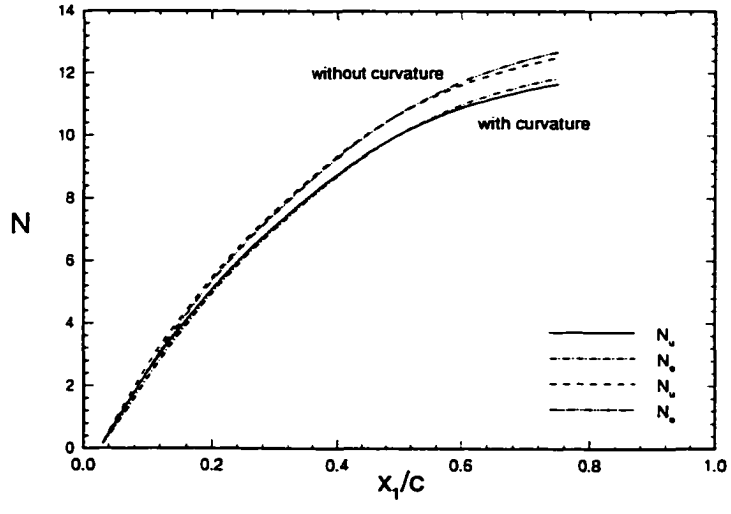

Figure 8.11: N-factors with and without surface curvature (λ_{x_2}=λ_{max})

disturbance energy and the chordwise velocity component. At x_1/c=0.5, the difference between the maximal N-factors obtained with and without curvature is about $\Delta N \simeq 0.75$, which is not negligible when considering that the experimentally observed transition location was between x_1/c=0.5 and x_1/c=0.6.

Concluding the linear stability analysis, a comparison of computed and experimentally obtained values is provided in table 8.5. Arnal et al. [10] reported an almost constant value of four for the ratio of the locally most amplified wavelength and the local boundary layer thickness along the chordwise direction. As shown in table 8.5, the agreement with the here obtained results is good.

Table 8.5: Ratios of the most amplified wavelength and the boundary layer thickness

x_1/c	λ_{x_2}[mm]	δ [mm]	λ_{x_2}/δ
0.1	2.30	0.51	4.5
0.2	2.94	0.70	4.2
0.3	3.41	0.84	4.1
0.4	3.82	0.97	3.9
0.5	4.09	1.11	3.7

8.3.3 Nonlinear Stability Analysis using the Implicit PSE

From the linear stability results, it is seen that the disturbance with a wavelength of $2/3 \cdot \lambda_{max}$ shows a strong initial growth that is followed be a rapid decay. Encouraged by this good qualitative agreement with the findings of the ASU experiment [4], this subsection documents results from nonlinear computations that attempt to qualitatively model the experimental observations of a passive transition control mechanism originating from leading edge roughness. For the solution of the nonlinear PSE, the newly developed, efficient and very robust implicit PSE solver documented in Chapter 7 is utilized. According to the experimental observations, four cases are considered :

1. "Natural transition", dominated by the most amplified disturbance (λ_{max}=3mm).

2. Forcing of the fundamental disturbance (λ_{max}=3mm).

3. Forcing of a subharmonic wave number-disturbance (λ_{x_2}=6mm).

4. Forcing of a superharmonic wave number-disturbance ($\lambda_{x_2}=2/3\cdot\lambda_{max}$=2mm).

An appropriate model for the forcing of selected disturbances by roughness elements requires an estimate of the initial disturbance amplitudes as given next, where the scaling influence of the receptivity coefficient is neglected. Taking the maximum boundary layer thickness of δ_0^* as length scale and the freestream velocity component in the chordwise direction U_∞^*=61.7m/s as velocity scale U_0^*, a typical time scale t_0^* is obtained. Assuming that this time scale is also representative for the location where the disturbances are introduced, the roughness height is estimated as in equation 8.2.

$$t_0^* = \frac{\delta_0^*}{U_0^*} = \frac{0.002\text{m}}{61.7\text{m/s}} = \frac{k_{rough}^*}{A \cdot U_\infty^*} = \text{const.} \;\; ; \;\; k_{rough}^* = A \cdot U_\infty^* \cdot t_0^* = A \cdot 0.002\text{m} \qquad (8.2)$$

Hence, an amplitude of A=0.002 corresponds to a roughness height of k_{rough}^*=4μm. This compares to the experimental value of k_{rough}^*=6μm [4]. Due to the lack of other information, and since this amplitude choice leads to realistic saturation amplitudes of the disturbances, A=0.2% is chosen as a base line amplitude to model the cases with forced disturbances. For the cases without forcing, an initial amplitude of A=0.008% is specified according to the ratio of k_{rough}^* and the distributed surface roughness in the experiment ($k_{rough}^*/k_{distrib}^*$=24). The four investigated cases are defined in table 8.6.

Table 8.6: Definition of the passive control cases

Case	λ_1 [mm]	λ_2 [mm]	λ_3 [mm]	A_1	A_2	A_3
1	3	-	-	0.008%	-	-
2	3	-	-	0.200%	-	-
3	6	3	2	0.200%	0.008%	0.008%
4	6	3	2	0.008%	0.008%	0.200%

8.3.3.1 Natural Transition (Case 1)

For the purpose of establishing a reference case that the cases with forced disturbances can be compared to, the case of a "natural transition" is considered first. The influence of a small distributed roughness height near the leading edge is modeled by assuming the dominance of the most amplified disturbance with a spanwise wavelength of λ_{x_2}=3mm and a small initial amplitude of A=0.008% in the downstream evolution.

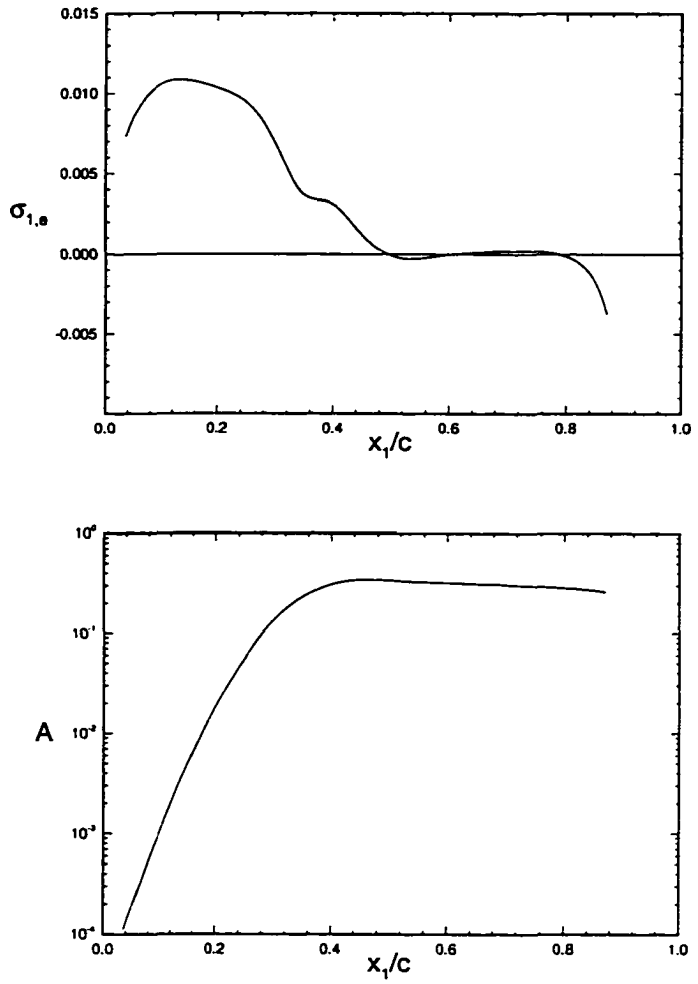

Figure 8.12: Growth rate and amplitudes for Case 1 (λ_{x_2}=3mm, A=0.008%)

The growth rate based on the disturbance energy and the u_1-amplitudes of the fundamental disturbance in the chordwise direction are plotted in figure 8.12. The u_1-

component of the 3mm mode grows over about 40% of the chord, and the growth rates based on disturbance energy does not saturate until $x_1/c \simeq 0.50$.

The amplitudes of the u_1-component of the 3mm mode reach a level of A=10% at x_1/c=0.28, and a final saturation amplitude of A=34.0% is reached at x_1/c=0.46.

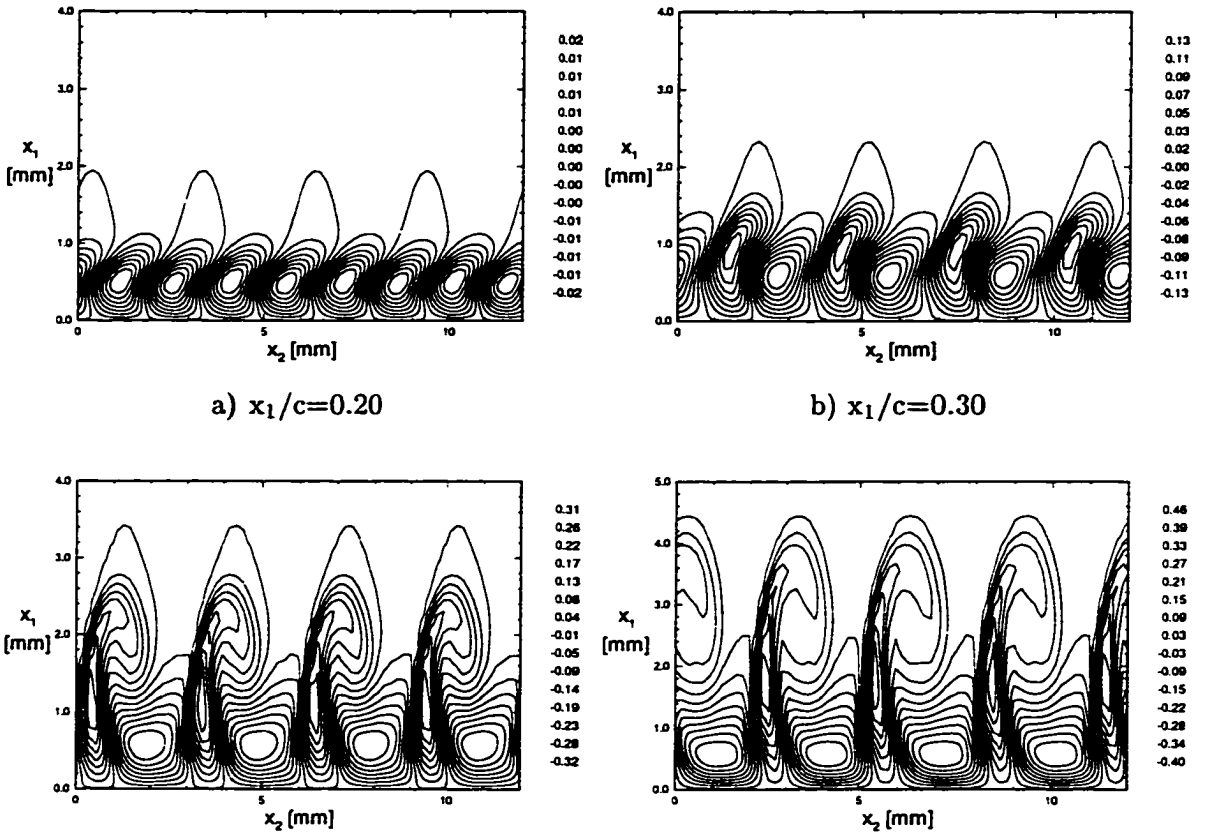

a) x_1/c=0.20 b) x_1/c=0.30

c) x_1/c=0.40 d) x_1/c=0.50

Figure 8.13: Contours of the u_1-disturbance at different streamwise locations (Case 1)

Figure 8.13 shows contours of the total u_1-disturbance component in the plane parallel to the leading edge. According to the fundamental wavelength, the crossflow vortices develop at a spanwise spacing of 3mm. The development of the total amplitude of the u_1-disturbance in the streamwise direction will be compared with the following cases in the summary at the end of this chapter.

8.3.3.2 Fundamental Forcing (Case 2)

Simulating the presence of roughness elements at a spanwise spacing of 3mm near the leading edge by increasing the initial amplitude of the 3mm disturbance from A=0.008% to A=0.2%, the disturbance evolution is largely modified in comparison to Case 1. Figure 8.14 shows the computed growth rate based on the disturbance energy

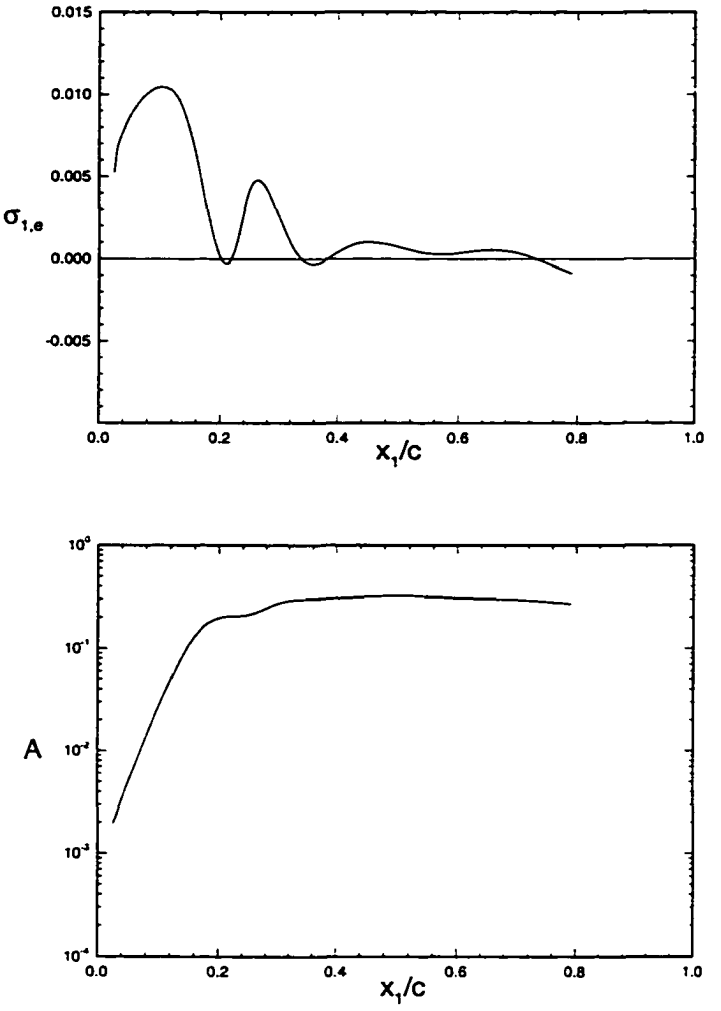

Figure 8.14: Growth rate and amplitudes for Case 2 (λ_{x_2}=3mm, A=0.2%)

and the amplitude of the fundamental u_1-disturbance component. Here, the amplitudes of the u_1-component reach a level of A=10% already at x_1/c=0.15, and after a stronger

secondary growth at x_1/c=0.26, the u_1-disturbance saturates at $x_1/c \simeq 0.50$ at an amplitude level of A=32%.

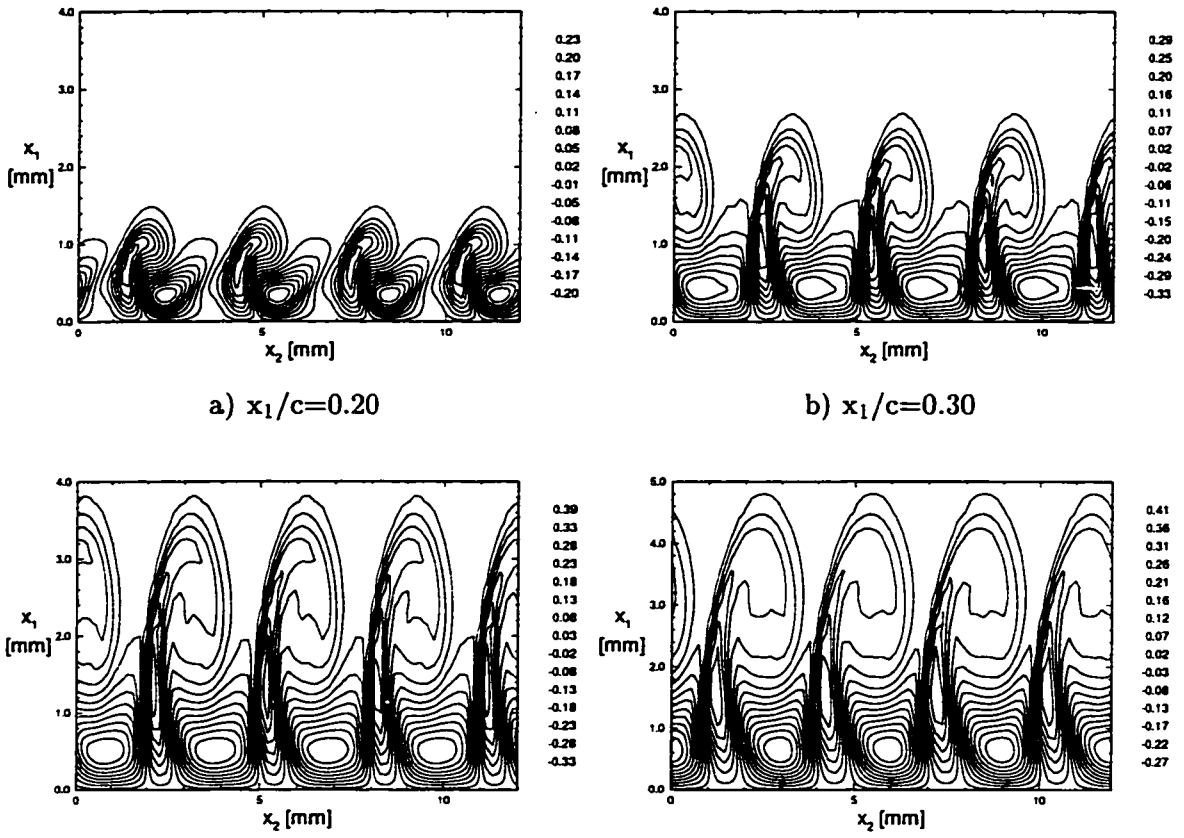

a) x_1/c=0.20 b) x_1/c=0.30

c) x_1/c=0.40 d) x_1/c=0.50

Figure 8.15: Contours of the u_1-disturbance at different streamwise locations (Case 2)

As for the "natural transition" in Case 1, figure 8.15 shows contours of the total u_1-disturbance. According to the higher initial amplitude of the disturbance, the distortion of the boundary layer by the presence of the crossflow vortices is observed much earlier than in Case 1. Here, a well-defined crossflow vortex with disturbance amplitudes of $A \simeq 0.30$ is already present at x_1/c=0.30. Otherwise, there is no qualitative change in the evolution of the crossflow vortices in comparison to Case 1.

8.3.3.3 Subharmonic Forcing (Case 3)

A qualitatively different disturbance evolution is observed when disturbances with a wavelength that is twice the most amplified wavelength are forced by placing roughness elements at a spanwise spacing of 6mm.

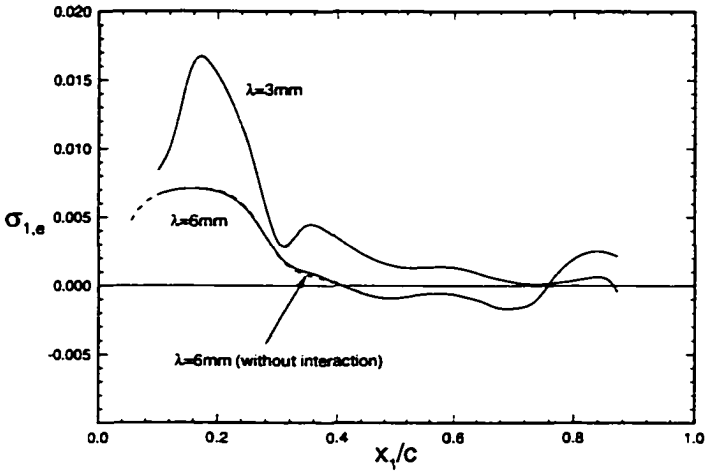

Figure 8.16: Growth rates for Case 3 (λ_1=6mm, A=0.2%; λ_2=3mm, A=0.008%; λ_3=2mm, A=0.008%)

Following the development of the forced disturbance and its first superharmonic, figures 8.16 shows the growth rates based on the disturbance energy. Also plotted is the growth rate of the 6mm disturbance with the same initial amplitude when there is no nonlinear interaction ($A_{\lambda_{2mm}} = A_{\lambda_{3mm}}$=0.). It is noted that the growth rate of the 3mm disturbance is largely modified due to the forcing of the 6mm disturbance in comparison with the previous two cases. This is caused by the large initial amplitude of the (1,0) mode (λ=6mm).

A disturbance can either grow on its own, or its growth can be initiated by the nonlinear interaction of other disturbances. Here, the nonlinear contribution from the (0,1) mode to the (0,2) mode (λ=3mm) is much larger than the initial amplitude of the 3mm mode. Thus, the linear growth of the 3mm mode is completely suppressed in favor

of its nonlinear excitation by the 6mm mode. It is also seen from figure 8.16 that the 6mm mode is hardly affected by the nonlinear interaction.

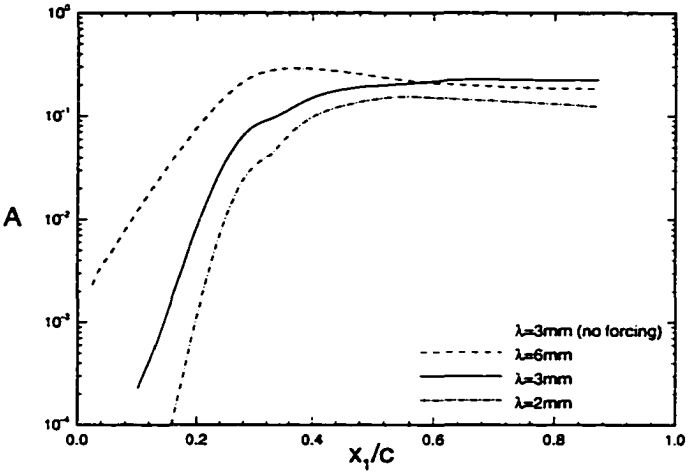

Figure 8.17: Amplitudes for Case 3 (λ_1=6mm, A=0.2%; λ_2=3mm, A=0.008%; λ_3=2mm, A=0.008%)

Figure 8.17 shows the u_1-disturbance amplitudes of the forced 6mm mode and its first two superharmonics. For comparison, the amplitude evolution of the 3mm mode in Case 1 is also plotted. The 6mm-disturbance forcing, that excites the 3mm mode nonlinearly, strongly affects the development of the 3mm mode. After an initially slower growth than in the natural case, the disturbances start to grow faster than in the reference case at $x_1/c \simeq 0.15$. Due to nonlinear interaction with the strong 6mm mode, they start saturating much earlier than in Case 1 at an amplitude level of $A \simeq 0.10$ near $x_1/c \simeq 0.30$. A secondary growth at $x_1/c \simeq 0.35$ delays the final saturation until $x_1/c \simeq 0.66$, where the amplitude level of the u_1-disturbance reaches a value of A=0.23. Hence, the growth of the most amplified disturbance is largely suppressed by the forced subharmonic 6mm mode. Despite the suppression of the most amplified 3mm mode, the large initial amplitude and the long growth of the 6mm mode until $x_1/c \simeq 0.40$ (see figure 8.16) in the present case would probably result in an earlier transition than in the reference case.

The qualitative difference of Case 3 to the two previous cases is clearly seen in the contour plots of the total u_1-disturbance in figure 8.18. Starting with a spanwise spacing of 6mm at $x_1/c=0.20$ that is due to the forced disturbances, the crossflow vortices are modified by the superharmonic disturbances starting at $x_1/c=0.35$. At this streamwise location, the 3mm and the 2mm modes have reached amplitude levels of A=0.11 and A=0.06, respectively. From figure 8.18(b), it is seen that the negative portion of the 6mm crossflow vortex devides into vortex structures with a smaller wavelength according to the superharmonic wave numbers. This wavelength modulation becomes stronger in the streamwise direction, and at $x_1/c=0.50$, new vortex structures with dif-

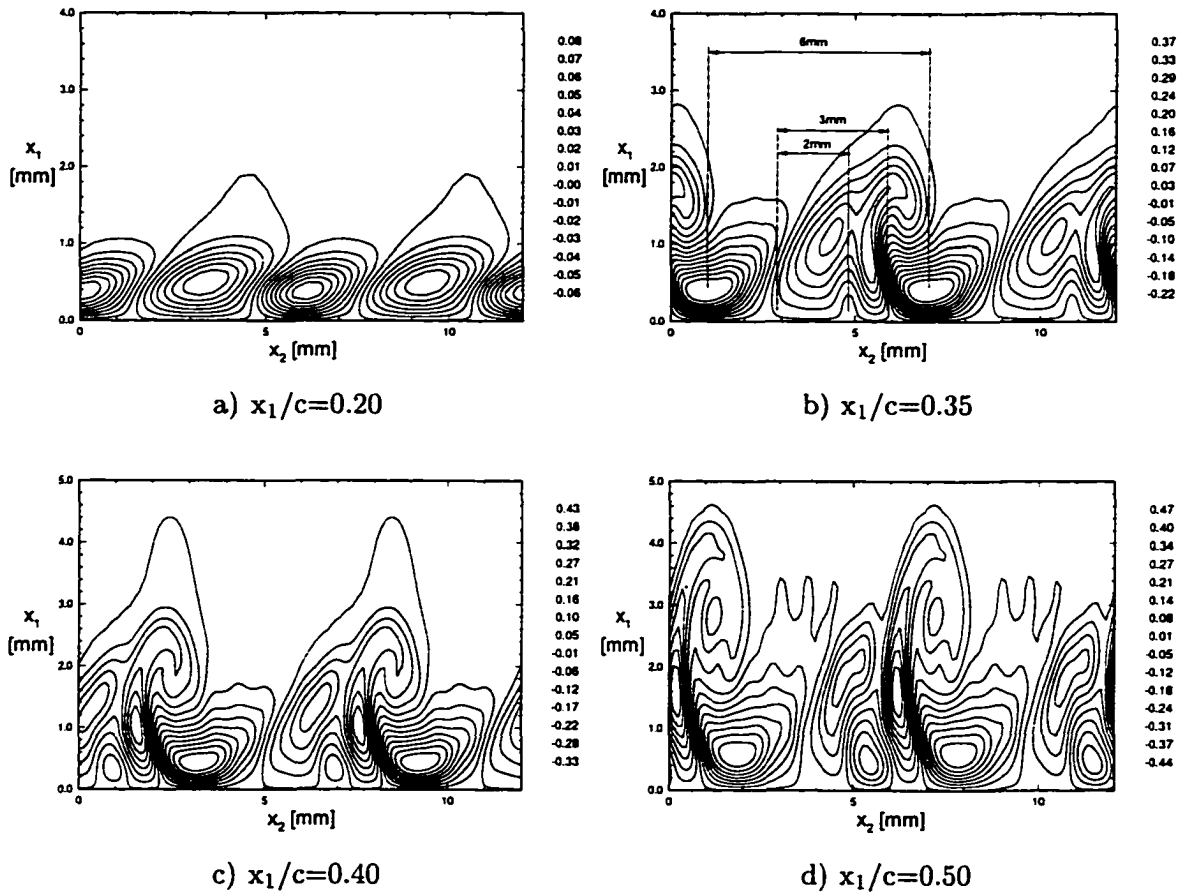

a) $x_1/c=0.20$ b) $x_1/c=0.35$

c) $x_1/c=0.40$ d) $x_1/c=0.50$

Figure 8.18: Contours of the u_1-disturbance at different streamwise locations (Case 3)

ferent wavelengths are present in the flow. In figure 8.18(d) the 6mm wavelength is still distinguishable. Also, the 3mm vortex from figure 8.18 has become more dominant and forms an intricate Λ-shaped vortex structure in conjunction with the 6mm vortex.

8.3.3.4 Superharmonic Forcing (Case 4)

From the observations in the ASU experiment [4], one expects that forcing the initially fast growing $2/3 \cdot \lambda_{max}$ mode is the most efficient means of controlling the transition onset. Therefore, the following case will simulate the placement of roughness

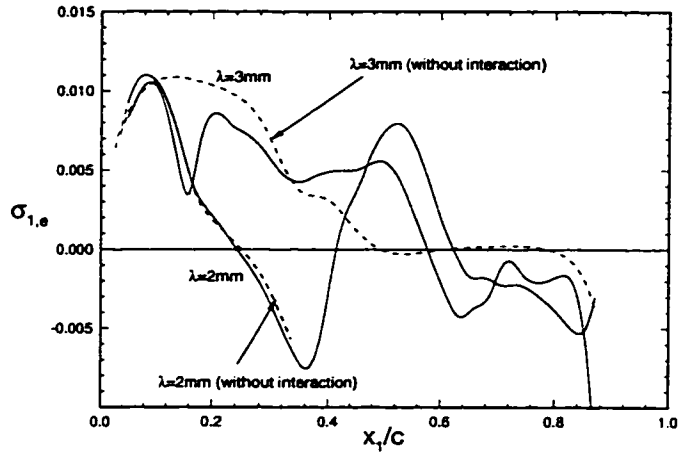

Figure 8.19: Growth rates for Case 4 (λ_1=6mm, A=0.008%; λ_2=3mm, A=0.008%; λ_3=2mm, A=0.2%)

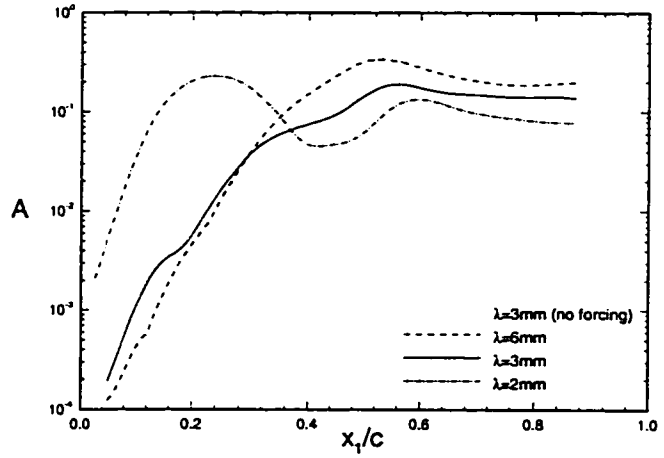

Figure 8.20: Amplitudes for Case 4 (λ_1=6mm, A=0.008%; λ_2=3mm, A=0.008%; λ_3=2mm, A=0.2%)

elements at a spanwise spacing of 2mm. Investigating the influence of the same roughness height as in Cases 2 and 3, the initial amplitude of the forced 2mm disturbance is specified as A=0.002. Figures 8.19 and 8.20 show the growth rates and the amplitudes of the forced disturbance and the fundamental disturbance with λ_1=3mm, as well as the growth rates of the 2mm and the 3mm disturbances with the same initial amplitudes in the cases without nonlinear interaction. In agreement with the observations in Case 3 where the development of the forced disturbances was not altered by nonlinear interaction, the evolution of the forced 2mm mode is not affected at all (see figure 8.19). However, the growth of the fundamental mode is largely affected, and its development shows significant differences to the previously investigated Cases 1-3.

First of all, the initial growth of the fundamental disturbance is largely suppressed, as seen in the early tendency towards a saturation at x_1/c=0.16. Secondly, three local maxima in the growth rate based on the disturbance energy are observed before the u_1-disturbance component saturates at the very late chordwise location of $x_1/c \simeq$ 0.55. Despite the late saturation, the earlier tendency towards saturation before the subsequent rise to two other growth rate maxima keeps the 3mm disturbance mode at very low amplitude levels. The u_1-component of the 3mm mode does not reach its maximal amplitude level of A=19.0% until x_1/c=0.56, and hence, the 3mm mode is considered to be succesfully supressed.

Due to its strong initial growth, however, the forced 2mm mode reaches high amplitude levels at early chordwise positions. For example, the amplitude level of A=0.20 is already reached at x_1/c=0.20. Due to the absence of experimental data regarding the disturbance amplitudes in the transition region, it is therefore not possible to make a statement about a succesful delay of the transition in the present case.

On the other hand, the experimentally observed mechanisms in the case of superharmonic disturbance forcing (see the description of the 8mm case in Section 8.2) are very well captured in the present simulation. This is shown in figure 8.21, where contours of the total u_1-disturbance are plotted at different streamwise stations. At x_1/c=0.20, the forced 2mm mode dominates the disturbance development and the crossflow vortices are spaced accordingly. At x_1/c=0.35, however, the relatively strong 6mm mode with an amplitude of A$\simeq$ 10% (see figure 8.20) is also distinguished. This represents the onset of a subharmonic disturbance growth which is in accordance to the results by Saric et al. [4]. There, the excitation of the 8mm mode initiated the growth of the 16mm and

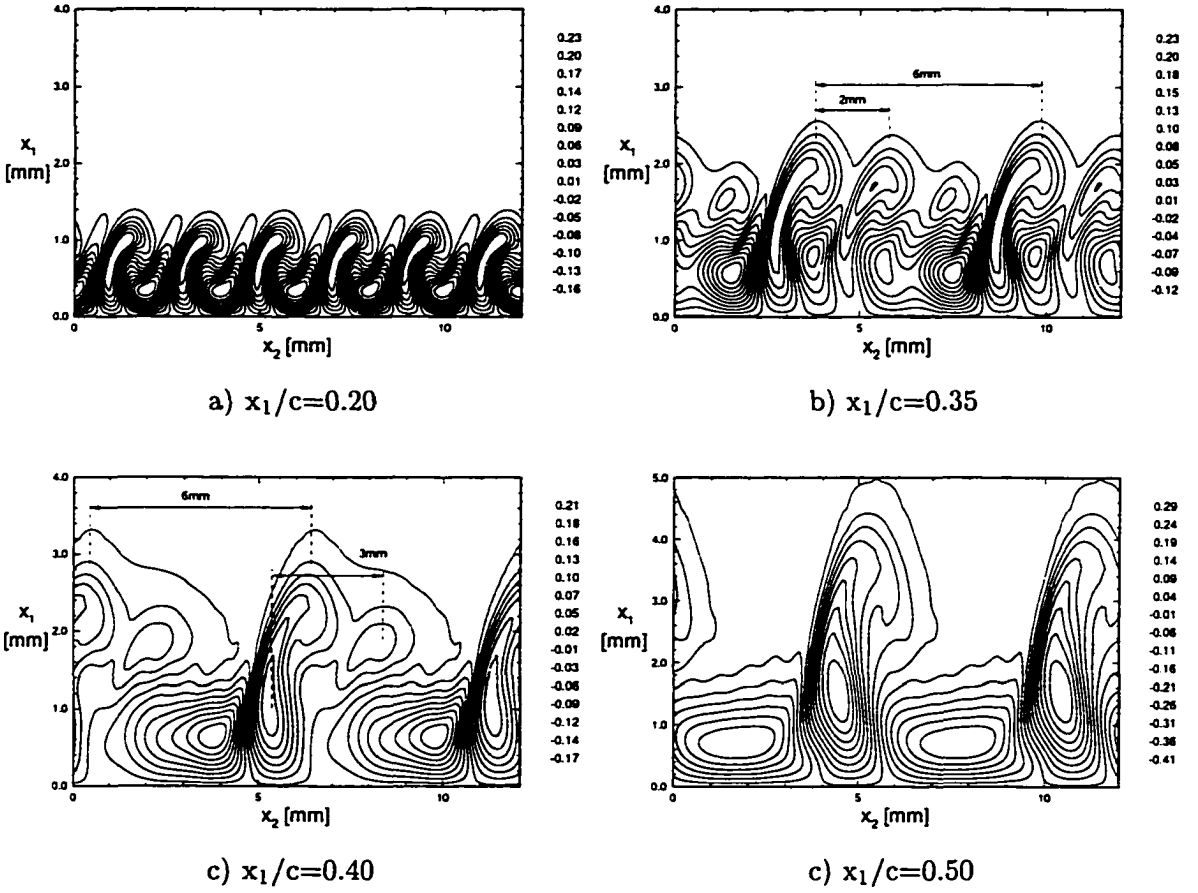

a) x_1/c=0.20 b) x_1/c=0.35

c) x_1/c=0.40 c) x_1/c=0.50

Figure 8.21: Contours of the u_1-disturbance at different streamwise locations (Case 4)

the 24mm modes. Further downstream at x_1/c=0.40, the footprint of the 2mm mode has disappeared and the 3mm mode can be distinguished instead. Finally at x_1/c=0.50, the 6mm mode clearly dominates the crossflow vortex pattern.

8.4 Summary

In the presented study and in accordance with the experimental observations by Saric et al. [4], the existence of a nonlinear wave-interaction mechanism in swept wing flows that favorably modifies the evolution of the most amplified disturbances has been documented. By a proper placement of micron-sized leading edge roughness near the neutral point of the stationary disturbances, the growth of the most amplified disturbance can be successfully delayed, if not suppressed, which indicates a possibly useful technique for the passive control of laminar three-dimensional boundary layer flows.

The computations using the implicit PSE solver were performed considering eight wave number modes in the Fourier space. For only three of these modes, however, the chordwise wave numbers were computed directly. The wave numbers of the remaining modes were then determined based on the mode with the largest amplitude. During

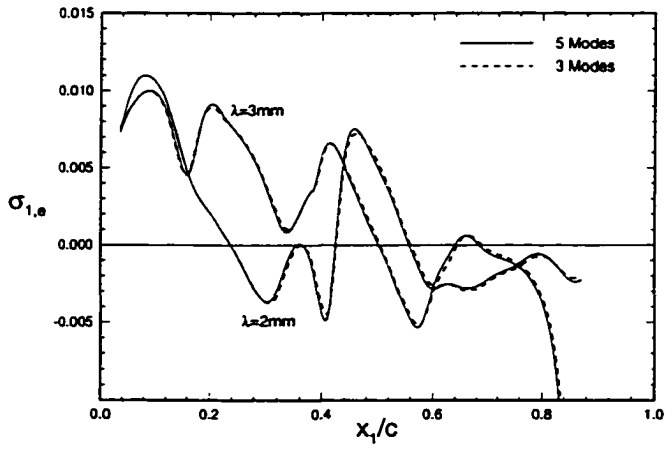

Figure 8.22: Growth rates for two iteration options ($A_{\lambda_1=3mm}$=0.02%; $A_{\lambda_2=2mm}$=0.2%)

the computations, no quantitative difference was observed when the wave numbers were computed directly for five modes instead. This is seen in figure 8.22 that shows the growth rates obtained for both iteration options.

Summarizing the presented cases, table 8.7 lists the initial amplitudes and the wavelengths of the considered disturbances, the chordwise locations where the disturbance components reach certain amplitude levels, as well as the maximal amplitude levels and their chordwise locations for the u_1-disturbance component.

Table 8.7: Evolution of the u_1-disturbance amplitudes

Case	λ [mm]	$A_{init.}$ [%]	x_1/c ($A_{10\%}$)	x_1/c ($A_{20\%}$)	A_{max} [%]	x_1/c (A_{max})
1	3	0.008	0.28	0.33	0.36	0.46
2	3	0.200	0.15	0.20	0.28	0.50
3	6	0.200	0.22	0.27	0.30	0.36
	3	0.008	0.34	0.53	0.23	0.66
	2	0.008	0.40	-	0.15	0.55
4	6	0.008	0.36	0.43	0.34	0.53
	3	0.008	0.46	-	0.19	0.56
	2	0.200	0.14	0.20	0.23	0.23

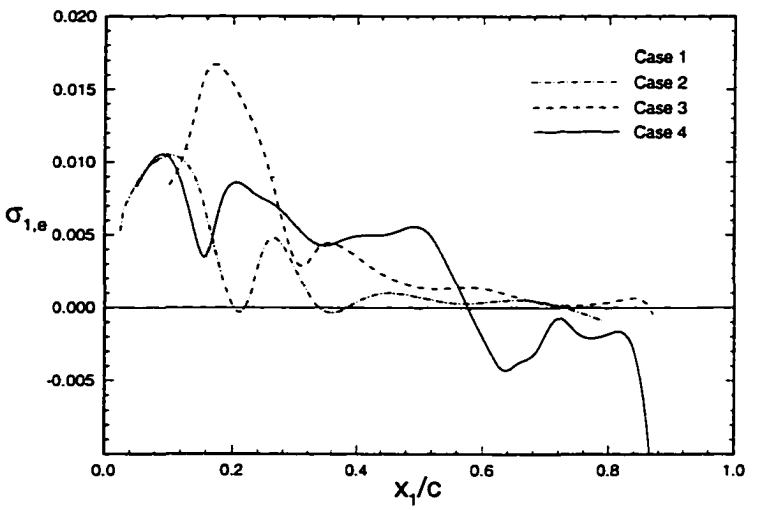

Figure 8.23: Growth rates of the fundamental disturbance (λ=3mm)

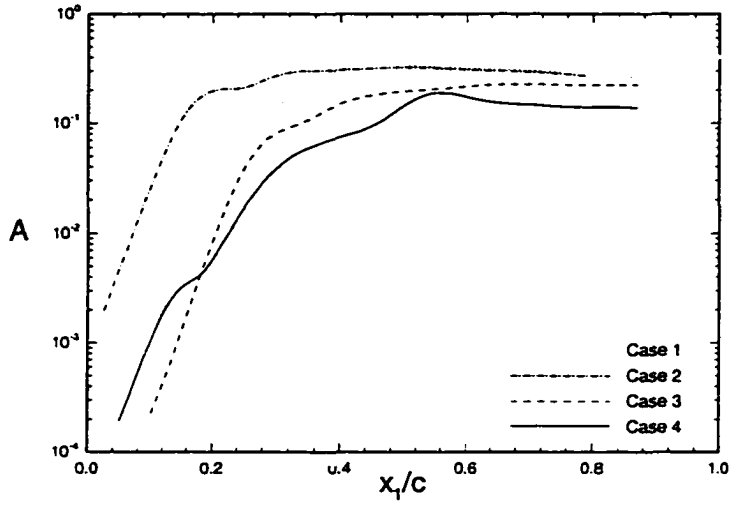

Figure 8.24: u_1-disturbance amplitudes of the fundamental disturbance (λ=3mm)

Considering the results presented in Subsections 8.4.2.1-8.4.2.4, the plots of the growth rates and the u_1-disturbance amplitudes of the fundamental disturbance for the four investigated cases (see figure 8.24), as well as the data listed in table 8.7, the following is concluded.

- Forcing the most amplified disturbance leads to an earlier disturbance saturation at the same high amplitude level as in the "natural transition" case which results in an earlier transition (Case 2).

- Forcing a subharmonic wave number disturbance with a wavelength larger than the most amplified one leads to an initial dominance of the forcing disturbance that results in a significant suppression of the most amplified mode. After the saturation of the forcing disturbance at high amplitude levels, the nonlinear disturbance interaction causes a break-up of the forced disturbance into its superharmonics (Case 3).

- Forcing a superharmonic wave number disturbance leads to a very strong initial growth of the forced disturbance that entirely suppresses the most amplified disturbances over large regions of the chord. After its strong initial growth, the forced disturbance saturates early and its decay gives rise to the growth of subharmonic wave number disturbances. These become dominant in the downstream direction and eventually lead to transition, if the transition was not caused earlier by the forced disturbance (Case 4).

However, for the prediction of the transition onset in comparison with experimental data, the evolution of the total disturbance amplitude rather than the amplitudes of individual modes needs to be considered. Concluding this chapter, figure 8.25 presents the amplitude evolution of the total u_1-disturbance component for the four different cases. Plotted is an average of the total disturbance quantity in the spanwise direction.

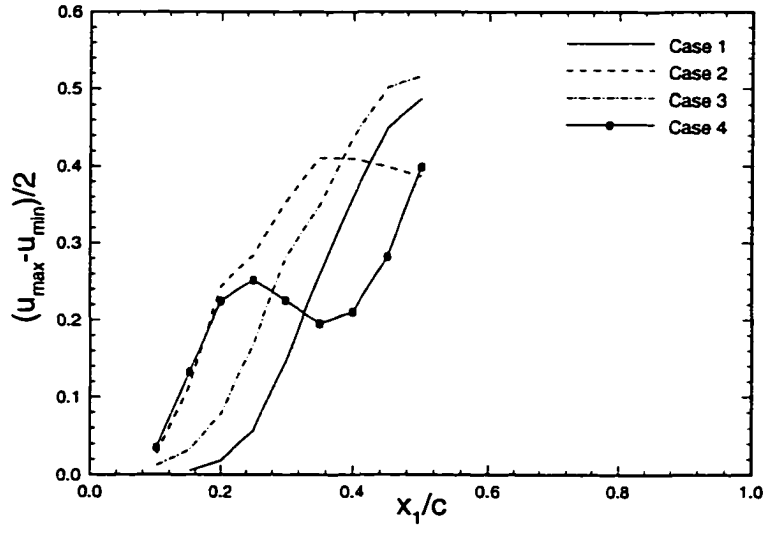

Figure 8.25: Amplitude evolution for the total u_1-disturbance component

In agreement with the experimental observations (see Section 8.2) and confirming the conclusions for the evolution of the individual modes, the following observations

can be made. Both Cases 2 and 3 would definetely cause an earlier transition, since the region of a strong rise in the amplitudes is moved towards the leading edge in comparison with the "natural transition" in Case 1. In contrast, the development of the total disturbance amplitude in Case 4 exactly corresponds to the experimental observations for the case with a succesful delay of the transition. A strong initial amplitude growth is followed by a region of amplitude saturation (A=0.25 at x_1/c=0.25) and amplitude decay, before a second region of amplitude growth sets in at x_1/c=0.40. Hence, the region of a second amplitude growth in Case 4 is located about 10% chord behind the corresponding region in the "natural transition" case. As mentioned before, due to the lack of experimental data for the ONERA D-wing, a strong statement about a succesfully delayed transition cannot be made.

For practical applications of this mechanism, the challenge consists in decreasing the primary peak in the total disturbance amplitude. From the conducted research and the experimental results, it is assumed that both the maximum of the primary saturation amplitude and its chordwise location depend on the freestream Reynolds number, on the individual height of the distributed roughness of the wing surface and of the roughness elements, as well as on the ratio of the two roughness heigths.

CHAPTER 9

CONCLUSIONS

9.1 Overview

The linear, nonlinear, and secondary stability of incompressible three-dimensional boundary layers was numerically investigated using PSE methods. Using a fourth-order-accurate compact scheme formulation in body-oriented coordinates, the accuracy of the developed methods and algorithms was validated using the model problem of Swept Hiemenz flow and the results of the DLR Transition experiment on a swept flat plate. Both explicit and implicit solution algorithms for the PSE were presented, and their efficiency and robustness documented. The confirmation of an experimentally observed passive control mechanism for the laminar-turbulent transition on infinite swept wings concludes the presentation of the results.

In Chapter 1, the scope of the present research was motivated and outlined. A survey of the literature on the stability of three-dimensional boundary layer flows was given in Chapter 2. Beginning with a historical review of the research on the stability of the considered flows, the survey focused on relevant experimental work, theoretical developments and numerical methods.

Chapter 3 explained the approach to the solution of the boundary layer equations for infinite swept geometries. Using the developed fourth-order-accurate compact scheme formulation, the mean flows for the DLR Transition experiment (Chapter 6) and for the ONERA D-wing experiment (Chapter 8) were computed directly from the outer velocity distributions, which is in contrast to previous work.

The development of the explicit formulation for the solution of the PSE, the documentation of the developed local and adapted global solver for the arising large eigenvalue problems of the established Floquet Theory, as well as the present understanding of the secondary instability mechanism were the focuses of Chapter 4.

In Chapters 5 and 6, extensive linear and nonlinear stability analyses preceded a detailed investigation of the secondary instability in the highly nonlinear region of disturbance saturation. Documenting the developed implicit solution method for the PSE, as well as its efficiency and robustness in comparison with the explicit approach in Chapter 7, the implicit method was used for the investigation of a passive laminar flow control method using leading edge roughness elements on the ONERA D-wing in Chapter 8.

9.2 Discussion

The developed PSE methods represent a powerful tool for the detailed analysis of transitional three-dimensional boundary layer flows. If used as a hybrid of the explicit solution method in the region of moderate nonlinearity, and the implicit solution method in the later region of nonlinear saturation and secondary instability, they are very effective in accurately capturing and predicting experimentally observed flow phenomena related to the laminar-turbulent transition.

The stability of a three-dimensional boundary layer immediately prior to transition was studied by considering the model of a steady mean flow that is modified by the presence of a stationary crossflow vortex. Due to the action of the stationary vortices, the boundary layer is largely distorted and becomes susceptible to high-frequency disturbances. Pursuing one possible approach of the investigation of this secondary instability

mechanism, the modified mean flow was computed using the PSE and then investigated for its secondary instability characteristics using temporal Floquet Theory. In the region of a strong secondary instability, connections from both the linear eigenvalue spectrum of the undisturbed mean flow and from the continuous spectrum to highly unstable secondary eigenvalues could be established. It is concluded that the receptivity to high-frequency disturbances in the region of a strong boundary layer distortion might be one path by which the secondary disturbances enter the boundary layer from the continuous outer spectrum.

In the investigation using the temporal Floquet Theory, the utilization of the Implicitly Restarted Arnoldi Method proved to be very efficient for the solution of selected regions of interest in the eigenvalue spectrum of the secondary disturbances.

Modeling the secondary instability in a more physical and direct approach using the spatial frame work of the PSE, a second approach was pursued. In agreement with the definition of the secondary instability given in Chapter 4, an explosive growth of high-frequency disturbances was observed in the highly nonlinear region of amplitude saturation. There, the development of a counter-clockwise rotating secondary vortex close to the wall, as well as the splitting of large vortex structures into several weaker vortices was observed. From DNS-computations, it was reported that these smaller vortices eventually lead to transition. It is argued that the nonlinear interaction of stationary and traveling disturbances is important for the strong growth of the secondary disturbances.

From both the Floquet Theory approach and the PSE computations for the investigation of the secondary instability, the onset of secondary instabilities was found for saturation amplitudes of the stationary disturbances of $A \simeq 10\%$.

Starting from PSE results that were found in good agreement with the measurements, a temporal investigation of the secondary instability in the DLR Transition experiment resulted in the documentation of an absolute instability in the region of nonlinear amplitude saturation. It is this absolute instability that might explain experimental observations of a time-dependent explosive growth of high-frequency disturbances.

Finally, the basic physical mechanisms of an experimentally detected passive laminar flow control mechanism on infinite swept wings were modeled using the implicit PSE formulation. For the ONERA D-wing, the presence of micron-sized roughness elements near the leading edge was modeled by forcing different wave number disturbances. It was found that forcing a superharmonic wave number disturbance with a wave length of $\lambda_{x_2}=2/3\cdot\lambda_{x_2,max}$ entirely suppresses the most amplified disturbance with a wave length of $\lambda_{x_2,max}$ over large regions of the chord. This is due to a strong initial growth of the forced disturbance. The subsequent decay of the forced disturbance gives rise to the growth of subharmonic wave number disturbances that eventually cause transition. For practical applications, it is crucial to limit the initial growth of the forced disturbance in order to avoid an earlier transition than in the natural transition case due to the disturbance forcing.

9.3 Recommendations for Future Research

In spite of the variety of presented applications of nonlinear PSE methods in the research community, their implementation for large-scale parameter studies demanded by the industry has not yet been accomplished. Further, the full potential of PSE methods is still to be utilized by developing them for fully three-dimensional flows without the assumption of infinite geometries. Finally, most of the flows across swept geometries

that are of practical interest are dominated by both the crossflow and the Tollmien-Schlichting instabilities. The physics of these flows are more complex than in the purely crossflow-instability dominated flows investigated in the presented work. Thus, the key areas in which future research is recommended are as follows :

- Optimizing the computational efficiency of the PSE methods by implementing multiprocessor algorithms.
- Application of the nonlinear PSE to a systematic investigation of flows where CF- and TS-instabilities are present.
- Further investigation of passive and hybrid laminar flow control mechanisms on swept wings.
- Adapting and implementing nonlinear PSE methods into design-packages for industrial applications.
- Extending the PSE methods to a fully three-dimensional formulation.

APPENDIX I

DEFINITION OF ANGLES AND COORDINATE SYSTEMS

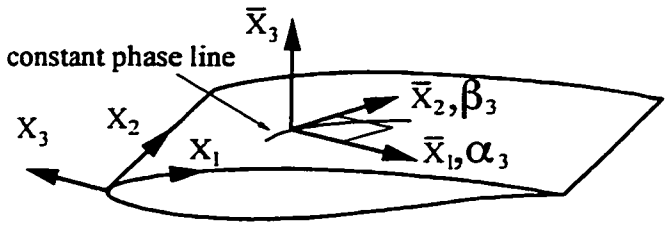

Figure I.1: Body-fixed and Galilean coordinate system

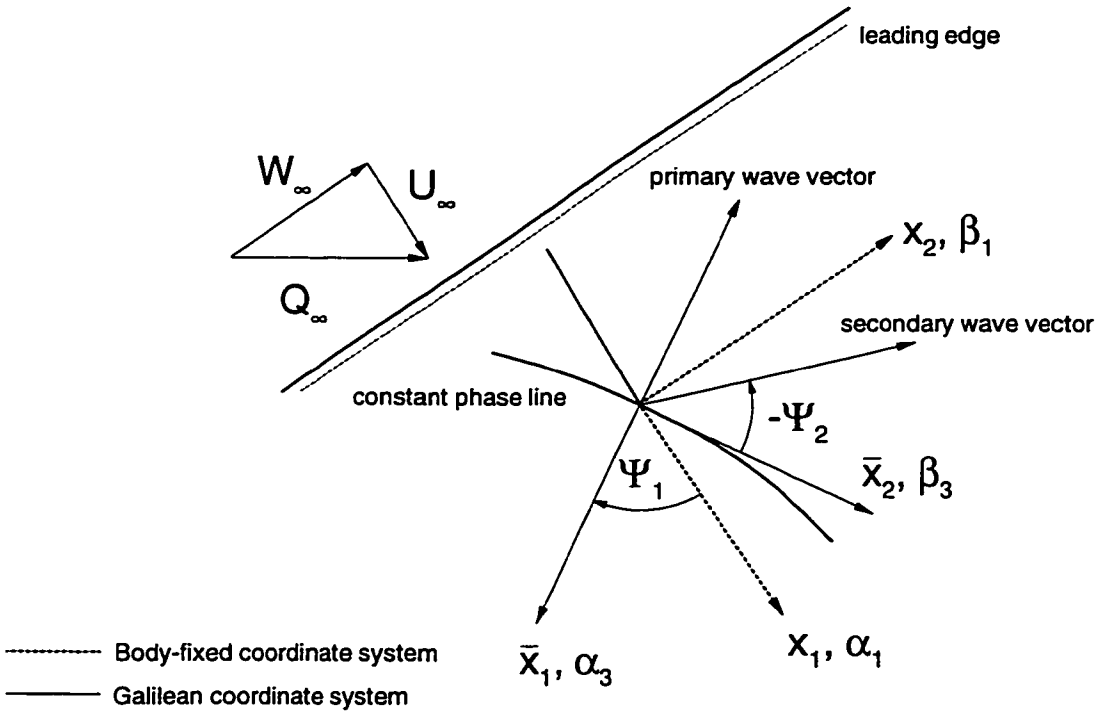

Figure I.2: Angle definitions

APPENDIX II

ONERA D SYMMETRIC WING SECTION

The profile is generated using the following formulas [96].

$$P(x/c) = \sum_{i=0}^{n}$$

For $x/c \leq 0.044$:

$$z/c = \sqrt{x/c} \cdot P(x/c)$$

$$a0 = 0.189830875843790$$

$$a1 = 0.31813568315041E - 1$$

$$a2 = -0.79875599950822E2$$

$$a3 = 0.19826412221164E4$$

$$a4 = -0.75862963116995E5$$

$$a4 = -0.17124203429644E5$$

$$a5 = -0.83765417234613E4$$

$$a6 = 0.89884596073744E6$$

$$a7 = -0.35691922706000E7$$

For $0.044 \leq x/c \leq 0.945$:

$$z/c = P(x/c)$$

$$\begin{aligned}
a0 &= 0.205117E-1 \\
a1 &= 0.27338051409795 \\
a2 &= -0.12221782415231E1 \\
a3 &= 0.3886472060892E1 \\
a4 &= -0.75862963116995E1 \\
a5 &= 0.68359355107744E1 \\
a6 &= -0.73185676985056 \\
a7 &= -0.27540347977852E1 \\
a8 &= 0.12790983175276E1
\end{aligned}$$

For $0.945 \leq x/c \leq 1.0$:

$$z/c = -0.127 \cdot (x/c - 0.945) + 0.0077958$$

BIBLIOGRAPHY

[1] Lehoucq, R., Sorensen, D., and Yang, C., "ARPACK Users Guide," *ftp://ftp.caam.rice.edu/pub/software/ARPACK*, Mar. 1997.

[2] Deyhle, H. and Bippes, H., "Disturbance growth in an unstable three-dimensional boundary layer and its dependence on environmental conditions," *Journal of Fluid Mechanics*, Vol. 316, Jun. 1996, pp. 73–113.

[3] Wagner, M., "Numerische Untersuchungen zum laminar-turbulenten Übergang in zwei- und dreidimensionalen Grenzschichten," *DLR-FB 92-36*, Jul. 1992.

[4] Saric, W., Carillo, R., and Reibert, M., "Leading edge roughness as a transition control mechanism," *AIAA Paper 98-0781*, Jan. 1998.

[5] Coustols, E., "Stabilite et Transition en Encoulement tridimensional : Cas des Ailes en Fleche," *Dissertation*, L'Ecole National Superieure, Jun. 1983.

[6] Gray, W., "The effects of wing sweep on laminar flow," 1952, RAE TM 255, (ARC 14, 929).

[7] Gregory, N. and Love, E., "Laminar flow on a swept leading edge," Oct. 1965, National Physical Lab., Final Progress Report, NPL Aero. Memo., Vol. 26.

[8] Gaster, M., "Laminar flow on a swept leading edge - final progress report," *The Aeronautical Quarterly*, Vol. 18, May 1967, pp. 165–184.

[9] Pfenninger, W., "Laminar flow control - Laminarization. Special course on concepts for drag reduction," Mar. 1977, AGARD Report 654.

[10] Arnal, D., Coustols, E., and Juillen, J., "Experimental and theoretical study of transition phenomena on an infinite swept wing," *Recherche Aérospatiale*, Vol. 4, 1984, pp. 39–54.

[11] Arnal, D. and Juillen, J., "Three-dimensional transition studies at ONERA/CERT," *AIAA Paper 87-1335*, Jun. 1987.

[12] Arnal, D., Gasparian, G., and Salinas, H., "Recent advances in theoretical methods for laminar-turbulent transition-prediction," *AIAA Paper 98-0223*, Jan. 1998.

[13] Nitschke-Kowsky, P., "Experimentelle Untersuchungen zu Stabilität und Umschlag dreidimensionaler Grenzschichten," *DLR-FB 86-24*, Jun. 1986.

[14] Bippes, H. and Nitschke-Kowsky, P., "Experimental study of instability modes in a three-dimensional boundary layer," *AIAA Paper 87-1336*, Jun. 1987.

[15] Müller, B. and Bippes, H., "Experimental study of instability modes in a three-dimensional bounday layer," 1988, Proceedings AGARD Symposium on Fluid Dynamics of 3D-turbulent shear flows and transition, Cesme, Turkey, AGARD CP-438.

[16] Fischer, T. and Dallmann, U., "Theoretical investigation of secondary instability of three-dimensional boundary layer flows with application to the DFVLR-F5 model wing," *DLR-FB 87-44*, Sep. 1987.

[17] Bippes, H., Müller, B., and Wagner, M., "Measurements and stability calculations of the disturbance growth in an unstable three-dimensional boundary layer," *Physics of Fluids*, Vol. 3, No. 10, 1991, pp. 2371–2377.

[18] Deyhle, H., Hoehler, G., and Bippes, H., "Experimental investigation of instability wave propagation in a three-dimensional boundary layer flow," *AIAA Journal*, Vol. 31, Apr. 1993, pp. 637–645.

[19] Takagi, S. and Itoh, N., "Observation of traveling waves in the three-dimensional boundary layer along a yawed cylinder," *Fluid Dynamics Research*, Vol. 14, 1994, pp. 167–189.

[20] Kohama, Y., Onodera, T., and Egami, Y., "Design and control of crossflow instability field," *IUTAM Symposium on Nonlinear Instability and Transition in 3D-Boundary Layers*, Kluwer Academic Publishers, Jun. 1996, pp. 147–156.

[21] Takagi, S., Itoh, N., and Tokugawa, N., "Characteristics of streamline-curvature disturbances in a rotating-disc flow," *AIAA Paper 98-0341*, Jan. 1998.

[22] Mack, L., "Three-dimensional effects in boundary layer stability," *Twelfth Symposium on Naval Hydrodynamics*, Jun. 1978, pp. 1–31.

[23] Malik, M., Li, F., and Chang, C., "Crossflow disturbances in three-dimensional boundary layers: Nonlinear development, wave interaction and secondary instability," *Journal of Fluid Mechanics*, Vol. 268, Jun. 1994, pp. 1–36.

[24] Saric, W. and Yeates, L., "Experiments on the stability of crossflow vortices in swept wing flows," *AIAA Paper 85-0493*, Jan. 1985.

[25] Reed, H., "Wave interactions in swept wing flows," *Physics of Fluids*, Vol. 30, No. 11, 1987, pp. 3419–3426.

[26] Dagenhart, J., Saric, W., Mousseux, M., and Stack, J., "Crossflow-vortex instability and transition on a 45 degree swept wing," *AIAA Paper 89-1892*, Jun. 1989.

[27] Kohama, Y., Saric, W., and Hoos, J., "A high-frequency secondary instability of crossflow vortices that leads to transition," *Proceedings R.Ae.S. Boundary Layer Transition and Control*, Cambridge U.K., Apr. 1991.

[28] Radeztsky, R., Reibert, M., and Saric, W., "Development of stationary crossflow vortices on a swept wing," *AIAA Paper 94-2373*, Jun. 1994.

[29] Reibert, M., Saric, W., and Carillo, R., "Experiments in nonlinear saturation of stationary crossflow vortices in a swept wing boundary layer," *AIAA Paper 96-0184*, Jan. 1996.

[30] Chapman, K., Glauser, M., Reibert, M., and Saric, W., "A multi-point correlation analysis of crossflow-dominated boundary layer," *AIAA Paper 96-0186*, Jan. 1998.

[31] Chapman, K., Reibert, M., Saric, W., and Glauser, M., "Boundary layer transition detection and structure identification through surface shear stress measurements." *AIAA Paper 98-0782*, Jan. 1998.

[32] Poll, D., "Some observations of the transition process on the winward face of long yawed cylinder," *Journal of Fluid Mechanics*, Vol. 150, 1985, pp. 329–356.

[33] Kachanov, Y., "Generation, development and interaction of instability modes inswept-wing boundary layer," *IUTAM Symposium on Nonlinear Instability and Transition in 3D-Boundary Layers*, Kluwer Academic Publishers, Jun. 1996, pp. 115–132.

[34] Gregory, N., Stuart, J., and Walker, W., "On the stability of three-dimensional boundary layers with application to the flow due to a rotating disc," *Philosophical Transactions of the Royal Society of London*, 1955, pp. 155–198.

[35] Mack, L., "Boundary layer stability theory," Nov. 1969, JPL Report No. 900-277.

[36] Gaster, M., "A note on a relation between temporally and spatially increasing disturbances in hydrodynamic stability," *Journal of Fluid Mechanics*, Vol. 14, 1962, pp. 222–224.

[37] Saric, W. and Nayfeh, A., "Nonparallel stability of boundary layers with pressure gradients and suction," 1988, AGARD Report No.224.

[38] Drazin, P. and Reid, W., *Hydrodynamic Stability*, Cambridge University Press, 1981.

[39] Choudhari, M., Ng, L., and Streett, C., "A general approach for the prediction of localized instability generation in boundary layer flows," *Proceedings R.Ae.S. Boundary Layer Transition and Control*, Cambridge U.K., Apr. 1991.

[40] Herbert, T. and Bertolotti, F., "Stability analysis of non-parallel boundary layers," *Bulletin of the American Physical Society*, Vol. 32, No. 10, 1987, pp. 2079.

[41] Herbert, T., "Boundary layer transition - analysis and prediction revisited," *AIAA Paper 91-0737*, Jan. 1991.

[42] Herbert, T., "Progress in applied transition analysis," *AIAA Paper 96-1993*, Jun. 1996.

[43] Herbert, T., "Transition analysis of flows over aerodynamic bodies," *AIAA Paper 96-1908*, Jun. 1996.

[44] Herbert, T., "Parabolized stability equations," *Annual Review of Fluid Mechanics*, Vol. 29, 1997, pp. 245–283.

[45] Herbert, T., "On the stability of three-dimensional boundary layers," *AIAA Paper 97-1961*, Jun. 1997.

[46] Malik, M., Chuang, S., and Hussaini, M., "Accurate numerical solution of compressible, linear stability equations," *ZAMP*, Vol. 33, No. 2, 1982, pp. 189–201.

[47] Lele, S., "Compact finite difference schemes with spectral-like resolution," *Journal of Computational Physics*, Vol. 103, 1992, pp. 16–42.

[48] Li, F. and Malik, M., "Mathematical nature of parabolized stability equations," *Laminar-Turbulent Transition*, edited by R. Kobayashi, Springer Verlag, New York, 1995, pp. 205–212.

[49] Bieler, H., "Theoretische Untersuchungen über primäre Instabilitäten in dreidimensionalen Grenzschichtströmungen," *DLR-FB 86-54*, 1986.

[50] Balakumar, P. and Malik, M., "Waves produced from a harmonic point source in a supersonic boundary layer flow," *Journal of Fluid Mechanics*, Vol. 245, Dec. 1992, pp. 229–247.

[51] Balakumar, P. and Malik, M., "Discrete modes and continuous spectra in supersonic boundary layers," *Journal of Fluid Mechanics*, Vol. 239, Jun. 1992, pp. 631–656.

[52] Stuckert, G., Herbert, T., and Esfahanian, V., "Stability and transition on swept wings," *AIAA Paper 93-0078*, Jan. 1993.

[53] Reed, H., Saric, W., and Arnal, D., "Linear stability theory applied to boundary layers," *Annual Review of Fluid Mechanics*, Vol. 28, 1996, pp. 389–428.

[54] Schrauf, G., "Transition prediction using different linear stability analysis strategies," *AIAA Paper 94-1848*, Jun. 1994.

[55] Schrauf, G., Perraud, J., Vitiello, D., and Lam, F., "A comparison of linear stability theories using F100 flight tests," *AIAA Paper 97-2311*, 1997.

[56] Lingwood, R., "On the impulse response for swept boundary layer flows," *Journal of Fluid Mechanics*, Vol. 344, Aug. 1997, pp. 317–334.

[57] Cooper, A. and Carpenter, P., "The stability of rotating-disc boundary layer flow over a compliant wall. Part 1: Type I and II instabilities," *Journal of Fluid Mechanics*, Vol. 350, Nov. 1997, pp. 231–259.

[58] Cooper, A. and Carpenter, P., "The stability of rotating-disc boundary layer flow over a compliant wall. Part 2: Absolute instability," *Journal of Fluid Mechanics*, Vol. 350, Nov. 1997, pp. 261–270.

[59] Bertolotti, F., Herbert, T., and Spalart, P., "Linear and nonlinear stability of the Blasius boundary layer," *Journal of Fluid Mechanics*, Vol. 242, Sep. 1992, pp. 441–474.

[60] Herbert, T., Stuckert, G., and Esfahanian, V., "Effects of freestream turbulence on boundary layer transition," *AIAA Paper 93-0488*, Jan. 1993.

[61] Bertolotti, F., "On the birth and evolution of disturbances in three-dimensional boundary layers," *IUTAM Symposium on Nonlinear Instability and Transition in 3D-Boundary Layers*, Kluwer Academic Publishers, Jun. 1996, pp. 247–256.

[62] Klebanoff, P., Tidstrom, K., and Sargent, L., "The three-dimensional nature of boundary layer instability," *Journal of Fluid Mechanics*, Vol. 12, Jan. 1962, pp. 1–34.

[63] Görtler, H. and Witting, H., "Theorie der sekundären Instabilität der laminaren Grenzschichten," *Proceedings IUTAM Symposium on Boundary Layer Research*, edited by H. Görtler, Springer Verlag Berlin, 1958, p. 110.

[64] Orszag, S. and Patera, A., "Secondary instability of wall-bounded shear flows," *Journal of Fluid Mechanics*, Vol. 128, Mar. 1983, pp. 347–385.

[65] Herbert, T., "Secondary instability of plane channel flow to subharmonic three-dimensional disturbances," *Physics of Fluids*, Vol. 26, No. 4, 1983, pp. 871–874.

[66] Herbert, T., "Secondary instability of boundary layers," *Annual Review of Fluid Mechanics*, Vol. 20, 1988, pp. 487–526.

[67] Fischer, T. and Dallmann, U., "Primary and secondary instability analysis of a three-dimensional boundary layer flow," *Physics of Fluids*, Vol. 3, No. 10, 1991, pp. 2378–2391.

[68] Koch, W., "On a degeneracy of temporal secondary instability modes in Blasius boundary-layer flow," *Journal of Fluid Mechanics*, Vol. 243, Oct. 1992, pp. 319–351.

[69] Balachandar, S., Streett, C., and Malik, M., "Secondary instability in rotating-disc flow," *Journal of Fluid Mechanics*, Vol. 242, Sep. 1992, pp. 323–347.

[70] Fischer, T., Hein, S., and Dallmann, U., "A theoretical approach for describing secondary instability features in three-dimensional boundary layer flows," *AIAA Paper 93-0080*, Jan. 1993.

[71] Fischer, T., "Ein mathematisch-physikalisches Modell zur Beschreibung transitioneller Grenzschichten," *DLR-FB 95-06*, 1995.

[72] Fasel, H., "Investigation of the stability of boundary layers by a finite-difference model of the Navier-Stokes Equations," *Journal of Fluid Mechanics*, Vol. 78, Nov. 1976, pp. 355–383.

[73] Meyer, F. and Kleiser, L., "Numerical investigation of transition in three-dimensional boundary layers," 1988, Proceedings AGARD Symposium on Fluid Dynamics of 3D-turbulent shear flows and transition, Cesme, Turkey, AGARD CP-438.

[74] Joslin, R., Streett, C., and Chang, C.-L., "Validation of three-dimensional incompressible spatial direct numerical simulation code," 1992, NASA Technical Paper 3205.

[75] Joslin, R., Streett, C., and Chang, C.-L., "Spatial Direct Numerical Simulation of boundary layer transition Mechanisms : Validation of PSE theory," *Journal of Theoretical and Computational Fluid Dynamics*, Vol. 4, 1993, pp. 1–18.

[76] Joslin, R. and Streett, C., "The role of stationary crossflow vortices in boundary layer transition on swept wings," *Physics of Fluids*, Vol. 6, No. 10, 1994, pp. 3442–3453.

[77] Müller, W., Bestek, H., and Fasel, H., "Nonlinear development of traveling waves in a three-dimensional boundary layer," *IUTAM Symposium on Nonlinear Instability and Transition in 3D-Boundary Layers*, Kluwer Academic Publishers, Jun. 1996, pp. 217–226.

[78] Wintergerste, T. and Kleiser, L., "Direct Numerical Simulation of transition in a three-dimensional boundary layer," *Transitional Boundary Layers in Aeronautics*, edited by R.A.W.M. Henkes and J.L. van Ingen, North-Holland, Amsterdam, Oxford, New York, Tokyo, 1996, pp. 145–153.

[79] Liu, C., Liu, Z., and McCormick, S., "Multilevel adaptive methods for incompressible flow in grooved channels," *Journal of Computational and Applied Mathematics*, Vol. 38, Dec. 1991, pp. 283–295.

[80] Liu, Z., Xiong, G., and Liu, C., "Receptivity to freestream vorticial disturbance of two- and three-dimensional airfoils," *AIAA Paper 96-2084*, Jun. 1996.

[81] Liu, Z., Zhao, W., and Liu, C., "Direct Numerical Simulation of transition in a subsonic airfoil boundary layer," *AIAA Paper 97-0752*, Jan. 1996.

[82] Liu, Z., Zhao, W., and Liu, C., "Direct Numerical Simulation of flow transition in a compressible swept wing boundary layer," *Advances in DNS/LES, Proceedings of the First AFOSR International Conference on DNS/LES*, Greyden Press, Columbus, OH, U.S.A., Aug. 1997, pp. 223–232.

[83] Radeztsky, R., Reibert, M., Saric, W., and Takagi, S., "Effect of micron-sized roughness on transition in swept wing flows," *AIAA Paper 93-0076*, Jan. 1993.

[84] Balakumar, P. and Hall, P., "Optimum suction distribution for transition control," *AIAA Paper 96-1950*, Jan. 1996.

[85] Kuethe, A. and Chow, C., *Foundations of Aerodynamics - Bases of Aerodynamic Design*, 4th edition, Wiley and Sons, 1985.

[86] Mack, L., "Transition prediction and linear stability theory," *Laminar-Turbulent Transition*, 1977, pp. 1.1–1.22, AGARD CP-224.

[87] Arnoldi, W., "The principle of minimized iterations in the solution of the matrix eigenvalue problem," *Quarterly of Applied Mathematics*, Vol. 9, No. 1, Apr. 1951, pp. 17–29.

[88] Saad, Y., "Variations on Arnoldi's method for computing eigenelements of large unsymmetric matrices," *Linear Algebra and its Applications*, Vol. 34, Dec. 1980, pp. 269–295.

[89] Sorensen, D., "Implicit application of polynomial filters in a k-step Arnoldi method," *SIAM Journal on Matrix Analysis and Applications*, Vol. 13, Jan. 1992, pp. 357–385.

[90] Golub, G. and Loan, C. V., *Matrix Computations*, 2nd edition, The John Hopkins University Press, 1989.

[91] Saad, Y., *Iterative Methods for Sparse Linear Systems*, PWS Publishing Company, 1996.

[92] Schlichting, H., *Boundary Layer Theory*, McGraw-Hill, 1987.

[93] Balakumar, P., "Finite amplitude stability of attachment-line boundary layers," *AIAA Paper 98-0338*, Jan. 1998.

[94] Meyer, F., "Numerische Simulation der Transition in dreidimensionalen Grenzschichten," *DLR-FB 89-12*, Jul. 1989.

[95] Balakumar, P., "Finite amplitude equilibrium solutions for plane Poiseuille-Couette flow," *Theoretical and Computational Fluid Dynamics*, Vol. 9, 1997, pp. 103–119.

[96] Balakumar, P. and Malik, M., "Stability and N-factor computations for the ONERA D- and NACA 64_2 A015-Wing," 1995, High Technonlogy Corporation (HTC)-Contractor Report.

[97] Corke, T. and Knasiak, K., "Stationary traveling crossflow mode interactions on a rotating disc," *Journal of Fluid Mechanics*, Vol. 355, Jan. 1998, pp. 285–315.

VITA

Erik Janke was born on April 2, 1965 in Berlin, Germany. His fascination with flying objects was strongly encouraged by his parents, in particular by his father Dieter Janke, who still has a strong interest in the ongoing space programs around the world.

Due to the demolition of the national aerospace industry in East Germany by the soviet government in the late 1960's, the only existing curriculum directly related to Aerospace Engineering was available at the Institute of Traffic and Transportation in Dresden, where Erik started his undergraduate studies in the field of Technology of Air-transportation in 1986. With the fall of The Wall and the related dramatic changes in East Germany in 1989, an opportunity arose to continue his graduate studies of Aerospace Engineering at the Technical University in Berlin where he received his Diplom-Ingenieur degree in 1993.

Following a recommendation of his advisor at the TU Berlin, Professor Dr. W. Nitsche, Erik continued his studies of Fluid Dynamics at Old Dominion University, Norfolk, Virginia, U.S.A. starting in August 1994 under the supervision of Professor P. Balakumar.

After graduation in 1998, he will return to Germany in order to take a postdoctoral position with the Deutsches Zentrum für Luft- und Raumfahrt (DLR) in Göttingen. There, he will be working on the topic of modeling and controlling of laminar-turbulent transition scenarios in transonic flows across wings of commercial transport aircraft.

IMAGE EVALUATION
TEST TARGET (QA-3)

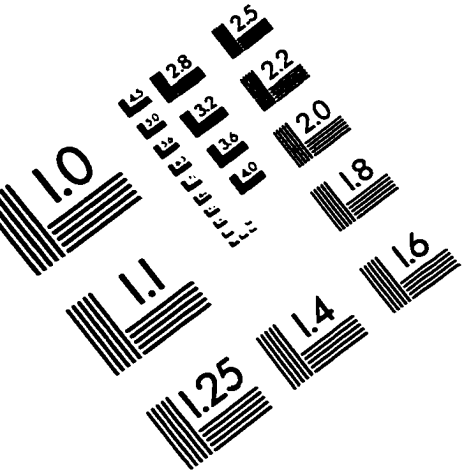

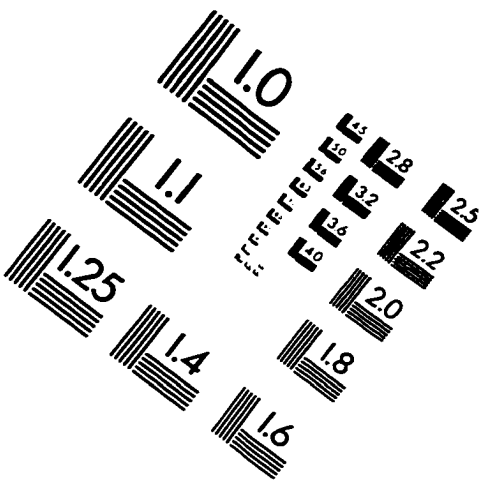

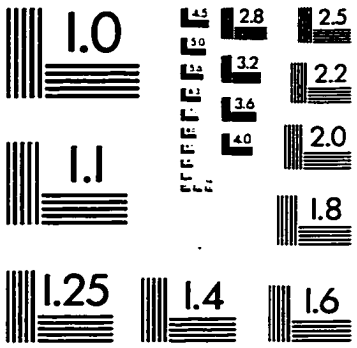

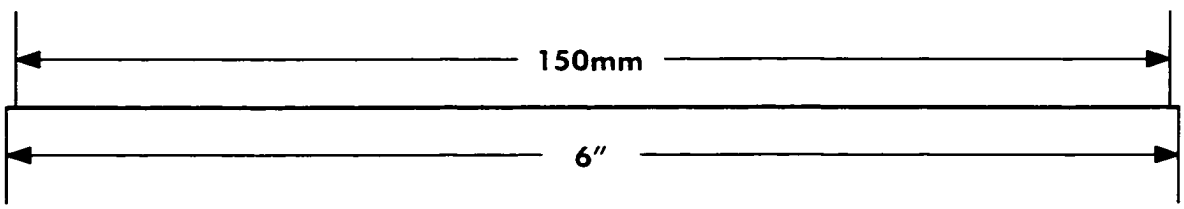

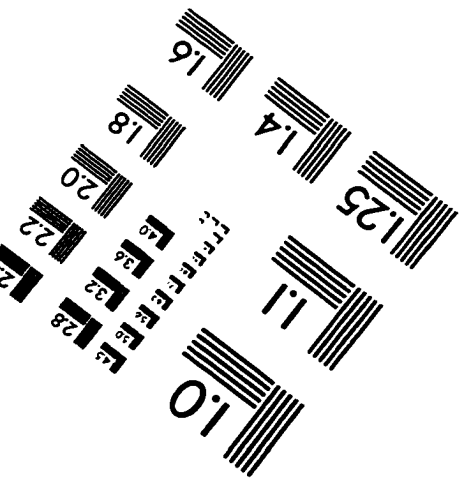

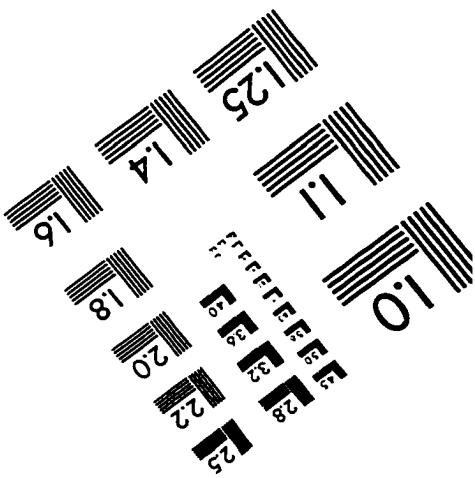

APPLIED IMAGE, Inc
1653 East Main Street
Rochester, NY 14609 USA
Phone: 716/482-0300
Fax: 716/288-5989